UNIVERSITÀ DEGLI STUDI DELLA TUSCIA

Department of Economics, Engineering,
Society and Business

Ph.D. Program

Engineering for Energy and Environment
XXXVIII Cycle

Funded by the PNRR Ministerial Decrees April 9th 2022, No. 352, thematic *"Multiphysics and multicode approach for the evaluation of Vertical Displacement Events related loads to support the design of the DTT vacuum vessel and in-vessel components"*

Ph.D. Thesis

"Development of a 2D axisymmetric FEM solver for plasma equilibria and design of the magnetic diagnostics layout based on synthetic signals for a TRUST-like tokamak"

S.S.D. IIET-01/A

Ph.D. Candidate
Dr. Matteo Notazio

Ph.D. Coordinator
Prof. Andrea Luigi Facci

Supervisor
Prof. Giuseppe Calabrò

Co-supervisor
Prof. Flavio Crisanti
Dr. Riccardo Lombroni

Academic Year 2024 – 2025

Contents

Abstract

Magnetic equilibrium and disruption analyses are fundamental to the design, operation, and protection of present and future tokamaks. This thesis addresses both aspects through a combined numerical and methodological effort, with specific emphasis on the TRUST device currently under design at Università degli Studi della Tuscia. The work is structured in three interconnected parts.

The first part focuses on disruption modelling using the legacy MAXFEA code, a 2D finite element solver widely adopted for electromagnetic analyses of plasma disruptions. A database of reference scenarios for EU-DEMO and TRUST has been produced, covering different vertical displacement events. The results provide quantitative assessments of halo currents, eddy currents and global electromagnetic loads.

The second part presents the development of a draft version of PECAN, a modern finite element code written in Python and based on DOLFINx, specifically tailored for solving the Grad–Shafranov equilibrium equation in both steady-state and transient regimes. The solver implements a Galerkin formulation, Picard iteration for the nonlinear problem, and monolithic integration with circuit equations. PECAN reproduces plasma equilibria for a range of devices, including DEMO, DTT, ST40 and TRUST, and has been benchmarked against MAXFEA. The extension to transient regimes enables the study of eddy currents in passive components and the dynamic coupling between plasma and external circuits, thus bridging equilibrium modelling and EM load assessment in a single framework, with application to VDEs in both EU-DEMO and TRUST. The results obtained were systematically compared with those previously produced using MAXFEA, showing consistent trends and validating the new implementation.

The third part applies these tools to TRUST, a compact university tokamak. Stationary equilibria were obtained and used as the basis for defining a preliminary layout of magnetic diagnostics. Synthetic signals from flux loops and magnetic probes were generated with PECAN and tested against reconstruction performed with EFIT, operated through the OMFIT framework. The results demonstrated that with a limited number of magnetic probes and flux loops, in a machine TRUST like, without any nuclear implication and where the environment noise is relatively low, the plasma boundary can be reliably reconstructed with an acceptable level of error across different plasma configurations and at various time instants within the discharge scenario, thus validating the proposed diagnostic layout. It should be noted, however, that this configuration represents a preliminary layout to be considered as a starting point, that along the TRUST life will be subject to studies finalised to

find out the minimum and most solid number of magnetic probes necessary on tokamaks reactor relevant.

Overall, this work advances the numerical modelling of plasma equilibrium and disruption dynamics, while directly supporting the design of TRUST-like devices. Beyond the immediate application, the methodologies developed herein contribute to the broader fusion community by integrating modern finite element methods with classical reconstruction tools, enabling both detailed EM analysis and practical diagnostic design.

Contributions

In addition to the work presented in this thesis, contributions were provided to research activities involving the use of the electromagnetic finite-element code MAXFEA and complementary tools such as ANSYS APDL. In particular:

- Electromagnetic analyses on the DTT Neutral Beam Injector (NBI) shielding structure to evaluate the influence of ferromagnetic materials on the plasma region using ANSYS APDL code;
- Co-author of “Development of SPARC plasma disruption database through electromagnetic predictive MAXFEA modelling” (2024), M. Scarpari; R. Lombroni; A. Mele; S. Carusotti; S. Minucci; G. Liuzzo; **M. Notazio**; V. Riccardo; G. Calabrò; P. Fanelli, Fusion Engineering and Design, Elsevier
    - *Post-processing of disruption analyses using MATLAB and generation of related figures.*
- Co-author of “Divertor Tokamak Test facility project: status of design and implementation“ (2024), Romanelli, F.; Abate, D.; Acampora, E.; Aggiuaro, D.; Agnello, R.; Agostinetti, P.; Agostini, M.; Aimetta, A.; Albanese, R.; Alberti, G.; et al., Nuclear Fusion, IOP Publishing
    - *Contribution to the DTT project, including plasma equilibrium simulations for both steady-state and disruption scenarios using MAXFEA code, the development of a MATLAB tool for the visualization and post-processing of MAXFEA input and output data, and electromagnetic analyses on the NBI shielding structure to assess the influence of ferromagnetic materials on the plasma region using ANSYS APDL code.*
- Co-author of “Physics basis for the divertor tokamak test facility” (2024), Crisanti, F.; Ambrosino, R.; Falessi, M.V.; Gabellieri, L.; Giruzzi, G.; Granucci, G.; Innocente, P.; Mantica, P.; Ramogida, G.; Vlad, G.; et al., Nuclear Fusion, IOP Publishing
    - *Contribution to the DTT project, including plasma equilibrium simulations for both steady-state and disruption scenarios using MAXFEA code, the development of a MATLAB tool for the visualization and post-processing of MAXFEA input and output data, and electromagnetic analyses on the NBI shielding structure to assess*

    - *the influence of ferromagnetic materials on the plasma region using ANSYS APDL code.*

- Co-author of "Preliminary Modeling of Disruption Plasma Scenario in View of a Shattered Pellet Injection in DTT Machine" (2025), L. Melaragni; M. Scarpari; S. Carusotti; M**. Notazio**; R. Lombroni; G. Ramogida; S. Migliori; A. Frattolillo; M. Angelucci; G. Calabrò, Fusion Science and Technology, Taylor & Francis
    - *Supervision of disruption simulations performed with the MAXFEA code and review of the obtained results.*
- Co-author of "Preliminary study on alternative magnetic layout (AML) for tokamaks reactors in the TRUST project framework" (2025), S. Carusotti, R. Lombroni, M. Scarpari, **M. Notazio**, A. Pizzuto, F. Crisanti, P. Fanelli, G.Calabrò, Engineering and Design, Elsevier
    - *Modelling of the equilibria for the preliminary plasma scenario using MAXFEA code*
- Co-author of "Overview of university-class Tokamak TRUST: Preliminary characterization of plasma scenario and disruption studies" (2025), S. Carusotti; R. Lombroni; M. Scarpari; **M. Notazio**; P. Fanelli; G. Calabrò, Engineering and Design, Elsevier
    - *Disruption simulations using MAXFEA code and plasma growth-rate analysis to define the optimal position of the stabilising plates.*

Part I – Scientific and Numerical Background

1. Magnetic Confinement Fusion

This chapter provides a general introduction to nuclear fusion and to the principles of plasma confinement by magnetic fields. It begins with an overview of fusion energy production and the physical basis of magnetic confinement, emphasizing the requirements in terms of plasma temperature, density, and confinement time. The discussion then moves to the tokamak configuration, which represents the most advanced and widely adopted magnetic confinement device. The main features of the tokamak are presented, including its magnetic field structure, operational principles, and relevance for present and future experimental programs. Overall, the chapter establishes the physical and technological background necessary to understand the subsequent developments discussed in the thesis.

1.1 Fusion energy and magnetic confinement principle

Throughout history, energy has represented a cornerstone of human development, enabling the rise of civilizations and sustaining economic growth. The Industrial Revolution, driven by the widespread exploitation of coal, initiated a profound transformation in technology and infrastructure, reshaping global energy consumption patterns. Since that turning point, energy demand has risen dramatically, fueled by industrial expansion, urban growth, and increasing population. Fossil fuels—namely coal, oil, and natural gas—have dominated the energy mix, providing more than 80% of the world's supply. These sources have been essential to the functioning of industries, transportation networks, and electricity systems, becoming the backbone of modern society. Yet, heavy dependence on fossil fuels presents critical issues. Their finite nature raises concerns over long-term availability, while their extraction and combustion remain the main drivers of greenhouse gas emissions. As highlighted by the International Energy Agency (IEA) [1], nearly three-quarters of anthropogenic CO_2 emissions originate from the global energy sector, intensifying climate change and undermining environmental balance. The consequences of this phenomenon—such as global warming, more frequent extreme weather events, and rising sea levels—emphasize the pressing necessity of a transition toward cleaner and more sustainable energy sources. In reaction to these challenges, the world is undergoing an energy transition marked by a growing commitment to renewable sources such as solar, wind, and hydropower. Over the past decades, these technologies have advanced significantly, benefiting from substantial cost reductions and notable gains in efficiency.

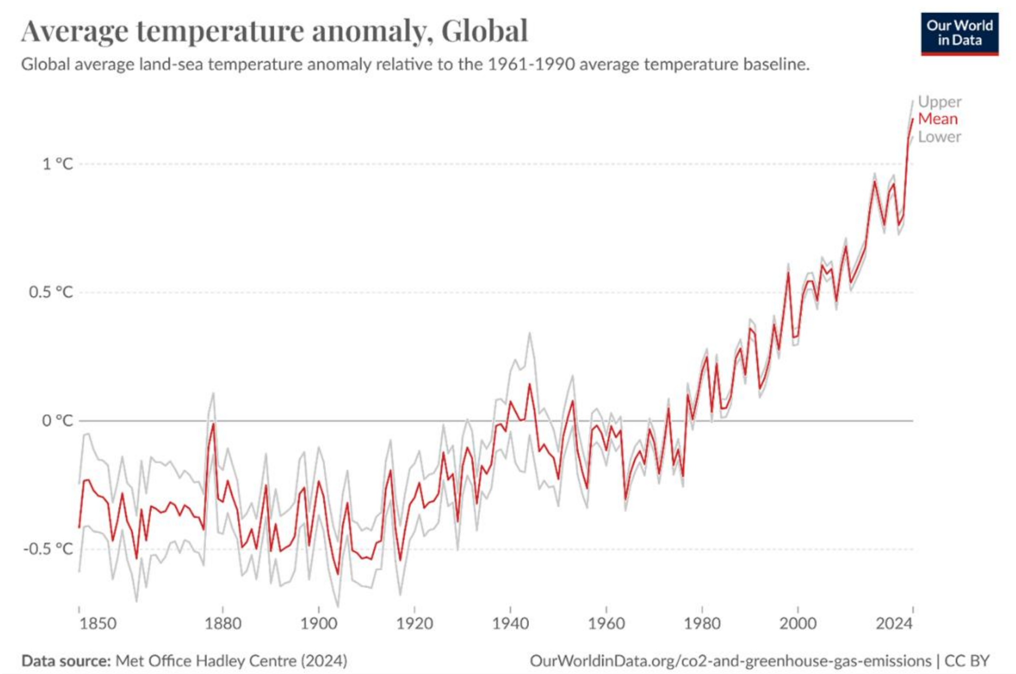

(a)

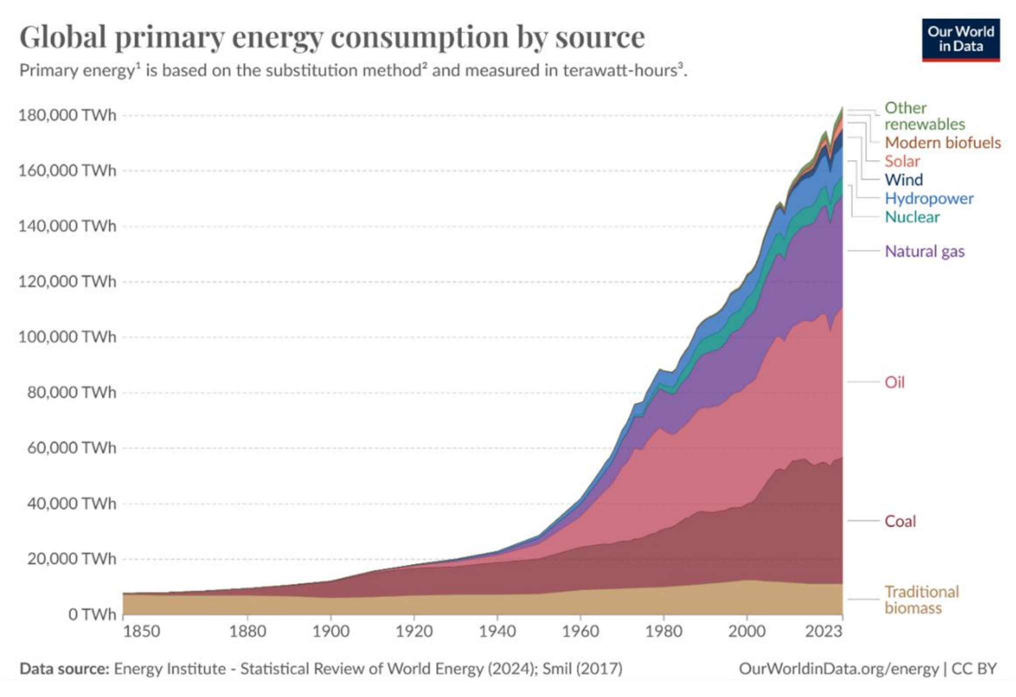

(b)

Figure 1: (a) Global energy average temperature anomaly and (b) Global primary energy consumption by typology of source.

Data from the International Renewable Energy Agency (IRENA) indicate that almost 80% of the new global electricity generation capacity installed in 2022 came from renewable sources. While this marks a major achievement, such technologies are not without constraints. Variability due to weather, intermittency, and location-specific availability limit their capacity to fully address the rising global demand for stable and continuous electricity supply [2]. Projections from the IEA's World Energy Outlook 2024 suggest that worldwide electricity consumption could nearly double by 2050, driven by demographic expansion, urban development, and the accelerating electrification of energy systems. Ensuring that this demand is satisfied while still adhering to climate objectives requires the deployment of complementary energy technologies capable of delivering large-scale, reliable, and low-carbon power. Within this framework, nuclear fusion is increasingly recognized as a promising candidate.

Fusion is the reaction in which light atomic nuclei merge to form heavier ones, releasing a large amount of energy in the process. It naturally takes place in stellar cores, where extreme temperatures and intense gravitational pressures allow hydrogen nuclei to overcome their mutual electrostatic repulsion and fuse together. This mechanism sustains stars such as the Sun, producing vast quantities of energy that radiate throughout the universe. For decades, replicating these conditions on Earth has been a central pursuit of the scientific community, since nuclear fusion offers the prospect of a virtually limitless and environmentally friendly energy source. Among the possible reactions, the most extensively investigated for terrestrial use is the fusion of deuterium and tritium, two isotopes of hydrogen. Their combination produces helium and a high-energy neutron, accompanied by a release of 17.6 MeV. Unlike chemical processes, which are governed by electron rearrangements, fusion draws its extraordinary energy yield from the conversion of mass into energy, as explained by Einstein's equation $E = mc^2$. The energetic neutron can be slowed down in a blanket surrounding the reactor, transferring its kinetic energy as heat, which can then be exploited by conventional power cycles to generate electricity. A key advantage of fusion lies in the availability of its fuels. Deuterium, a stable isotope, is plentiful in seawater, with about 33 grams contained in every cubic meter. Tritium, though scarce in nature, can be bred from lithium using fusion neutrons; lithium itself is widespread in both the Earth's crust and oceans, ensuring long-term accessibility. Unlike fossil fuels, often confined to specific regions and linked to geopolitical dependence, fusion fuels are evenly distributed and practically inexhaustible, offering a sustainable basis for global energy security [3][4].

Fusion represents a clean and intrinsically safe energy option, overcoming many of the drawbacks associated with conventional sources. In contrast to nuclear fission, which generates large quantities of long-lived radioactive waste and carries the possibility of severe accidents, fusion produces only limited radioactivity, mainly in the form of short-lived isotopes confined to reactor materials. Furthermore, fusion systems are inherently stable: they cannot sustain uncontrolled chain reactions, and any disturbance in the required conditions of temperature, pressure, or magnetic confinement leads to the immediate shutdown of the process, preventing large-scale incidents [5]. Another major advantage is that fusion does not emit greenhouse gases during operation, positioning it as a pivotal technology for meeting international climate goals. Replacing fossil fuels with fusion in the global energy mix would drastically cut carbon dioxide emissions, reduce the pace of climate change, and facilitate the transition toward a sustainable low-carbon future.

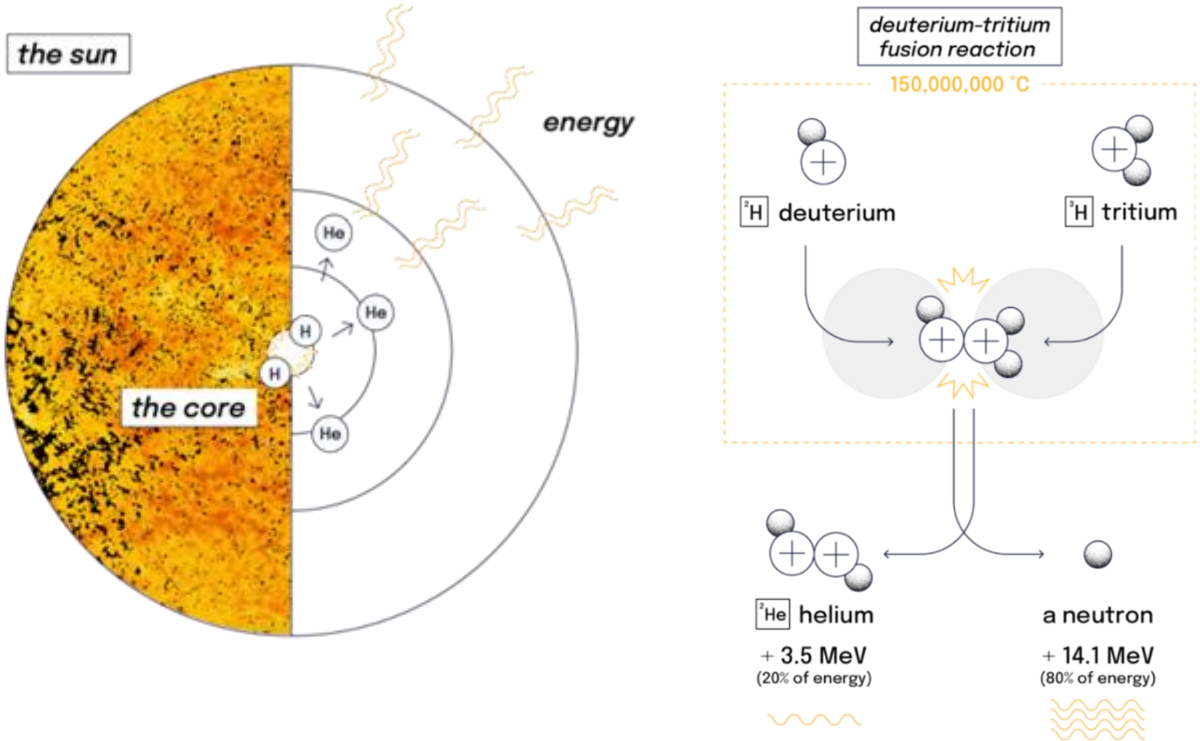

Figure 2: Schematic view of the nuclear fusion reaction occurring in the Sun. Light nuclei of hydrogen isotopes fuse under extreme temperature and pressure conditions, forming helium and releasing large amounts of energy that power stellar processes.

(Image: ITER Organization)

Despite its vast potential, realizing controlled nuclear fusion as a practical energy source remains one of the greatest scientific and technological challenges of our time. Fusion demands extreme physical conditions—temperatures exceeding 100 million degrees Celsius, sufficiently high particle densities, and adequate confinement durations. Under such circumstances, matter exists in the plasma state, where electrons and nuclei are fully separated. To sustain fusion reactions, this plasma must be stably confined, preventing direct contact with the reactor structure. Magnetic confinement devices, such as tokamaks, employ strong magnetic fields to contain the plasma within a toroidal configuration, thereby reducing energy losses and protecting structural integrity. Yet, maintaining plasma stability while enhancing confinement efficiency remains a critical obstacle, requiring advanced numerical simulations supported by experimental validation. Alongside these scientific hurdles, fusion development is also limited by major engineering and economic constraints. Reactor systems must be capable of withstanding the harsh fusion environment, including intense neutron fluxes and extreme thermal stresses. The use of advanced materials, particularly for plasma-facing components, is indispensable to guarantee both resilience and performance. Furthermore, economic considerations play a decisive role: fusion plants must not only achieve net energy production—generating more energy than they consume—but also adopt designs that can be scaled up and compete in cost with established energy technologies [6][7].

1.2 The tokamak machine

Among the different magnetic confinement concepts explored since the mid-20th century, the tokamak has emerged as the most advanced and widely adopted approach for controlled nuclear fusion. Developed in the Soviet Union and first demonstrated with convincing success in the late 1960s, the tokamak outperformed alternative configurations by achieving plasma parameters—particularly temperature and confinement time—orders of magnitude higher than those obtained in previous devices [5][8]. Its toroidal geometry, in which the plasma is contained within a doughnut-shaped vacuum vessel, enables the superposition of toroidal and poloidal magnetic fields. The resulting helical field lines guide charged particles, thereby minimizing transport losses and improving plasma stability [9][10].

The fundamental principle of tokamak operation lies in its capacity to confine plasma—an ionized state of matter consisting of free electrons and atomic nuclei—at temperatures exceeding 100 million degrees Celsius. Under such conditions, the plasma reaches the energy density required for fusion reactions, in which light nuclei such as deuterium and tritium merge into heavier nuclei, releasing considerable energy [5]. Magnetic confinement is indispensable, as it prevents the plasma from touching the reactor walls, where any contact would cause a rapid loss of heat and suppress the reaction. This confinement is achieved by combining toroidal magnetic fields, which encircle the reactor, with poloidal fields that loop around the plasma cross-section. The superposition of these fields generates helical magnetic trajectories that retain the charged particles inside the tokamak [9]. The toroidal field arises from powerful toroidal field (TF) coils surrounding the device, whereas the poloidal component is primarily sustained by currents induced in the plasma itself, driven by a central solenoid [10]. Together, these magnetic systems ensure not only the confinement of the plasma but also the preservation of its equilibrium and configuration within the chamber [5][9].

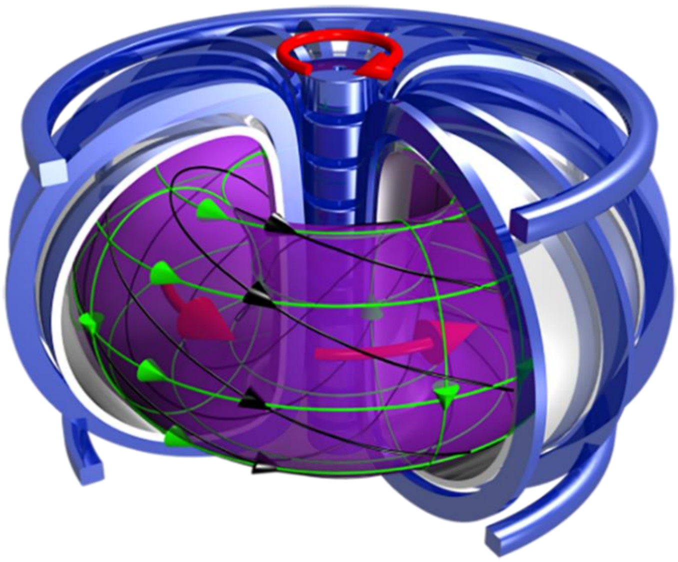

Figure 3: Schematic of plasma confinement in a tokamak. An electric field induced by the central solenoid drives a current through the plasma (red arrows), which in turn generates a poloidal magnetic field (green vertical circle). Together with the externally applied toroidal magnetic field (green horizontal circle), this results in helical magnetic field lines (black) that effectively confine the plasma within the doughnut-shaped vacuum vessel. (Image: Max Planck Institute for Plasma Physics, Germany)

Tokamaks are highly sophisticated devices composed of multiple interdependent subsystems, each essential for sustaining and regulating the fusion process:

- Vacuum Vessel (VV): The plasma is confined within a vacuum chamber maintained at ultra-high vacuum conditions to minimize contamination from impurities, which could otherwise cool the plasma and disrupt the reaction. The vessel must also accommodate diagnostic instruments and cooling systems while withstanding severe thermal and mechanical stresses during operation [11].
- Magnetic Coils: Plasma confinement relies on strong toroidal and poloidal magnetic fields generated by external coils. Modern designs employ advanced superconducting materials, such as Nb_3Sn or high-temperature superconductors (HTS), to efficiently produce the required magnetic fields [12][14].

- Central Solenoid (CS): Positioned at the centre of the device, the central solenoid induces the plasma current that generates the poloidal field, playing a crucial role in plasma initiation, ramp-up, and sustainment [12][14].
- Plasma-Facing Components (PFCs): Elements such as limiters and divertors protect the reactor walls from extreme heat and particle fluxes. The divertor is particularly important, as it removes helium ash and impurities while distributing thermal loads [12].
- Breeding Blanket (BB): Surrounding the plasma chamber, the breeding blanket absorbs energetic neutrons from the fusion reaction, converting their energy into heat for power generation. It also incorporates lithium to breed tritium through neutron–lithium interactions. Advanced blanket concepts are designed to maximize neutron capture, tritium production, and heat extraction while providing structural shielding [12].
- Cryogenic Systems: Superconducting magnets require cryogenic systems capable of maintaining temperatures close to absolute zero to ensure efficient operation and the generation of high magnetic fields [11].
- Auxiliary Heating Systems: In addition to ohmic heating from the plasma current, external heating methods are necessary to reach fusion-relevant temperatures. Neutral beam injection (NBI) introduces energetic neutral particles, while radiofrequency (RF) systems couple electromagnetic waves into the plasma to increase particle energy [12].
- Diagnostics: Comprehensive diagnostic suites continuously measure key plasma parameters—including temperature, density, and magnetic field structure—enabling precise control and optimization of plasma performance [13].

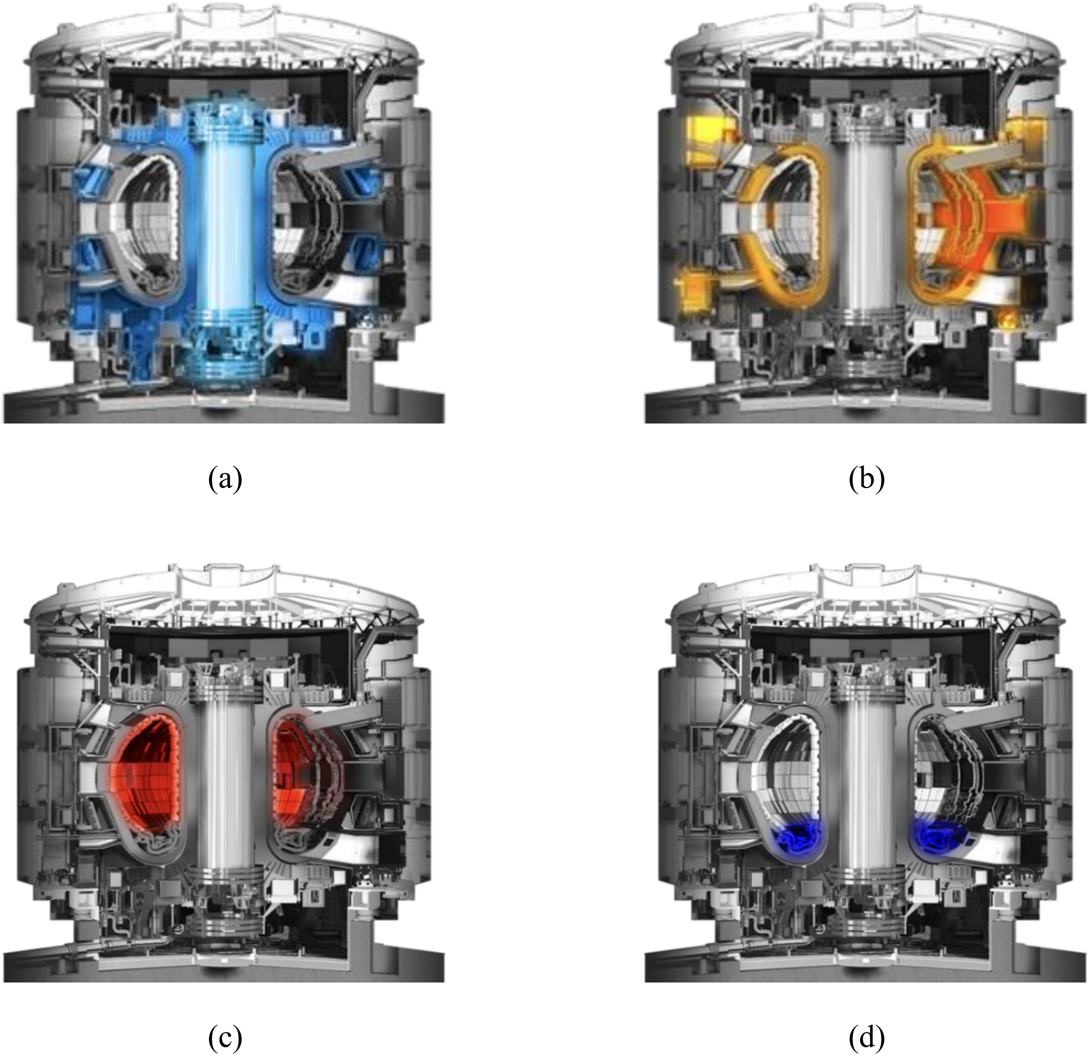

Figure 4: Tokamaks main systems: (a) TF and PF coils, (b) VV, (c) BB and (d) Divertor (Image: ITER Organization)

The evolution of tokamaks spans several decades, with numerous devices worldwide shaping the understanding of plasma physics and advancing the development of fusion technology. One of the most significant milestones has been the Joint European Torus (JET) in the United Kingdom [15], which has achieved record fusion power levels and generated critical datasets for the design of future large-scale facilities such as ITER. JET has been particularly valuable in demonstrating deuterium–tritium (D–T) operation, in developing advanced plasma regimes, and in testing materials for plasma-facing components. These achievements have firmly established JET as a cornerstone in international fusion research, providing the foundation for subsequent reactor-scale projects.

Currently under construction in France, ITER [3][7] represents the next major step forward. Designed to demonstrate, for the first time, the possibility of achieving net energy gain from fusion at reactor scale, ITER consolidates decades of experience from earlier machines. Its objectives include advancing magnet technologies, improving plasma control strategies, and validating tritium breeding blanket concepts. With its unprecedented size and complexity, ITER is expected to act as a pivotal bridge between experimental facilities and commercial fusion power plants.

In parallel, the European DEMOnstration Power Plant (EU-DEMO) [16][17] is being developed under the EUROfusion program as the successor to ITER. EU-DEMO is conceived to deliver net electricity to the grid while operating with a closed fuel cycle, thus providing the first integrated demonstration of a fusion power plant. Its design activities focus on high-availability superconducting magnets, tritium self-sufficiency, heat exhaust systems, and maintainability, aiming to bridge the gap between ITER's scientific mission and the requirements of commercial deployment.

Alongside ITER and EU-DEMO, other specialized tokamaks address particular challenges in the path to fusion energy. In Italy, the Divertor Tokamak Test (DTT) [18][19] is dedicated to investigating advanced divertor solutions, aimed at managing the extreme heat and particle exhaust expected in next-generation reactors. This facility is central for exploring strategies to ensure the safe operation of ITER and its successors. Meanwhile, in the United States, Commonwealth Fusion Systems in collaboration with MIT is developing SPARC [20][21], a compact, high-magnetic-field tokamak that leverages cutting-edge superconducting magnet technology. SPARC's goal is to demonstrate a high energy gain in a device of relatively small footprint, showing the potential of compact tokamaks to accelerate the transition from research to power production.

University-scale devices also play a vital role, both as testbeds for innovative technologies and as training grounds for future generations of fusion scientists. At MIT, the Alcator C-Mod [22] pioneered high-field, compact designs, demonstrating the ability to achieve enhanced plasma performance in reduced volumes and proving the importance of high magnetic fields for confinement. In Japan, Kyushu University operates QUEST [23], focusing on achieving steady-state plasmas through radiofrequency-driven current drive and exploring plasma–wall interaction phenomena. In the Czech Republic, the GOLEM tokamak [24], one of the oldest machines still operational, is primarily devoted to education and outreach, allowing students and researchers worldwide to gain hands-on experience and even participate in remote operation experiments. In Spain, the University of Seville has recently commissioned SMART [25], a small-aspect-ratio tokamak specifically designed to explore negative triangularity configurations in spherical tokamaks, with the aim of improving stability and confinement in compact geometries. Collectively, these academic machines contribute to the refinement of plasma control, the study of steady-state operation, and the exploration of innovative configurations, thereby complementing large-scale international projects.

A particularly promising branch of research focuses on spherical tokamaks [26], which adopt a low-aspect-ratio design. Unlike conventional devices with a large central aperture, spherical tokamaks feature a compact core resembling a cored apple, enabling higher magnetic field strength relative to size. This geometry allows improved plasma pressure and confinement while maintaining reduced device volume and construction costs. In the United Kingdom, the MAST Upgrade [27] explores advanced divertor concepts and plasma stability in such configurations, while in the United States, the National Spherical Torus Experiment (NSTX) [28] has pioneered the study of low-aspect-ratio plasmas. Both facilities address the challenge of controlling plasma instabilities and mitigating the mechanical stresses concentrated on the central column housing the toroidal field coils. Complementing these efforts, the privately developed ST40 tokamak [29][30][31] by Tokamak Energy in the UK demonstrates the potential of compact high-field spherical tokamaks. ST40 has already reached plasma temperatures above 100 million degrees Celsius, a critical threshold for proving the feasibility of efficient and economically viable fusion energy in smaller devices.

Within this landscape, the Tuscia Research University Small Tokamak (TRUST) represents a new academic-scale device currently under design at the University of Tuscia (UNITUS). Conceived as a flexible and cost-effective platform, TRUST aims to train the next generation of fusion engineers and physicists while addressing key scientific issues such as long-pulse power exhaust, in close connection with the research programs of EU-DEMO and DTT. The conceptual design targets an initial single-null plasma configuration with major parameters $R_0 = 0.3\ \mathrm{m}$, aspect ratio $A = 2.5$, plasma current $I_p = 110\ \mathrm{kA}$, toroidal field $B_T = 0.8\ T$, and safety factor $q_{95} = 3.2$. The device has been conceived with a modular approach, enabling straightforward replacement of plasma-facing components and the integration of innovative solutions, such as metamaterials and future upgrades of the poloidal field coils with high-temperature superconductors (HTS) operating at 77 K. In addition to the baseline single-null scenario, TRUST is designed to operate in double-null and upper single-null configurations, expanding its experimental versatility. Preliminary studies have investigated magnetic equilibrium, vertical stability, and thermal loads on the first wall and divertor, as well as disruption dynamics, leading to the establishment of a first disruption scenario database. Furthermore, an alternative magnetic layout (AML) has been proposed to facilitate assembly and disassembly procedures. With these features, TRUST stands as a valuable addition to the European fusion ecosystem, combining education, innovation, and technology development [32][33].

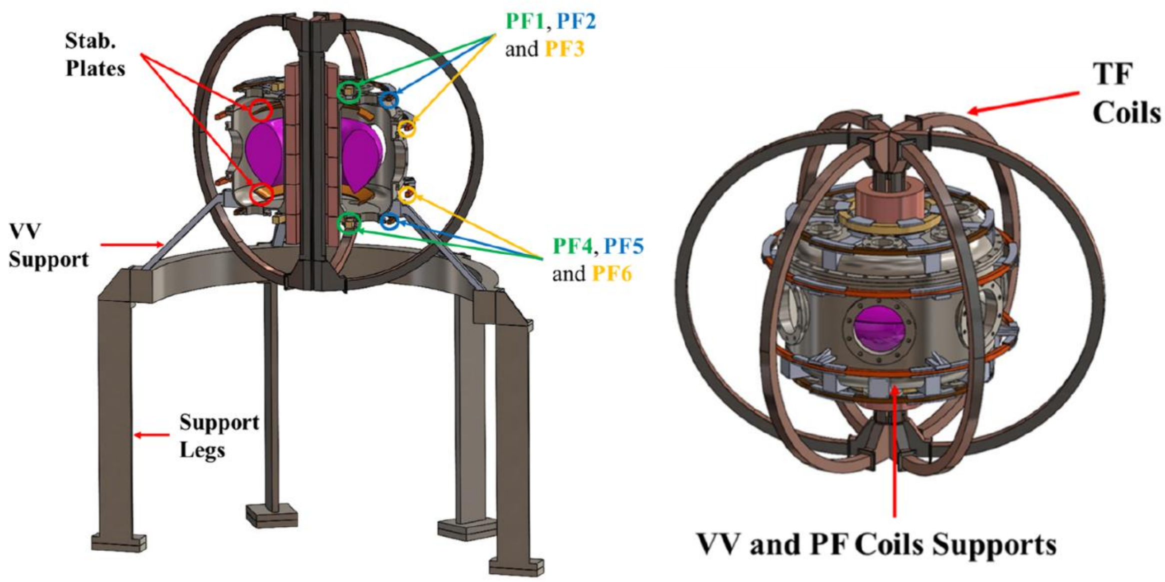

Figure 5: Schematic view of the TRUST conceptual layout, showing the assembly of the main subsystems.

2. Plasma Equilibrium in Tokamaks

This chapter introduces the fundamental aspects of plasma equilibrium in tokamaks, focusing on the balance between magnetic and kinetic forces that govern confined plasmas. The discussion begins with the theoretical framework of magnetohydrodynamics (MHD), which provides the basis for describing plasma behaviour in the presence of strong magnetic fields. Particular emphasis is placed on the derivation and interpretation of the Grad–Shafranov model, which represents the cornerstone of axisymmetric equilibrium studies in toroidal devices.

2.1 The Grad–Shafranov model

As described in Chapter 1, plasma is magnetically confined inside a toroidal chamber in tokamaks. The principle is based on transformer action: a toroidal plasma current is induced, generating a poloidal magnetic field. When combined with the externally applied toroidal magnetic field, this produces helical field lines that enclose the plasma, effectively confining charged particles. Since the toroidal component B_ϕ is usually about one order of magnitude stronger than the poloidal field B_θ, the guiding centres of the particles follow helical trajectories with a slow poloidal winding. Once the magnetic configuration is known, the position and shape of the plasma are uniquely determined [5].

The temporal behaviour of the plasma in a magnetically confined device such as a tokamak is determined by a complex interplay: on one side, diffusive phenomena within the plasma itself, and on the other side, electromagnetic interactions involving coils, passive structures, and the plasma. To reduce the complexity, a commonly adopted description is that of ideal magnetohydrodynamics (MHD), formulated under the assumptions of axial symmetry and null plasma resistivity. While in reality plasmas are characterized by a finite resistivity, the ideal MHD model is nonetheless sufficiently accurate to reproduce the main features of plasma current evolution and position, and is therefore extensively used in equilibrium and control studies [41].

The system of equations of the ideal MHD are governed by quasi-stationary Maxwell's equations [41]:

$$\nabla \times \mathbf{E} = -\frac{\partial \mathbf{B}}{\partial t} \tag{2.1}$$

$$\nabla \times \mathbf{H} = \mathbf{J} \tag{2.2}$$

$$\nabla \cdot \mathbf{B} = 0 \tag{2.3}$$

with the material constitutive relationships:

$$\mathbf{B} = \mu\mathbf{H} \tag{2.4}$$

$$\mathbf{J} = \sigma(\mathbf{E} + \mathbf{v} \times \mathbf{B}) \tag{2.5}$$

Here, $\mathbf{E}$ denotes the electric field, $\mathbf{B}$ the magnetic induction, $\mathbf{H}$ the magnetic field, $\mathbf{J}$ the current density, μ the magnetic permeability, σ the electrical conductivity and $\mathbf{v}$ the plasma velocity. Inside the plasma, the velocity is obtained from the momentum balance:

$$\rho\frac{d\mathbf{v}}{dt} = \mathbf{J} \times \mathbf{B} - \nabla p \tag{2.6}$$

Plasma pressure p, velocity $\mathbf{v}$ and density ρ are coupled with the continuity and conservation of energy equations, assuming adiabatic behaviour and entropy conservation for the fluid:

$$\frac{d}{dt}\left(\frac{p}{\rho^{\gamma}}\right) = 0 \tag{2.7}$$

$$\frac{\partial\rho}{\partial t} + \nabla \cdot (\rho\mathbf{v}) = 0 \tag{2.8}$$

Adopting cylindrical coordinates (R, ϕ, Z) and assuming axisymmetry (i.e., no dependence on the toroidal angle ϕ), the Equation (2.3) can be written as:

$$\frac{1}{R}\frac{\partial}{\partial R}(RB_R) + \frac{\partial B_Z}{\partial Z} = 0 \tag{2.9}$$

It is so possible to express $\mathbf{B}$ as function of a stream function Ψ for the poloidal magnetic field:

$$B_R = -\frac{1}{R}\frac{\partial\Psi}{\partial Z} \qquad B_Z = \frac{1}{R}\frac{\partial\Psi}{\partial R} \tag{2.10}$$

Where $\Psi = RA_\phi$ and A_ϕ is the toroidal component of the vector potential. The scalar function Ψ is defined as poloidal flux per unit radian $\Psi = \Psi_p/2\pi$, where Ψ_p represents the poloidal flux in the plasma:

$$\Psi_p = \int \mathbf{B_p} \cdot d\mathbf{A} \tag{2.11}$$

Where $\mathbf{B_p}$ denotes the poloidal magnetic field. Substituting the expression for the magnetic field into the Ampere's law, Equation (2.2), the current density $\mathbf{J}$ can be written as:

$$\mu_0\mathbf{J} = \mu_0 J_\phi \mathbf{e_\phi} + \frac{1}{R}\nabla(RB_\phi) \times \mathbf{e_\phi} \tag{2.12}$$

Where $\mathbf{e_\phi}$ is the toroidal unit vector. Hence, the RB_ϕ term is a free surface function named poloidal current function F (or f):

$$F(\Psi) = RB_\phi \tag{2.12}$$

The toroidal component $\boldsymbol{J_\phi}$ of the current density can be expressed as:

$$\mu_0 J_\phi = -\frac{1}{R}\,\Delta^*\Psi \tag{2.13}$$

The term $\boldsymbol{\Delta}^*$ is a second-order differential operator defined by:

$$\Delta^*\Psi \equiv \mathrm{R}^2\nabla\cdot\left(\frac{\nabla\Psi}{\mathrm{R}}\right) = R\frac{\partial}{\partial R}\left(\frac{1}{R}\frac{\partial\Psi}{\partial R}\right) + \frac{\partial^2\Psi}{\partial Z^2} \tag{2.14}$$

By further assuming that inertial effects can be neglected—an approximation justified by the extremely small plasma mass and by the characteristic time scales of plasma evolution (such as those associated with disruptions)—Equation (2.6) reduces to:

$$\mathbf{J}\times\mathbf{B} = \nabla p \tag{2.15}$$

From these relations it follows that $\mathbf{J}\cdot\nabla p = 0$ and $\mathbf{B}\cdot\nabla p = 0$, The latter implies that the plasma pressure is constant along magnetic field lines, and therefore can be expressed as a flux function, $p = p(\Psi)$, thus identifying it as a surface quantity. Considering Equations (2.10) and (2.12), these relations yields to $\nabla\Psi\cdot\nabla p = 0$ and $\mathbf{e_\phi}\cdot\nabla\Psi\times\nabla(RB_\phi) = \mathbf{e_\phi}\cdot\nabla\Psi\times\nabla F = 0$.

Considering these relations and introducing (2.10) and (2.12) in the equilibrium condition (2.15), with some algebra it is possible to obtain:

$$\Delta^*\Psi = -\mu_0 R^2\frac{dp}{d\Psi} - F\frac{dF}{d\Psi} \tag{2.16}$$

That is the so-called Grad-Shafranov equation. In addition:

$$\mathbf{B} = \frac{1}{\mathrm{R}}\nabla\Psi\times\mathbf{e_\phi} + \frac{F}{R}\,\mathbf{e_\phi} \tag{2.17}$$

$$\mu_0\mathbf{J} = \frac{1}{R}\frac{dF}{d\Psi}\nabla\Psi\times\mathbf{e_\phi} - \frac{1}{R}\,\Delta^*\Psi\,\mathbf{e_\phi} \tag{2.18}$$

2.2 Plasma magnetic configurations

Rigorously, the functions $p(\Psi)$ and $F(\Psi)$ should be obtained by solving the transport equations (2.6), (2.7) and (2.8). Nevertheless, it is well established that magnetohydrodynamic (MHD) equilibria can be adequately described by a limited number of scalar degrees of freedom (DOF). In particular, [44] demonstrates that the plasma current profile can be satisfactorily represented using only three global parameters: the total plasma current I_p, the poloidal beta β_p, and the normalized internal inductance ℓ_i. These quantities are defined as:

$$\beta_p = \frac{4}{\mu_0 R_0 I_p^2} \int_{\Sigma_p} p \ d\Sigma \tag{2.19}$$

$$\ell_i = \frac{2\pi}{\mu_0^2 R_0 I_p^2} \int_{\Sigma_p} B_p^2 \ d\Sigma \tag{2.20}$$

Where Σ_p represents the plasma volume and R_0 is the reference machine radius, expected to be approximately equal to the plasma geometric radius and comparable to the plasma current barycentre $\left(R_p, Z_p\right)$ defined as:

$$R_p = \frac{1}{I_p} \int_{\Omega_p} R\, J_p(\Psi) \ d\Omega \tag{2.21}$$

$$Z_p = \frac{1}{I_p} \int_{\Omega_p} Z\, J_p(\Psi) \ d\Omega \tag{2.22}$$

Using this approximation, the functions (Ψ) and $F(\Psi)$ can be expressed in terms of I_p, β_p and ℓ_i. Therefore, (2.16) becomes a free-boundary problem, where the plasma boundary is one of the unknowns. The equilibrium at each time is obtained once the plasma parameters of I_p, β_p and ℓ_i are prescribed, and the toroidal current density in the external conductors is given or dynamically determined. These two macroscopic quantities β_p and ℓ_i, which define the equilibrium of the plasma pinch in tokamaks, are correlated each other as defined by Shafranov in [45] for plasmas characterized by $a/R \ll 1$:

$$\beta_p + \frac{\ell_i}{2} = \frac{s_1}{2} + s_2 \tag{2.23}$$

Where R and a are respectively the plasma major and minor radii, the terms s_1 and s_2 are surface integrals of products of the poloidal magnetic field components outside the plasma which can, in principle, be measured [45].

The plasma boundary is conventionally defined as the outermost closed magnetic flux surface entirely contained inside the vacuum vessel and is determined through an iterative calculation. Topologically, the boundary is either the last flux contour not intersecting any solid object or a separatrix, i.e. a surface containing an x-point where the poloidal magnetic field vanishes and the flux function exhibits a saddle point. The comparison between the flux at the x-point Ψ_{xp} and the maximum flux along the first wall Ψ_{FW} establishes the plasma configuration. If $\Psi_{xp} > \Psi_{FW}$, the separatrix is internal to all flux surfaces that touch the wall, and the plasma is in a diverted configuration, with the boundary defined by the separatrix itself. Conversely, if this condition is not satisfied, the plasma is in a limited configuration, where the boundary physically contacts the first wall at the limiter point P_{lim}, characterized by $\Psi(P_{lim}) = \Psi_{FW}$.

Over the years, several numerical codes relying on iterative procedures have been developed to solve the axisymmetric MHD equilibrium problem. Among the most widely used for ITER design are CarMa0NL [46], DINA, and TSC [47].

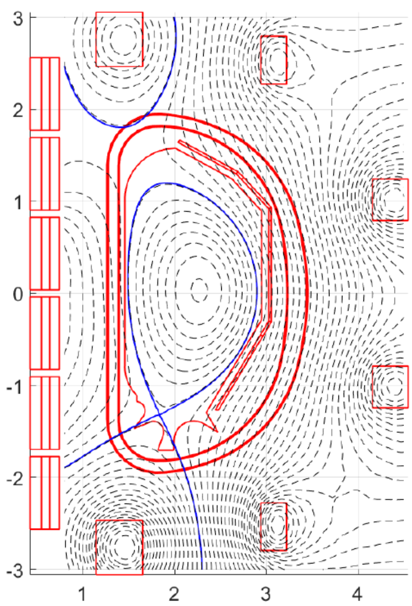

Figure 6:Example of the poloidal flux map for a diverted plasma configuration, with the separatrix highlighted in blue.

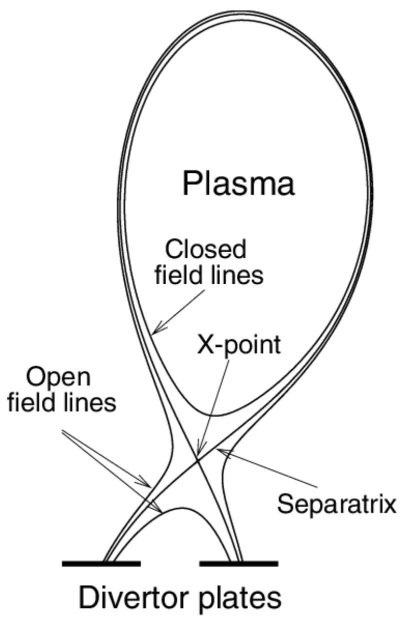

Figure 7: Schematic representation of the plasma in a diverted configuration.

2.3 Disruptions

During tokamak operation, the plasma can occasionally experience abrupt terminations of the discharge known as disruptions, which are among the most critical transient events in magnetically confined fusion plasmas. These events are characterized by a sudden loss of thermal and magnetic energy, leading to intense heat fluxes and electromagnetic (EM) loads on in-vessel and ex-vessel structures [4][5][12]. Despite significant progress in feedback control, their complete avoidance remains one of the main technological and scientific challenges for present and future devices, from ITER to DEMO [14][17].

A complete disruption is conventionally divided into two main phases:

1. The thermal quench (TQ) marks the collapse of the plasma temperature in a few milliseconds, caused by strong transport enhancement and impurity radiation losses. As a result, the plasma resistivity rises by several orders of magnitude, leading to a drastic loss of confinement and the deposition of concentrated heat loads on plasma-facing components [57].
2. Subsequently, during the current quench (CQ), the plasma current I_p decays rapidly, typically within tens to hundreds of milliseconds. The associated time variation of the magnetic flux induces strong voltage transients that generate eddy currents in surrounding conducting structures and halo currents through the vessel walls where plasma–wall contact occurs [35][49][50][51]. The interaction between these current systems gives rise to large Lorentz forces, often exceeding the nominal operational loads.

Among the various disruption typologies, Vertical Displacement Events (VDEs) play a particularly relevant role for the mechanical design of the tokamak. A VDE occurs when the plasma column loses vertical stability and drifts upward or downward until it strikes the vessel wall. The resulting interaction between the plasma current and the induced image currents in the surrounding structures produces substantial electromagnetic forces, sometimes highly asymmetric. Such asymmetries can generate significant net vertical forces and torques on the vacuum vessel [37][43] reaching tens of meganewtons in large-scale devices such as ITER and DEMO [35][36]. The understanding of these mechanisms is thus fundamental for ensuring the structural integrity of the vacuum vessel, stabilizing plates, supports, and all conductive components exposed to transient fields [30][31].

The complexity of plasma–structure coupling during disruptions has motivated the development of extensive experimental databases, such as the ITPA Disruption Database [34], which collects data from multiple tokamaks worldwide to classify disruptions based on their characteristic timescales, plasma current decay constants, and vertical displacement dynamics. These databases have provided a benchmark for the definition of “slow” and “fast” disruption scenarios, later used in numerical modelling for design and validation purposes. Complementary analyses have been carried out on medium and small-sized tokamaks such as DTT [57], ST40 [30][31], QUEST [23], and GOLEM [24], further extending experimental insight into disruption dynamics and providing valuable data for code benchmarking and validation.

From a computational standpoint, accurate prediction of the electromagnetic loads induced during disruptions requires numerical solvers capable of coupling the evolution of the plasma current with the response of surrounding conducting structures. Finite element (FEM) formulations have proven particularly suitable for this purpose, as they allow representing realistic geometries, spatially varying material properties, and mutual coupling with external circuits. Over the past decades, the MAXFEA code [48] has become a reference tool for disruption analysis, widely employed to evaluate eddy and halo current distributions, induced voltages, and mechanical load envelopes in devices such as IGNITOR, DEMO, DTT, and ST40. More recently, novel computational environments have been developed to take advantage of modern numerical libraries and high-level programming architectures, such as CARMA0NL. Among them, the PECAN framework represents the prototype of a new generation of finite-element solvers designed to simulate both stationary equilibria and transient plasma–structure coupling within a unified formulation.

PECAN extends the modelling capability of classical tools like MAXFEA by integrating a modular object-oriented structure and leveraging high-performance finite element backends. It enables consistent treatment of equilibrium, VDEs, and current-quench transients while facilitating coupling with diagnostic and control models—an essential aspect for future tokamak design, such as TRUST at the University of Tuscia [33].

The study of plasma disruptions thus provides not only a benchmark for electromagnetic solvers but also a crucial motivation for the development of new computational frameworks capable of handling both equilibrium and transient regimes.

3. Plasma Equilibria: Computational Tools

This chapter presents the computational frameworks employed in this work, focusing on two finite element (FEM) solvers for axisymmetric tokamak equilibria: MAXFEA and PECAN. MAXFEA is a well-established code that has been developed and benchmarked over the years, and has been extensively applied to several tokamak devices for the analysis of both stationary equilibria and plasma disruptions [43]. Its robustness and long-standing validation make it a natural reference tool for preliminary studies and for providing benchmark cases.

Building on this foundation, the PECAN project is introduced as a new development effort aimed at extending the modelling capabilities by exploiting modern numerical libraries and software design strategies. PECAN is conceived as a flexible and modular environment that enables both equilibrium and transient analyses in a consistent framework, with the long-term goal of integrating advanced plasma models and diagnostics.

3.1 MAXFEA: finite element code for axisymmetric plasma equilibrium and disruptions

The MAXFEA code is a two-dimensional FEM solver developed by Pietro Barabaschi in 1991-1992 [48] for the simulation of plasma equilibrium and transient events in axisymmetric magnetic confinement devices. It is fully written in Fortran77 and provides a Graphical User Interface (GUI) that makes it accessible not only as a physics solver but also as an engineering tool.

MAXFEA includes several unique features that are rarely available in other plasma equilibrium codes [49]:

- a CAD environment with a free triangular mesh generator, allowing the creation and modification of machine geometries;
- an electromagnetic module capable to solve the Grad-Shafranov equation (2.16) for the free boundary problem, both in the stationary and transient cases.

  Different regions of the computational domain are described by distinct expressions of the toroidal current density J_ϕ:

  - Vacuum and air, where $J_\phi = 0$
  - Active conductors (CS and PF coils), where $J_\phi = J_0$, prescribed by the coil current and geometry.

- Passive conducting structures, where the Faraday law implies:

$$J_e(\Psi) = -\frac{\sigma}{\mathrm{R}}\frac{\partial\Phi}{\partial t} \tag{3.2}$$

With σ is the conductivity and Φ is the total poloidal flux Ψ concatenated to the passive structures, describing induced eddy currents distribution.

- Plasma region:

$$J_\phi = J_p(\bar{\Psi}) = \lambda\left[\frac{R}{R_0}\beta - \frac{R_0}{R}(1-\beta)\right](1-\bar{\Psi}^\alpha)$$
$$\bar{\Psi} = \frac{\Psi - \Psi_{axis}}{\Psi_{boundary} - \Psi_{axis}} \tag{3.3}$$

Where α and β are profile parameters, R is the generic radial coordinate, R_0 is the reference radius (for instance, the machine radius) and λ is a scaling factor chosen by the code to match a prescribed target value of the plasma current.

According to the Grad-Shafranov equation (2.16), the expression of J_p can be rewritten as:

$$J_p(\bar{\Psi}) = \lambda\left[\frac{R}{R_0}\beta - \frac{R_0}{R}(1-\beta)\right](1-\bar{\Psi}^\alpha) = Rp'(\bar{\Psi}) + \frac{1}{\mu_0 R}FF'(\bar{\Psi}) \tag{3.4}$$

Within the equilibrium codes, usually the profiles p' and FF' are expressed in terms of the profile parameters α and β:

$$p'(\bar{\Psi}) = \frac{\lambda\beta}{R_0}(1-\bar{\Psi}^\alpha) \tag{3.5}$$

$$FF'(\bar{\Psi}) = \lambda\mu_0 R_0(1-\beta)(1-\bar{\Psi}^\alpha) \tag{3.6}$$

The plasma pressure p and poloidal current function F are so defined as:

$$p(\bar{\Psi}) = \int_{\bar{\Psi}}^{1} p'\,d\bar{\Psi} = \frac{\lambda\beta}{R_0}\frac{(1-\bar{\Psi})^{\alpha+1}}{\alpha+1} \tag{3.6}$$

$$F^2(\bar{\Psi}) = 2\int_{\bar{\Psi}}^{1} FF'\,d\bar{\Psi} = -2\lambda\mu_0 R_0\frac{(\beta-1)(1-\bar{\Psi})^{\alpha+1}}{\alpha+1}$$
$$F(\bar{\Psi}) = \sqrt{F_0^2 + F^2(\bar{\Psi})} \tag{3.7}$$

Where $F_0 = R_0 B_T$, with B_T corresponds to the toroidal magnetic field value at machine radius for the vacuum case.

- a comprehensive post–processor, enabling both spatial distribution and time–evolution visualization of plasma and conductor quantities.

The MAXFEA code solves the coupled electromagnetic problem of coils, plasma, and passive structures through a finite element (FE) formulation, assembling all contributions into a single linear system. This approach allows for the consistent treatment of mutual inductive effects between active and passive components. The same formulation has later been adopted in PECAN, which replicates the coupling strategy of MAXFEA within a modern FEM framework. The detailed derivation of the governing equations and their weak form is reported in Part III, Chapter 5.1.

When used for disruptions simulations, MAXFEA allows to evolve a reference starting equilibrium according to a predefined disruption scenario following a series of pre-programmed or user activated events. In addition to provide a complete description of the plasma evolution in terms of plasma movement, current distribution, magnetic field, and so forth, MAXFEA provides information on the EM loads acting on the components as result of the interaction between the toroidal currents, both external and induced, and the poloidal field. This kind of interaction is typically the dominant term in the eddy current related global forces in the components. Therefore, MAXFEA provides a good approximation in terms of total currents and forces induced in the structures.

In this context, Halo Current (HC) represent one of the main EM loads on the components during disruptions. MAXFEA code treats the HC with a first-principle method. Since MAXFEA assumes that plasma evolves with quasi-static approximation, the plasma is always in a state of mechanical equilibrium and therefore the following force balance holds:

$$F_{pla} = F_{coils} + F_{eddy} + F_{halo} = 0 \tag{3.4}$$

Where F_{coils} is the force that the external active coils exert on the plasma, while F_{eddy} is the force that the plasma experiences due to the presence of induced eddy currents in the surrounding structures. From this force balance, MAXFEA estimates the global force that halo currents (HC) exert on the surrounding structures. The halo behaviour is modelled by redefining the plasma boundary as the magnetic surface corresponding to a flux equal to that of the last closed flux surface (LCFS) minus a prescribed fraction, specified as an input parameter. Based on this assumption for the halo region width and the force balance, the total HC magnitude is evaluated. This approach enables MAXFEA to simulate the plasma evolution while accounting for the presence of halo currents. However, the code does not resolve the detailed distribution or paths of the HC within the structures, but instead provides only global information on the expected total poloidal halo current.

3.2 PECAN: the new project for a modular framework for plasma equilibria

The Plasma Equilibrium Coupled ANalysis (PECAN) project was originally conceived by Dr. Riccardo Lombroni and Dr. Ivan Alessio Maione as a new-generation computational framework for plasma equilibrium studies. Its primary aim is to provide a python-based flexible and modular tool capable of treating self-consistent non-linear axisymmetric plasma evolutions in the presence of three-dimensional conducting structures. Thanks to its modular design, PECAN is envisioned to support a wide spectrum of activities that are of central importance in fusion reactor research and design, including equilibrium and scenario optimization, magnetic control, disruption simulation, and the assessment of electromagnetic loads on passive and active components.

A distinctive feature of PECAN is its potentiality to operate in synergy with different external electromagnetic environments—both commercial (e.g. ANSYS, COMSOL, MATLAB) and open-source frameworks—thus offering users the possibility to carry out analyses with a wide range of numerical tools and methodologies [50]. Although this coupling capability has not yet been implemented, it represents a planned extension of the code development and will be addressed in forthcoming stages of the project. This open and interoperable philosophy is intended to foster adaptability and integration, making PECAN a versatile environment suitable for both physics-driven investigations and engineering-oriented applications.

While MAXFEA has proven extremely valuable for decades of applications to a variety of tokamak scenarios, from compact devices to DEMO-scale machines, its Fortran77 structure and monolithic architecture impose limitations in terms of extensibility, numerical flexibility, and integration with modern computational workflows. PECAN addresses these challenges by adopting a modular software architecture, designed to accommodate new physics models and coupling strategies, while fully exploiting state-of-the-art open-source FEM libraries.

Within this project, the author has contributed as a code developer, representing the University of Tuscia, with a specific focus on the design of a draft version of a full finite element (FEM) 2D architecture based on DOLFINx [52]. This prototype has been developed to explore the implementation of FEM formulations for the solution of the Grad–Shafranov equation in the free-boundary problem [53], addressing both the static equilibrium and the time-dependent evolution. In this way, the draft code extends PECAN’s capability to capture axisymmetric plasma equilibria coupled with the electromagnetic response of surrounding conductors, providing a consistent framework for stationary and transient regimes. The mathematical formulation adopted is discussed in detail in Chapter 5.

The DOLFINx-based approach not only offers a modern and high-performance backend for numerical computations, but also ensures long-term maintainability, modularity, and scalability of the solver. Importantly, the architecture of this draft version has been conceived taking inspiration from the MAXFEA code, which for decades has been employed for 2D axisymmetric analyses of plasma equilibrium and disruptions. By reinterpreting the methodological foundations of MAXFEA within a modern FEM framework, the new implementation aims to provide a versatile environment that combines the robustness of established approaches with the flexibility of contemporary open-source tools.

Overall, PECAN combines the physics fidelity of FEM formulations with the flexibility of modern modular design, positioning itself as a promising successor to MAXFEA and as a valuable platform for the academic and industrial fusion communities.

Part II – Preliminary Work with MAXFEA

4. Preliminary Benchmark Disruption Studies with MAXFEA

This chapter illustrates the preliminary activities conducted with the MAXFEA code, conceived as a preparatory stage for the subsequent development of PECAN. The work provides a twofold benefit. First, it enables the creation of a benchmark database of reference disruption scenarios, which will be systematically reproduced within PECAN to validate its accuracy and robustness. Second, it establishes a reliable framework for electromagnetic analyses applicable to both large-scale devices such as EU-DEMO and university-scale experiments like TRUST.

The significance of these studies is confirmed by their recognition in different contexts: in the case of DEMO, the disruption analyses performed with MAXFEA have been formally evaluated and endorsed by the EUROfusion consortium [54]; for TRUST, the results have been presented to the scientific community and disseminated through a dedicated publication [33].

4.1 Benchmark Disruption Studies for EU-DEMO using MAXFEA

In the framework of the new EU-DEMO Low Aspect Ratio (LAR) 2024 concept, a dedicated electromagnetic activity has been carried out using the MAXFEA code. The objective was to implement a MAXFEA model capable of simulating a set of representative plasma disruption scenarios in DEMO with the updated baseline configuration. The selected cases include:

- Fast upward vertical displacement event (fast UVDE),
- Slow upward vertical displacement event (slow UVDE),
- Fast downward vertical displacement event (fast DVDE),
- Slow downward vertical displacement event (slow DVDE)

The classification between slow and fast Vertical Displacement Events (VDEs) adopted for the simulations is based on the reference time scales reported in the ITPA Multi-Machine Disruption Database [34], which provides experimentally derived ranges for current-quench (CQ) durations observed across several tokamaks. Both for DEMO and TRUST, these ITPA reference values were used as a guideline to define representative decay constants for the prescribed plasma-current evolution, as applied in [21].

For DEMO, the CQ time constants adopted in this work, ranging from about 80 ms up to about 500 m, are consistent with those reported in recent DEMO design studies, such as [35] and [56] which in turn align with the characteristic “fast” and “slow” regimes identified in the ITPA database.

Adopting the formulas in [34] for DEMO, we can assume $S \approx 50\ m^2$ for the plasma poloidal cross-section and approximate the dimensionless plasma self-inductance L^* as:

$$L^* = \ln\left(\frac{8R}{a}\right) - 1.75 \approx 1.4 \qquad (4.1)$$

Considering $R = 8.6\ m$ and $a = 3\ m$. Imposing $18.79\ MA$ as plasma current, J_p can be approximated as $\sim 0.4\ MA/m^2$ and $\Delta t_{80-20}/(SL^*)$ can be estimated as $\sim 0.7\ ms/m^2$ from the graph in [34]. Reversing the formula, $\Delta t_{80-20} = 49\ ms$ can be obtained representing the 60% of the CQ duration for the fast events. The total duration of the CQ can be easily obtained as:

$$CQ_{fast} = \frac{\Delta t_{80-20}}{0.6} \approx 82\ ms \qquad (4.2)$$

This value has been increased by the 5% for a conservative approximation, obtaining the value of 86 ms adopted for the simulations. The duration of the CQ for the slow events has been considered ~6 times the duration of the fast ones [21].

Similarly, for TRUST, parametric decay times were selected for the simulations reported in Chapter 4.2 within the same experimental range to ensure physical consistency with observed VDE dynamics in comparable medium scale tokamaks.

In this framework, the “slow” and “fast” categories therefore retain a direct correspondence with the phenomenological regimes documented by the ITPA database, while remaining compatible with the purely electromagnetic nature of the MAXFEA and PECAN models, in which the plasma current evolution is prescribed analytically rather than derived from transport equations.

As mentioned above, this preliminary work is intended as a preparatory step for the subsequent developments within PECAN. By establishing a set of reference disruption cases with MAXFEA, a consolidated database of plasma evolutions and corresponding EM loads can be created. These reference cases will then serve as a benchmark for the validation and further extension of PECAN, enabling a consistent comparison between the two solvers and supporting the long-term goal of performing reliable disruption analyses for DEMO.

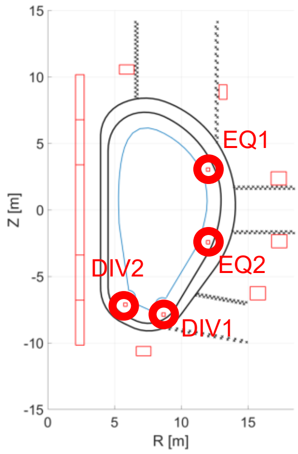

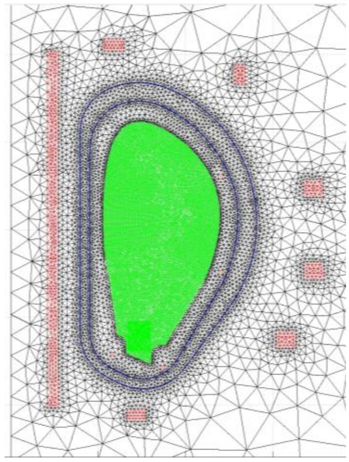

(a) *(b)*

Figure 8: (a) Overview of the DEMO LAR model. Compared to the previous baseline configurations, this concept introduces four in-vessel coils (IVCs), namely EQ1, EQ2, DIV1, and DIV2. These IVCs form two passive circuits: the EQ circuit, obtained by connecting EQ1 and EQ2 in anti-series, and the DIV circuit, obtained in the same way by the anti-series connection of DIV1 and DIV2. (b) Overview of the 2D mesh on plasma region.

Equilibrium

The starting point for the VDE simulations has been the plasma equilibrium at the End of Flat-top (EOF) instant reported in Figure 9, which is considered as the reference operating condition for disruption analyses in DEMO LAR. As a benchmark, the reference equilibrium generated with the CREATE-NL code [38] has been adopted, and the strategy to reproduce it within MAXFEA follows the same approach already applied in previous disruption studies for EU-DEMO [56] and experimental data validation for ASDEX, JET and ST40 [30][31].

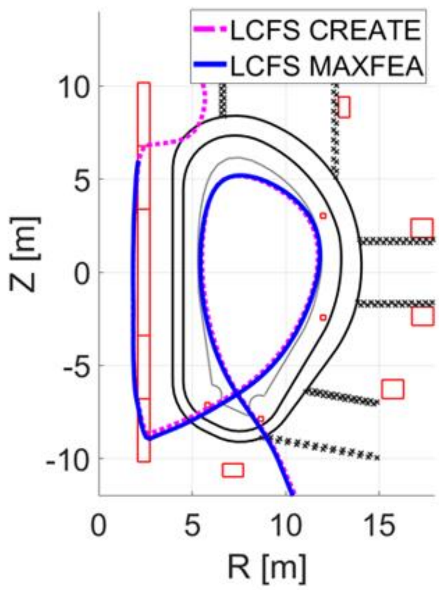

Figure 9: MAXFEA LCFS at EOF CREATE-NL vs MAXFEA for the VDEs.

The MAXFEA equilibrium solution has been considered acceptable when exact correspondence with the CREATE-NL reference values for ℓ_i and β_p is achieved by iteratively changing the plasma input parameters α and β. Furthermore, the parameters R_{axis} and Z_{axis} has been calibrated by the user such that the deviation from the magnetic axis position provided by CREATE remains within a maximum error threshold of around 3%. Since the formulation of ℓ_i and β_p in MAXFEA is not explicitly documented, it would be necessary to extract the formulas by conducting a detailed analysis of the source code. Given the scope of this task, it has been assumed that MAXFEA adopts the same formulation as that implemented by the CREATE-NL code.

$$\beta_p = \frac{4W_p}{\mu_0 R_{\ell_i} I_{pl}^2} \tag{4.1}$$

$$\ell_i = \frac{4W_m}{\mu_0 R_{\ell_i} I_{pl}^2} \tag{4.2}$$

The MAXFEA equilibrium has been considered reliable, given the main plasma parameters listed in Table 1 and the procedure described above.

Table 1: Comparison between CREATE-NL and MAXFEA main equilibrium parameters for DEMO baseline 2024 at the EOF instant. The percentage error has been estimated using CREATE-NL values as reference.

Quantity	CREATE-NL	MAXFEA	Percentage difference [%]
I_p [MA]	18.79	18.79	~ 0
β_p	0.91	0.91	~ 0
ℓ_i	0.68	0.68	~ 0
$\Psi_{boundary} - \Psi_{axis}$ [Vs]	-123.44	-119.13	-3.62
Minor radius [m]	3.11	3.19	2.50
B_T [T]	4.37	4.38	0.23
q_{95}	3.66	3.67	0.27
Elongation	1.87	1.83	-2.19
Triangularity	0.40	0.35	-14.29
Volume [m^3]	2726.01	2847.90	4.28
Current barycentre [m]	R=+8.91, Z=+0.14	R=+8.73, Z=0.096	2.15
Magnetic axis [m]	R=+9.17, Z=+0.38	R=+9.13, Z=+0.39	0.48
x-point [m]	R=+7.37, Z=-6.43	R=+7.41, Z=-6.54	1.36

The comparison between CREATE-NL and MAXFEA shows an overall very good agreement, with most equilibrium parameters differing by less than 5%. Core quantities such as plasma current, poloidal beta, normalized internal inductance, toroidal field, and safety factor are essentially identical. The largest discrepancies are observed in shape-related parameters (triangularity and volume), yet they remain within acceptable margins, confirming the reliability of the cross-validation between the two codes.

Fast Upward VDE

In the upward VDE, the plasma drifts toward the upper region of the first wall. The first case considered corresponds to a fast UVDE, characterized by a current quench (CQ) duration of approximately 86 ms. The adopted modelling strategy can be summarized as follows: a vertical kick of 4 kA is imposed as a perturbation in the radial field to trigger vertical instability, while minimizing the impact on induced currents in passive structures. During the vertical displacement, the plasma current is kept constant. The thermal quench (TQ) is initiated at $q_{95} = 2$ by imposing a linear reduction of the poloidal beta down to 1% of its nominal value within 4 ms. A current spike is subsequently modelled as a 5% increase of the plasma current relative to the equilibrium value. Finally, the CQ is enforced with a linear decay of Ψ_{axis}, adjusted to reproduce the characteristic timescale of 86 ms.

The halo current (HC) during the CQ is represented through an intermediate modelling approach, introducing a time-dependent halo width and generating a "medium" halo region. In MAXFEA, the halo modelling is based on time-variations of the parameters Ψ_{axis} and $\Psi_{boundary}$, which strongly affect the evolution of the CQ in terms of halo current peak, plasma shape dynamics, wall contact points, wetted surface, and overall temporal behaviour. To define realistic bounds, both upper and lower halo scenarios were considered. The upper bound corresponds to a "large" halo region, resulting in a wider wetted area on the first wall. Conversely, the lower bound assumes a "small" halo region, producing higher peak halo currents but localized on a more restricted surface.

These limits were obtained by tuning the free halo parameters close to the numerical convergence threshold, while avoiding unphysical conditions such as unrealistically low halo fractions, the no-wall limit, or anomalous plasma expansion. Although this procedure relies on user experience rather than on established experimental evidence, it ensures physically consistent simulations. Consequently, the definition of upper and lower bounds may lead to a wide spread of possible disruption outcomes, with the reference case identified as the "medium" halo region.

Table 2: List of the values for MAXFEA halo width used to model HC.

Disruption	Halo width
UVDE fast	0.25
UVDE slow	0.46
DVDE fast	0.37
DVDE slow	0.33
MD	0.41

Figure 10 reports five representative timesteps of the disruption: the initial equilibrium, the limiter configuration onset, the end of the thermal quench (TQ), and two phases of the current quench (CQ) corresponding to 60% and 30% of the plasma current, respectively. During the CQ, the formation and evolution of the halo region can be clearly identified.

The induced current evolution is illustrated in Figure 11: the yellow curve corresponds to eddy currents in the vacuum vessel (VV), while the red curve represents the halo current (HC). The eddy currents reach values comparable to the plasma current, up to ~17 MA, whereas the HC peaks at about 9% of the nominal plasma current value. Figure 13 details the behaviour of the in-vessel circuits (IVCs). The EQ coils exhibit the largest induced currents, as expected from their strong electromagnetic coupling with the plasma during vertical displacements. Their evolution follows the negative trend of the plasma vertical motion, consistent with the behaviour of a passive vertical control circuit. In contrast, the DIV coils display a current peak after the CQ termination, associated with rebound effects of electromagnetic energy exchange with the VV. This behaviour is observed in both the fast and slow UVDE cases.

The global vertical forces are reported in Figure 12 and Figure 14, which include the contributions from the VV, the HC, the IVCs, and their total sum. Both UVDE cases show qualitatively similar temporal evolutions, differing mainly in the magnitude of the loads. In particular, in the slow UVDE the dominant contribution arises from the HC. The force distribution on the IVCs is consistent with the induced current behaviour: the maximum load acts on the EQ coils, reaching ~5 MN, while the DIV coils are more stressed after the CQ, in agreement with the previously observed eddy current trends.

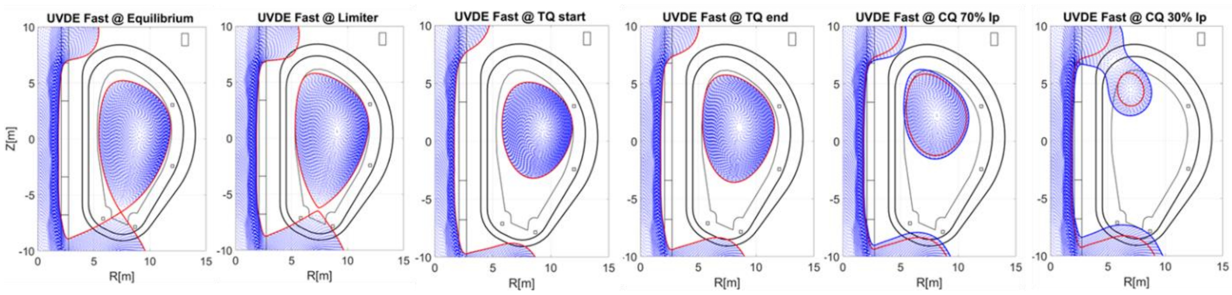

Figure 10: Snapshots of the plasma movement during the fast UVDE.

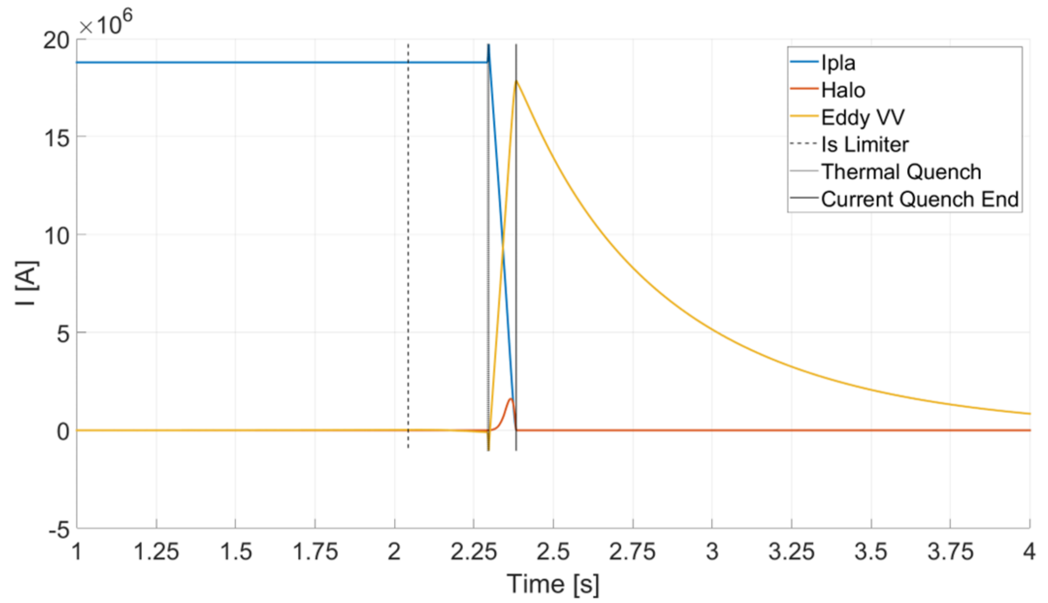

Figure 11: Evolution of the plasma current (Ipla) and induced eddy and halo currents during the fast UVDE.

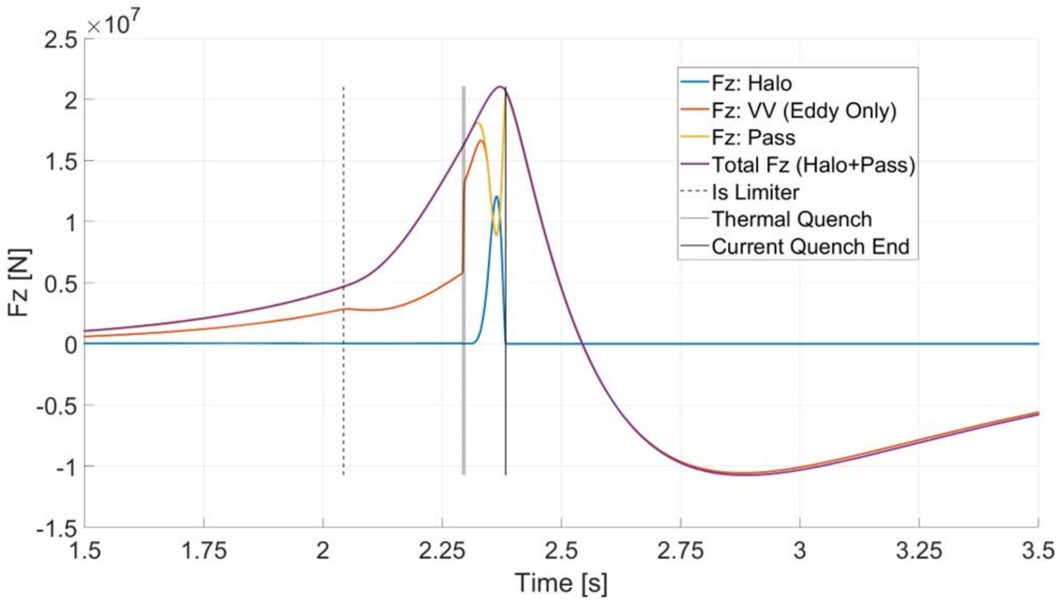

Figure 12: Evolution of the total vertical forces induced on the VV: the forces generated by HC (Fz: Halo), the forces induced on the VV by eddy currents (Fz: VV), the sum of the forces on the VV and on the EQ and DIV circuits (Fz: Pass) and the sum of all vertical forces, halo + eddy, (Total Forces), during a fast UVDE.

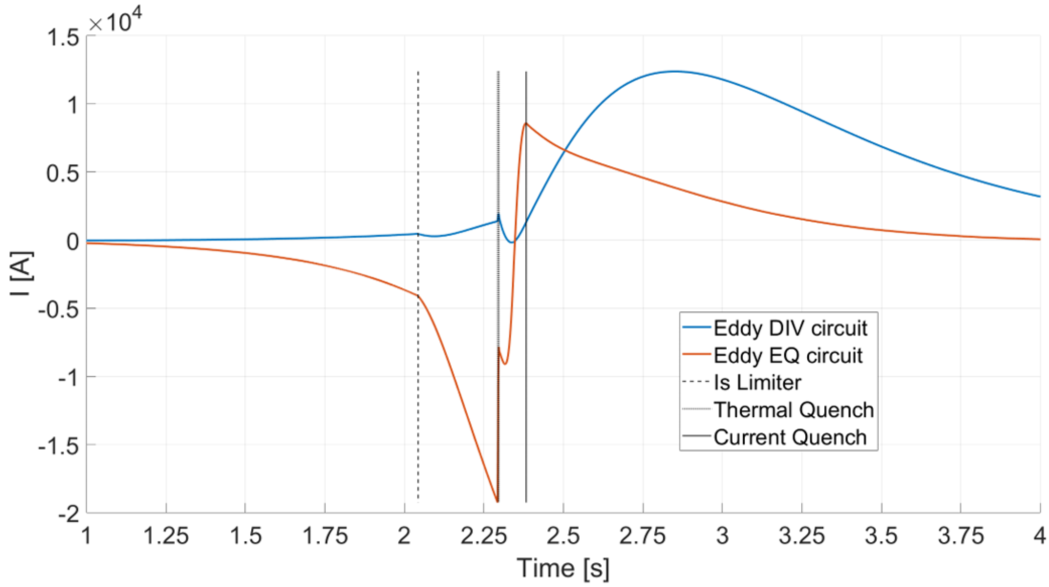

Figure 13: Evolution of the induced current in the EQ and in the DIV circuits, expressed as A per turn, during the fast UVDE.

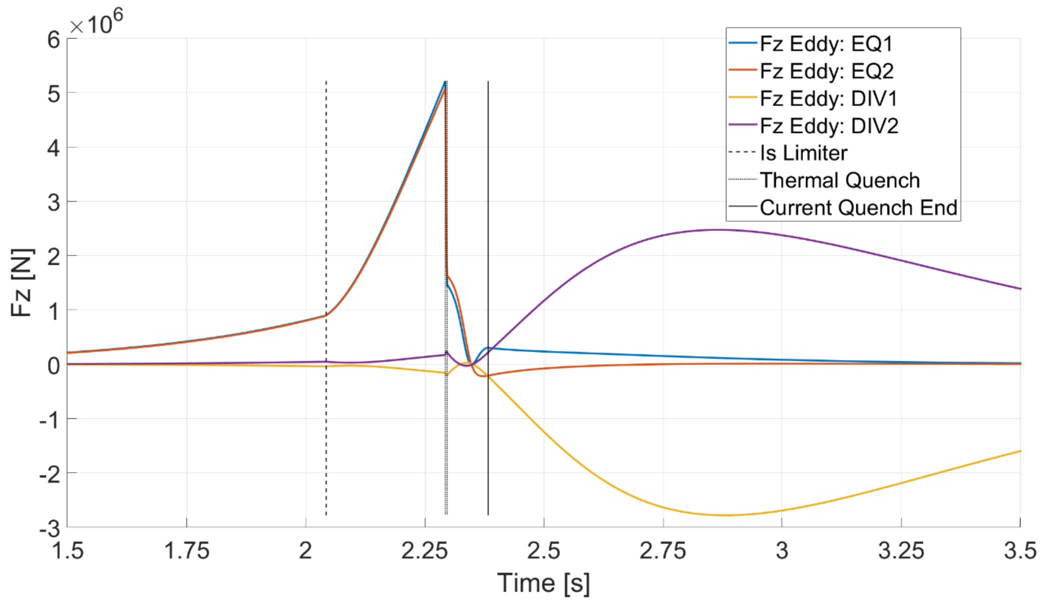

Figure 14: Evolution of the vertical forces induced on each coil of both the EQ and DIV circuits, during the fast UVDE.

Slow Upward VDE

The slow upward VDE differs from the fast case by the longer duration of the current quench (CQ), which extends to 500 ms. The modelling methodology is the same as for the fast event, with the only difference being the linear decay of Ψ_{axis}, adjusted to reproduce the extended CQ timescale.

Given the identical modelling strategy, the resulting plasma behaviour closely follows that of the fast UVDE, as illustrated in Figure 16 and Figure 18 for the induced currents, and in Figure 17 and Figure 19 for the vertical forces. However, the relative contributions are inverted: in the slow case, eddy currents peak at ~12 MA, significantly lower than in the fast event, while the halo current (HC) rises to nearly 17% of the nominal plasma current.

Regarding the in-vessel circuits (IVCs), the EQ coils exhibit a prolonged persistence of eddy currents due to the longer CQ phase, whereas the DIV circuit remains largely unaffected by the CQ duration. In terms of global loads, the largest contribution to the vertical forces originates from the HC, consistent with the increased fraction of plasma current diverted into the halo channel. Overall, the temporal trends remain analogous to those of the fast case, with variations primarily in magnitude.

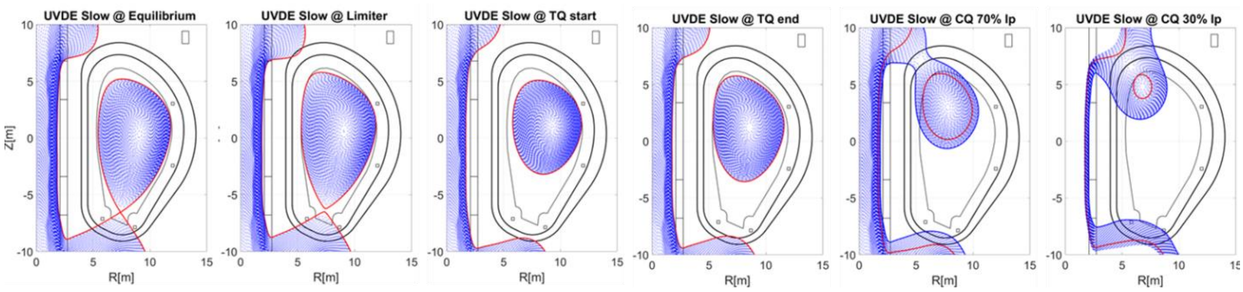

Figure 15: Snapshots of the plasma movement during the slow UVDE.

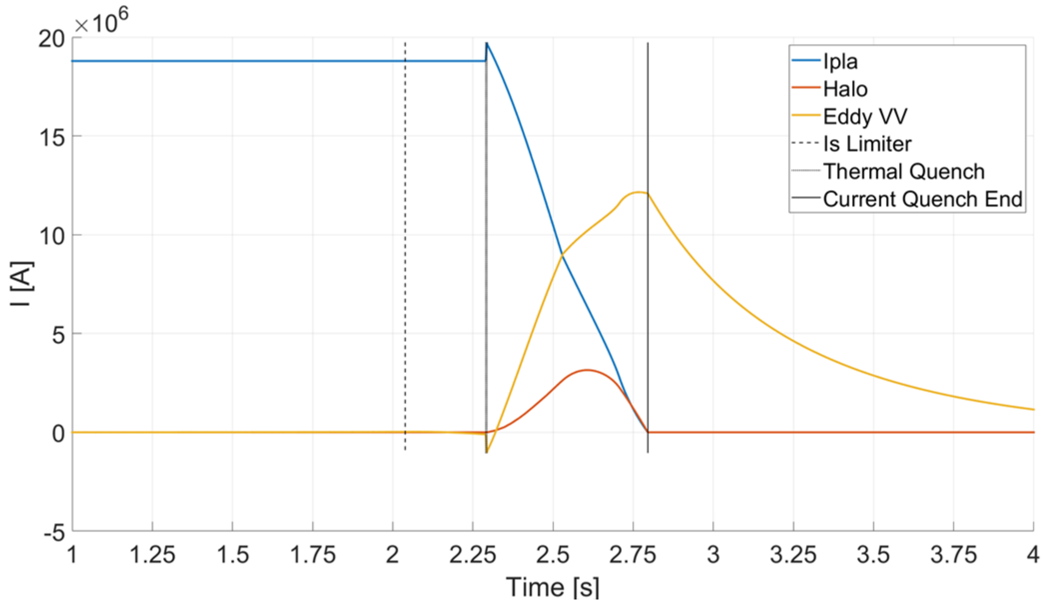

Figure 16: Evolution of the plasma current (Ipla) and induced eddy and halo currents during the slow UVDE.

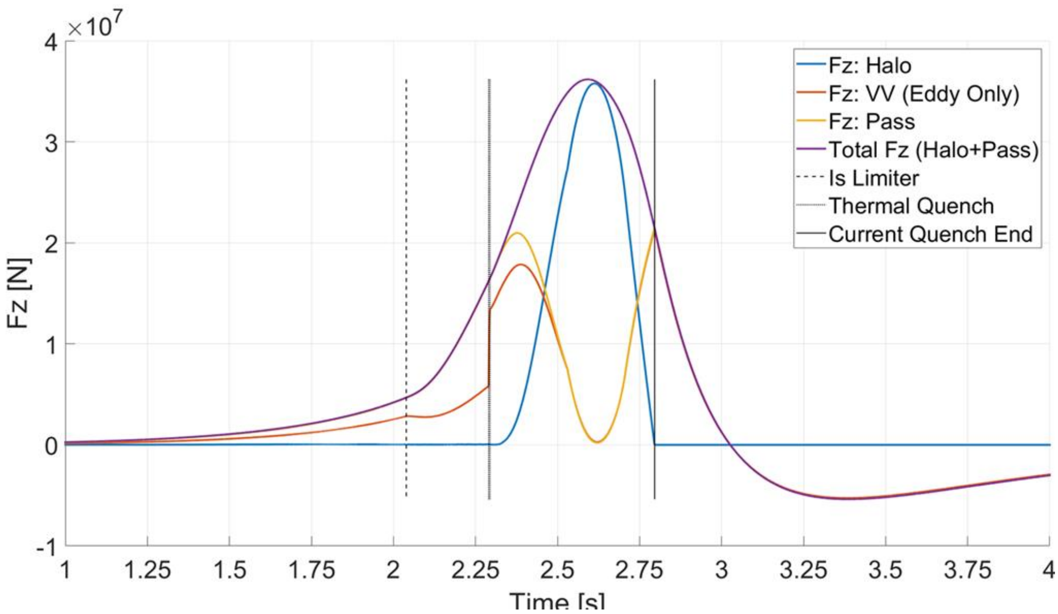

Figure 17: Evolution of the total vertical forces induced on the VV: the forces generated by HC (Fz: Halo), the forces induced on the VV by eddy currents (Fz: VV), the sum of the forces on the VV and on the EQ and DIV circuits (Fz: Pass) and the sum of all vertical forces, halo + eddy, (Total Forces), during a slow UVDE.

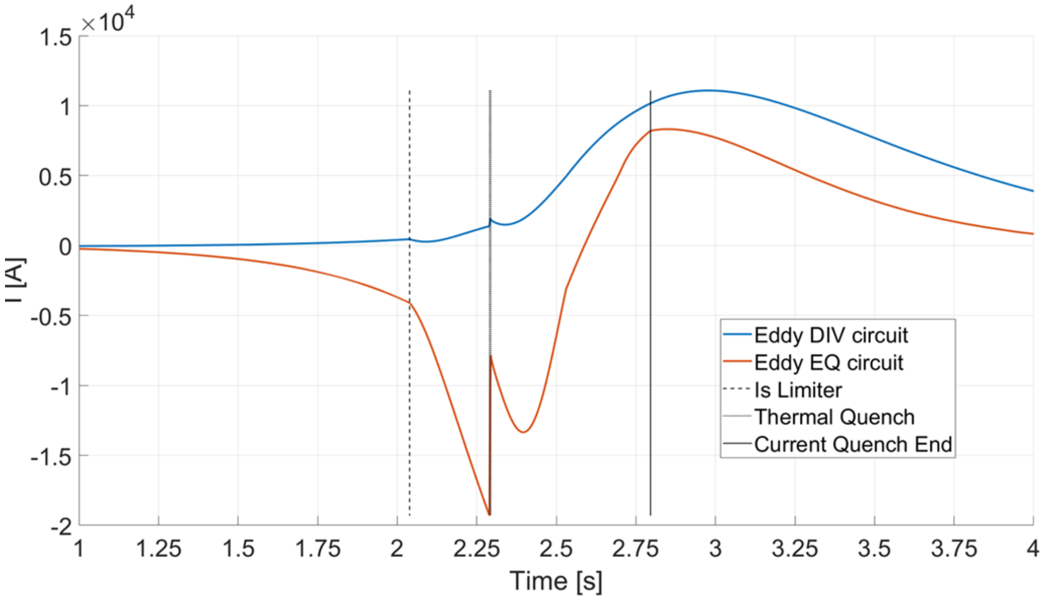

Figure 18: Evolution of the induced current in the EQ and in the DIV circuits, expressed as A per turn, during the slow UVDE.

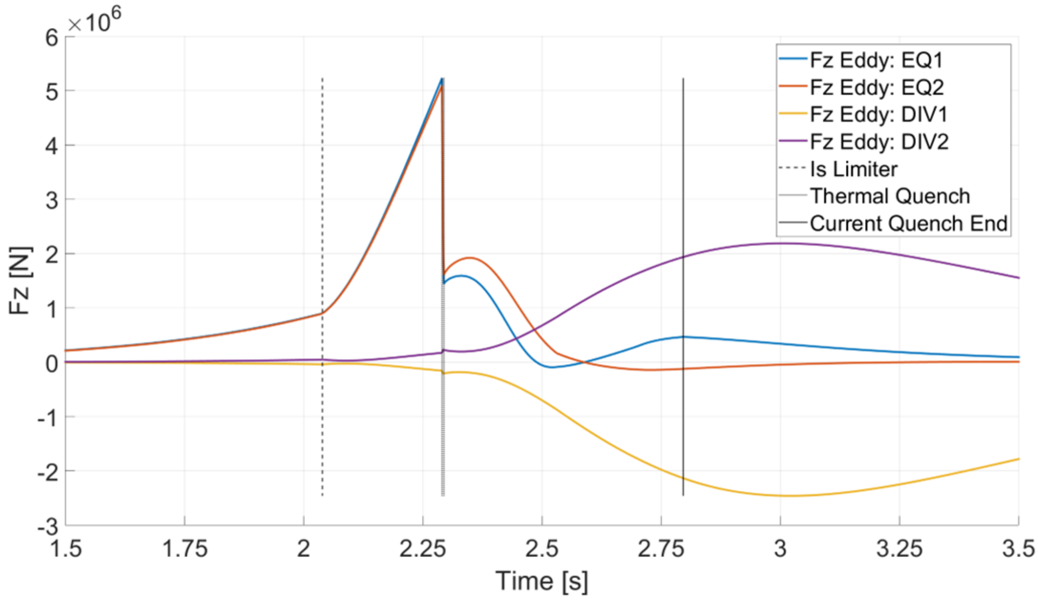

Figure 19: Evolution of the vertical forces induced on each coil of both the EQ and DIV circuits, during the slow UVDE.

Fast Downward VDE

In the downward vertical displacement event (DVDE), the plasma drifts toward the lower region of the first wall (FW). The case under consideration corresponds to a fast DVDE, characterized by a current quench (CQ) duration of 86 ms. The modelling strategy adopted to reproduce this event can is the same used for the previous cases.

The temporal evolution of the eddy currents is comparable to that observed in the fast UVDE. In particular, their amplitude reaches values close to the initial plasma current (≈18 MA in the fast case, Figure 21). The most significant difference lies in the intensity of the halo current, which reaches approximately 28% of the nominal plasma current. As regards the in-vessel components (IVCs), the EQ circuit is identified as the most stressed during the TQ, due to its proximity to the plasma, with the highest eddy current values induced (Figure 23). After the end of the CQ, the DIV circuit becomes dominant, as the plasma extinction occurs in the divertor region, which is subject to the largest flux variations associated with the dissipation of magnetic energy.

The global force evolution follows the same trend as the eddy currents. The maximum vertical force on the vacuum vessel (VV) is approximately 60 MN directed downward, reached at the end of the fast CQ, with only minor contributions from the passive circuits (Figure 22). The forces associated with the halo current show a specular behaviour with respect to the fast UVDE case; however, in this scenario their magnitude is larger, reaching nearly –55 MN. These observations are consistent with the evolution of the induced currents.

Similarly, the vertical forces on the IVCs exhibit the same behaviour as the associated eddy currents. Before the TQ, the EQ coils sustain the largest stress, experiencing a global downward vertical force. After the CQ, the DIV circuit becomes the most affected, consistent with the plasma displacement toward the divertor (Figure 24).

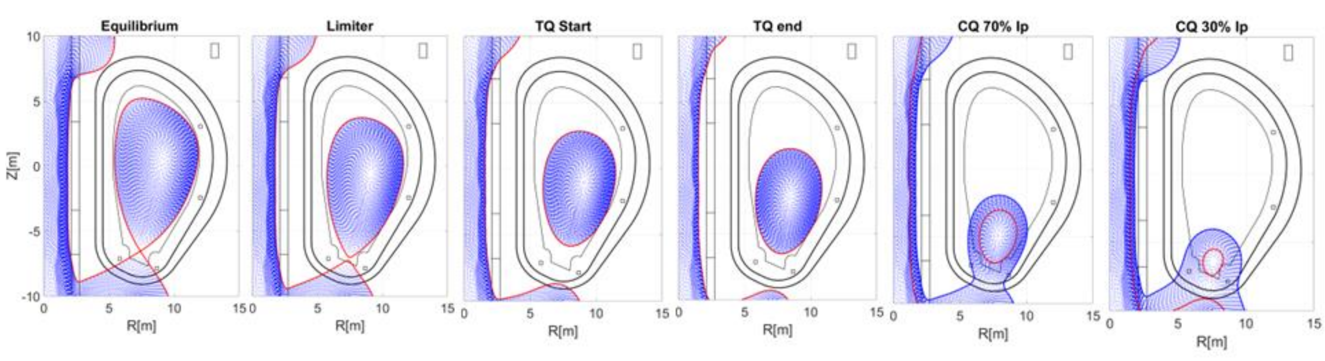

Figure 20: Snapshots of the plasma movement during the fast DVDE.

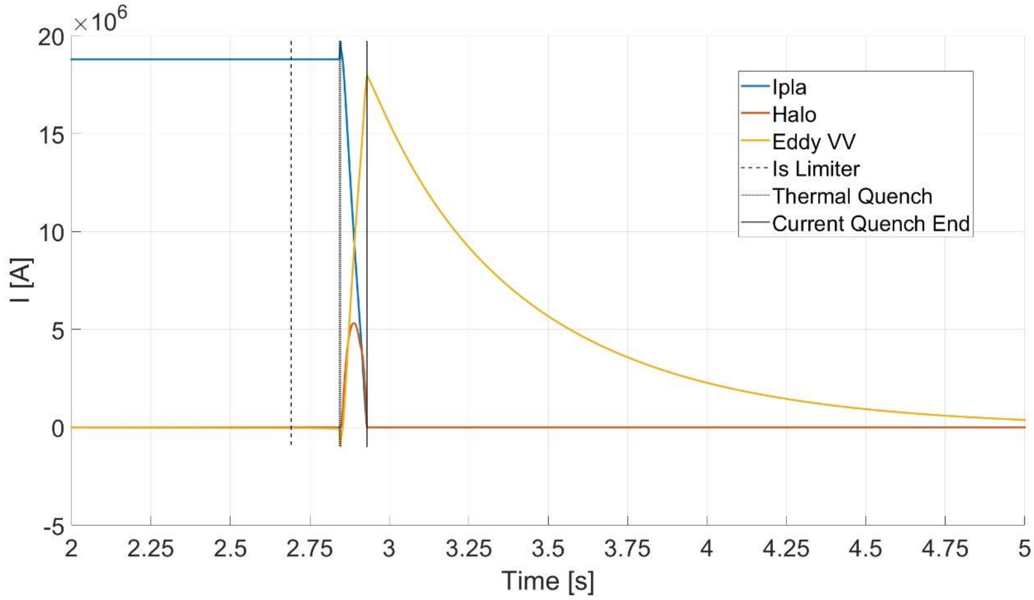

Figure 21: Evolution of the plasma current (Ipla) and induced eddy and halo currents during the fast DVDE.

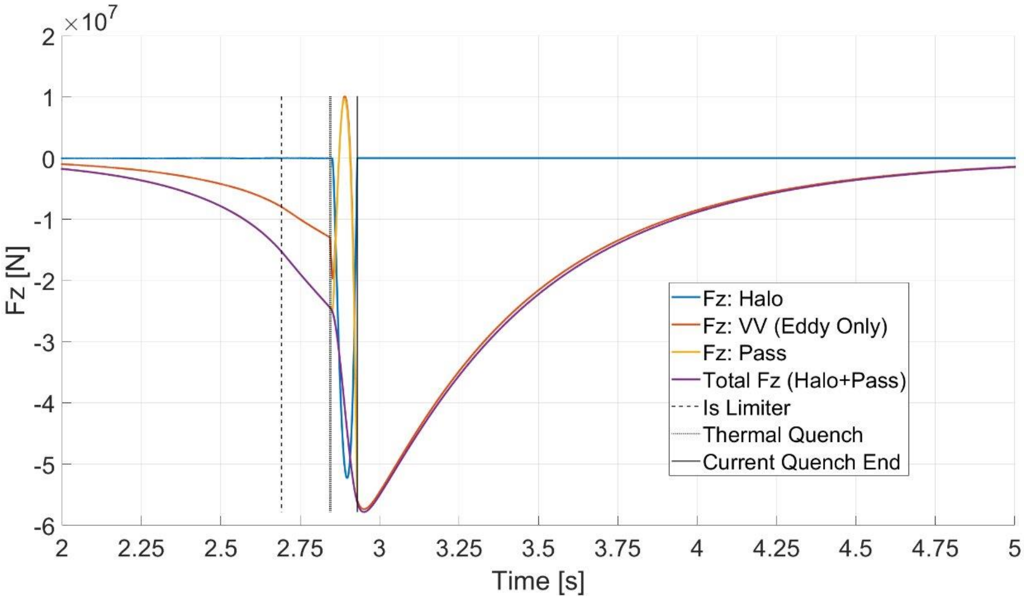

Figure 22: Evolution of the total vertical forces induced on the VV: the forces generated by HC (Fz Halo), the forces induced on the VV by eddy currents (Fz VV), the sum of the forces on the VV and on the EQ and DIV circuits (FZ Pass) and the sum of all vertical forces, halo + eddy, (Total Forces), during a fast DVDE.

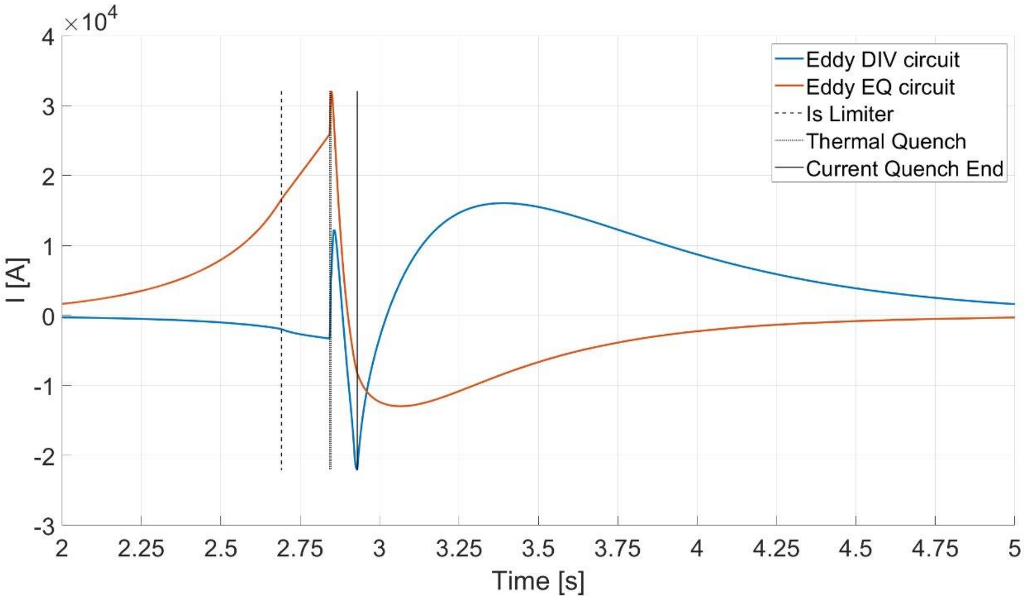

Figure 23: Evolution of the induced current in the EQ and in the DIV circuits, expressed as A per turn, during the fast DVDE.

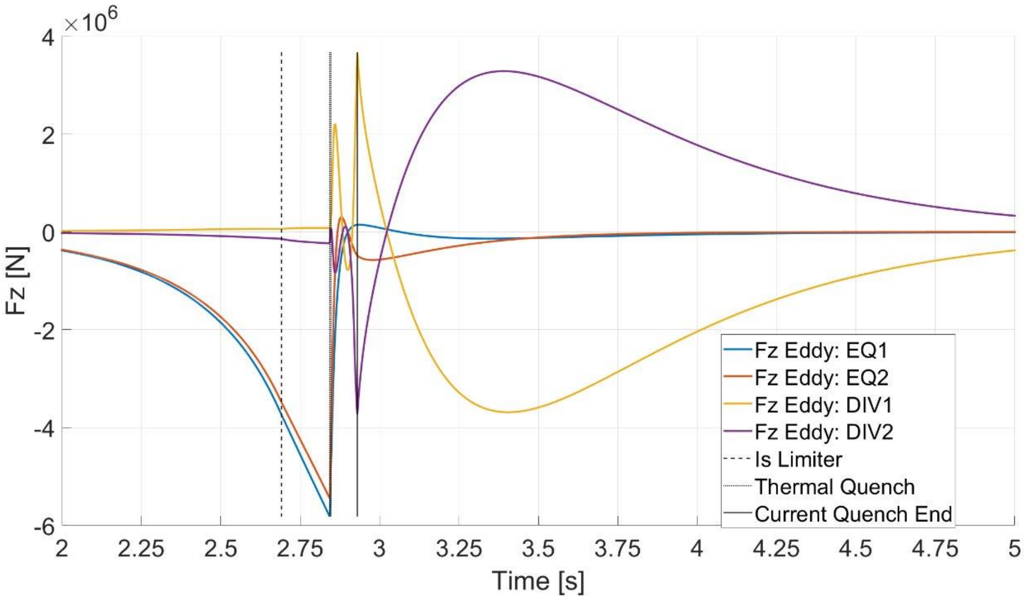

Figure 24: Evolution of the vertical forces induced on each coil of both the EQ and DIV circuits, during the fast DVDE.

Slow Downward VDE

The slow downward vertical displacement event (DVDE) differs from the fast case primarily in the duration of the current quench (CQ), which is extended to 500 ms. The modelling procedure follows the same methodology adopted for the fast DVDE, with the only modification being the longer linear decay of Ψ_{axis}.

As expected, given the same modelling assumptions, the overall behaviour of the slow DVDE reproduces the trends of the fast case. The time evolution of the induced currents is reported in Figure 26 and Figure 28, while the corresponding vertical forces are presented in Figure 27 and Figure 29.

The most relevant difference concerns the intensity of the induced currents. In this case, the eddy currents reach approximately 12 MA, which is significantly lower than in the fast DVDE, whereas the halo currents (HC) attain a higher relative intensity, approaching 43% of the nominal plasma current. Regarding the in-vessel circuits, the EQ circuit exhibits a prolonged persistence of induced currents due to the extended CQ phase, while the DIV circuit remains largely unaffected, its behaviour depending on the CQ duration.

In terms of vertical forces, the halo currents provide the largest contribution, driving the total force on the vacuum vessel to values exceeding 100 MN downward by the end of the CQ. The halo-induced forces themselves reach a maximum of approximately –135 MN. Overall, the observed trends remain consistent with those obtained for the fast DVDE, although with stronger contributions from the halo currents due to the longer CQ phase.

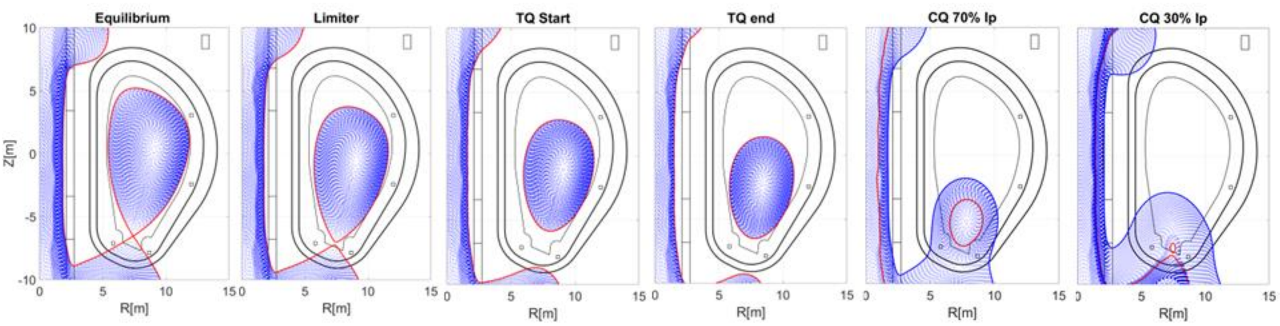

Figure 25: Snapshots of the plasma movement during the slow DVDE.

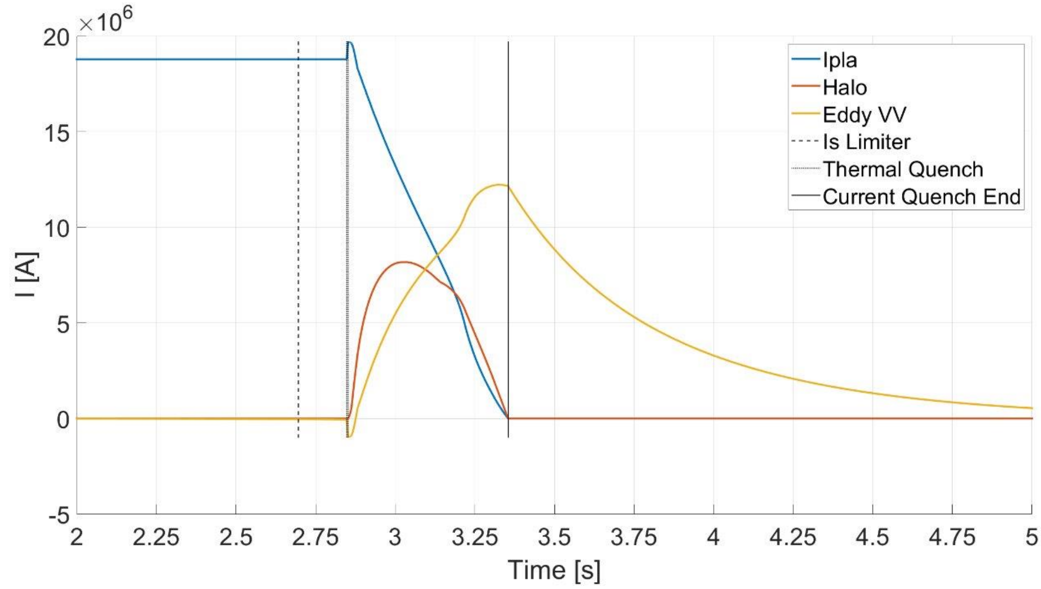

Figure 26: Evolution of the plasma current (Ipla) and induced eddy and halo currents during the slow DVDE.

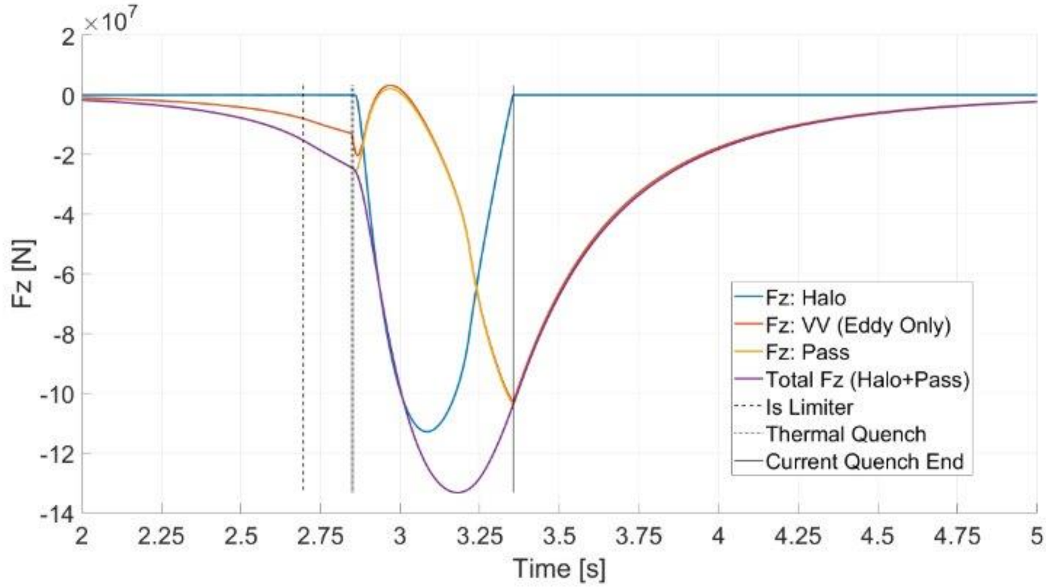

Figure 27: Evolution of the total vertical forces induced on the VV: the forces generated by HC (Fz: Halo), the forces induced on the VV by eddy currents (Fz: VV), the sum of the forces on the VV and on the EQ and DIV circuits (Fz: Pass) and the sum of all vertical forces, halo + eddy, (Total Forces), during a slow DVDE.

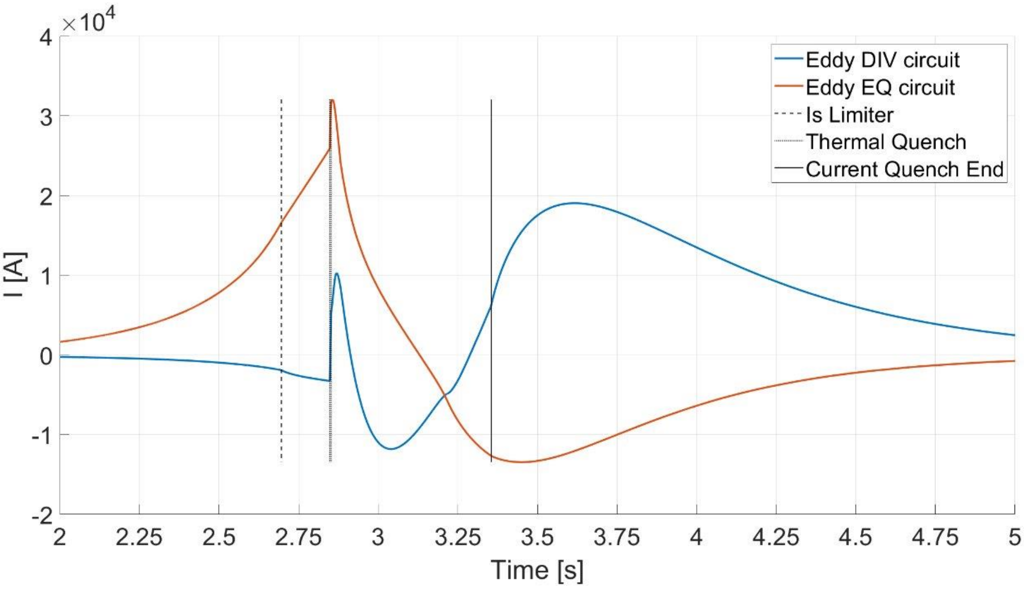

Figure 28: Evolution of the induced current in the EQ and in the DIV circuits, expressed as A per turn, during the slow DVDE.

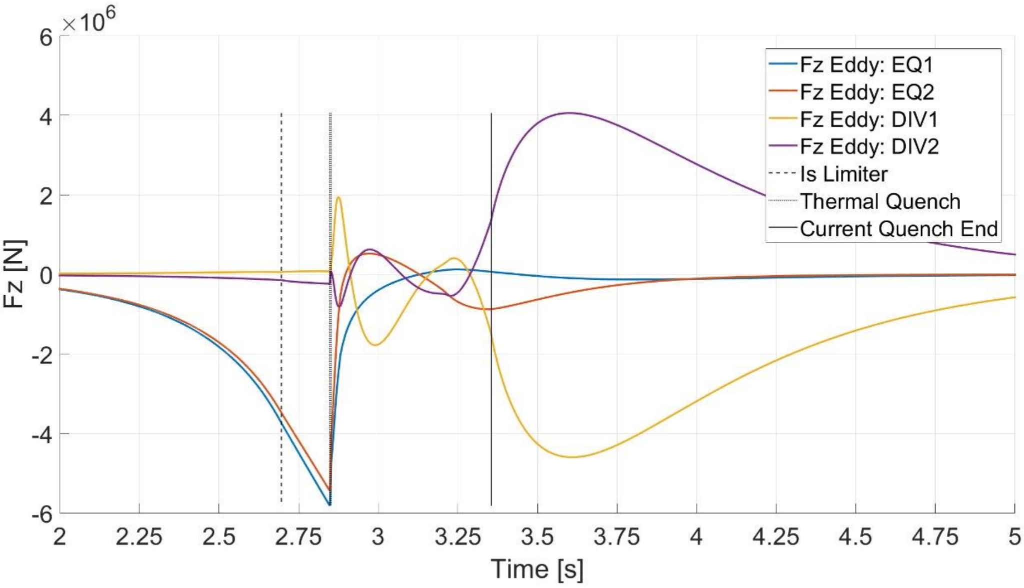

Figure 29: Evolution of the vertical forces induced on each coil of both the EQ and DIV circuits, during the slow DVDE.

The main outcomes of the analysis, in terms of electromagnetic (EM) loads associated with the five disruption scenarios investigated, are summarized in Table 3, providing a comparative overview of the induced currents and forces for each case.

In this thesis, only the electromagnetic loads have been evaluated, expressed as time histories of the global forces acting on the conducting structures. No structural allowables have been prescribed, as the acceptability of the computed loads cannot be established from the electromagnetic model alone. A complete three-dimensional structural assessment would be required, accounting for the actual supports, stiffness distribution, load paths, the applicable design code (ASME / RCC-MRx), and the relevant load combinations (VDE, halo, thermal, gravity, etc.).

Table 3: Summary of the EM loads for the analysed disruptions.

Case	TQ	CQ	Total Eddy	Total Fz (Halo + VV + IVC)	HC	Halo Peak
UVDE Fast	$q_{95} = 2$	86 ms	≈ 17,9 MA	≈ 21,0 MN	≈ 1,62 MA	8.63 %
UVDE Slow	$q_{95} = 2$	500 ms	≈ 12,2 MA	≈ 36,2 MN	≈ 3,15 MA	16.76 %
DVDE Fast	$q_{95} = 2$	86 ms	≈ 18,0 MA	≈ - 57,9 MN	≈ 5,33 MA	28.35 %
DVDE Slow	$q_{95} = 2$	500 ms	≈ 12,3 MA	≈ -133,2 MN	≈ 8,18 MA	43.55 %

Table 3 summarises the main results for the upward and downward vertical displacement events (UVDE and DVDE). Fast events are characterised by higher induced currents—approaching the nominal plasma current, with total eddy currents up to ≈ 18 MA—but comparatively lower vertical forces. In contrast, slow events exhibit smaller induced currents (≈ 12 MA) yet significantly larger vertical forces, reaching extreme values in the slow DVDE case (≈ –133 MN). The analysis of halo currents further confirms that DVDEs, particularly the slow one, represent the most demanding scenarios, with halo peaks up to ≈ 8.2 MA (≈ 44 % of the pre-disruption plasma current).

These results clearly demonstrate how the current-quench duration strongly influences the balance between induced currents and structural loads, identifying the slow DVDE as the reference case for assessing the mechanical robustness of the system. The obtained load magnitudes are consistent with those reported for DEMO-scale devices in the literature, where global vertical forces of the order of 10^8N (≈ 70–80 MN) have been identified for the most severe asymmetric VDEs [35].

The corresponding structural assessment carried out by [36] confirmed that the DEMO vacuum vessel can withstand vertical loads up to ≈ 146 MN (≈ 9 MN per 22.5° sector) without exceeding the allowable limits for 316L(N) stainless steel at 200 °C. These findings indicate that the load magnitudes obtained in the present work—ranging from a few tens to more than one hundred MN—are fully compatible with existing DEMO design margins.

Furthermore, [37] quantified asymmetric VDE loads for ITER, reporting vertical forces up to ≈ 108 MN on passive components, including the vacuum vessel and blanket structures, under the most severe asymmetric halo-current conditions (toroidal peaking factor TPF = 1, $I_{\text{halo}} \approx$ 8 MA). Finite-element analyses confirmed that these forces, although substantial, remain within the ITER structural design capability when assessed through coupled electromagnetic–mechanical models.

This order-of-magnitude comparison demonstrates that the electromagnetic loads computed in this thesis—up to ≈ 130 MN in the slow DVDE case—are physically realistic for DEMO-scale conditions and remain within the structural capacity envelope established for current fusion reactor designs. Nevertheless, a dedicated three-dimensional mechanical verification remains essential to capture the actual geometry, weld details, and local load paths accurately.

The results obtained for the disruption scenarios analysed with MAXFEA have been taken as reference for the analogous cases simulated with PECAN. In particular, the same modelling strategy for the thermal quench, current quench, and halo current has been adopted, ensuring consistency between the two approaches. The corresponding implementation within PECAN, together with the mathematical formulation, is presented in Chapter 6.

4.2 First Disruption Characterization for TRUST

In this section, a preliminary single-null (SN) plasma disruption database is presented with the objective of evaluating the disruption specification loads for TRUST. The analyses have been carried out considering the stabilizing plate reference position identified in the previous section. The expansion of the disruption case histories is aimed at identifying the most critical scenarios, both in terms of global loads on passive structures—such as the vacuum vessel and stabilizing plates—and in terms of localized effects on the vessel dome and its flanges. The assessment of the electromagnetic behaviour during disruptions is indeed a mandatory step for the reliable design of a tokamak. To this end, a collection of electromagnetic simulations has been performed using the 2D evolutionary equilibrium code MAXFEA, covering a range of plasma dynamic conditions within the operational space in terms of:

- Starting Time instant: starting from EOF or SOF can have a significant effect on the disruption loads due to the different starting set of currents in the PF coils and, consequently, differences in the evolution of poloidal magnetic field map (it is not possible to say at priori which is the worst case and an investigation is mandatory).
- Plasma trajectory**:** it is common practice that both upward and downward VDE (UVDE and DVDE) be analysed to evaluate the different loads that result from the two trajectories. This is because the machine in question lacks perfect up-down symmetry in terms of plasma configuration and surrounding structures (e.g. VV Dome flanges).
- Current Quench (CQ) duration: the duration of CQ represents a significant discriminating factor in the load resulting from a disruption, and it is typically necessary to consider both Fast and Slow events in this regard. From an initial assessment of the TRUST machine scale end performance, it can be determined that fast events have a CQ duration of 0.24 ms, while slow events have a CQ duration of 2.4 ms.

A total of eight disruptions simulation has collected: two Fast and Slow UVDE and two Fast and Slow DVDE starting from EOF (four in total from EOF); two Fast and Slow UVDE and two Fast and Slow DVDE starting from SOF (four in total from SOF). The methodology applied using MAXFEA, equilibrium code is fully explained and verified in [30][31][50][51]. The evolution of plasma in terms of movement, shape evolution and trajectory are reported in Figure 30 (b and c), while the main relevant EM loads deriving from the specific case of disruption in term of global vertical forces (b1) and Eddy currents (a1) are reported in Figure 31. The same information was produced for all cases but not reported for avoid repetitive contents.

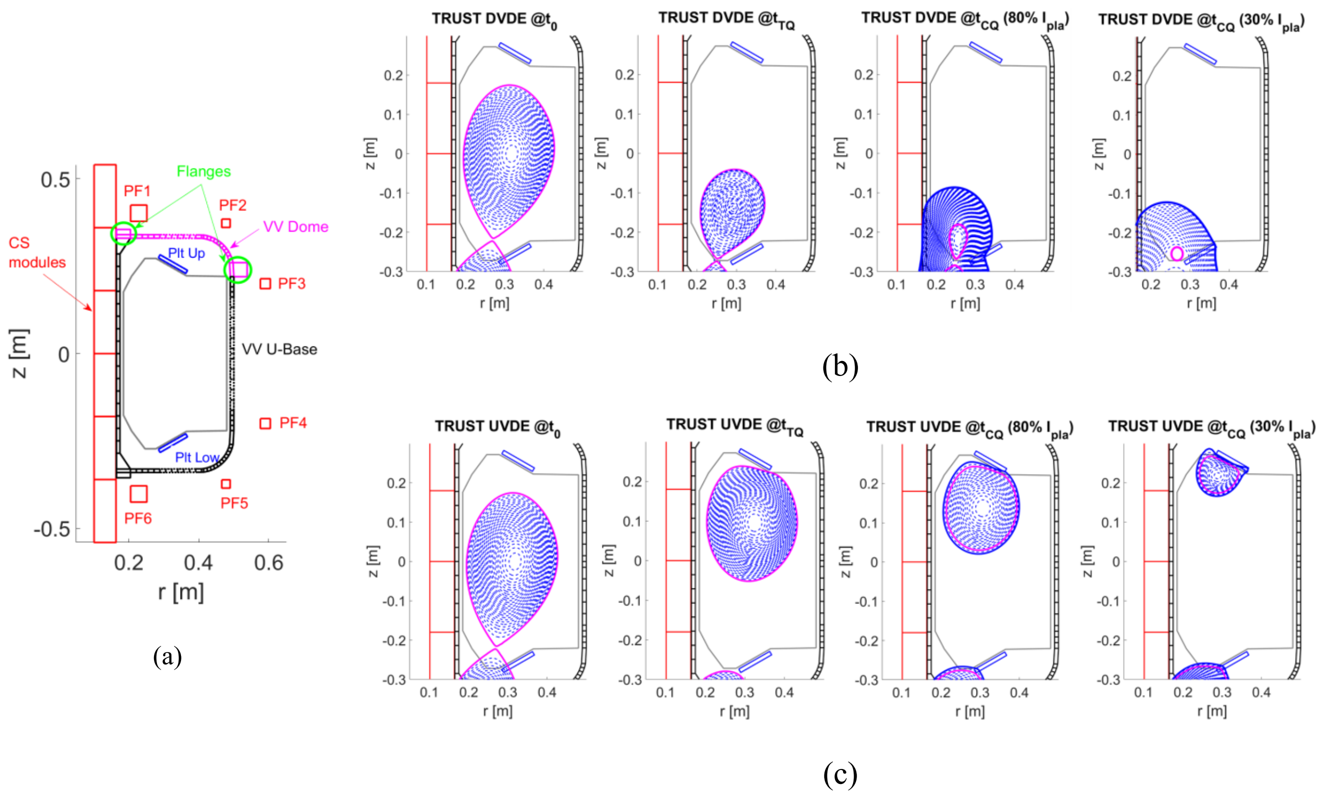

Figure 30: Labelling of TRUST 2D model structures (a) and evolution of plasma in terms of movement, shape evolution and trajectory for Fast DVDE starting from EOF (b) and Slow UVDE starting from EOF (c). Instants of snapshots in (b) end (c) are referred, considering a left to right order, to the following times: the equilibrium (t_0), start of the thermal quench (t_{TQ}), during CQ when the plasma current is 80% respect to the starting value (t_{CQ} 80% I_{pla}), during CQ when the plasma current is 30% respect to the starting value (t_{CQ} 30% I_{pla}).

Graphs in Figure 31 (a1)(a2) show: the plasma current and halo currents dynamics (blue and red lines, respectively) with their typical trends, the evolution of eddy currents considering the VV structure (yellow trend), the eddy currents trend on the VV Dome (purple curve) and the dynamics of total eddy currents considering the contribute of the upper and lower stabilising plates induced currents (dark red and green respectively). For what concerns the vertical forces (F_z), the trends in Figure 31 (b1)(b2) contain: force dynamics due to the halo currents effect is reported in blue, the evolution of total forces due to eddy currents on the stabilising plates (light blue for the upper and dark red for the lower), the total loads trend act on the VV structure considering the dynamics of total eddy currents on passives and the halo currents contribute is reported in black, the vertical force considering the VV Dome supports structures (flanges in Figure 30a) is in magenta, the F_z acting on the VV with the only eddy contribute is represented by the green trend.

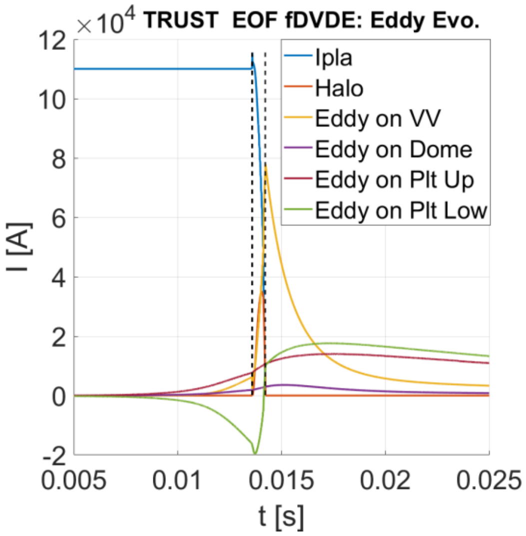

(a1)

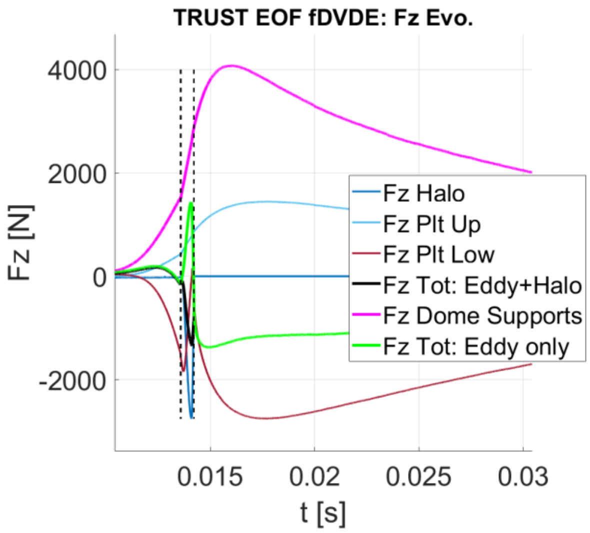

(b1)

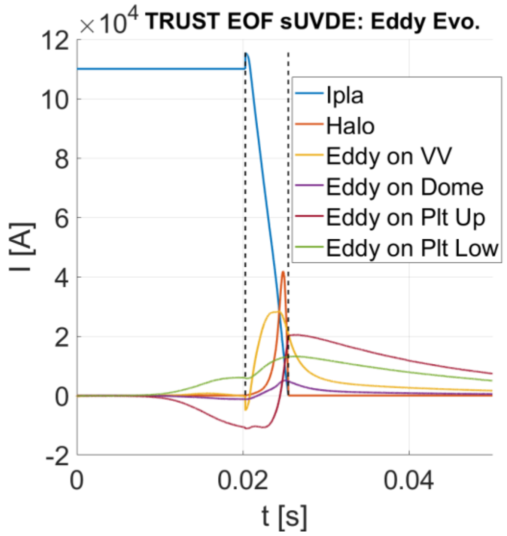

(a2)

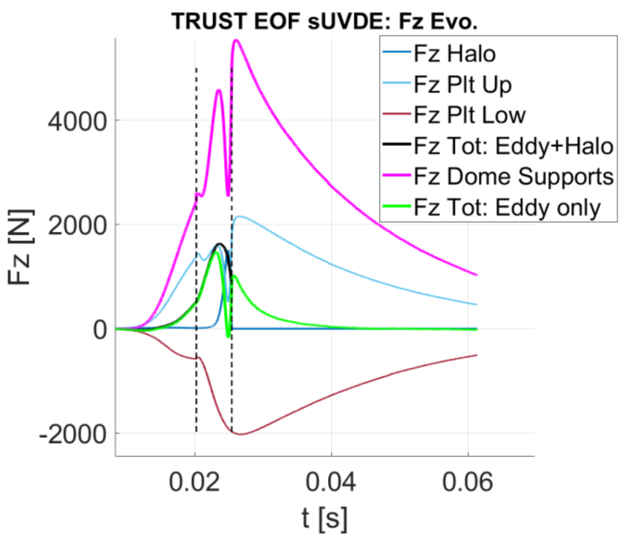

(b2)

Figure 31: *Examples of detailed MAXFEA output in terms of computed eddy currents (a) and 2D vertical forces (b) trends in time on TRUST components for EOF Fast DVDE (a1)(b1) and EOF Slow UVDE (a2)(b2).*

Figure 32 shows a qualitative preview of TRUST numerical disruptions collected to provide EM loads specifications. Additionally, Table 4 contains a summary aimed at outlining the corresponding main outcomes in terms of vertical forces on the different components and plasma trajectory and wall contact point during the VDE, obtained for each case.

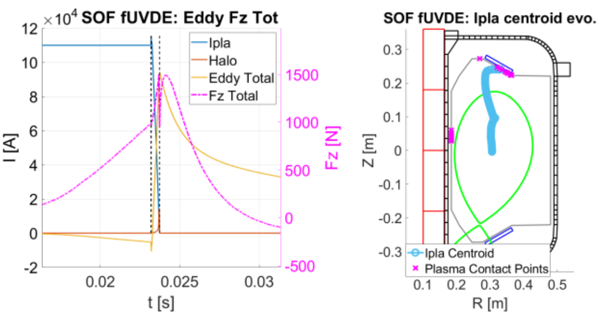

(a)

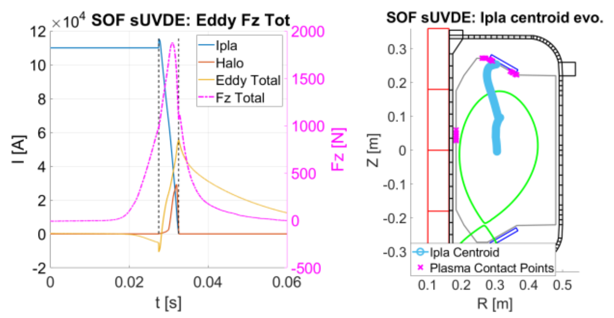

(b)

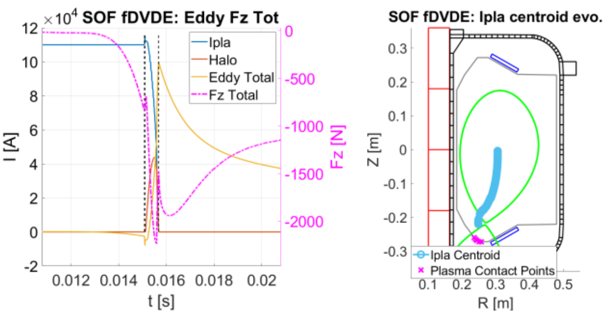

(c)

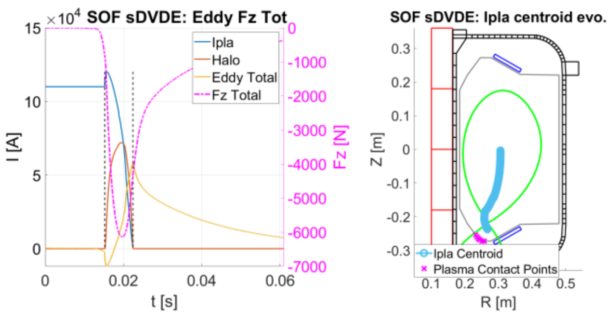

(d)

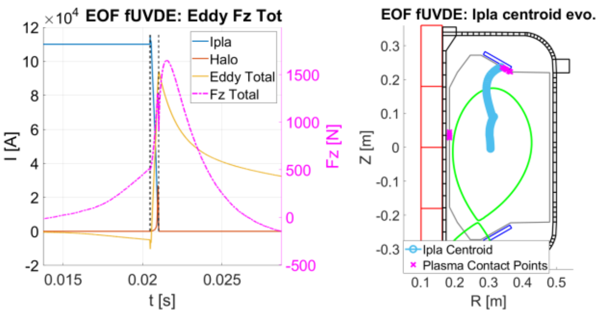

(e)

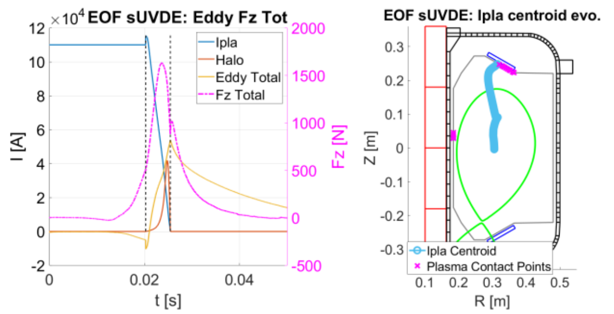

(f)

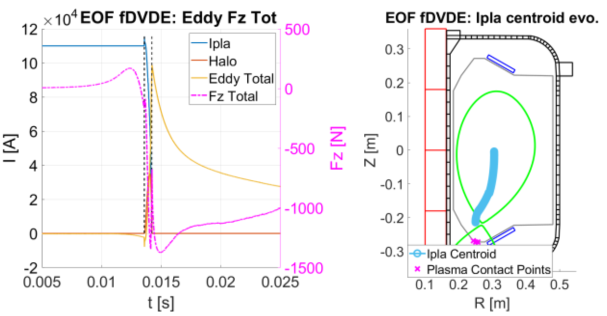

(g)

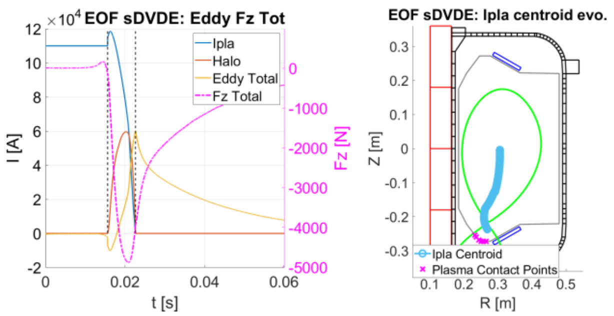

(h)

Figure 32: Preview of TRUST disruption specification. The following outcomes are reported: plasma current and halo currents (blue and red lines respectively), total eddy currents for all the passive structures in the model (yellow trends), total loads acting on the VV structure including the supported components (magenta dashed trends, refers to right ordinate axis). In addition, plasma centroid trajectory and wall contact points during the VDE are reported in the poloidal plane images (blue trend and magenta cross, respectively),

Table 4: TRUST disruption summary table reassuming the main outcomes in terms of vertical forces on the different components for each case. An important focus on the total loads peak act on the VV structure considering the dynamics of total eddy currents on passives and the halo currents contribute is presented (first row), together with the vertical forces peak acting on the VV structure from only eddy contribute (second row). As for the local forces, the vertical force peak considering the VV Dome supports structures and on the stabilizing plates are reported in the third and the fourth row, respectively.

	SOF Fast UVDE (a)	**SOF Slow UVDE (b)**	**SOF Fast DVDE (c)**	**SOF Slow DVDE (d)**	**EOF Fast UVDE (e)**	**EOF Slow UVDE (f)**	**EOF Fast DVDE (g)**	**EOF Slow DVDE (h)**
F_z PeakTotal - Halo+Eddy [kN]	1.450	1.877	-2.236	-6.141	1.650	1.636	-1.376	-4.879
F_z Peak total - Eddy only [kN]	1.492	1.585	-1.942	-4.271	1.650	1.471	1.435	-3.928
F_z Peak Dome Supports [kN]	4.614	4.978	3.309	2.520	5.433	5.537	4.068	3.078
F_z Peak Plates [kN]	-1.818	1.876	-2.829	-3.839	-2.172	2.153	-2.754	-3.650

Looking at Table 4, significant observations can be made regarding the disruption EM load specification for TRUST, together with a preliminary identification of the worst case for the various components. It is evident that the worst disruption case in terms of global vertical forces results to be the SOF Slow DVDE, with an Fz peak of 4.271 kN downward (6.141 kN is also the Halo contribution is considered). The same case result to be the design driver case for the plates supports, with an Fz peak acting on the lower stabilising plates of 3.839 kN downward. In another hand, the target case to be considered for the design of the VV Dome supports is the EOF Slow UVDE, with an Fz peak acting on the flanges of 5.537 kN upward. Although the estimated loads are nowhere near the design driver loads of the world's large tokamaks [21] [50][51],the knowledge gained from this data collection on the EM loads from disruption is a necessary step in the design of TRUST. The EM loads obtained will be refined with detailed 3D EM analyses that will also provide information on the 3D effects of the loads not considered in this 2D analysis (such as force concretions or out-of-plane loads). It will then be possible to carry out the first structural analyses for the design of leg supports, stabiliser plates supports and the VV dome flanges, as well as in-vessel components such as the divertor, for which the information provided on Halo currents will a key input [21] [50][51]. Furthermore, AISI 316L stainless steel has been selected as the baseline structural material for TRUST. At room temperature, this material can withstand stresses up to approximately 200 MPa, which—based on preliminary evaluations—exceeds the maximum stress levels expected under the electromagnetic loads calculated in the present study.

Part III – The PECAN project

5. Prototype of a Full 2D FEM Architecture for PECAN

This section presents the preliminary development of a full two-dimensional finite element (FEM) module for PECAN, implemented using the DOLFINx framework. The intention of this work is to introduce a first draft of the architecture designed to solve the Grad–Shafranov equation in the free-boundary configuration, accounting for both stationary equilibrium and transient plasma evolution.

It should be emphasized that this module is not to be regarded as a final product. Rather, it represents a prototype under active development, which will undergo internal review and further refinement within the PECAN team. The results and formulations reported here therefore constitute a first step toward extending PECAN's capabilities to consistently capture axisymmetric plasma equilibria coupled with the electromagnetic response of surrounding conductors.

The code is organized into distinct modules, each addressing a specific aspect of the simulation framework. The mesh module manages the generation and handling of the computational domain. At the current stage of development, no dedicated mesher is implemented within PECAN. Instead, the first-order meshes are generated externally through Python scripts that exploit the Gmsh [55] API, allowing full parametric control of geometry, refinement, and physical tagging. The resulting models are then converted to DOLFINx objects using its built-in import and conversion utilities, ensuring seamless interoperability between the meshing stage and the finite element environment.

Similarly to MAXFEA, each physical region—plasma, air, coils, and passive structures—is identified by a unique region ID (or tag). By default, the air domain is assigned ID = 1, the plasma region ID = 50, while the active coils occupy IDs in the range 2–49, and passive conductors are defined with IDs greater than 50. This tagging system enables the automatic identification of material domains and the consistent assignment of physical properties such as electrical conductivity and magnetic permeability. Boundary tags are used to distinguish key interfaces, including the outer vacuum boundary and the symmetry axis. On both boundaries—the axis at $R = 0$ and the external edge of the computational domain—Dirichlet boundary conditions are imposed, setting $\Psi = 0$, as specified in Eq. (5.2).

The finite element discretization adopts continuous Lagrange (CGn) elements for the poloidal flux Ψ and discontinuous Galerkin (DG0) elements for the toroidal current density J. The element order n is user-selectable (typically $n = 1$ or 2), while quadrature rules are automatically selected by DOLFINx to match the polynomial degree and ensure optimal numerical integration. The magnetic field B, being derived from the spatial derivatives of Ψ, is represented using Lagrange functions of order $(n-1)$, in agreement with the formulation introduced in Eq. (2.10). This configuration enables a consistent representation of both smooth magnetic-flux fields and discontinuous current distributions across material interfaces.

The machine module defines the overall tokamak configuration, incorporating materials, electrical circuits (both active and control), as well as magnetic diagnostics—currently limited to flux loops and magnetic probes.

The plasma module specifies the equilibrium parameters and the formulation of the plasma current density, while also including a simplified zero-dimensional model for the halo current, used to represent its evolution during the disruption analysis. Finally, the equilibria module provides two complementary solvers: a static solver for the free-boundary Grad–Shafranov equilibrium, and a transient solver that extends the formulation to time-dependent scenarios by coupling the plasma dynamics with the induced currents in the surrounding conductors. In addition, it introduces a flexible event-based mechanism that allows users to define triggers and associated actions on plasma parameters or machine circuits, thereby supporting the simulation of disruption sequences and other dynamic phenomena.

Analogously to MAXFEA, PECAN can be employed to simulate disruption scenarios starting from a reference equilibrium and evolving it according to pre-defined or user-driven events. The code provides a complete description of the plasma evolution, including plasma displacement, current redistribution, magnetic field variation, and the associated electromagnetic loads acting on the machine components. A key difference with respect to MAXFEA, however, lies in the treatment of the plasma current during the current quench (CQ): while in MAXFEA the Ψ_{axis} must be directly controlled in order to enforce a linear decay of the plasma current, in PECAN the plasma current itself can be prescribed to decay linearly, with Ψ_{axis} evolving in a self-consistent manner with the imposed current variation.

```
Event(
    name="start_CQ",
    trigger=[("Ip", ">=", 19.7e6)],
    actions=[("halo.width", 0.2), ("plasma.Ip", "lambda: Ip_now * (1 - (t - t_now)/0.086)")],
),
```

Figure 33: Example of an event programmed for a fast UVDE in DEMO LAR 2024. At the beginning of the CQ, the halo width is prescribed, and the plasma current is set to decay linearly over a time interval of 86 ms.

5.1 Mathematical Formulation

In the Grad–Shafranov equation (2.15), the sum of the two terms on the right-hand side corresponds to the toroidal plasma current density $J_p(\Psi)$ in the plasma domain Ω_p. The equation governs the equilibrium and quasi-static evolution of an isotropic plasma, i.e., one exhibiting the same physical properties in all directions. This formulation can be naturally extended to the different domains in which the poloidal flux is defined. In particular, it can be noted that, by analogy with Poisson's equation, $\Delta^*\Psi = 0$ in the vacuum region Ω_v, while in the domain occupied by poloidal field coils or other external conductors Ω_ϕ, $\Delta^*\Psi$ is proportional to the external toroidal current density $J_{\phi,ext}$.

In summary, plasma equilibrium on the poloidal plane can be fully described by the following nonlinear partial differential equation [42]:

$$\Delta^*\Psi = \begin{cases} 0 & in\ \Omega_v \\ -\mu_0 R J_p(\Psi) & in\ \Omega_p \\ -\mu_0 R J_{\phi,ext} & in\ \Omega_\phi \end{cases} \tag{5.1}$$

To solve the system of equations in (5.1), Dirichlet boundary conditions can be applied:

$$\begin{gathered} \Psi(0, \mathrm{Z}) = 0 \\ \lim_{R^2+Z^2\to\infty} \Psi(R, \mathrm{Z}) = 0 \end{gathered} \tag{5.2}$$

Where the toroidal coordinate ϕ has been omitted due to the axisymmetric nature of the problem.

The computational domain in PECAN is intentionally extended far in radius and height to correctly approximate the boundary conditions imposed in Eq. 5.2. Since the Grad–Shafranov equation is solved in a finite region, the outer boundary must emulate the theoretical condition at infinity.

To minimise truncation errors and artificial reflections of the magnetic field lines, the mesh is extended sufficiently far outside the vacuum vessel — typically several times the plasma major radius (or the machine radius). In this region the operator $\Delta^*\Psi=0$ becomes formally similar to the Laplace equation, but a different sign on the first derivative in cylindrical coordinates, and the solution decays as 1/R, so placing the boundary far away ensures that both Ψ and its gradient are practically zero at the numerical edge. This is a standard approach in free-boundary equilibrium solvers, such as CREATE-NL and MAXFEA, to guarantee that the magnetic flux and mutual couplings are unaffected by the artificial truncation of the domain.

Assuming the following functional form for the plasma current density $J_p(\Psi)$:

$$J_p(\Psi) = \lambda\left[\frac{R}{R_0}\beta - \frac{R_0}{R}(1-\beta)\right](1-\bar{\Psi}^{\alpha_m})^{\alpha_n}$$
$$\bar{\Psi} = \frac{\Psi - \Psi_{axis}}{\Psi_{boundary} - \Psi_{axis}} \tag{5.3}$$

Where α_m, α_n and β are profile parameters, R_0 is the reference radius (for instance, the machine radius) and λ is a scaling factor chosen to match a prescribed target value of the plasma current:

$$\lambda = \frac{I_p^{target}}{\int_{\Omega_p} J_p(\Psi, \lambda = 1)\, d\Omega} \tag{5.3}$$

By coupling Eq. 5.3 with the well-known Grad-Shafranov equation (2.16), it is possible to define the plasma profile p' and FF' as function of the profile parameters, as already done for MAXFEA in Chapter 3.1:

$$J_p(\Psi) = \lambda\left[\frac{R}{R_0}\beta - \frac{R_0}{R}(1-\beta)\right](1-\bar{\Psi}^{\alpha_m})^{\alpha_n} = Rp'(\bar{\Psi}) + \frac{1}{\mu_0 R}FF'(\bar{\Psi}) \tag{5.4}$$

$$p'(\bar{\Psi}) = \frac{\lambda\beta}{R_0}(1-\bar{\Psi}^{\alpha_m})^{\alpha_n} \tag{5.5}$$

$$FF'(\bar{\Psi}) = \lambda\mu_0 R_0(1-\beta)(1-\bar{\Psi}^{\alpha_m})^{\alpha_n} \tag{5.6}$$

The plasma pressure p and the poloidal current function F are obtained by the integrals:

$$p(\bar{\Psi}) = \int_{\bar{\Psi}}^{1} p'\, d\bar{\Psi} \tag{5.7}$$

$$F^2(\bar{\Psi}) = 2\int_{\bar{\Psi}}^{1} FF'\, d\bar{\Psi}$$
$$F(\bar{\Psi}) = \sqrt{F_0^2 + F^2(\bar{\Psi})} \tag{5.8}$$

Defined the computational domain $\Omega \cup [\Omega_v, \Omega_p, \Omega_\phi]$, the weak form of (5.1) is:

$$-\int_{\Omega} \frac{1}{2\pi R}\frac{1}{\mu_0}\nabla\Psi \cdot \nabla w\, d\Omega = \int_{\Omega_\phi} J_{\phi,ext}\, w\, d\Omega + \int_{\Omega_p} J_p(\Psi)\, w\, d\Omega \tag{5.9}$$

where w is a suitable test function. In the formulation adopted, the external toroidal current density $J_{\phi,ext}$ can be exploited as the sum of two distinct contributions. The first term J_c represents the current density associated with the active poloidal field coils, defined over the domain Ω_c. The second term, J_σ, accounts for the eddy currents induced in passive conducting structures:

$$J_\sigma = -\frac{\sigma}{2\pi R}\frac{\partial \Phi}{\partial t} \tag{5.10}$$

where σ denotes the electrical conductivity of the material and Φ is the total poloidal flux Ψ concatenated to the passive structures. The expression directly follows from Faraday's law, describing the response of passive conductors to time variations of the poloidal magnetic flux. Equation (5.9) can be rewritten as:

$$-\int_\Omega \frac{1}{2\pi R}\frac{1}{\mu_0}\nabla\Psi \cdot \nabla w \, d\Omega = \int_{\Omega_c} J_c \, w \, d\Omega - \int_{\Omega_\sigma} \frac{\sigma}{2\pi R}\frac{\partial \Phi}{\partial t} w \, d\Omega + \int_{\Omega_p} J_p(\Psi) \, w \, d\Omega \tag{5.11}$$

Given a finite element discretization of the domain Ω, and denoting by λ_i the hat function associated with the i-th node of the mesh, the unknown can Ψ be expanded over Ω as:

$$\Psi = \sum_{i \in N} \Psi_i \lambda_i \tag{5.12}$$

Where N is the set of indices of the nodes inside Ω. Using the Galerkin method, the Equation (5.6) becomes:

$$\bar{\bar{\mathbf{A}}}\bar{\mathbf{\Psi}} = \bar{\mathbf{b}} \tag{5.13}$$

Where:

$$\begin{aligned} A_{i,j} &= -\int_\Omega \frac{1}{2\pi R}\frac{1}{\mu_0}\nabla\lambda_i \cdot \nabla\lambda_j \, d\Omega, && i,j \in N \\ b_j &= \int_{\Omega_c} J_c \, \lambda_j \, d\Omega - \int_{\Omega_\sigma} \frac{\sigma}{2\pi R}\frac{\partial\left(\sum_{i \in N} \Psi_i \lambda_i\right)}{\partial t}\lambda_j \, d\Omega + \int_{\Omega_p} J_p\left(\sum_{i \in N} \Psi_i \lambda_i\right) \lambda_j \, d\Omega, && i,j \in N \end{aligned} \tag{5.14}$$

By inverting Equation (5.13), it is possible to obtain the poloidal flux Ψ_i at each node of the domain Ω. In the case of active conductors, the formulation in equation (5.6) is sufficient, since the external toroidal current density can be prescribed directly as a source term. However, when passive circuits are considered, such as in-vessel coils and stabilising plates, this approach is no longer adequate. In these situations, the induced currents are not imposed, but rather determined by the electromagnetic coupling with the plasma and the surrounding structures. Consequently, the governing equations must be extended to include the dynamics of passive loops, where two or more coils can be electrically connected in series, anti-series, or parallel configurations. At the current stage of development, PECAN supports only series and anti-series connections, while the implementation of general parallel configurations is planned for future releases.

To account for this effect, PECAN couples the two-dimensional FEM formulation of the Grad–Shafranov problem with a set of zero-dimensional circuit equations. The additional contribution associated with the passive loops is expressed through Faraday's law:

$$\frac{\partial \Phi}{\partial t} + RI = V_{ext} \tag{5.15}$$

where Φ denotes the poloidal magnetic flux linked to a generic passive circuit, consistently obtained from the finite element solution of the poloidal flux Ψ, R the equivalent resistance, I the eddy current and V_{ext} is the external voltage applied to the circuit (zero for purely passive circuits).

To advance this system in time, PECAN adopts the implicit Euler scheme, which ensures stability in the diffusion-dominated regime of eddy currents. By discretizing equation (5.9) over a timestep Δt, the circuit equation takes the form:

$$R\Delta t I^{n+1} + \Phi^{n+1} - \Phi^{n} = \Delta t V_{ext} \tag{5.16}$$

Where n is a generic time step. This relation is then assembled with the weak form of the Grad–Shafranov equation, yielding the monolithic 2D–0D system:

$$\begin{bmatrix} A & -C \\ C^T & R\Delta t \end{bmatrix} = \begin{bmatrix} \Psi^{n+1} \\ I^{n+1} \end{bmatrix} = \begin{bmatrix} b \\ \Delta t V_{ext} + C^T \Psi^{n} \end{bmatrix} \tag{5.17}$$

The FEM–circuit coupling operator C is constructed as:

$$C_{i,k} = \sum_{m \in k} \frac{N_m}{A_m} \int_{\Omega_m} \lambda_i \, d\Omega, \quad i \in N \tag{5.18}$$

With N_m the number of turns, A_m the cross-sectional area, and Ω_m the domain associated with passive circuit k.

In PECAN, as well as in MAXFEA, mutual and internal inductances are not introduced explicitly in the equations because they are implicitly represented within the finite-element operators that couple the magnetic field and circuit equations. The magnetic flux linked to each circuit is obtained directly from the FE solution of the poloidal flux Ψ and from the coupling operator C (Eq. 5.18). Differentiating the flux linkage with respect to the circuit currents gives the full inductance matrix $L = \partial\Phi/\partial I$, which naturally contains both self (internal) and mutual inductances of the plasma, passive structures, and coils.

The Grad–Shafranov equation is intrinsically nonlinear, due to the dependence of the plasma current density $J_p(\Psi)$ on the poloidal flux function itself. To address this nonlinearity, PECAN adopts a fixed-point (Picard) iterative scheme. The procedure begins with an initial guess of the plasma current distribution, typically a circular profile with current uniformly applied to the plasma cross-section. At each iteration, the FEM problem defined in (5.17) is solved to update the poloidal flux Ψ. The new flux solution is then used to recompute the plasma source term $J_p(\Psi)$, together with the related profile functions $p'(\Psi)$ and $FF'(\Psi)$. The updated source is inserted into the weak formulation and the process is repeated until convergence is achieved, according to a prescribed tolerance on the variation of Ψ. This iterative approach ensures numerical stability and allows a consistent determination of both the plasma equilibrium and its coupling with passive conductors. The Picard scheme also provides a flexible basis for extending the solver to transient problems, where each time step can be advanced by combining the implicit Euler discretization of the circuit equations with the nonlinear equilibrium update.

The macroscopic plasma parameters, in particular β_p and ℓ_i, are computed from volume integrals over the plasma domain Ω_p, following the same definitions used, for reference, in the FreeGS [39] Grad– Shafranov solver. The poloidal beta corresponds to the formulation $\beta_p(1)$, defined as

$$\beta_p = 2\mu_0 \frac{\int_{\Omega_p} p \, dV}{\int_{\Omega_p} B_p^2 \, dV} \tag{5.19}$$

where both the plasma pressure and the poloidal magnetic field are averaged over the plasma volume. The internal inductance, corresponding to $\ell_i(3)$, is evaluated as:

$$\ell_i = 2 \frac{\int_{\Omega_p} B_p^2 \, dV}{\mu_0^2 R_{geo} I_p^2} \tag{5.20}$$

using the geometric major radius as the reference length. This choice of formulations for β_p and ℓ_i is motivated by the need to ensure consistency and direct comparability with the output provided by MAXFEA, which adopts the same definitions. Similarly, the computation of the safety factor q_{95} follows the same formulation adopted in FreeGS:

$$q_{95} = \frac{F(\overline{\Psi} = 0.95)}{2\pi} \oint_{\overline{\Psi}=0.95} \frac{ds}{R^2 B_p} \tag{5.21}$$

In addition, halo currents have been included following a similar modelling principle adopted in MAXFEA and described in Section 3.1. In this approach, the plasma boundary is redefined to account for a finite halo width, and the associated poloidal halo current is determined from the global vertical force balance. The halo current application is implemented by extending the definition of the region of the plasma current density application beyond the plasma last closed surface in such a way that this region is divided in two parts - the plasma core and halo region - according to:

$$\Psi_{boundary}(t) = \Psi_{boundary}(t-1) + V_{axis}(t)\, w_{halo}\, \Delta t \tag{5.22}$$

Where w_{halo} represents the halo width, defined as the fraction of the total plasma poloidal cross section specified by the user (with a value between 0 and 1), and V_{axis} is the e.m.f. on the magnetic axis:

$$V_{axis}(t) = \frac{\Psi_{axis}(t) - \Psi_{axis}(t-1)}{\Delta t} \tag{5.23}$$

In PECAN, the poloidal halo current is calculated as [41]:

$$I_{pol} = \frac{2\pi}{\mu_0}(F_{lim} - F_0) \tag{5.24}$$

Where F_{lim} is the value of the poloidal current function evaluated at the plasma limiter surface, while F_0 is the reference vacuum value at machine radius calculated as $R_0 B_T$ (B_T represents the toroidal magnetic field).

In the present formulation, all conductive components are assumed to be axisymmetric, allowing the three-dimensional electromagnetic problem to be reduced to a two-dimensional (R–Z) cross-section. Non-axisymmetric features such as cuts, joints, toroidal ports, and feeders are accounted for in an approximate manner by assigning an effective electrical resistivity to the corresponding 2D regions. This equivalent resistivity is calibrated to reproduce the average toroidal current continuity observed in the real geometry.

For example, in the case of toroidal ports, the resistivity can be scaled according to the ratio between the total cross-sectional area and the effective conducting area, thus compensating for the presence of voids or openings within the actual 3D structure.

This approach preserves the overall electromagnetic coupling between plasma and passive conductors, while maintaining computational efficiency within the axisymmetric framework. Nevertheless, it neglects local 3D current effects and should therefore be complemented by dedicated 3D analyses when evaluating detailed load patterns on complex geometries.

6. Case Studies

In this chapter, a series of case studies is presented with the aim of validating and benchmarking the newly developed FEM-based solver for plasma equilibrium and transient simulations. The analysis covers both stationary equilibria and disruption scenarios, performed on a representative set of tokamak machines: EU-DEMO (baseline 2022 [56] and LAR 2024), DTT [57], ST40, and TRUST. The stationary cases are complemented by disruption simulations, including one fast upward vertical displacement event (UVDE) for DEMO 2022, four disruptions for DEMO LAR 2024 (fast and slow UVDE, fast and slow downward VDE), and two VDEs for TRUST, upward and downward fast events specifically (downward single-null configuration at EOF instant).

For consistency, the comparison between PECAN and MAXFEA has been carried out under the same modelling conditions. In particular, all simulations have been performed using identical computational meshes, the same prescribed currents in the active poloidal field coils, and an equivalent formulation of the plasma current density, using the same shaping parameters α_m, α_n, and β (with α_n fixed to 1.0 and α_m, set equal to α used in MAXFEA code, so as to reproduce the same profile adopted in MAXFEA described in 3.1). Regarding disruption scenarios, common modelling criteria were applied in terms of the imposed vertical kick, the triggering of the thermal quench (TQ) and the characteristic duration of the current quench (CQ). Furthermore, the same assumptions on halo current (HC) modelling were adopted, by using exactly the same values of halo width as those applied in MAXFEA and selecting the intermediate configuration as the reference case.

In PECAN and MAXFEA, the vertical instability is obtained from the nonlinear time evolution of the coupled plasma–structure system. A small vertical perturbation ("kick") is applied to the plasma equilibrium to mimic the arise of an instability, and the subsequent free-boundary evolution is computed by solving, at each time step, the full Grad– Shafranov equation coupled to the circuit equations of the active and passive conductors. The growth rate γ of the vertical displacement is then determined from the exponential fit of the plasma centroid position $Z_p(t)$ before wall contact. This is a standard approach in free-boundary equilibrium solvers, MAXFEA included. This approach differs from the classical rigid-current (non-deformable) model, in which the plasma current distribution and inductance are fixed and only the centroid motion is allowed. In PECAN, the plasma is represented as a deformable current distribution Jp(Ψ), so that both the shape and inductance of the plasma ℓ_i can change consistently with the evolving magnetic field. This is physically more realistic during a VDE, where flux surfaces are distorted and the plasma column elongates or contracts as it moves vertically, thus altering its mutual coupling with the surrounding structures. The deformable model therefore captures variations in the plasma inductance, β_p, and coupling coefficients, providing a more accurate prediction of the instability growth rate and induced currents than rigid-body approximations.

In PECAN, as well as in MAXFEA, the plasma equilibrium formulation never explicitly includes resistivity. The plasma resistivity is not solved for, and its effect is only implicitly represented through the pressure term and through the prescribed evolution of the plasma current during the disruption. It is of course clear that resistivity can appear when coupling with passive structures is considered, since these are treated through fully electromagnetic equations. However, in a first-order approximation, the variation of plasma resistivity between the hot and cold phases is assumed to be implicitly captured by the chosen current decay law, which acts as an input to define how the plasma current decreases in time.

The percentage differences between PECAN and MAXFEA results are consistently evaluated as:

$$\Delta X[\%] = \left(\frac{X_{PECAN}}{X_{MAXFEA}} - 1\right) \cdot 100 \tag{6.1}$$

where X denotes the considered physical quantity. For geometric quantities expressed as coordinates (for instance, magnetic axis, current barycentre, and x-point), the error has been normalized with respect to the machine radius.

Nevertheless, it is worth noting that the two codes adopt different finite element formulations for the solution of the poloidal flux. MAXFEA employs first-order finite elements, while PECAN simulations have been run using second-order Lagrange polynomials to reduce numerical errors.

A crucial preliminary step consisted of verification tests carried out in the absence of plasma. These tests were designed to ensure that the FEM formulation had been implemented correctly before introducing plasma sources. Selected verification and validation (V&V) tests aimed at assessing the accuracy of the electromagnetic solver in both steady-state and transient regimes are reported in Appendix. As a representative example, one verification study is reported for DEMO 2024 in Figure 34, where a ramp-down of the current in a central solenoid (CS) module was imposed. The induced currents on the vacuum vessel (VV) and on the in-vessel coils (IVCs) were then evaluated and compared with the reference results obtained with the MAXFEA code. The good agreement between the two codes confirmed the correctness of the electromagnetic formulation.

Building on this verification phase, the focus is shifted to stationary plasma equilibria. These equilibria were computed for the selected machines and systematically compared with the analogous cases simulated with MAXFEA. The comparison allowed for a direct assessment of the solver's accuracy in reproducing key plasma parameters, flux surfaces, and equilibrium geometries.

Subsequently, transient disruption scenarios were simulated, starting from the previously obtained stationary equilibria as initial conditions. The disruption cases—UVDEs and DVDEs, with both fast and slow time scales for the current quench (CQ) phase—were studied for DEMO and TRUST, enabling a broad exploration of the code capabilities. As for the stationary cases, the transient evolutions were benchmarked against MAXFEA, focusing on the induced currents and electromagnetic loads on passive structures.

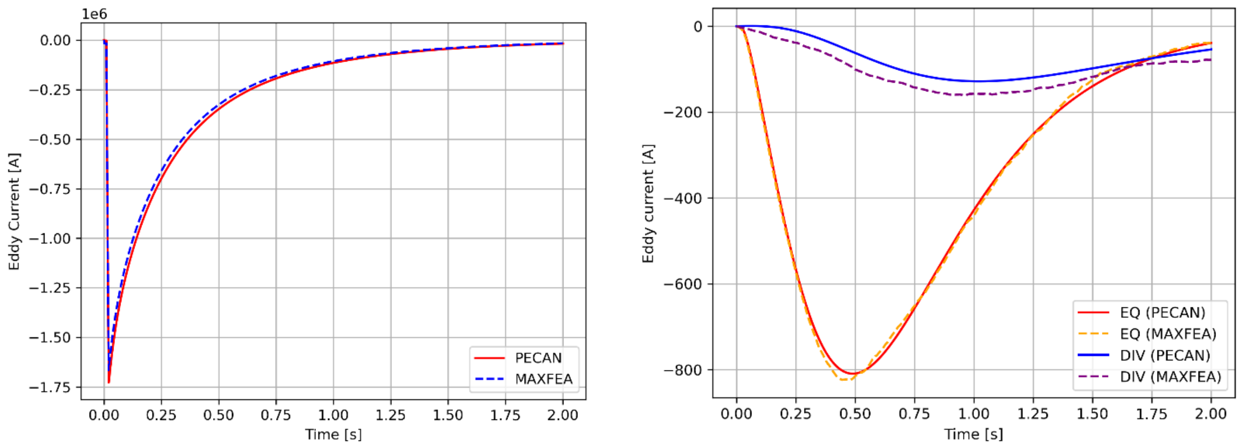

(a) (b)

Figure 34: Vacuum test using DEMO LAR 2024 as the reference model. A ramp-down of the current in a central solenoid (CS) module was imposed. (a) Induced currents on the vacuum vessel and (b) on the in-vessel coils, compared with reference results obtained with the MAXFEA code.

6.1 Stationary plasma equilibria

DEMO 2022

This section presents the results for the stationary equilibrium at the EOF corresponding to the EU-DEMO baseline 2022. In particular:

- Figure 35 shows the geometry of the domain and the mesh adopted by both codes for the simulation;
- Figure 36 illustrates the poloidal flux map obtained with PECAN;
- Figure 37 reports the comparison between the magnetic axis, the x-point, and the plasma boundary as computed by PECAN and MAXFEA;

- Table 5 summarizes the main equilibrium quantities, reporting side-by-side values obtained from the two codes.

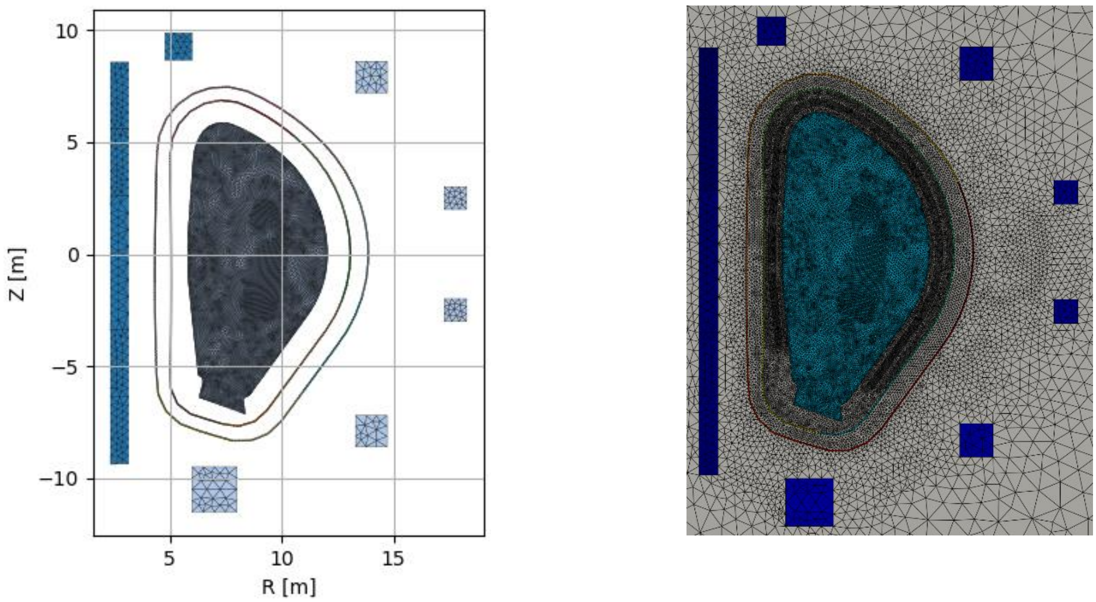

(a) (b)

Figure 35: Geometry (a) and mesh (b) for plasma equilibrium simulations of the DEMO 2022 baseline.

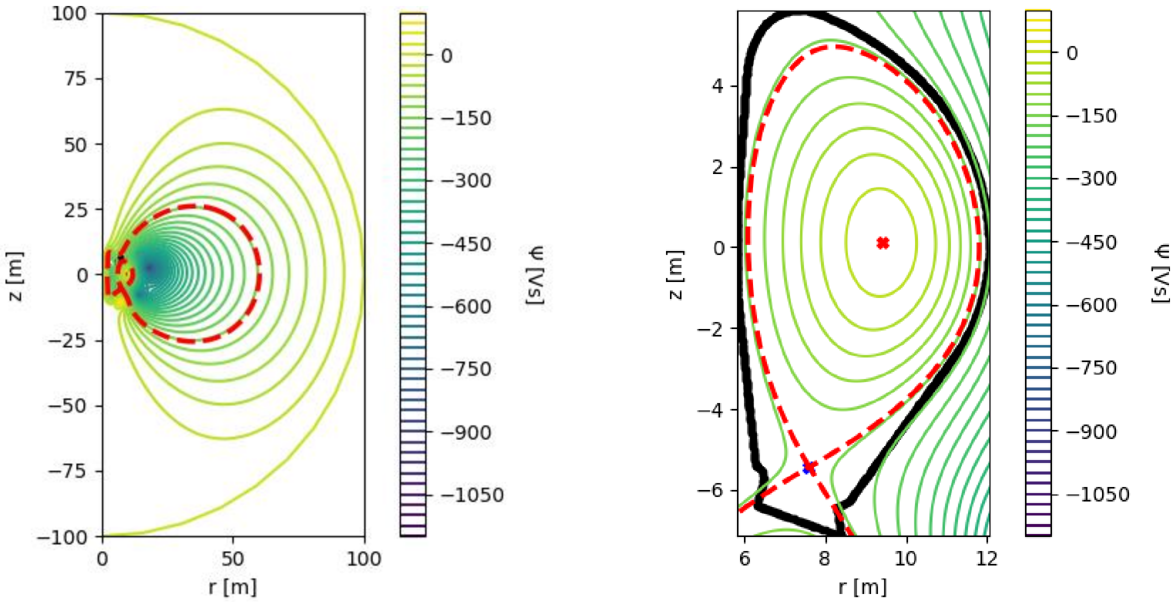

(a) (b)

Figure 36: Poloidal flux maps at the EOF instant for the DEMO baseline 2022. (a) Full-domain map; (b) zoom on the plasma region. The red dashed lines indicate the plasma boundary, while the red cross and the blue cross mark the magnetic axis and the x-point, respectively.

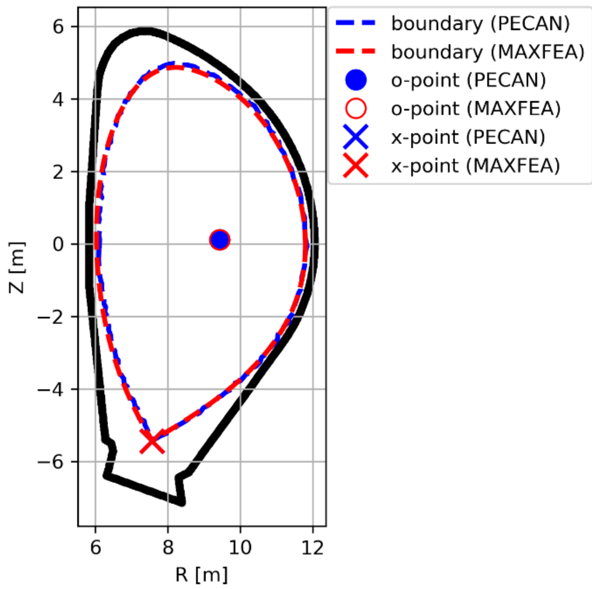

Figure 37: Comparison between PECAN and MAXFEA plasma boundaries at the EOF equilibrium for the DEMO 2022 baseline, including the location of the magnetic axis (o-point) and the x-point.

In Table 5 a comparison of the main equilibrium parameters obtained with the two codes is provided.

Table 5: Comparison between PECAN and MAXFEA main equilibrium parameters for the DEMO 2022 baseline at the EOF instant.

Quantity	PECAN	MAXFEA	Percentage difference [%]
I_p [MA]	19.07	19.07	~ 0
$\Psi_{axis} - \Psi_{boundary}$ [Vs]	137.73	142.99	-3.68
Elongation	1.80	1.79	0.64
Triangularity	0.38	0.36	5.92
Major radius [m]	8.96	8.92	0.51
Minor radius [m]	2.88	2.88	-0.09
Aspect ratio	3.11	3.09	0.61
Volume [m³]	2382.72	2354.86	1.18
β_p	1.36	1.33	1.97
ℓ_i	0.78	0.81	-3.50
q_{95}	2.91	2.90	0.63
Magnetic axis [m]	R=+9.428, Z=+0.107	R=+9.428, Z=+0.107	~ 0
Current barycenter [m]	R=+9.185, Z=+0.108	R=+9.174, Z=+0.076	0.39
x-point [m]	R=+7.566, Z=-5.445	R=+7.566, Z=-5.445	~ 0

An examination of the results indicates an excellent overall agreement between PECAN and MAXFEA. The discrepancies in the principal equilibrium quantities are consistently very small, in most cases remaining below a few percent. The plasma current is reproduced with negligible deviation, while the positions of the magnetic axis and the x-point coincide exactly in both simulations. Geometric descriptors such as elongation, triangularity, and aspect ratio show relative differences of the order of 1–6%, whereas the plasma volume and the poloidal beta β_p differ by approximately 1–2%. The largest discrepancy is observed for the internal inductance ℓ_i, with a relative difference of −3.5%, which nonetheless remains within an acceptable range for equilibrium modeling. Overall, these findings demonstrate the reliability of PECAN in reproducing the stationary equilibrium of the EU-DEMO 2022 baseline, confirming its consistency with the well-established results obtained with MAXFEA.

DEMO LAR 2024

This section discusses the stationary equilibrium results at EOF for the EU-DEMO LAR 2024 configuration. Owing to the flexibility of the plasma current density formulation introduced in Section 5.1, it was possible to benchmark PECAN not only against MAXFEA but also against the CREATE-NL code, thus extending the comparison to three equilibrium solvers, beyond the two-code analysis already presented in Section 4.1. In particular, the PECAN–MAXFEA comparison was carried out by adopting the same formulation employed in MAXFEA and reported in Section 3.1, whereas the PECAN–CREATE-NL benchmark was based on the formulation implemented in CREATE-NL.

A summary of the figures and tables is provided below.

- Figure 38 depicts the computational domain together with the discretization employed in PECAN and MAXFEA codes;
- Figure 39 presents the distribution of the poloidal flux as reconstructed by PECAN;
- Figure 39 highlights the comparison of the plasma profiles p' and FF' between PECAN, MAXFEA and CREATE-NL;
- Figure 41 highlights the comparison of the magnetic axis, x-point, and last closed flux surface between PECAN, MAXFEA and CREATE-NL;
- Table 6 and Table 7 summarize the main equilibrium quantities, reporting side-by-side values obtained from the three codes.

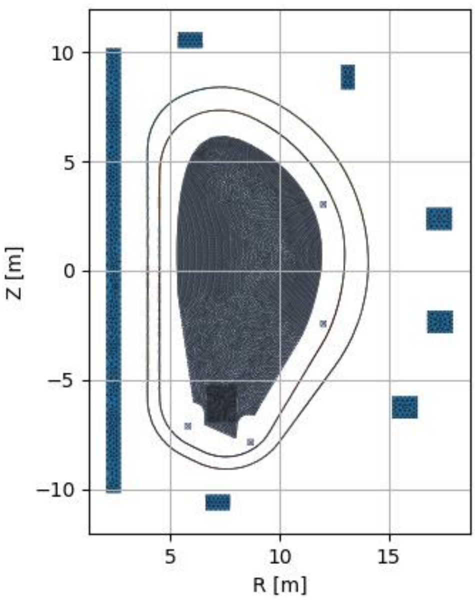

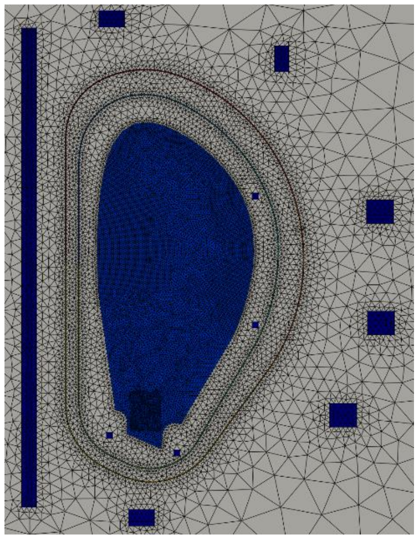

(a) (b)

Figure 38: Geometry (a) and mesh (b) for plasma equilibrium simulations of the DEMO 2024 baseline.

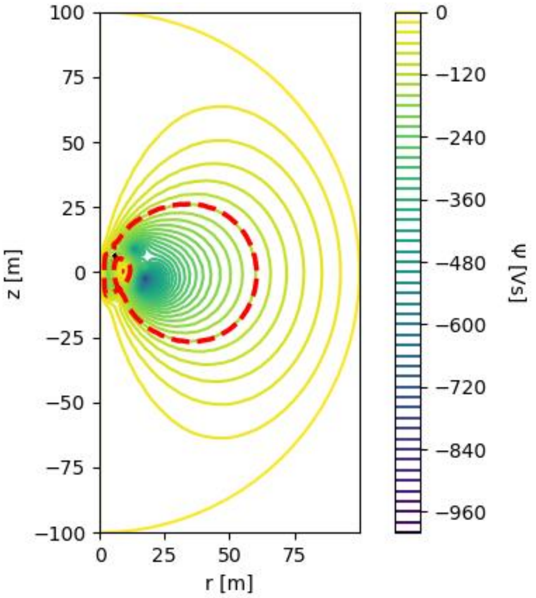

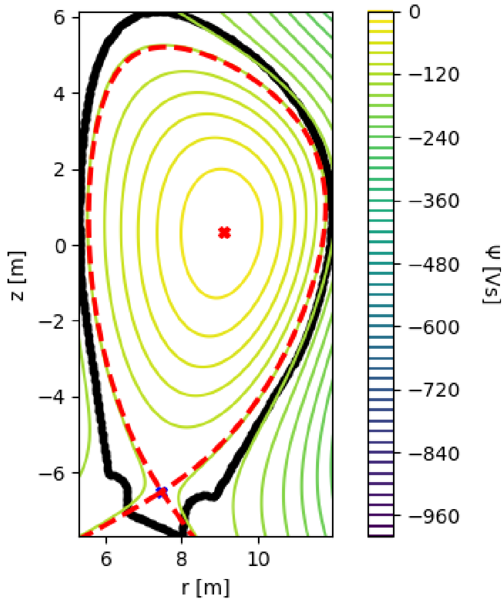

(a) (b)

Figure 39: Poloidal flux maps at the EOF instant for the DEMO baseline 2024. (a) Full-domain map; (b) zoom on the plasma region. The red dashed lines indicate the plasma boundary, while the red cross and the blue cross mark the magnetic axis and the x-point, respectively.

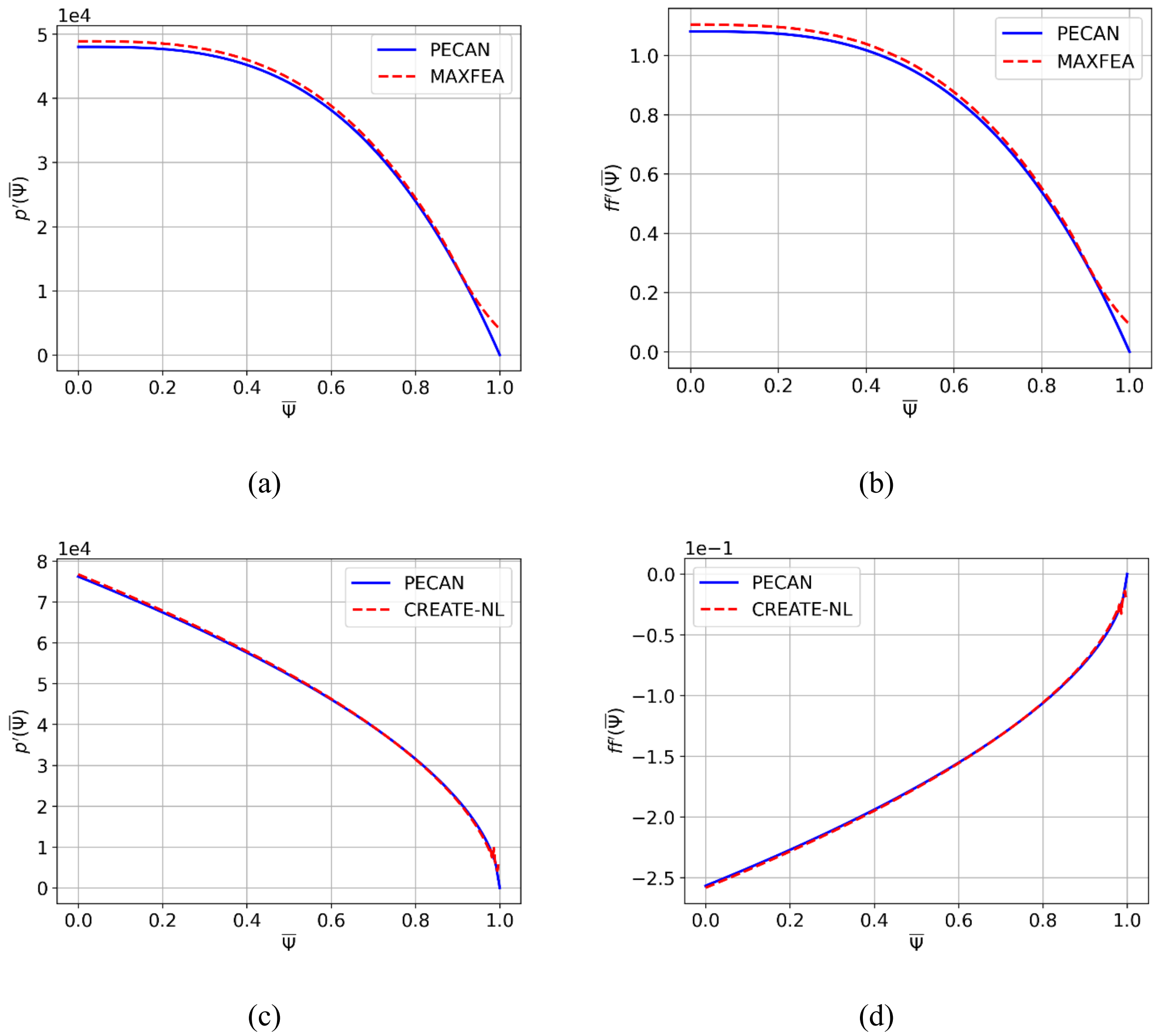

Figure 40: Comparison of plasma profiles: (a) p' and (b) ff', PECAN vs MAXFEA; (c) p' and (d) ff', PECAN vs CREATE-NL.

Figure 40 shows the comparison of the plasma profiles p' and FF' as computed with PECAN, MAXFEA, and CREATE-NL, demonstrating an excellent level of agreement across the three codes. A minor difference can be observed between PECAN and MAXFEA in correspondence with the plasma boundary, where the latter does not impose the conditions $p' = 0$ and $FF' = 0$. Such consistency is particularly significant, as it highlights the capability of PECAN to reproduce reference results obtained with well-established equilibrium solvers, despite the different underlying formulations. In particular, the flexibility of PECAN in defining the plasma current density profile allows the code to adapt to different modelling strategies, ensuring that direct cross-comparisons with other numerical tools can be carried out in a consistent and reliable manner. This feature represents a crucial prerequisite for performing robust benchmarking studies, thereby increasing the overall confidence in the quality and reliability of PECAN outputs.

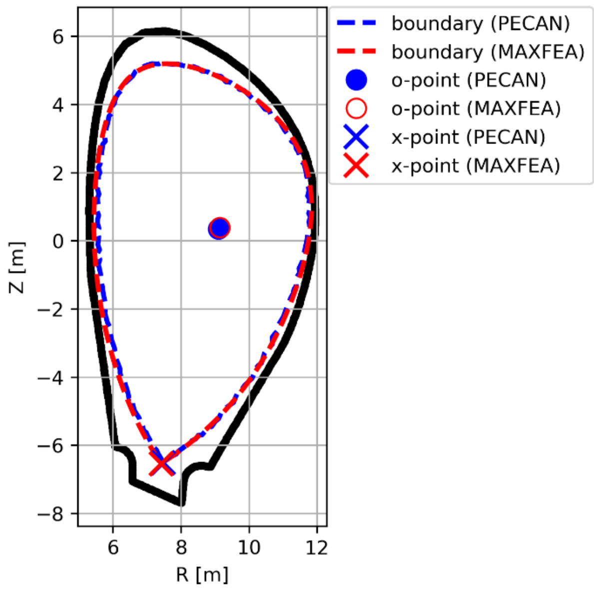

(a)

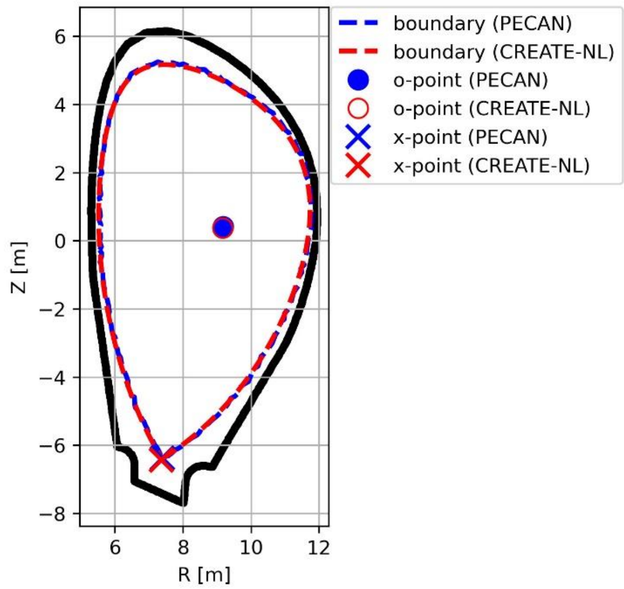

(b)

Figure 41: Comparison between (a)PECAN and MAXFEA and (b) PECAN and CREATE-NL plasma boundaries at the EOF equilibrium for the DEMO 2024 baseline, including the location of the magnetic axis (o-point) and the x-point.

Table 6 and Table 7 report the comparison of the main equilibrium parameters obtained with PECAN, MAXFEA, and CREATE-NL for the DEMO 2024 baseline configuration at the EOF instant.

Table 6: Comparison between PECAN and MAXFEA main equilibrium parameters for the DEMO 2024 baseline at the EOF instant.

Quantity	PECAN	MAXFEA	Percentage difference [%]
I_p [MA]	18.79	18.79	~ 0
$\Psi_{axis} - \Psi_{boundary}$ [Vs]	114.14	119.13	-4.19
Elongation	1.87	1.83	1.92
Triangularity	0.38	0.35	8.88
Major radius [m]	8.67	8.64	0.35
Minor radius [m]	3.14	3.20	-1.93
Aspect ratio	2.76	2.70	2.30
Volume [m³]	2798.84	2847.91	-1.72
β_p	1.08	0.91	18.43
ℓ_i	0.65	0.68	-3.59
q_{95}	3.57	3.67	-2.86
Magnetic axis [m]	R=+9.100, Z=+0.347	R=+9.133, Z=+0.396	0.69
Current barycenter [m]	R=+8.730, Z=+0.104	R=+8.731, Z=+0.096	0.09
x-point [m]	R=+7.477, Z=-6.513	R=+7.418, Z=-6.540	0.75

Table 7: Comparison between PECAN and CREATE-NL main equilibrium parameters for the DEMO 2024 baseline at the EOF instant.

Quantity	PECAN	CREATE-NL	Percentage difference [%]
I_p [MA]	18.79	18.79	~ 0
$\Psi_{axis} - \Psi_{boundary}$ [Vs]	124.36	123.44	0.74
Elongation	1.86	1.87	-0.5
Triangularity	0.41	0.40	2.50
Major radius [m]	8.66	8.63	0.35
Minor radius [m]	3.13	3.11	0.64
Aspect ratio	2.77	2.77	~ 0
Volume [m³]	2759.64	2726.01	1.23
β_p	1.34	0.91	47.30
ℓ_i	0.70	0.68	2.94
q_{95}	3.61	3.66	-1.37
Magnetic axis [m]	R=+9.187, Z=+0.417	R=+9.170, Z=+0.380	0.47
Current barycenter [m]	R=+8.857, Z=+0.162	R=+8.910, Z=+0.140	0.67
x-point [m]	R=+7.394, Z=-6.377	R=+7.370, Z=-6.430	0.68

In both cases, a very good agreement is observed across the three codes, with most parameters showing differences well below 5%. In particular, global geometric quantities such as elongation, triangularity, major and minor radii, and the plasma volume are consistently reproduced, confirming the robustness of PECAN in capturing the equilibrium shape and size. The comparison of the magnetic axis position, current barycentre, and x-point coordinates further corroborates this agreement, with discrepancies normalized to the machine size remaining below 1%, thus validating the consistency of the equilibrium reconstruction.

The agreement with MAXFEA is essentially exact for the plasma current and very good for all other parameters, thereby demonstrating the reliability of PECAN with respect to a legacy finite-element solver routinely employed for disruption and load studies. When compared to CREATE-NL, PECAN again reproduces with high fidelity the main geometric and magnetic parameters, although a larger deviation is observed for the poloidal beta β_p (around 47%). This difference can be ascribed not to an inconsistency in the equilibrium solution, but rather to the distinct definitions adopted in the two codes. As discussed in Section 4.1, CREATE-NL evaluates β_p according to its own normalization formula (5.1), whereas PECAN currently computes β_p using a different definition as $\beta_p(1)$, defined by Eq. 5.19.

Consequently, the numerical values cannot be directly compared even when the underlying equilibrium is essentially the same.

This discrepancy is therefore methodological rather than physical. In fact, if PECAN outputs are post-processed by applying the same definition of β_p as employed in CREATE-NL, the residual difference is expected to shrink substantially, bringing the two results into the same level of agreement already observed for all other equilibrium quantities. This confirms that PECAN provides reliable and flexible outputs, while also highlighting the importance of adopting consistent definitions when benchmarking against external codes. Overall, these results demonstrate that PECAN can be confidently employed for predictive analyses and cross-validation studies within the DEMO framework.

DTT v15

This section presents the results for the stationary equilibrium at the EOF corresponding to the DTT baseline v15 [57]. In particular:

- Figure 42 shows the geometry of the domain and the mesh adopted by both codes for the simulation;
- Figure 43 illustrates the poloidal flux map obtained with PECAN;
- Figure 44 reports the comparison between the magnetic axis, the x-point, and the plasma boundary as computed by PECAN and MAXFEA;
- Table 8 summarizes the main equilibrium quantities, reporting side-by-side values obtained from the two codes.

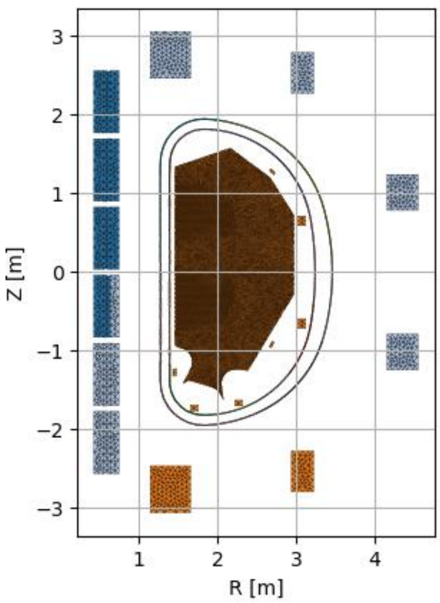

(a)

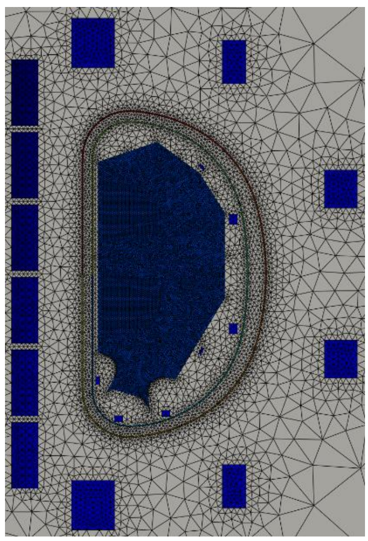

(b)

Figure 42: Geometry (a) and mesh (b) for plasma equilibrium simulations of the DTT v15 baseline.

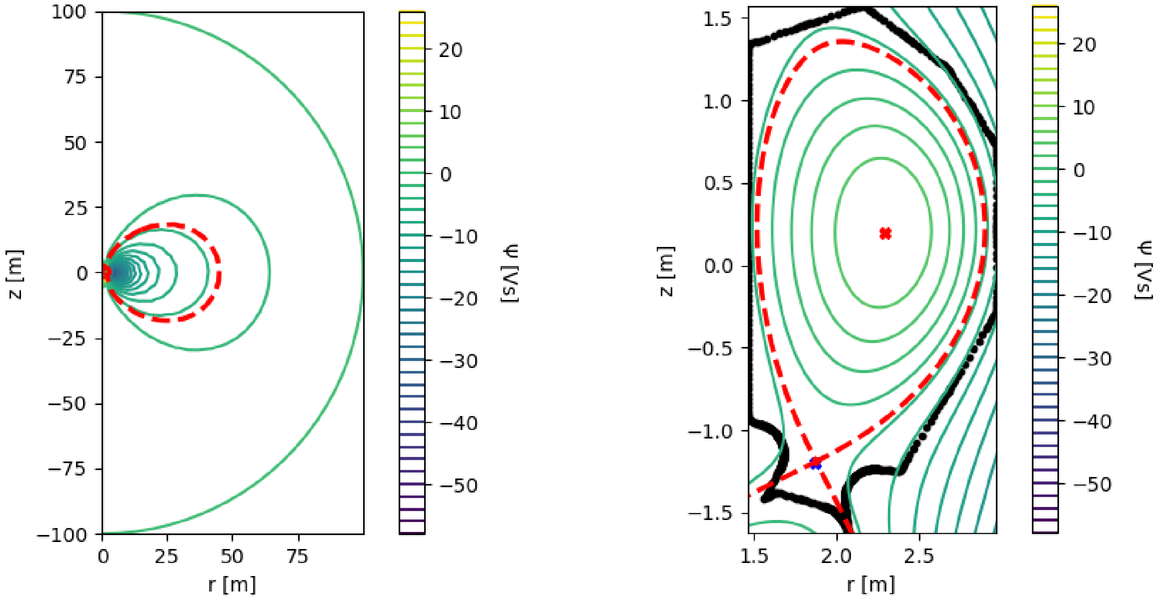

(a) (b)

Figure 43: Poloidal flux maps at the EOF instant for the DTT baseline v15. (a) Full-domain map; (b) zoom on the plasma region. The red dashed lines indicate the plasma boundary, while the red cross and the blue cross mark the magnetic axis and the x-point, respectively.

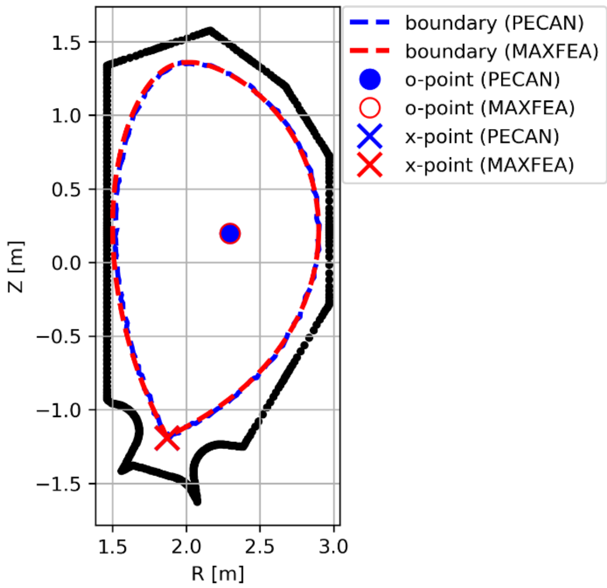

Figure 44: Comparison between PECAN and MAXFEA plasma boundaries at the EOF equilibrium for the DTT v15 baseline, including the location of the magnetic axis (o-point) and the x-point.

Table 8 reports the comparison between the stationary equilibrium results obtained with PECAN and MAXFEA at EOF for DTT.

Table 8: Comparison between PECAN and MAXFEA main equilibrium parameters for the DTT v15 baseline at the EOF instant.

Quantity	PECAN	MAXFEA	Percentage difference [%]
I_p [MA]	5.50	5.50	~ 0
$\Psi_{axis} - \Psi_{boundary}$ [Vs]	9.52	9.86	-3.45
Elongation	1.84	1.83	0.73
Triangularity	0.40	0.36	12.15
Major radius [m]	2.21	2.20	0.45
Minor radius [m]	0.69	0.70	-0.89
Aspect ratio	3.19	3.15	1.39
Volume [m³]	35.02	34.99	0.09
β_p	0.98	0.93	5.22
ℓ_i	0.75	0.78	-3.74
q_{95}	2.83	2.87	-1.37
Magnetic axis [m]	R=+2.297, Z=+0.197	R=+2.297, Z=+0.197	~ 0
Current barycenter [m]	R=+2.234, Z=+0.185	R=+2.229, Z=+0.188	0.29
x-point [m]	R=+1.869, Z=-1.194	R=+1.869, Z=-1.194	~ 0

The agreement between the two solvers is overall very satisfactory, with most global quantities showing percentage differences below 5%. The plasma current is identical by construction, while the poloidal flux difference between axis and boundary exhibits a small underestimation in PECAN (−3.45%). The geometric descriptors of the plasma shape (elongation, triangularity, major and minor radius, aspect ratio, and volume) are also in close agreement; among these, triangularity shows the largest deviation (≈12%), though the absolute difference remains modest.

The plasma parameters β_p and ℓ_i are reproduced with good accuracy, showing relative deviations of +5.2% and −3.7%, respectively, whereas the safety factor at 95% flux surface differs by −1.4%. The magnetic axis position is perfectly consistent between the two codes, while the current barycenter differs only marginally. Finally, the x-point position is exactly matched, further confirming the robustness of the equilibrium reconstruction.

ST40

This section presents the results for the stationary equilibrium at the SOF corresponding to the ST40 model adopted in [30][31]. In particular:

- Figure 45 shows the geometry of the domain and the mesh adopted by both codes for the simulation;
- Figure 46 illustrates the poloidal flux map obtained with PECAN;

- Figure 47 reports the comparison between the magnetic axis, the x-point, and the plasma boundary as computed by PECAN and MAXFEA;
- Table 9 summarizes the main equilibrium quantities, reporting side-by-side values obtained from the two codes.

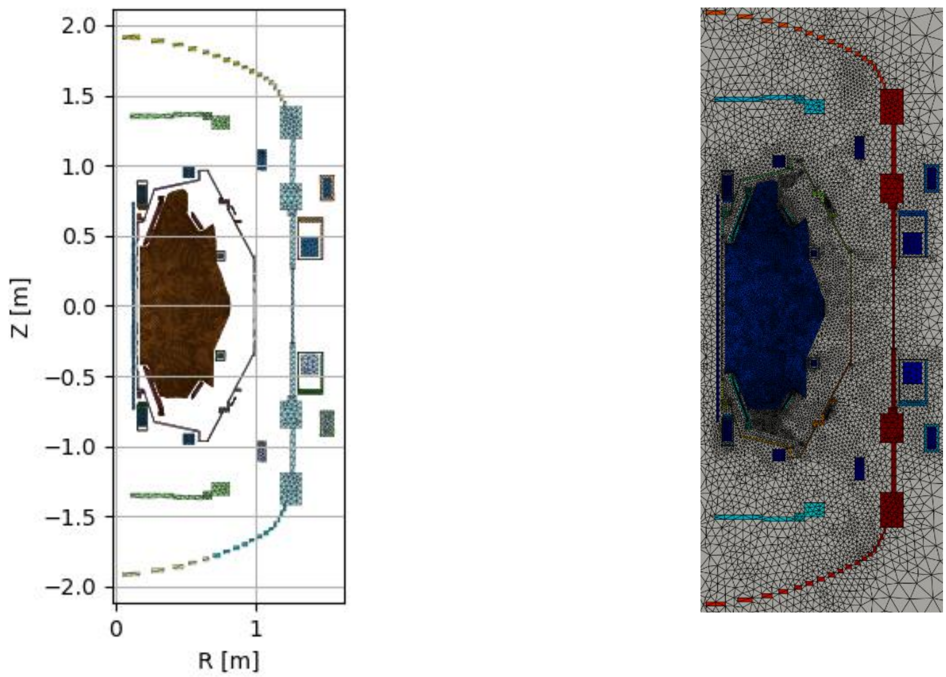

(a) (b)

Figure 45: Geometry (a) and mesh (b) for plasma equilibrium simulations of ST40.

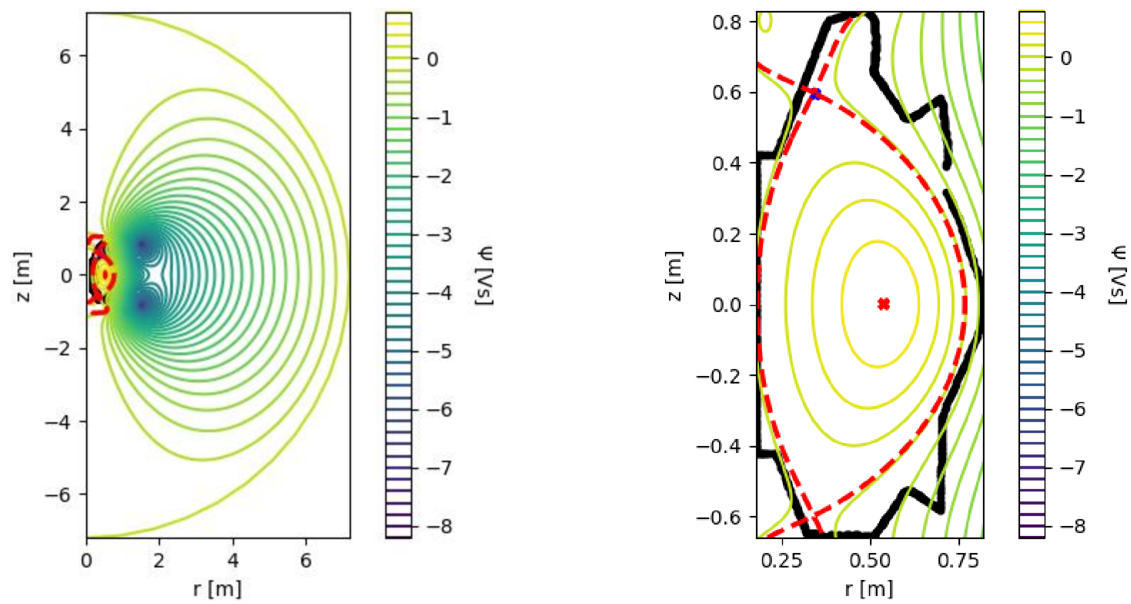

(a) (b)

Figure 46: Poloidal flux maps at the SOF instant for ST40. (a) Full-domain map; (b) zoom on the plasma region. The red dashed lines indicate the plasma boundary, while the red cross and the blue cross mark the magnetic axis and the x-point, respectively.

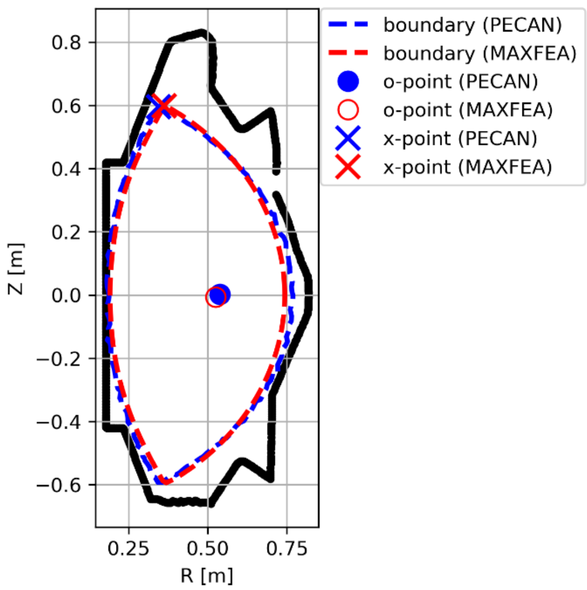

Figure 47: Comparison between PECAN and MAXFEA plasma boundaries at the SOF equilibrium for ST40, including the location of the magnetic axis (o-point) and the x-point.

In Table 9 a comparison of the main equilibrium parameters obtained with the two codes is provided.

Table 9: Comparison between PECAN and MAXFEA main equilibrium parameters for ST40 at the SOF instant.

Quantity	PECAN	MAXFEA	Percentage difference [%]
I_p [MA]	2.00	2.00	~ 0
$\Psi_{axis} - \Psi_{boundary}$ [Vs]	0.71	0.71	0.68
Elongation	2.01	2.16	-6.98
Triangularity	0.41	0.37	10.79
Major radius [m]	0.47	0.47	1.47
Minor radius [m]	0.30	0.28	6.91
Aspect ratio	1.61	1.69	-5.09
Volume [m³]	1.39	1.30	6.95
β_p	0.67	0.62	7.05
ℓ_i	0.71	0.70	1.81
q_{95}	4.65	4.32	7.78
Magnetic axis [m]	R=+0.538, Z=+0.003	R=+0.525, Z=-0.006	3.22
Current barycenter [m]	R=+0.483, Z=+0.000	R=+0.479, Z=+0.000	0.81
x-point [m]	R=+0.344, Z=+0.595	R=+0.363, Z=+0.599	3.78

The two codes show a generally good agreement, with plasma current and poloidal flux difference nearly identical. The geometric descriptors exhibit slightly larger discrepancies than in previous benchmarks: the elongation is underestimated by PECAN (−7%), while the triangularity and the minor radius are overestimated by about 11% and 7%, respectively. These differences reflect directly on the aspect ratio (−5%) and on the plasma volume (+7%).

The internal plasma parameters β_p, ℓ_i and q_{95} show deviations of 7%, 2%, and 8%, respectively, which remain acceptable in view of the different implementations. The magnetic axis position differs by ~3% both radially and vertically, while the current barycenter is well reproduced. Finally, the x-point position shows a moderate deviation (≈3.8%), still within the expected range for this configuration. Overall, PECAN is able to reproduce the main equilibrium features of ST40 with satisfactory accuracy, confirming the consistency of the formulation.

Validation with ST40 Experimental Data

The PECAN finite element solver was validated against experimental data from the ST40 spherical tokamak, considering shot #14437 at 120 ms, which represents a well-characterized operating point for benchmarking equilibrium reconstruction codes. The validation was carried out through a direct comparison with the results of GSFit [73]—the official magnetic reconstruction code developed by Tokamak Energy—and with MAXFEA.

The benchmarking was performed using the same updated geometry of the ST40 device, including the detailed configuration of the vacuum vessel, central solenoid, and poloidal field coils. The same mesh and circuit data were used in all solvers, ensuring full geometric and numerical consistency.

Both PECAN and MAXFEA implemented the same analytical expression for the plasma current density, consistent with the linear experimental profiles of pressure and toroidal field derivatives (p' and FF') kindly provided by Tokamak Energy. The adopted formulation is:

$$J_p(\Psi) = \lambda \left[\frac{R}{R_0}\beta - \frac{R_0}{R}(1-\beta)\right](1-\bar{\Psi}) \tag{6.2}$$

With the profile parameters $\alpha_m = \alpha_n = 1$.

The comparison was enabled by the fact that PECAN natively generates standard gEQDSK files, allowing a one-to-one cross-validation with GSFit and MAXFEA using the same data exchange format. For this purpose, PECAN relies on the open-source FreeQDSK library [40], which has been extended to support additional metadata and compatibility with free-boundary equilibrium workflows. This feature confirms the interoperability of PECAN with existing analysis and visualization tools commonly adopted in the magnetic confinement fusion community.

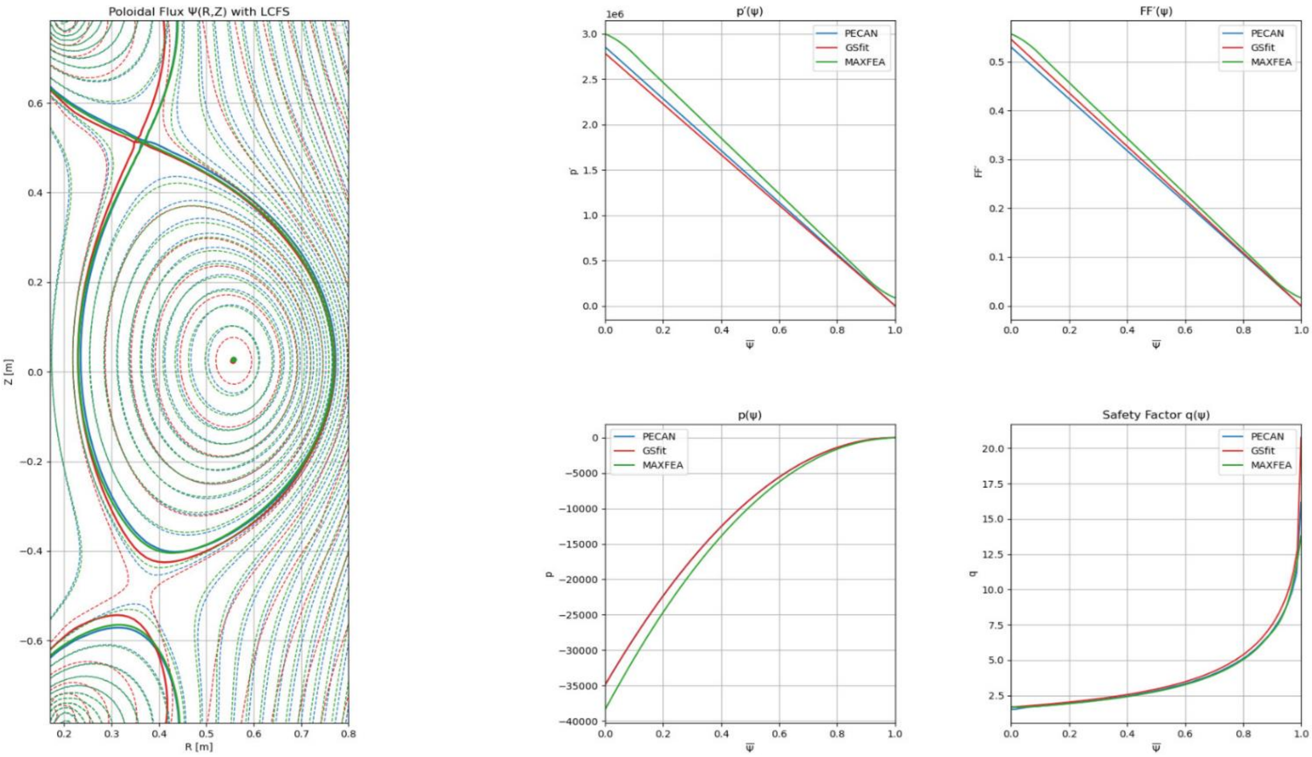

Figure 48: comparison of the poloidal flux maps and plasma profiles between PECAN, GSFit and MAXFEA using the gEQDSK format for shot #14437 at 120 ms of the the ST40 tokamak.

The quantitative assessment highlighted an excellent correspondence between the equilibrium solutions. The normalized root mean square error (RMSE) on the plasma boundary is approximately 2.8% of R_0, while the normalized displacement of the magnetic axis remains below 1% of R_0. The profiles of p', FF', pressure, and safety factor show a consistent shape and amplitude across the three codes, with RMSE values typically within a few percent for the comparison. This level of accuracy demonstrates that the finite element formulation implemented in PECAN reproduces the expected equilibrium topology and poloidal flux distribution with high fidelity.

It should be noted that this verification exercise was carried out neglecting the conductive passive structures, focusing solely on the plasma and active coil coupling. Therefore, eddy currents in the vacuum vessel and support structures were not included in the model. Despite this simplification, the observed agreement across all codes—both in terms of global equilibrium geometry and local magnetic profiles—confirms the robustness of the PECAN formulation. These results validate its capability to serve as a reliable free-boundary FEM equilibrium solver and as a modern, open framework compatible with experimental reconstruction workflows through the gEQDSK standard.

TRUST

This section presents the stationary equilibrium results for TRUST, obtained with the machine model reported in Figure 49. Three plasma configurations have been considered, namely the downward single-null (DSN), the upward single-null (USN), and the double-null (DN). For each configuration, equilibria have been computed at both the Start Of Flat-top (SOF) and End Of Flat-top (EOF) instants, in order to provide a comprehensive overview of the reference operational scenarios reported in Section 4.2.

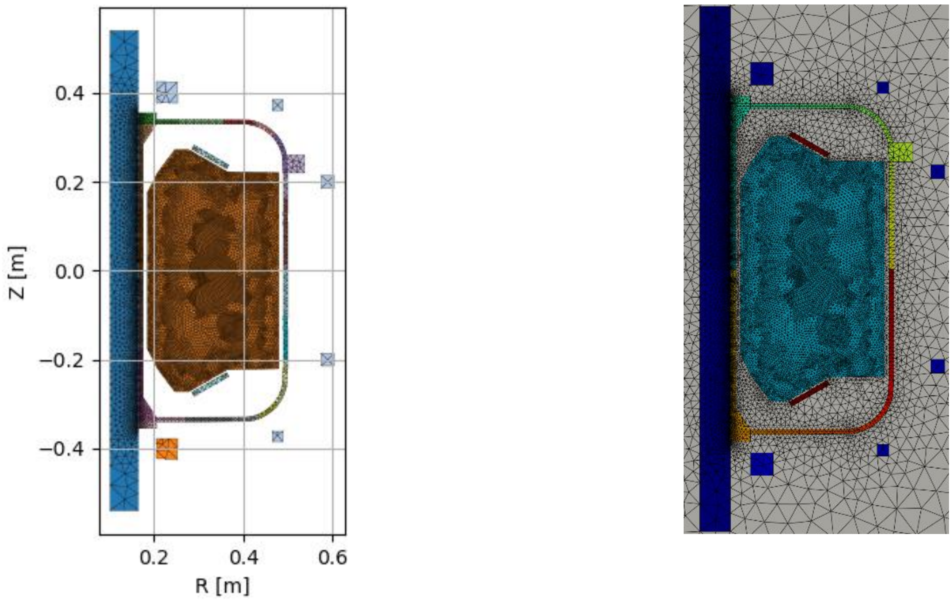

(a) (b)

Figure 49: Geometry (a) and mesh (b) for plasma equilibrium simulations of TRUST.

Downward single-null configuration

This section presents the results for the stationary equilibria at the SOF and EOF corresponding for TRUST in downward single-null configuration. In particular:

- Figure 50 illustrates the poloidal flux map obtained with PECAN;
- Figure 51 reports the comparison between the magnetic axis, the x-point, and the plasma boundary as computed by PECAN and MAXFEA;
- Table 10 and Table 11 summarize the main equilibrium quantities, reporting side-by-side values obtained from the two codes.

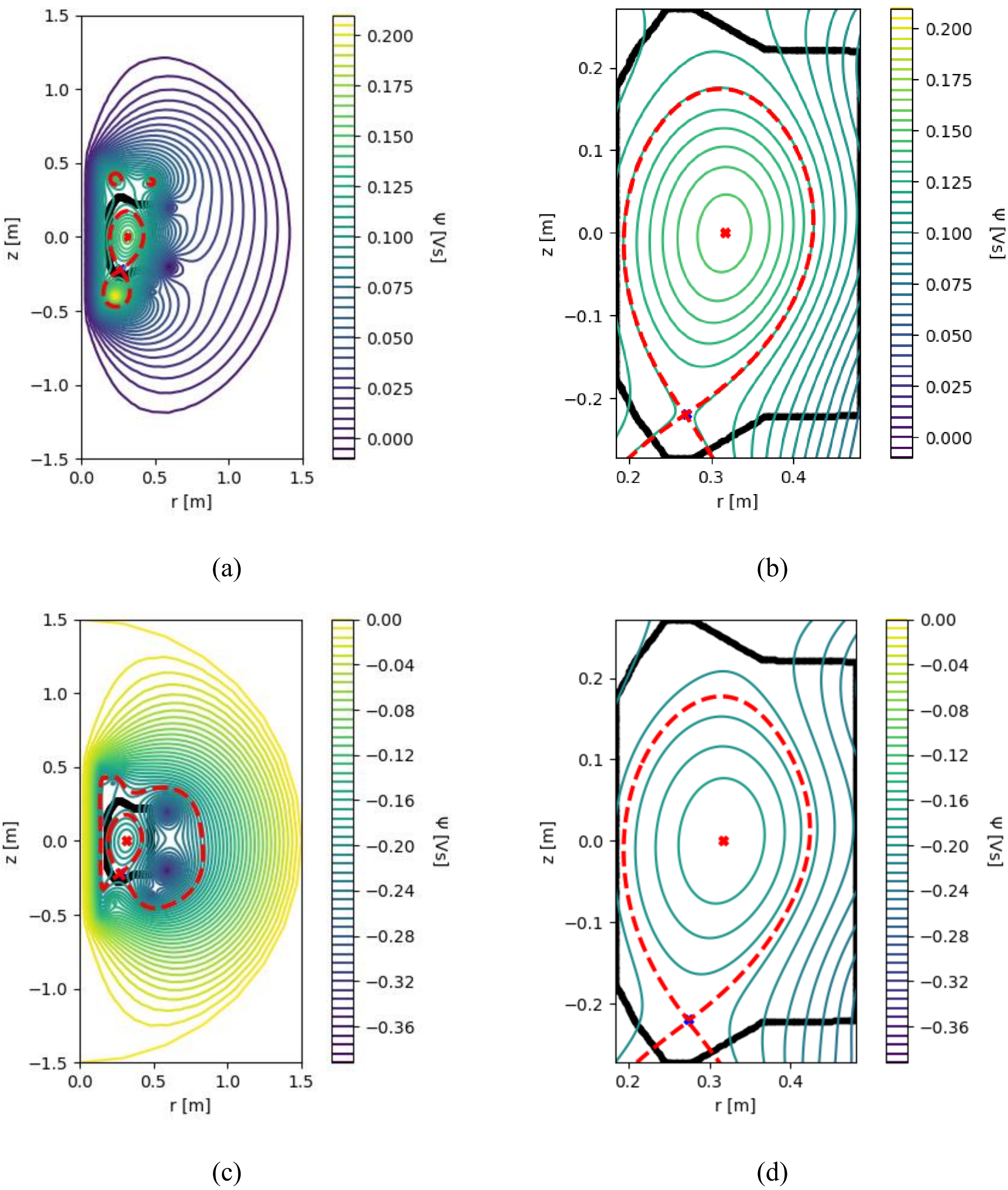

Figure 50: Poloidal flux maps for TRUST, downward single-null configuration. (a) Full-domain map and (b) zoom on the plasma region at the SOF instant; (c) Full-domain map and (d) zoom on the plasma region at the EOF instant. The red dashed lines indicate the plasma boundary, while the red cross and the blue cross mark the magnetic axis and the x-point, respectively.

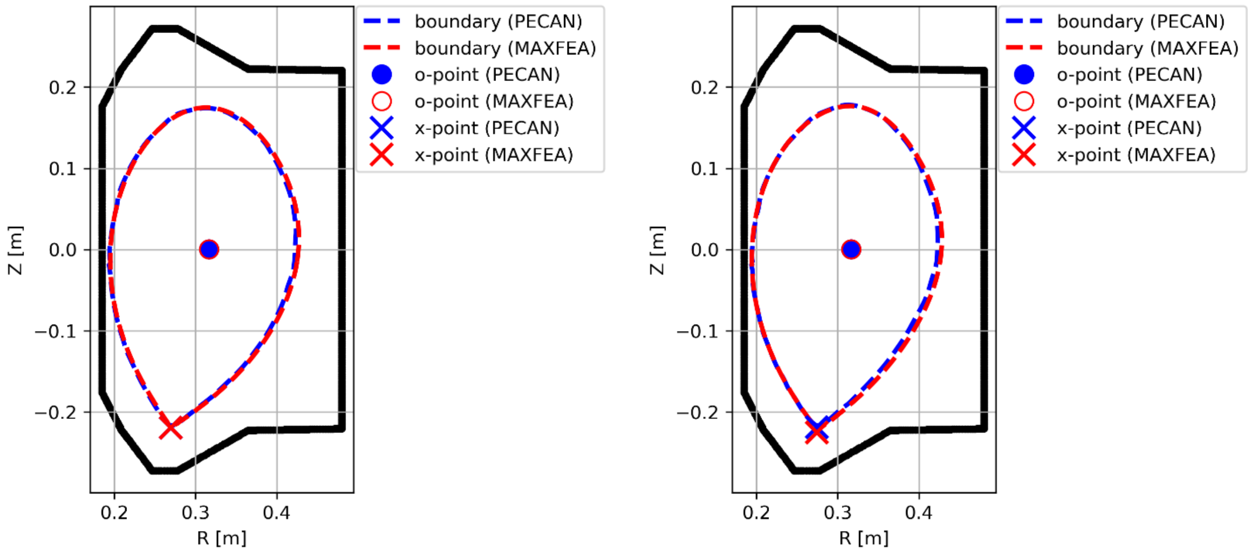

(a) (b)

Figure 51: Comparison between PECAN and MAXFEA plasma boundaries at (a) SOF and (b) EOF equilibria for TRUST (downward single-null configuration), including the location of the magnetic axis (o-point) and the x-point.

Table 10 and Table 11 report the comparison of the main equilibrium parameters obtained with PECAN and MAXFEA for TRUST downward single-null configuration at the SOF and EOF instants.

Table 10: Comparison between PECAN and MAXFEA main equilibrium parameters for TRUST at the SOF instant, downward single-null configuration.

Quantity	PECAN	MAXFEA	Percentage difference [%]
I_p [kA]	110.00	110.00	~ 0
$\Psi_{axis} - \Psi_{boundary}$ [Vs]	0.03	0.03	-4.24
Elongation	1.70	1.70	0.01
Triangularity	0.13	0.18	-27.10
Major radius [m]	0.31	0.31	-0.83
Minor radius [m]	0.12	0.12	-0.86
Aspect ratio	2.68	2.68	0.03
Volume [m³]	0.12	0.13	-1.03
β_p	0.12	0.11	3.39
ℓ_i	0.78	0.81	-3.66
q_{95}	3.20	3.17	0.93
Magnetic axis [m]	R=+0.317, Z=+0.000	R=+0.317, Z=+0.000	~ 0
Current barycenter [m]	R=+0.304, Z=-0.004	R=+0.306, Z=-0.004	0.84
x-point [m]	R=+0.269, Z=-0.219	R=+0.269, Z=-0.219	~ 0

Table 11: Comparison between PECAN and MAXFEA main equilibrium parameters for TRUST at the EOF instant, downward single-null configuration.

Quantity	PECAN	MAXFEA	Percentage difference [%]
I_p [kA]	110.00	110.00	~ 0
$\Psi_{axis} - \Psi_{boundary}$ [Vs]	0.03	0.03	-4.42
Elongation	1.72	1.70	1.38
Triangularity	0.12	0.15	-21.80
Major radius [m]	0.31	0.31	-0.91
Minor radius [m]	0.11	0.12	-1.87
Aspect ratio	2.69	2.66	0.98
Volume [m³]	0.12	0.13	-2.48
β_p	0.12	0.12	3.04
ℓ_i	0.77	0.81	-4.22
q_{95}	3.22	3.22	-0.11
Magnetic axis [m]	R=+0.317, Z=+0.000	R=+0.317, Z=+0.000	~ 0
Current barycenter [m]	R=+0.303, Z=-0.003	R=+0.306, Z=-0.004	0.90
x-point [m]	R=+0.275, Z=-0.219	R=+0.275, Z=-0.225	2.1129

Upward single-null configuration

This section presents the results for the stationary equilibria at the SOF and EOF corresponding for TRUST in upward single-null configuration. In particular:

- Figure 52 illustrates the poloidal flux map obtained with PECAN;
- Figure 53 reports the comparison between the magnetic axis, the x-point, and the plasma boundary as computed by PECAN and MAXFEA;
- Table 12 and Table 13 summarize the main equilibrium quantities, reporting side-by-side values obtained from the two codes.

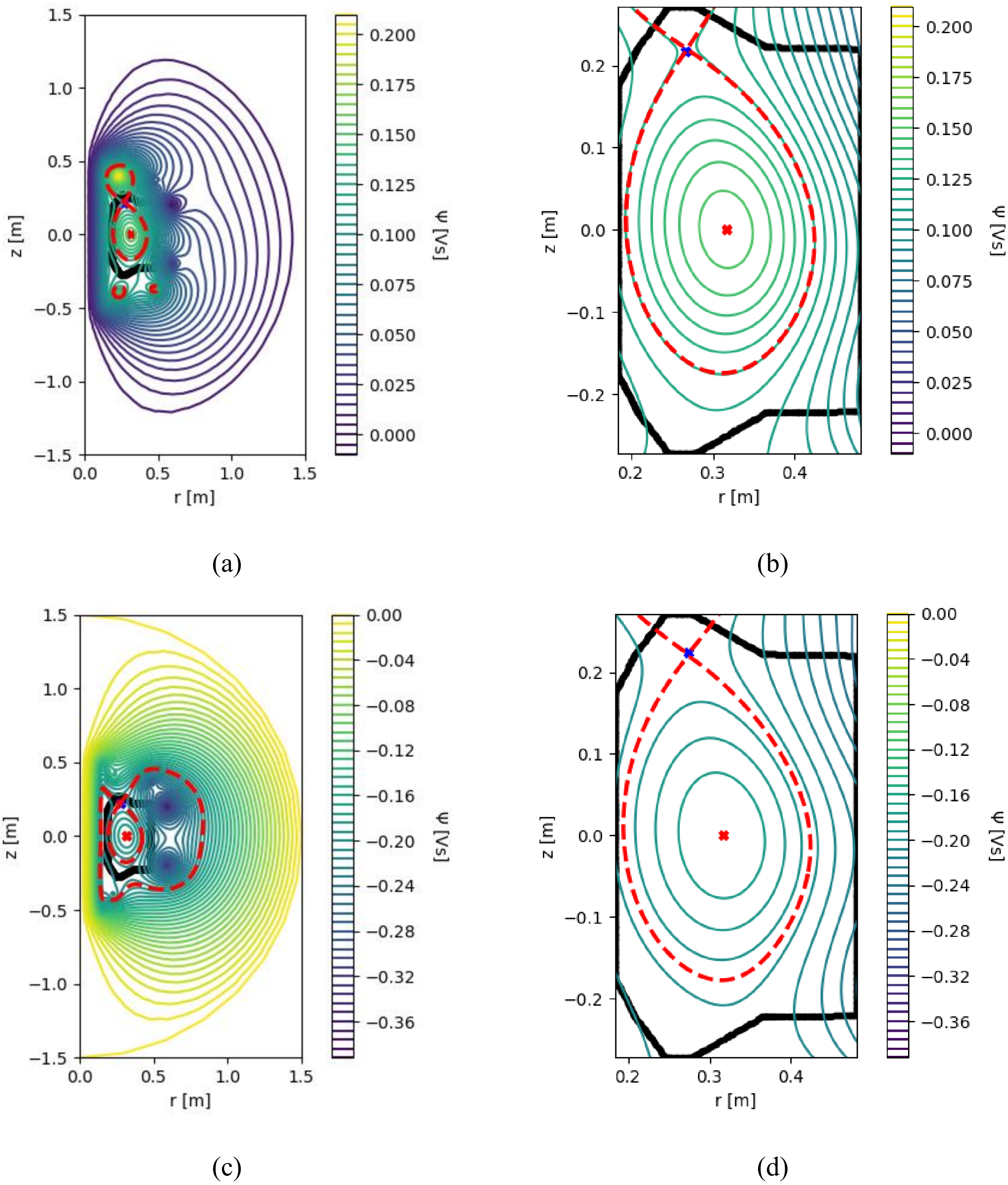

Figure 52: Poloidal flux maps for TRUST, upward single-null configuration. (a) Full-domain map and (b) zoom on the plasma region at the SOF instant; (c) Full-domain map and (d) zoom on the plasma region at the EOF instant. The red dashed lines indicate the plasma boundary, while the red cross and the blue cross mark the magnetic axis and the x-point, respectively.

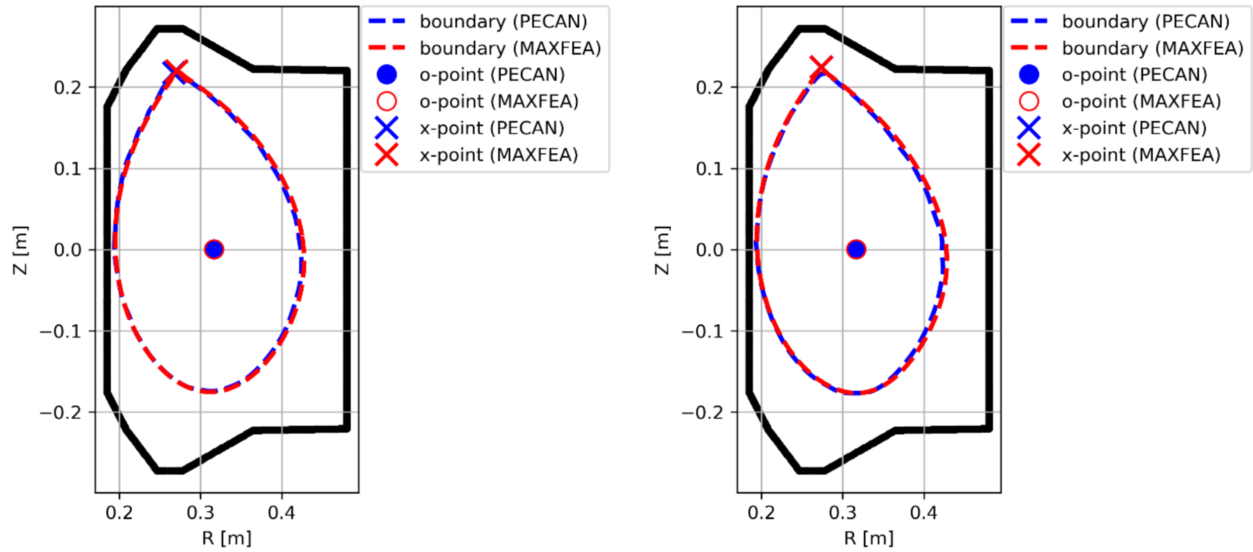

(a) (b)

Figure 53: Comparison between PECAN and MAXFEA plasma boundaries at (a) SOF and (b) EOF equilibria for TRUST (upward single-null configuration), including the location of the magnetic axis (o-point) and the x-point.

Table 12 and Table 13 report the comparison of the main equilibrium parameters obtained with PECAN and MAXFEA for TRUST upward single-null configuration at the SOF and EOF instants.

Table 12: Comparison between PECAN and MAXFEA main equilibrium parameters for TRUST at the SOF instant, upward single-null configuration.

Quantity	PECAN	MAXFEA	Percentage difference [%]
I_p [kA]	110.00	110.00	~ 0
$\Psi_{axis} - \Psi_{boundary}$ [Vs]	0.03	0.03	-4.26
Elongation	1.70	1.70	0.09
Triangularity	0.15	0.17	-12.43
Major radius [m]	0.31	0.31	-0.68
Minor radius [m]	0.12	0.12	-0.92
Aspect ratio	2.68	2.69	0.24
Volume [m³]	0.12	0.13	-1.48
β_p	0.12	0.11	3.32
ℓ_i	0.78	0.81	-3.81
q_{95}	3.20	3.18	0.54
Magnetic axis [m]	R=+0.317, Z=+0.000	R=+0.317, Z=+0.000	~ 0
Current barycenter [m]	R=+0.304, Z=-0.004	R=+0.306, Z=-0.004	0.86
x-point [m]	R=+0.267, Z=+0.217	R=+0.271, Z=+0.219	1.35

Table 13: Comparison between PECAN and MAXFEA main equilibrium parameters for TRUST at the EOF instant, upward single-null configuration.

Quantity	PECAN	MAXFEA	Percentage difference [%]
I_p [kA]	110.00	110.00	~ 0
$\Psi_{axis} - \Psi_{boundary}$ [Vs]	0.03	0.03	-4.32
Elongation	1.71	1.72	-0.56
Triangularity	0.12	0.16	-24.32
Major radius [m]	0.31	0.31	-0.92
Minor radius [m]	0.12	0.12	-1.44
Aspect ratio	2.68	2.66	0.52
Volume [m³]	0.12	0.13	-2.51
β_p	0.12	0.12	3.05
ℓ_i	0.77	0.81	-4.03
q_{95}	3.22	3.23	-0.26
Magnetic axis [m]	R=+0.317, Z=+0.000	R=+0.317, Z=+0.000	~ 0
Current barycenter [m]	R=+0.303, Z=-0.003	R=+0.306, Z=-0.004	0.91
x-point [m]	R=+0.274, Z=+0.225	R=+0.274, Z=+0.225	~ 0

Double-null configuration

This section presents the results for the stationary equilibria at the SOF and EOF corresponding for TRUST in double-null configuration. In particular:

- Figure 54 illustrates the poloidal flux map obtained with PECAN;
- Figure 55 reports the comparison between the magnetic axis, the x-point, and the plasma boundary as computed by PECAN and MAXFEA;
- Table 15 summarize the main equilibrium quantities, reporting side-by-side values obtained from the two codes.

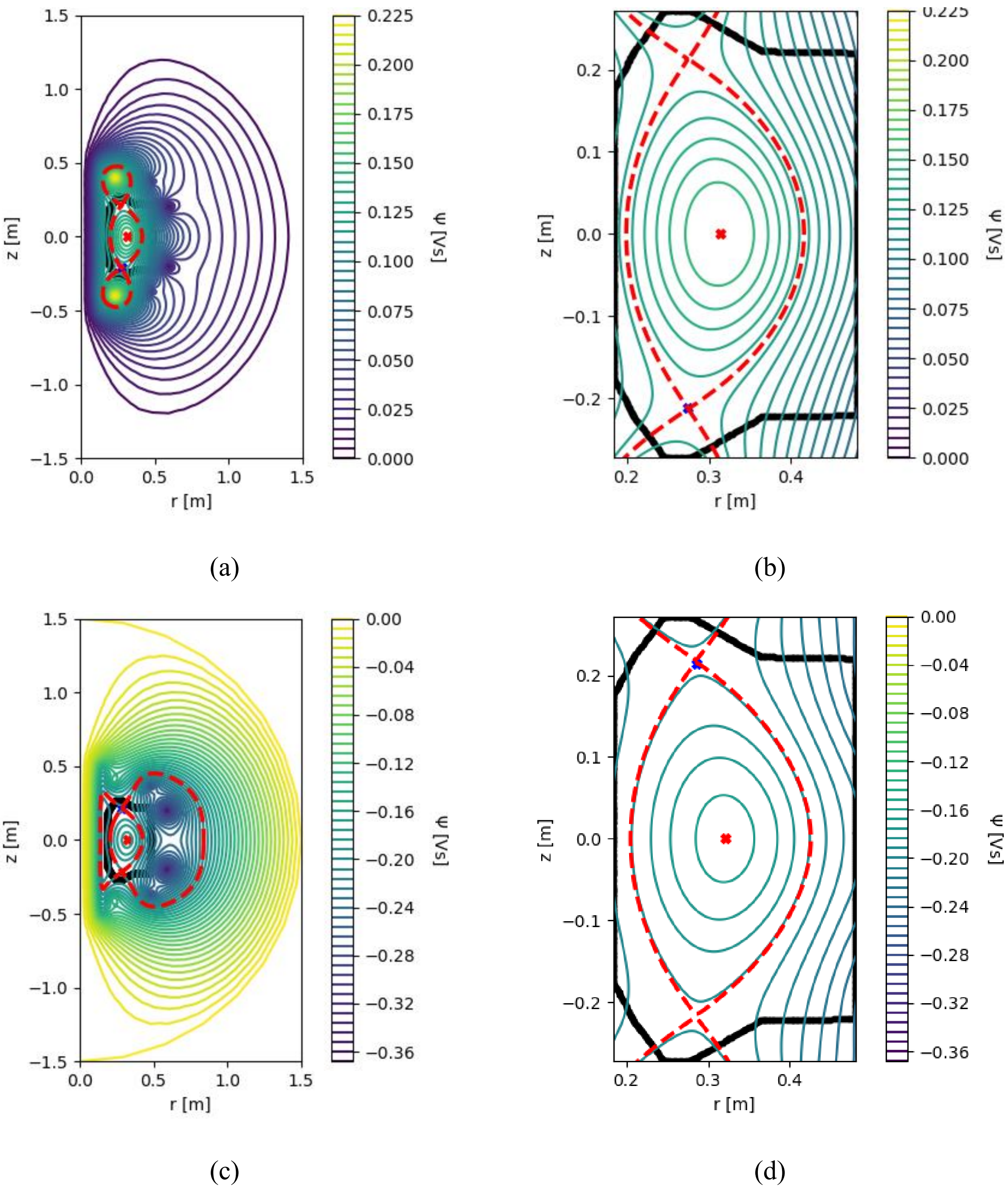

Figure 54: Poloidal flux maps for TRUST, double-null configuration. (a) Full-domain map and (b) zoom on the plasma region at the SOF instant; (c) Full-domain map and (d) zoom on the plasma region at the EOF instant. The red dashed lines indicate the plasma boundary, while the red cross and the blue cross mark the magnetic axis and the x-point, respectively.

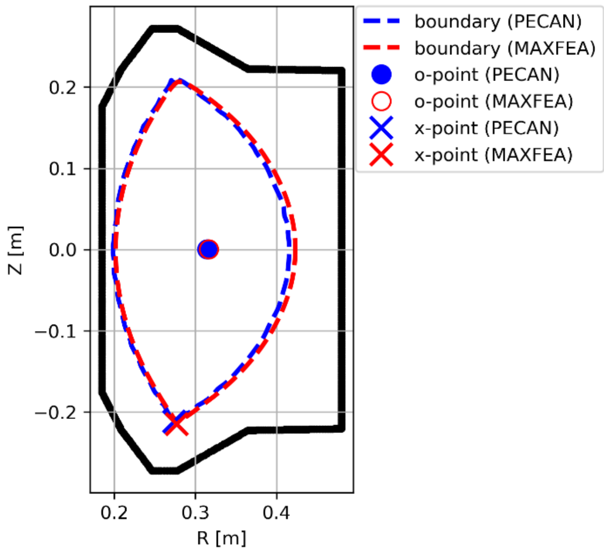

(a)

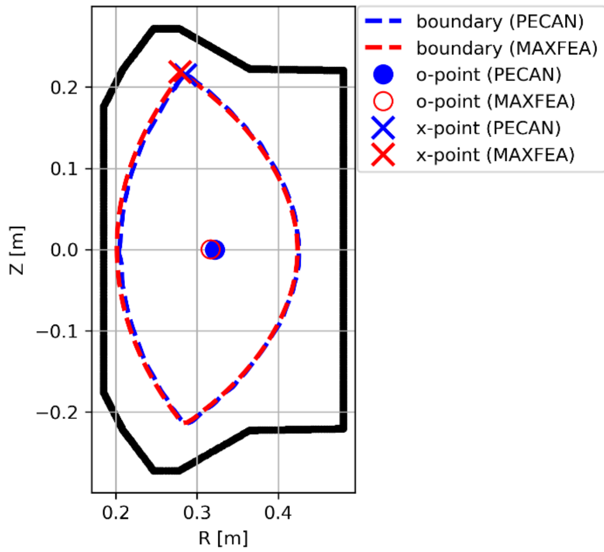

(b)

Figure 55: Comparison between PECAN and MAXFEA plasma boundaries at (a) SOF and (b) EOF equilibria for TRUST (double-null configuration), including the location of the magnetic axis (o-point) and the x-point.

Table 14 and Table 15 report the comparison of the main equilibrium parameters obtained with PECAN and MAXFEA for TRUST DN configuration at the SOF and EOF instants.

Table 14: Comparison between PECAN and MAXFEA main equilibrium parameters for TRUST at the SOF instant, double-null configuration.

Quantity	PECAN	MAXFEA	Percentage difference [%]
I_p [kA]	110.00	110.00	~ 0
$\Psi_{axis} - \Psi_{boundary}$ [Vs]	0.03	0.03	-5.43
Elongation	1.95	1.90	2.33
Triangularity	0.28	0.30	-5.45
Major radius [m]	0.31	0.31	-1.74
Minor radius [m]	0.11	0.11	-1.93
Aspect ratio	2.83	2.82	0.19
Volume [m³]	0.12	0.12	-2.9
β_p	0.10	0.11	-5.04
ℓ_i	0.78	0.81	-3.66
q_{95}	3.35	3.28	2.22
Magnetic axis [m]	R=+0.314, Z=+0.000	R=+0.317, Z=+0.000	0.86
Current barycenter [m]	R=+0.302, Z=-0.000	R=+0.307, Z=-0.000	1.73
x-point [m]	R=+0.274, Z=-0.212	R=+0.277, Z=-0.215	1.58

Table 15: Comparison between PECAN and MAXFEA main equilibrium parameters for TRUST at the EOF instant, double-null configuration.

Quantity	PECAN	MAXFEA	Percentage difference [%]
Ip [A]	110.00	110.00	~ 0
Psi boundary [Vs]	0.03	0.03	-2.61
Elongation	1.93	1.94	-0.80
Triangularity	0.23	0.28	-17.69
Major radius [m]	0.31	0.31	0.63
Minor radius [m]	0.11	0.11	-0.24
Aspect ratio	2.83	2.81	0.87
Volume [m^3]	0.12	0.12	0.41
betap(1)	0.11	0.11	-1.41
li(3)	0.78	0.81	-3.07
q95	3.28	3.36	-2.41
Magnetic axis [m]	R=+0.322, Z=+0.000	R=+0.317, Z=+0.000	1.72
Current barycenter [m]	R=+0.309, Z=-0.000	R=+0.307, Z=+0.000	0.75
x-point [m]	R=+0.286, Z=+0.215	R=+0.279, Z=+0.219	2.50

Table 15 summarize the comparison between PECAN and MAXFEA equilibrium results for the TRUST device in the three reference configurations, namely downward single-null, upward single-null, and double-null, both at SOF and EOF instants. Overall, the agreement between the two solvers is excellent across all scenarios. The plasma current is identical by construction, while the poloidal flux difference between axis and boundary shows systematic deviations of less than 5%.

The geometric descriptors (elongation, triangularity, major/minor radius, aspect ratio, and volume) are reproduced with good accuracy. Among these, triangularity is the most sensitive parameter, with differences up to 25% in some cases, although the absolute variation remains small due to the compact size of TRUST plasmas. Internal parameters such as β_p, ℓ_i, and q_{95} differ by less than 5–8% in all cases, indicating consistent reproduction of the current and pressure profiles.

The magnetic axis position coincides in all configurations, confirming the robustness of the solution strategy, while the current barycenter shows only marginal deviations. Finally, the x-point location is reproduced with excellent accuracy, with differences typically below 3%.

In conclusion, PECAN is able to replicate the main equilibrium features of TRUST with high fidelity across different plasma configurations, demonstrating its reliability and flexibility in handling small-size tokamak equilibria.

6.2 Disruptions analysis

This section presents a set of disruption case studies carried out to validate and benchmark the FEM-based solver against reference scenarios. The analysis includes:

- EU-DEMO baseline 2022: one fast upward VDE (UVDE). This model does not include IVCs.
- EU-DEMO LAR 2024: four cases (fast/slow UVDE, fast/slow downward VDE).
- TRUST: two fast VDEs (upward and downward).

These simulations complement the stationary equilibria discussed in the previous sections.

From an engineering standpoint, the main drivers considered in the disruption analyses are the halo current peak, the maximum eddy current, and the maximum vertical force. Nevertheless, these quantities should be regarded as input parameters for a broader design optimization process rather than as final values. In particular, they provide a first-order approximation to guide the assessment of component performance under disruption conditions. As in the case of the eddy currents and vertical forces, not only the absolute magnitude but also their spatial distribution on the structures must be taken into account in order to properly evaluate the mechanical response and inform robust design solutions.

It is important to underline that the disruption modelling for the cases reported above follows the same criteria described in Sections 4.1 and 4.2. All simulations have been performed by applying a current variation to the fictitious vertical stabilization circuit already used during the stationary equilibrium calculations as perturbation (also named "kick"). In order to "synchronize" the disruption onset across the different scenarios, the magnitude of the current kick has been slightly modified with respect to the values reported in the previous sections. Consequently, all the cases have also been re-run with MAXFEA using the same order of magnitude for the perturbation to ensure consistency in the benchmarking.

For the DEMO cases, the applied kick corresponds to a variation of less than 1% of the average nominal current in the PF coils (i.e. in the order of a few tens of kA). For TRUST, a similar approach has been adopted, with a kick of the order of 500 A. Although larger than the values employed in the disruptions discussed in [33], this still represents only about 2% of the average PF coils current at the EOF instant and is therefore consistent with the modelling assumptions. These choices can be justified by two main reasons: (i) to accelerate the disruption onset, thereby reducing the overall computational time; and (ii) to overcome potential numerical noise issues in PECAN, for example those arising from the transition between the stationary FEM formulation and the transient one, as well as from intrinsic differences between the two codes (e.g. different FEM cores).

Starting from this last point and considering the intrinsic differences in the FEM core of the two solvers, a time shift between PECAN and MAXFEA events during the disruption simulations is to be expected. Moreover, the total current distributions at the beginning of the transient (i.e. including both active coils and plasma) are not identical in the two codes, as they are influenced by the fictitious vertical stabilization circuits employed in the stationary equilibrium calculations. As a consequence, further discrepancies are also to be expected in terms of eddy current in the passive structures, plasma trajectory during the transient, and even the precise location and timing of the plasma–wall contact points, in addition to the observed time shift.

The primary purpose of this analysis is therefore not to obtain a point-by-point replication of the MAXFEA results, but rather to assess the validity of PECAN's FEM-based formulation in handling plasma transients. In this sense, the goal is to achieve comparable and consistent results across the codes, thereby confirming the reliability of PECAN for disruption modelling.

DEMO 2022 – Fast Upward VDE

This section presents the results for the fast upward vertical displacement event (UVDE) in the DEMO 2022 baseline scenario. The disruption event has been modelled starting from the static equilibrium at EOF instant reported in the previous section. The figures of merit for the comparison between PECAN and MAXFEA are summarized below.

- Figure 56 shows the time evolution of plasma current and halo current, together with the total eddy currents induced in the vacuum vessel and the resulting vertical force.
- Figure 57 contains the snapshots of the plasma boundary evolution during the disruptive event.
- Figure 58 shows the evolution of the plasma magnetic axis position during the disruption and the trend of the difference between axis and boundary flux.
- Figure 59 shows the plasma current barycentre trajectory during the disruption and the contact points between plasma and first wall.
- Table 16 summarizes the comparison between PECAN and MAXFEA main engineering parameters.

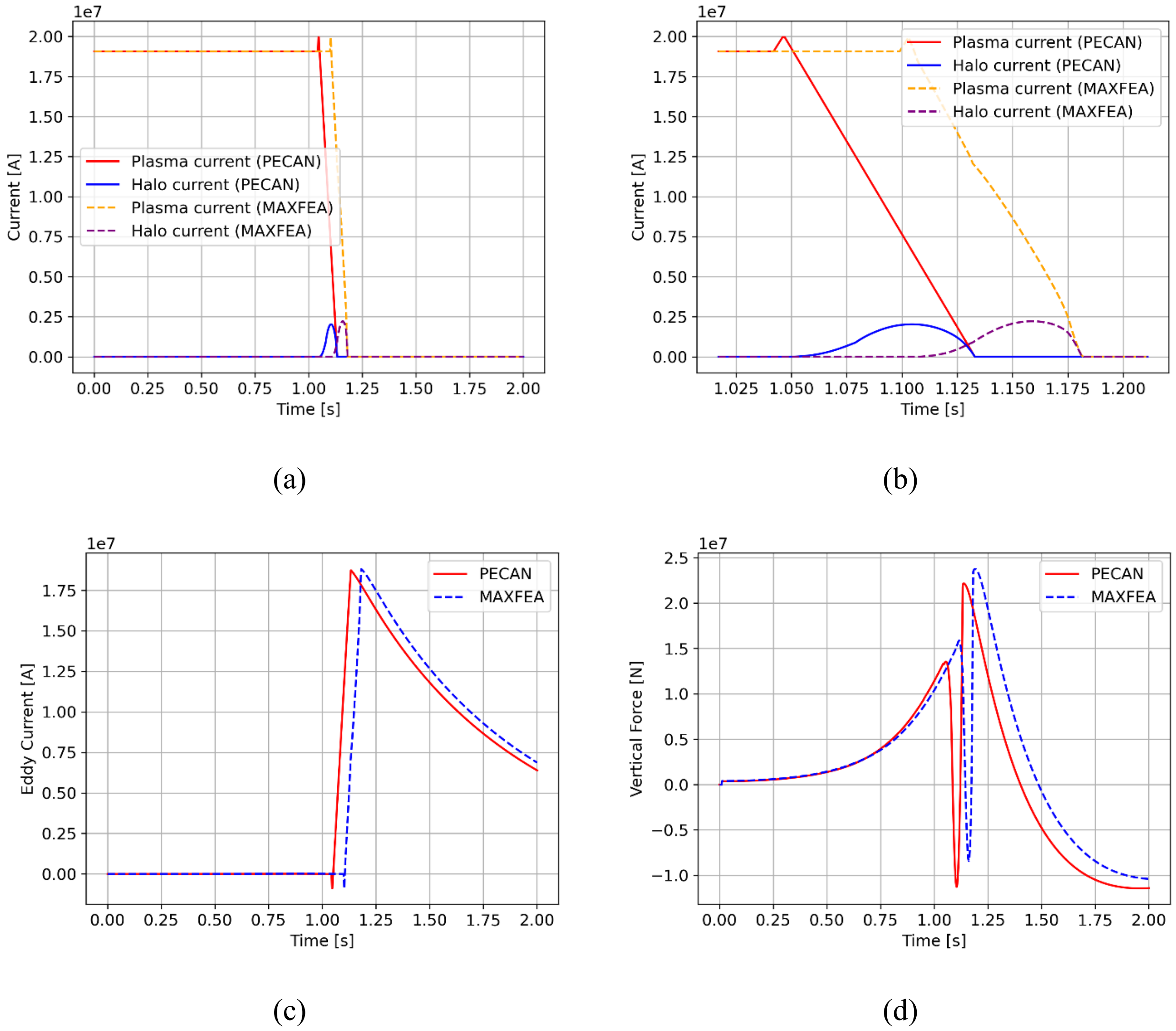

Figure 56: Comparison between PECAN and MAXFEA for a fast UVDE in DEMO baseline 2022. The plots show: (a,b) time evolution of plasma current and halo current, (c) total eddy currents induced in the VV, and (d) overall vertical force on the VV.

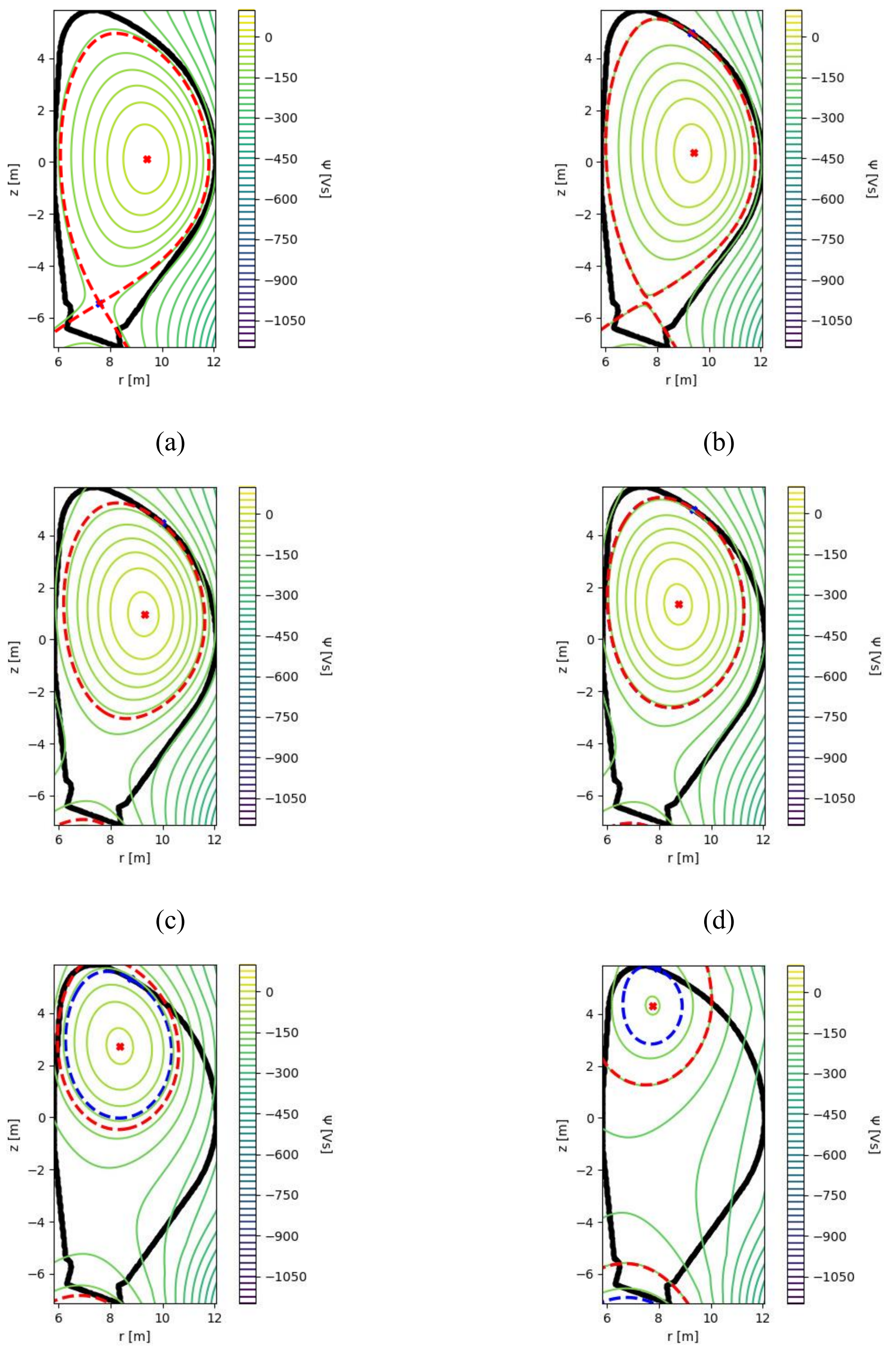

Figure 57: Snapshots of the plasma boundary evolution during a fast upward VDE in DEMO baseline 2022: (a) equilibrium, (b) diverted to limiter configuration, (c) start of the TQ, (d) start of the CQ, (d) plasma with halo current region carrying (e) ~70% and (f) ~30% of the nominal plasma current during the CQ phase.

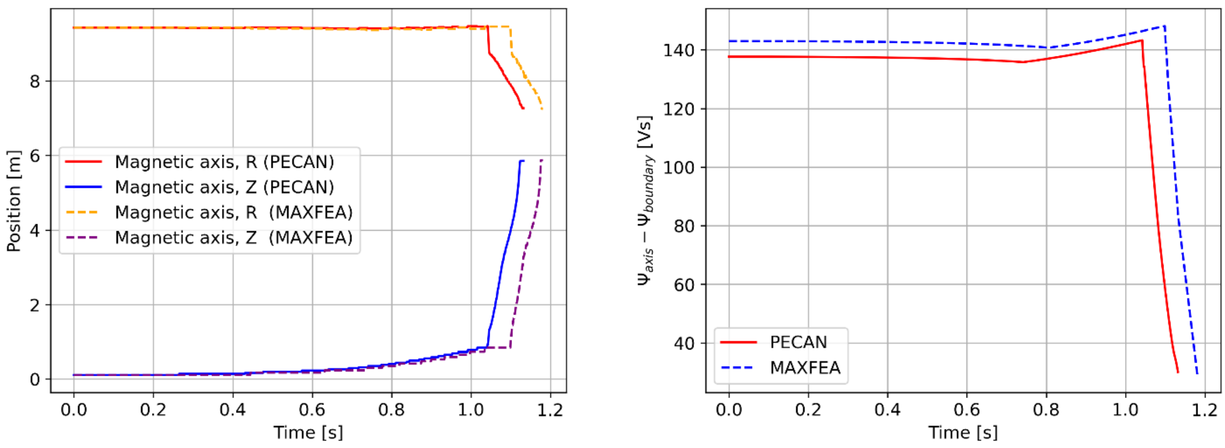

(a) (b)

Figure 58: Comparison between PECAN and MAXFEA for a fast UVDE in DEMO baseline 2022. The plots show: the evolution of (a) the plasma magnetic axis position and (b) the difference between axis and boundary flux during the disruption.

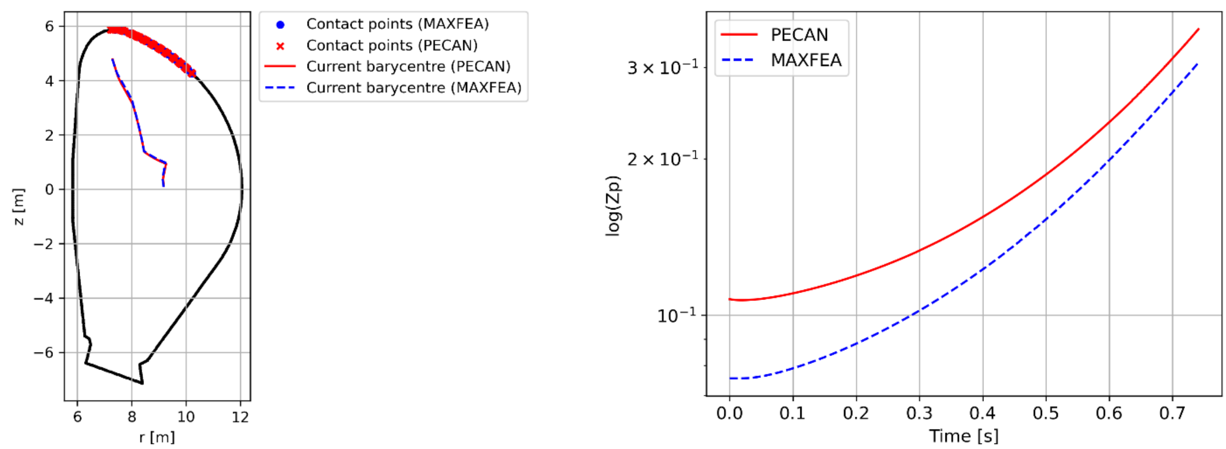

(a) (b)

Figure 59: Comparison between PECAN and MAXFEA for a fast UVDE in DEMO baseline 2022. The plots show: (a) the evolution of the plasma current barycentre trajectory during the disruption and (b) the natural logarithm of its vertical coordinate before the contact with the first wall.

The analysis of the merit figures highlights a time shift of about 50 ms between the two codes. From the analysis of Figure 59(b), it can be clearly observed that the instability growth rate estimated with PECAN amounts to $\gamma \approx 5.03\ s^{-1}$, while the corresponding value obtained with MAXFEA is $\gamma \approx 4.86\ s^{-1}$. The difference between the two values is approximately 3.5%, which, although limited in magnitude, is sufficient to explain the relative time shift that is observed between the two simulations. This result highlights how even small discrepancies in the computed growth rate can accumulate over the course of the disruption dynamics, leading to a measurable delay in the evolution of the plasma vertical displacement when comparing the outputs of the two codes.

Table 16 reports the comparison between PECAN and MAXFEA in terms of the main engineering parameters associated with the fast upward VDE in DEMO baseline 2022.

Table 16: Comparison between PECAN and MAXFEA main engineering parameters for a fast upward VDE in DEMO baseline 2022.

Quantity	PECAN	MAXFEA	Percentage difference [%]
Max. halo current [MA]	2.03	2.22	-8.15
Max. eddy current in the VV [MA]	18.73	18.81	0.42
Max. vertical force on the VV [MN]	22.16	23.75	-6.70

The maximum halo current shows a discrepancy of about 8%, with PECAN predicting a slightly lower value than MAXFEA. On the other hand, the peak eddy currents induced in the vacuum vessel are reproduced with very good agreement, with a difference below 0.5%. Finally, the maximum vertical force on the vacuum vessel is estimated to be about 6.7% lower in PECAN with respect to MAXFEA. Overall, the comparison confirms a satisfactory consistency between the two codes, with deviations remaining within a few percent for the key engineering quantities, thus supporting the reliability of the PECAN predictions.

DEMO LAR 2024 – Fast Upward VDE

This section presents the results for the fast upward vertical displacement event (UVDE) in the DEMO LAR 2024 baseline scenario. The disruption event has been modelled starting from the static equilibrium at EOF instant reported in the previous section. The figures of merit for the comparison between PECAN and MAXFEA are summarized below.

- Figure 60 shows the time evolution of plasma current and halo current, together with the total eddy currents induced in the vacuum vessel and the resulting vertical force.
- Figure 61 reports the evolution of the eddy currents in the IVCs.
- Figure 62 contains the snapshots of the plasma boundary evolution during the disruptive event.
- Figure 63 shows the evolution of the plasma magnetic axis position during the disruption and the trend of the difference between axis and boundary flux.

- Figure 64 shows the plasma current barycentre trajectory during the disruption and the contact points between plasma and first wall.
- Table 17 summarizes the comparison between PECAN and MAXFEA main engineering parameters.

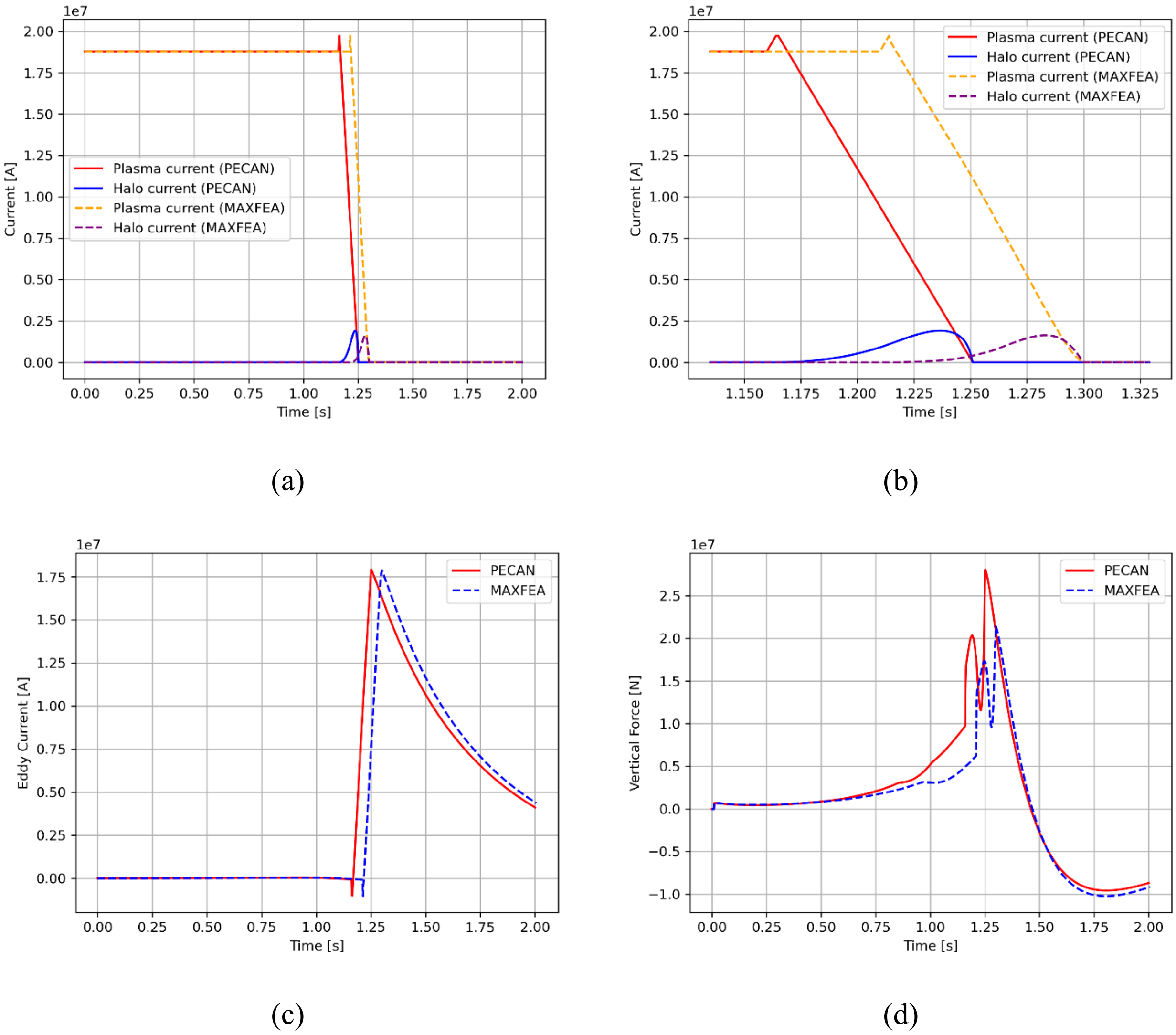

Figure 60: Comparison between PECAN and MAXFEA for a fast UVDE in DEMO baseline 2024. The plots show: (a,b) time evolution of plasma current and halo current, (c) total eddy currents induced in the VV, and (d) overall vertical force on the VV.

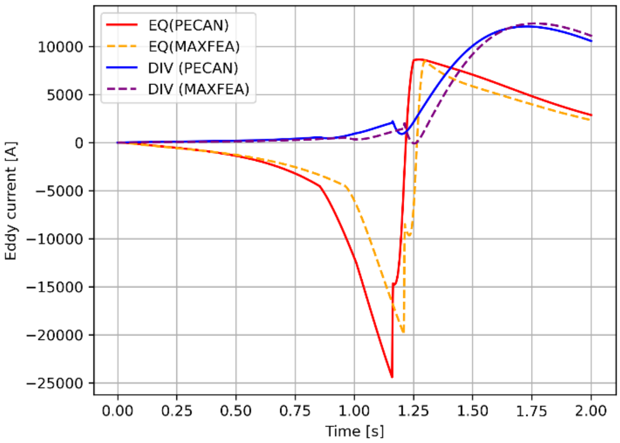

Figure 61: Comparison between PECAN and MAXFEA in-vessel coils currents for a fast UVDE in DEMO baseline 2024.

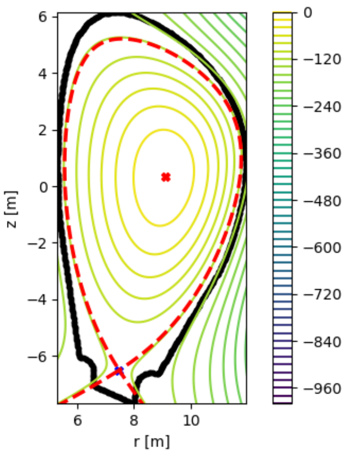

(a)

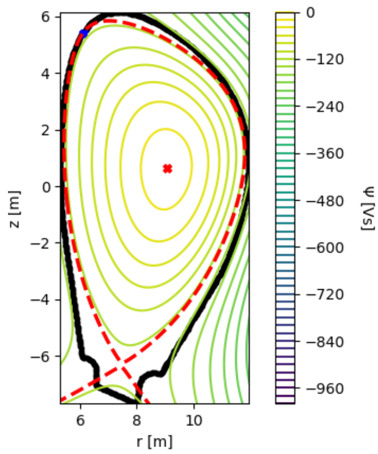

(b)

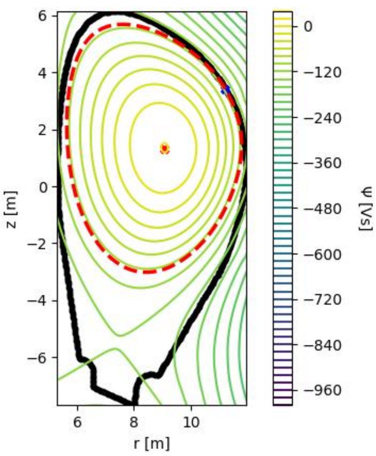

(c)

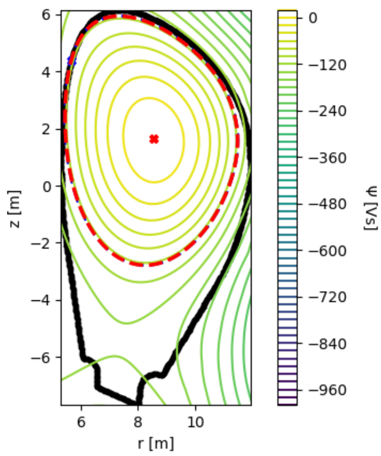

(d)

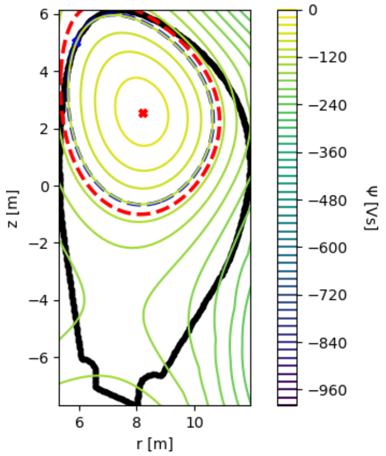

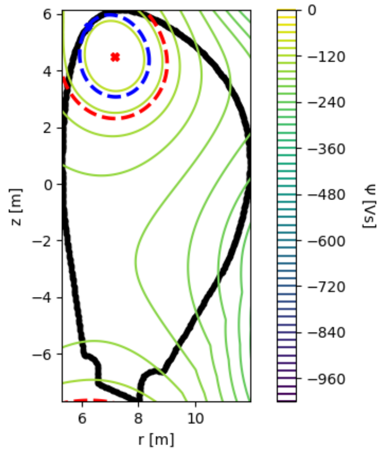

(e) (f)

Figure 62: Snapshots of the plasma boundary evolution during a fast upward VDE in DEMO baseline 2024: (a) equilibrium, (b) diverted to limiter configuration, (c) start of the TQ, (d) start of the CQ, (d) plasma with halo current region carrying (e) ~70% and (f) ~30% of the nominal plasma current during the CQ phase.

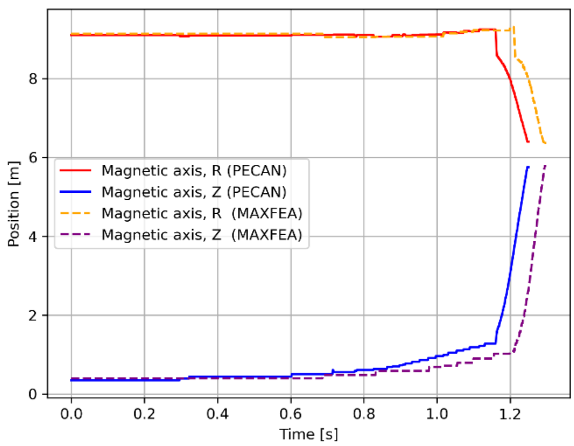

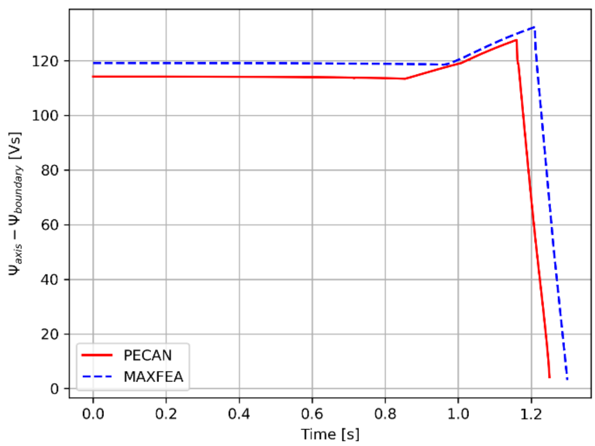

(a) (b)

Figure 63: Comparison between PECAN and MAXFEA for a fast UVDE in DEMO baseline 2024. The plots show: the evolution of (a) the plasma magnetic axis position and (b) the difference between axis and boundary flux during the disruption.

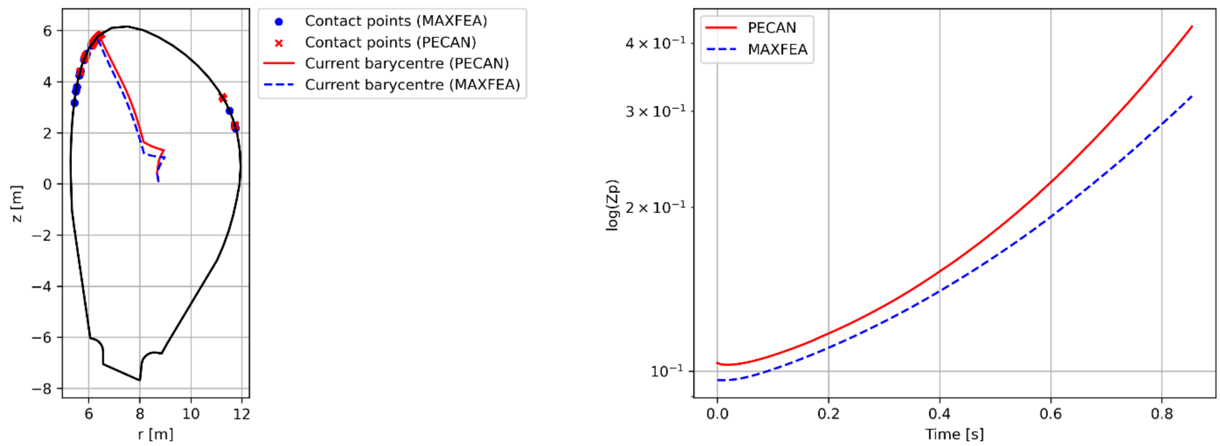

(a) (b)

Figure 64: Comparison between PECAN and MAXFEA for a fast UVDE in DEMO baseline 2024. The plots show: (a) the evolution of the plasma current barycentre trajectory during the disruption and (b) the natural logarithm of its vertical coordinate before the contact with the first wall.

The analysis of the merit figures highlights a time shift of about 40 ms between the two codes. From the analysis of Figure 63(b), it can be clearly observed that the instability growth rate estimated with PECAN amounts to $\gamma \approx 4.24\ s^{-1}$, while the corresponding value obtained with MAXFEA is $\gamma \approx 3.73\ s^{-1}$. The difference in growth rate of approximately 14% can be regarded as the main driver of the time shift observed between the two simulations. In addition, the higher values obtained in DEMO LAR 24 are likely influenced by the presence of the IVCs: as illustrated in Figure 61, a discrepancy appears in the absolute values of the eddy currents in the EQ and DIV circuits, with the EQ circuit showing a peak eddy current about 20% higher than that predicted by MAXFEA. This difference may not only arise from numerical aspects, but could also be related to the slight difference in the plasma–first wall contact points and in the plasma current barycentre trajectory, as highlighted in Figure 64(a).

The discrepancies observed between the two codes can reasonably be ascribed to two main factors. A first contribution may originate from the transition between the static and dynamic formulations in PECAN, which could introduce additional numerical differences in the computed evolution. Furthermore, the treatment of the IVCs is particularly critical, as their induced currents are strongly dependent on the distance from the vacuum vessel and on the discretization adopted in the neighbouring vessel regions. In this respect, it should be recalled that MAXFEA employs first-order finite elements, while PECAN uses second-order elements for the present simulations. Although the analysis was carried out using the same mesh for both solvers, the MAXFEA limitation to a maximum of about 30,000 elements implies that very small components, such as the IVCs or thin regions of the vacuum vessel, are represented with a reduced number of elements for modern solvers as DOLFINx. This restriction inevitably affects the accuracy of the local current distribution evaluated via PECAN, particularly in proximity to the IVCs, and may contribute significantly to the deviations highlighted in the comparison. For this reason, a dedicated mesh sensitivity analysis with more refined models – included at the end of this chapter– would be advisable in order to better assess the robustness of the results.

Table 17 reports the comparison between PECAN and MAXFEA in terms of the main engineering parameters associated with the fast upward VDE in DEMO baseline 2024.

Table 17: Comparison between PECAN and MAXFEA main engineering parameters for a fast upward VDE in DEMO baseline 2024.

Quantity	PECAN	MAXFEA	Percentage difference [%]
Max. halo current [MA]	1.92	1.64	17.04
Max. eddy current in the VV [MA]	17.93	17.87	0.31
Max. vertical force on the VV [MN]	28.07	21.41	31.11

The maximum halo current differs by approximately 17%, while the eddy currents in the vacuum vessel are in very close agreement, with a relative difference of only ~0.3%. Given the similar formulation adopted in PECAN and MAXFEA and considering the expression used for the calculation of the halo current (Eq. 5.13), the observed discrepancy could be attributable also to different values of the poloidal current function F at the plasma limiter surface. In fact, close to the plasma edge a difference in the FF' profile can be identified, as illustrated in Figure 40(b) for the stationary equilibrium case, which directly impacts the evaluation of the halo current. The largest deviation is observed in the vertical force, with a discrepancy of about 31%. This outcome is partly expected, since the vertical force scales quadratically with the current, so that even modest differences in the latter tend to be amplified in the corresponding forces. However, as already discussed for the IVCs, this result could also be interpreted in light of the fact that the induced currents in these components have a direct impact on the vertical force acting on the vacuum vessel, strongly depending on how the passive structures are modelled and on the accuracy of this modelling. In addition, it should be noted that the adopted mesh is not perfectly symmetric with respect to the up–down direction, which represents another aspect to be optimised in future refinements of the model.

Beyond this general scaling effect, there is also a methodological aspect. In the present MAXFEA evaluation, the force was computed directly from the first-order FEM field, where the poloidal-flux gradient is constant within each element. This representation is known to capture the strongly curved self-field inadequately, leading to an incomplete cancellation of its contribution (which, in principle, should yield a vanishing net vertical force). As a result, the raw FEM-based estimate of the force may be biased. This specific limitation of MAXFEA has been discussed in [58], where a dedicated post-processing method is proposed to reconstruct the magnetic field and stress consistently prior to integration. An analogous methodology should be applied here in order to obtain a more accurate evaluation of the vertical forces.

In PECAN, the forces are likewise evaluated at the element centroids, following the same strategy as in MAXFEA. In the present simulations, PECAN employs second-order Lagrange polynomials, and the interpolation from order 2 (quadratic basis functions) to order 0 (element centroids) introduces an additional source of error in the force calculation. Moreover, the use of second-order elements in PECAN, as opposed to first-order elements in MAXFEA, leads to differences in the representation of the local fields and thus in the corresponding force evaluation. Finally, as already noted, the modelling of the internal coils (IVCs) and the slight differences in the plasma–first wall contact points, as in the plasma current barycentre trajectory, also play a role, further contributing to the observed discrepancies in the computed vertical forces. Nevertheless, from an engineering perspective, PECAN provides more conservative results, thus reducing the risk of underestimating the loads acting on passive components.

The discrepancies observed with respect to MAXFEA in terms of eddy currents, halo, currebts, vertical forces, and the time shift of vertical displacement events suggest the need for further investigation. Future work should explore the origin of these differences, starting from refined mesh discretizations and more accurate numerical treatments.

DEMO LAR 2024 – Slow Upward VDE

This section presents the results for the slow upward vertical displacement event (UVDE) in the DEMO LAR 2024 baseline scenario. The disruption event has been modelled starting from the static equilibrium at EOF instant reported in the previous section. The figures of merit for the comparison between PECAN and MAXFEA are summarized below.

- Figure 65 shows the time evolution of plasma current and halo current, together with the total eddy currents induced in the vacuum vessel and the resulting vertical force.
- Figure 66 reports the evolution of the eddy currents in the IVCs.

- Figure 67 contains the snapshots of the plasma boundary evolution during the disruptive event.
- Figure 68Figure 68 shows the evolution of the plasma magnetic axis position during the disruption and the trend of the difference between axis and boundary flux.
- Figure 69 shows the plasma current barycentre trajectory during the disruption and the contact points between plasma and first wall.
- Table 18 summarizes the comparison between PECAN and MAXFEA main engineering parameters.

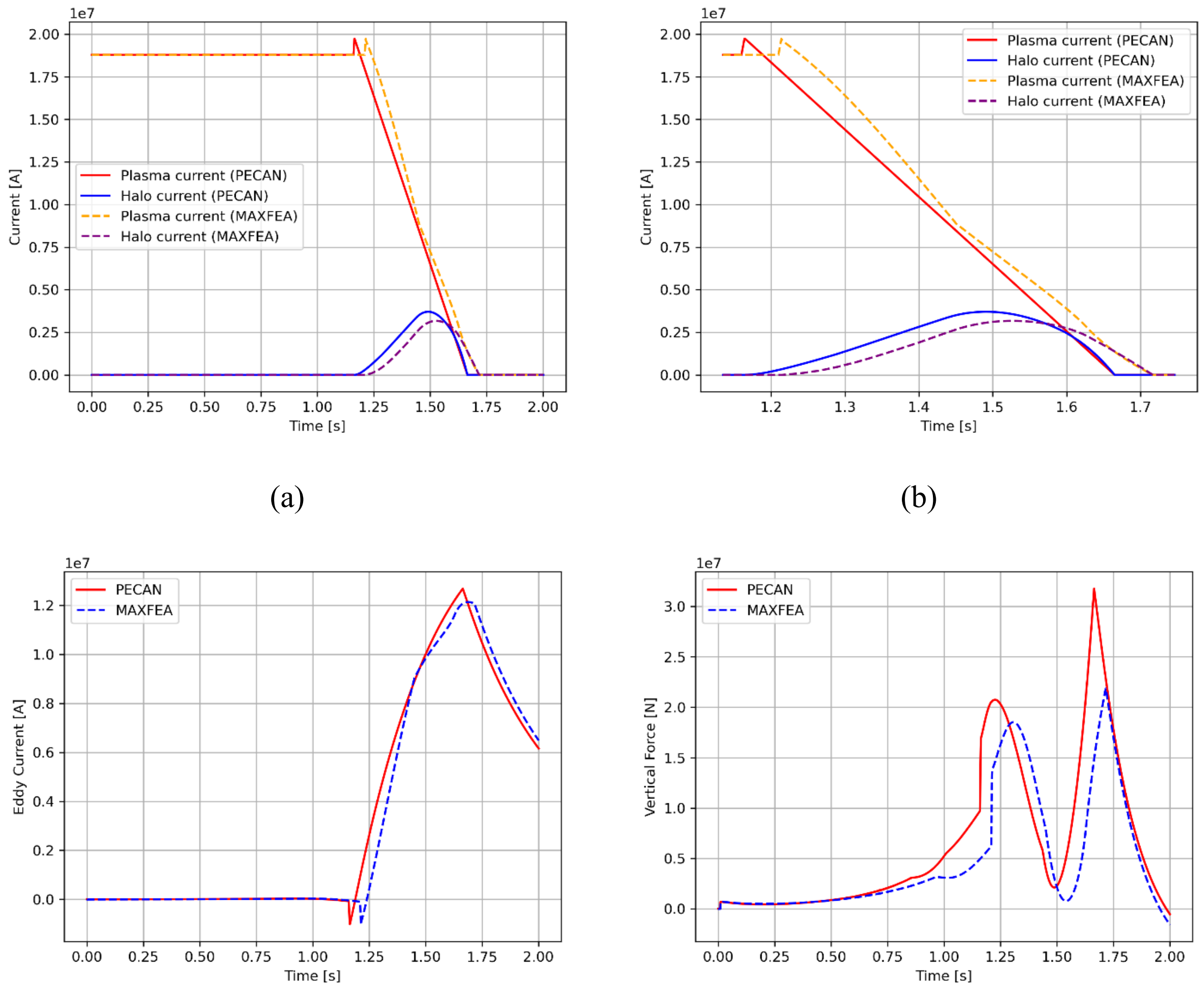

(a) (b) (c) (d)

Figure 65: Comparison between PECAN and MAXFEA for a slow UVDE in DEMO baseline 2024. The plots show: (a,b) time evolution of plasma current and halo current, (c) total eddy currents induced in the VV, and (d) overall vertical force on the VV.

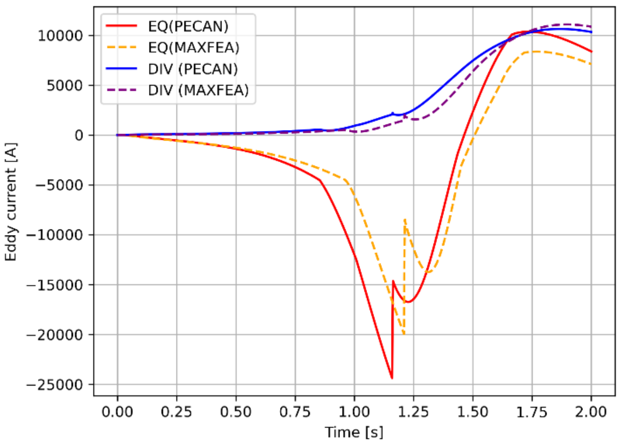

Figure 66: Comparison between PECAN and MAXFEA in-vessel coils currents for a slow UVDE in DEMO baseline 2024.

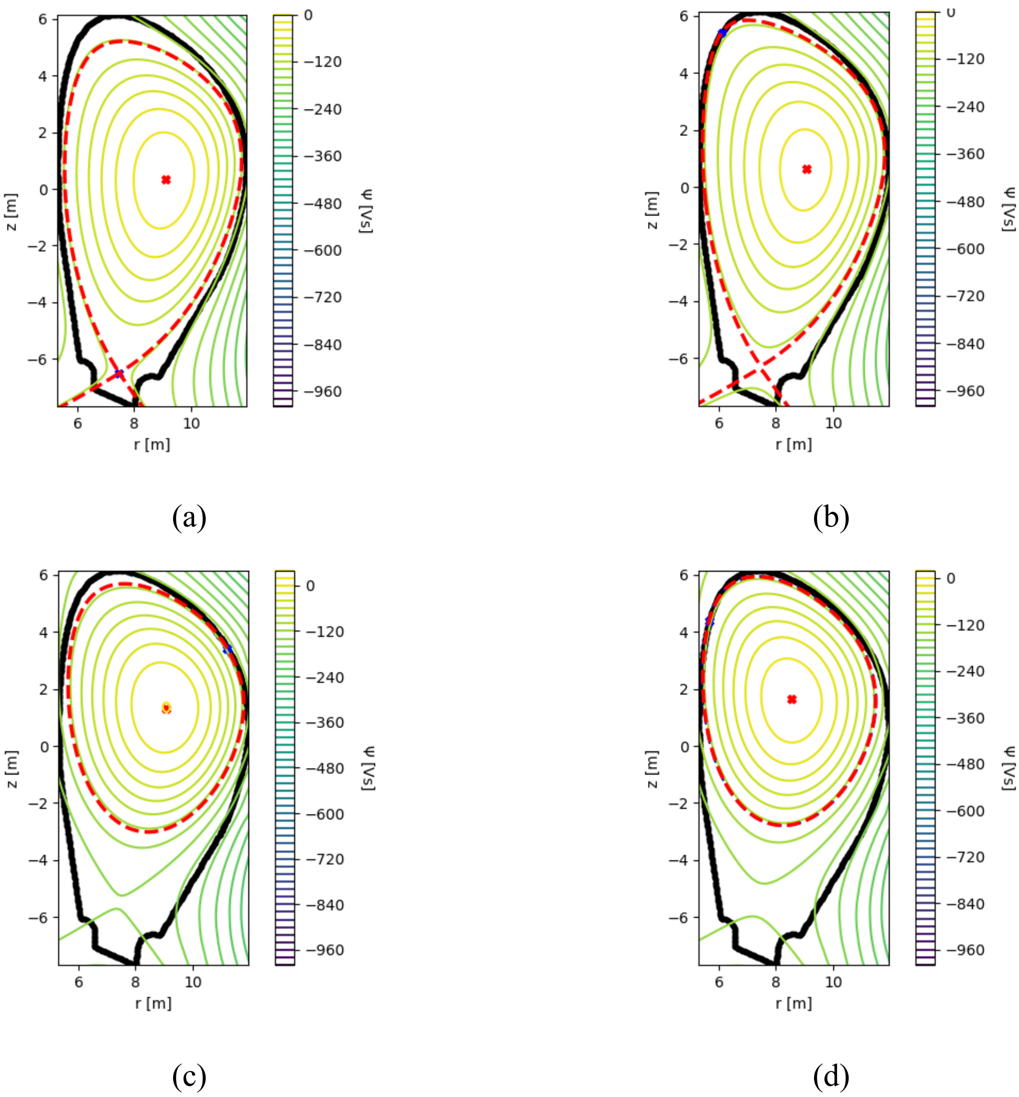

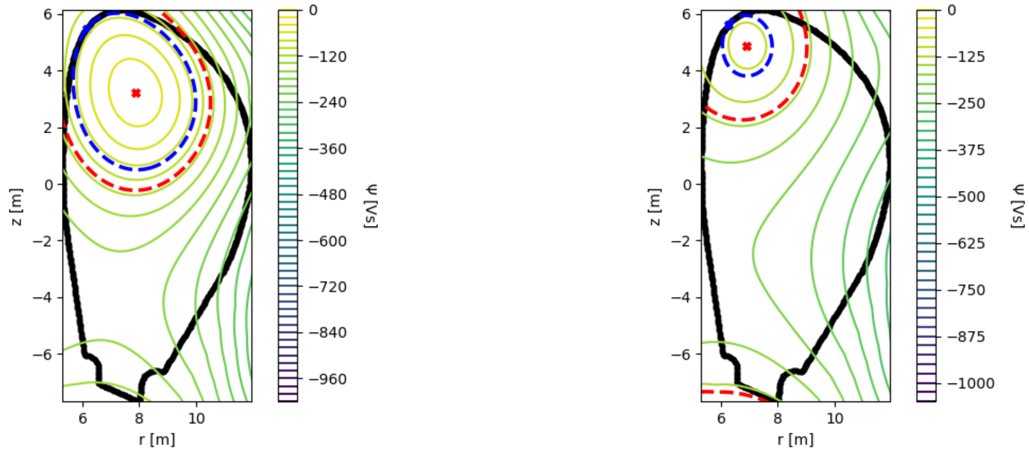

(e) (f)

Figure 67: Snapshots of the plasma boundary evolution during a slow upward VDE in DEMO baseline 2024: (a) equilibrium, (b) diverted to limiter configuration, (c) start of the TQ, (d) start of the CQ, (d) plasma with halo current region carrying (e) ~70% and (f) ~30% of the nominal plasma current during the CQ phase.

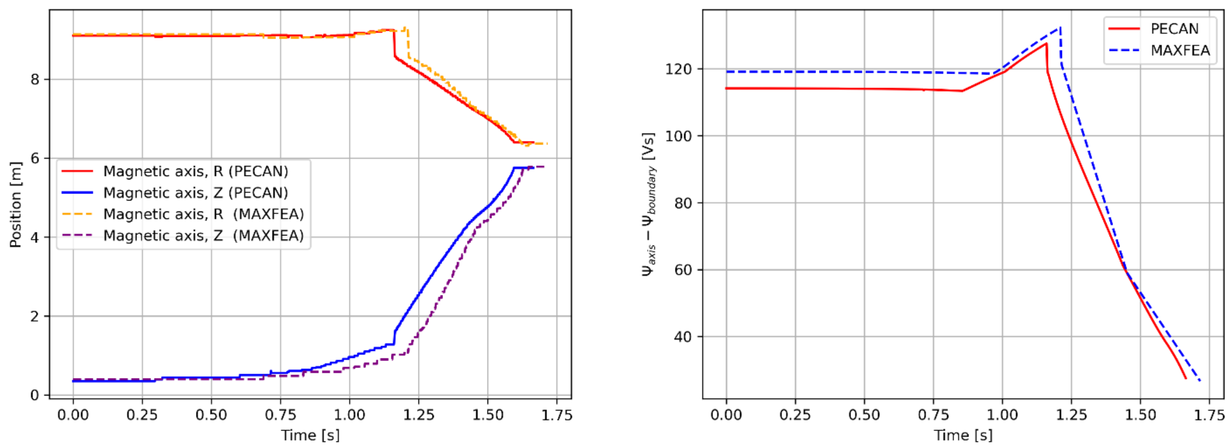

(a) (b)

Figure 68: Comparison between PECAN and MAXFEA for a slow UVDE in DEMO baseline 2024. The plots show: the evolution of (a) the plasma magnetic axis position and (b) the difference between axis and boundary flux during the disruption.

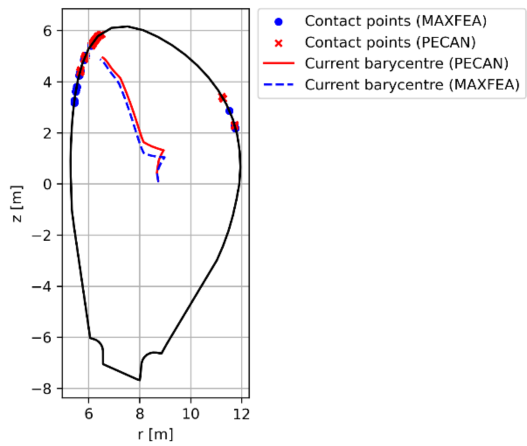

(a)

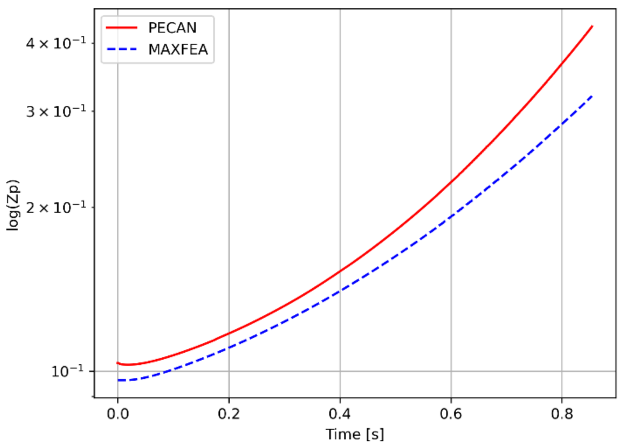

(b)

Figure 69: Comparison between PECAN and MAXFEA for a slow UVDE in DEMO baseline 2024. The plots show: (a) the evolution of the plasma current barycentre trajectory during the disruption and (b) the natural logarithm of its vertical coordinate before the contact with the first wall.

As in the fast case, also for the slow case the analysis of the merit figures highlights a time shift of about 40 ms between the two codes. The instability growth rate estimated with PECAN amounts to $\gamma \approx 4.24\, s^{-1}$, while the corresponding value obtained with MAXFEA is $\gamma \approx 3.73\, s^{-1}$. Consequently, all the considerations previously discussed remain valid in this case as well.

Table 18: Comparison between PECAN and MAXFEA main engineering parameters for a slow upward VDE in DEMO baseline 2024.

Quantity	PECAN	MAXFEA	Percentage difference [%]
Max. halo current [MA]	3.71	3.17	16.93
Max. eddy current in the VV [MA]	12.68	12.14	4.50
Max. vertical force on the VV [MN]	31.77	21.86	45.37

Table 18 reports the comparison between PECAN and MAXFEA for the main engineering parameters of a slow upward VDE in DEMO baseline 2024. The results show that, also for the slow upward VDE, the halo current differs by ~17% and the eddy currents in the VV agree within ~4.5%, while the vertical force displays the largest deviation (~45%). The considerations already discussed for the fast case remain valid here as well, with PECAN providing more conservative estimates, thus reducing the risk of underestimating the loads on passive components.

DEMO LAR 2024 – Fast Downward VDE

This section presents the results for the fast downward vertical displacement event (DVDE) in the DEMO LAR 2024 baseline scenario. The disruption event has been modelled starting from the static equilibrium at EOF instant reported in the previous section. The figures of merit for the comparison between PECAN and MAXFEA are summarized below.

- Figure 70 shows the time evolution of plasma current and halo current, together with the total eddy currents induced in the vacuum vessel and the resulting vertical force.
- Figure 71 reports the evolution of the eddy currents in the IVCs.
- Figure 72 contains the snapshots of the plasma boundary evolution during the disruptive event.
- Figure 73 shows the evolution of the plasma magnetic axis position during the disruption and the trend of the difference between axis and boundary flux.
- Figure 74 shows the plasma current barycentre trajectory during the disruption and the contact points between plasma and first wall.
- Table 19 summarizes the comparison between PECAN and MAXFEA main engineering parameters.

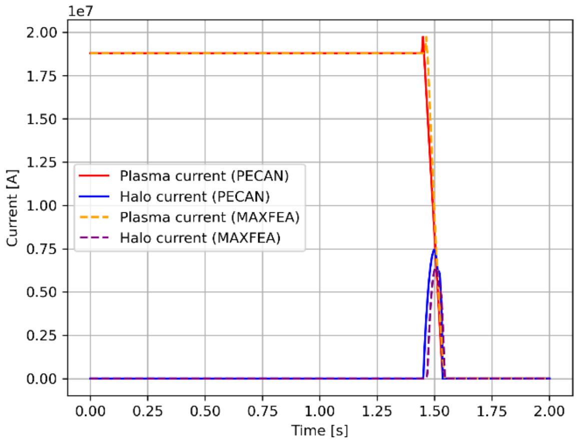

(a)

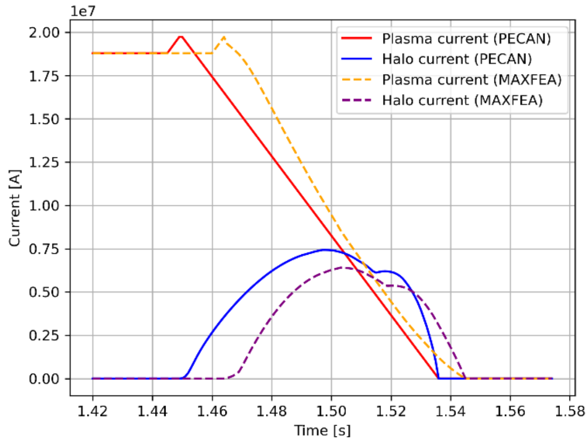

(b)

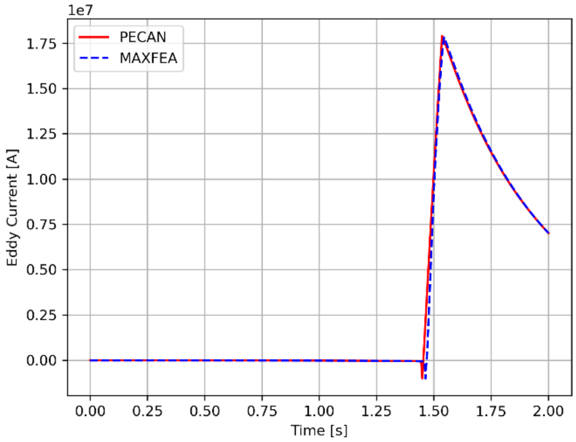

(c)

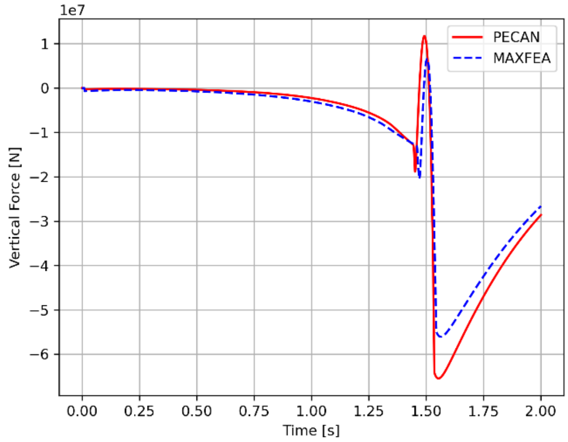

(d)

Figure 70: Comparison between PECAN and MAXFEA for a fast DVDE in DEMO baseline 2024. The plots show: (a,b) time evolution of plasma current and halo current, (c) total eddy currents induced in the VV, and (d) overall vertical force on the VV.

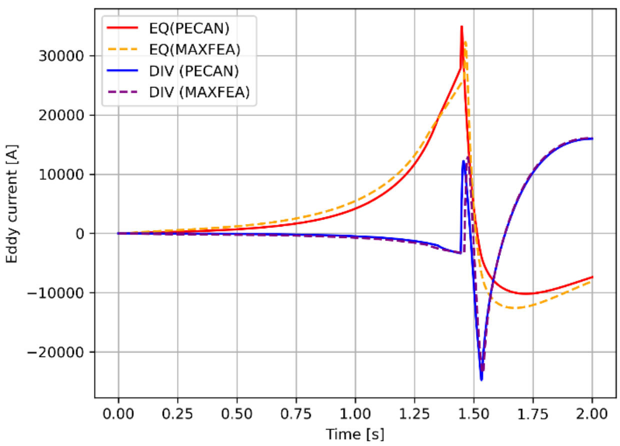

Figure 71: Comparison between PECAN and MAXFEA in-vessel coils currents for a fast DVDE in DEMO baseline 2024.

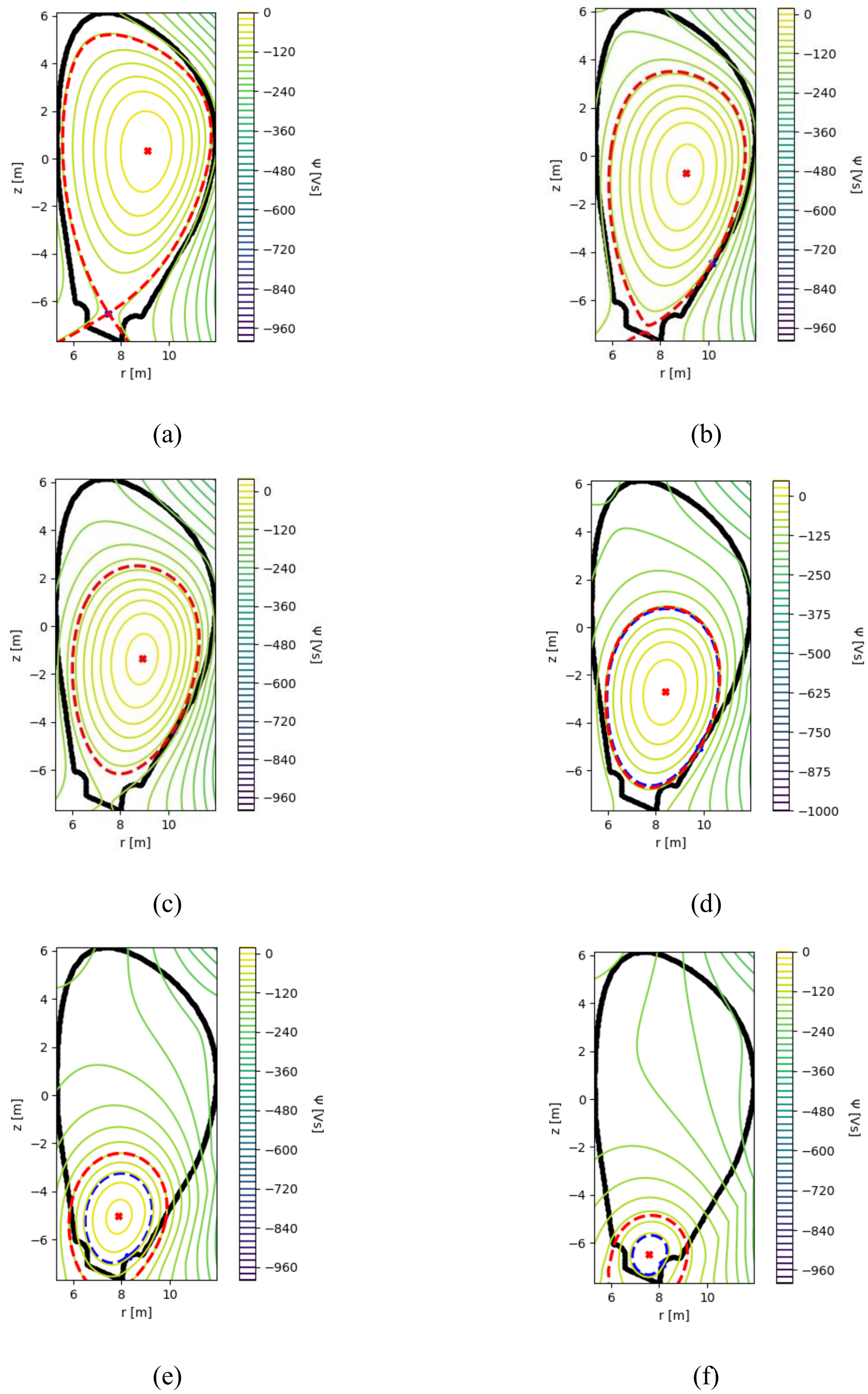

Figure 72: Snapshots of the plasma boundary evolution during a fast downward VDE in DEMO baseline 2024: (a) equilibrium, (b) diverted to limiter configuration, (c) start of the TQ, (d) start of the CQ, (d) plasma with halo current region carrying (e) ~70% and (f) ~30% of the nominal plasma current during the CQ phase.

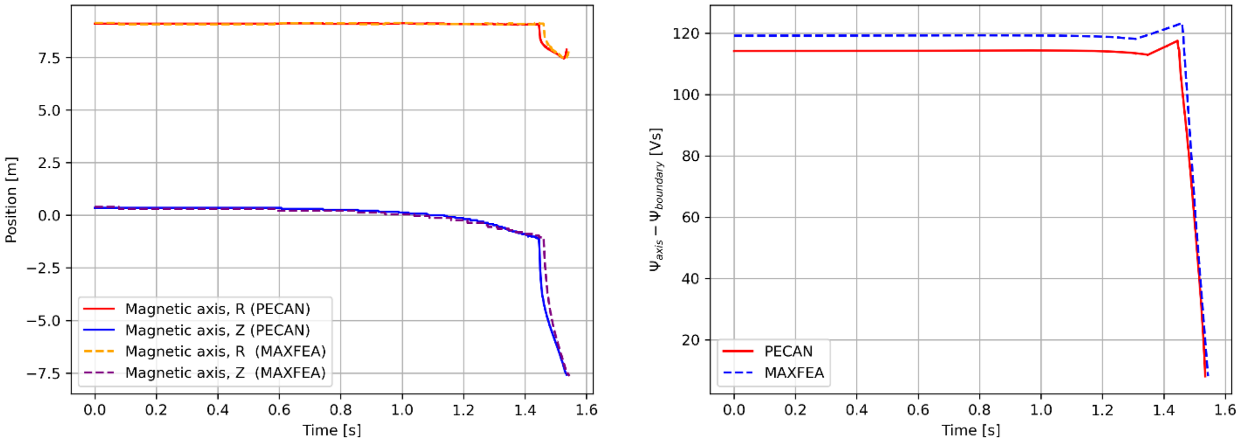

(a) (b)

Figure 73: Comparison between PECAN and MAXFEA for a fast DVDE in DEMO baseline 2024. The plots show: the evolution of (a) the plasma magnetic axis position and (b) the difference between axis and boundary flux during the disruption.

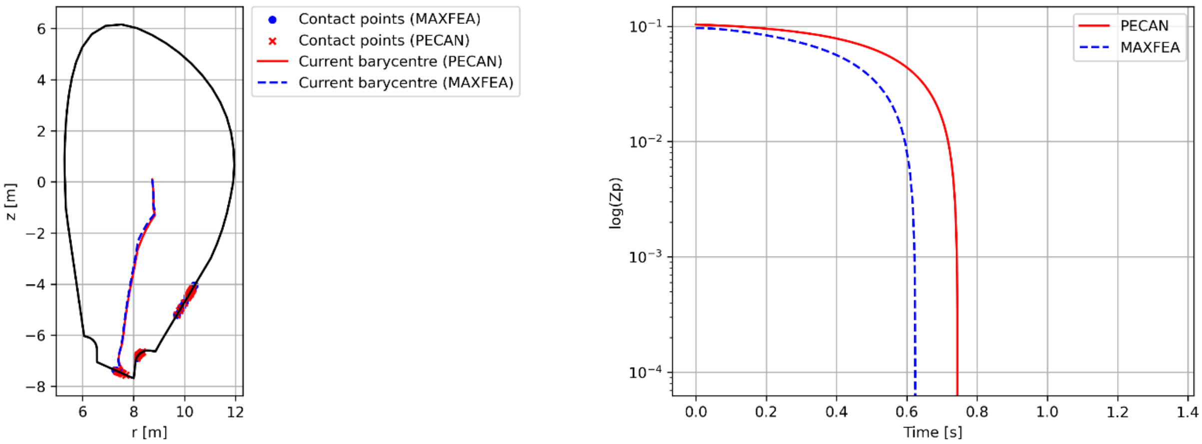

(a) (b)

Figure 74: Comparison between PECAN and MAXFEA for a fast DVDE in DEMO baseline 2024. The plots show: (a) the evolution of the plasma current barycentre trajectory during the disruption and (b) the natural logarithm of its vertical coordinate before the contact with the first wall.

As in the fast case, also for the slow case the analysis of the merit figures highlights a time shift in the order of 20 ms between the two codes. The instability growth rate estimated with PECAN amounts to $\gamma \approx 4.05\ s^{-1}$, while the corresponding value obtained with MAXFEA is $\gamma \approx 3.43\ s^{-1}$. Consequently, all the considerations previously discussed remain valid in this case as well.

Table 19: Comparison between PECAN and MAXFEA main engineering parameters for a fast downward VDE in DEMO baseline 2024.

Quantity	PECAN	MAXFEA	Percentage difference [%]
Max. halo current [MA]	7.43	6.41	15.98
Max. eddy current in the VV [MA]	17.89	17.82	0.42
Max. vertical force on the VV [MN]	-65.48	-56.08	16.76

Table 19 reports the comparison between PECAN and MAXFEA for the main engineering parameters of a fast downward VDE in DEMO baseline 2024. The results show that, also for the slow upward VDE, the halo current differs by ~16% and the eddy currents in the VV agree within ~0.4%, while the vertical force displays the largest deviation (~17%). The considerations already discussed for the upward cases remain valid here as well, with PECAN providing more conservative estimates, thus reducing the risk of underestimating the loads on passive components.

DEMO LAR 2024 – Slow Downward VDE

This section presents the results for the slow downward vertical displacement event (DVDE) in the DEMO LAR 2024 baseline scenario. The disruption event has been modelled starting from the static equilibrium at EOF instant reported in the previous section. The figures of merit for the comparison between PECAN and MAXFEA are summarized below.

- Figure 75 shows the time evolution of plasma current and halo current, together with the total eddy currents induced in the vacuum vessel and the resulting vertical force.
- Figure 76Figure 76 reports the evolution of the eddy currents in the IVCs.
- Figure 77 contains the snapshots of the plasma boundary evolution during the disruptive event.
- Figure 78 shows the evolution of the plasma magnetic axis position during the disruption and the trend of the difference between axis and boundary flux.
- Figure 79 shows the plasma current barycentre trajectory during the disruption and the contact points between plasma and first wall.
- Table 20 summarizes the comparison between PECAN and MAXFEA main engineering parameters.

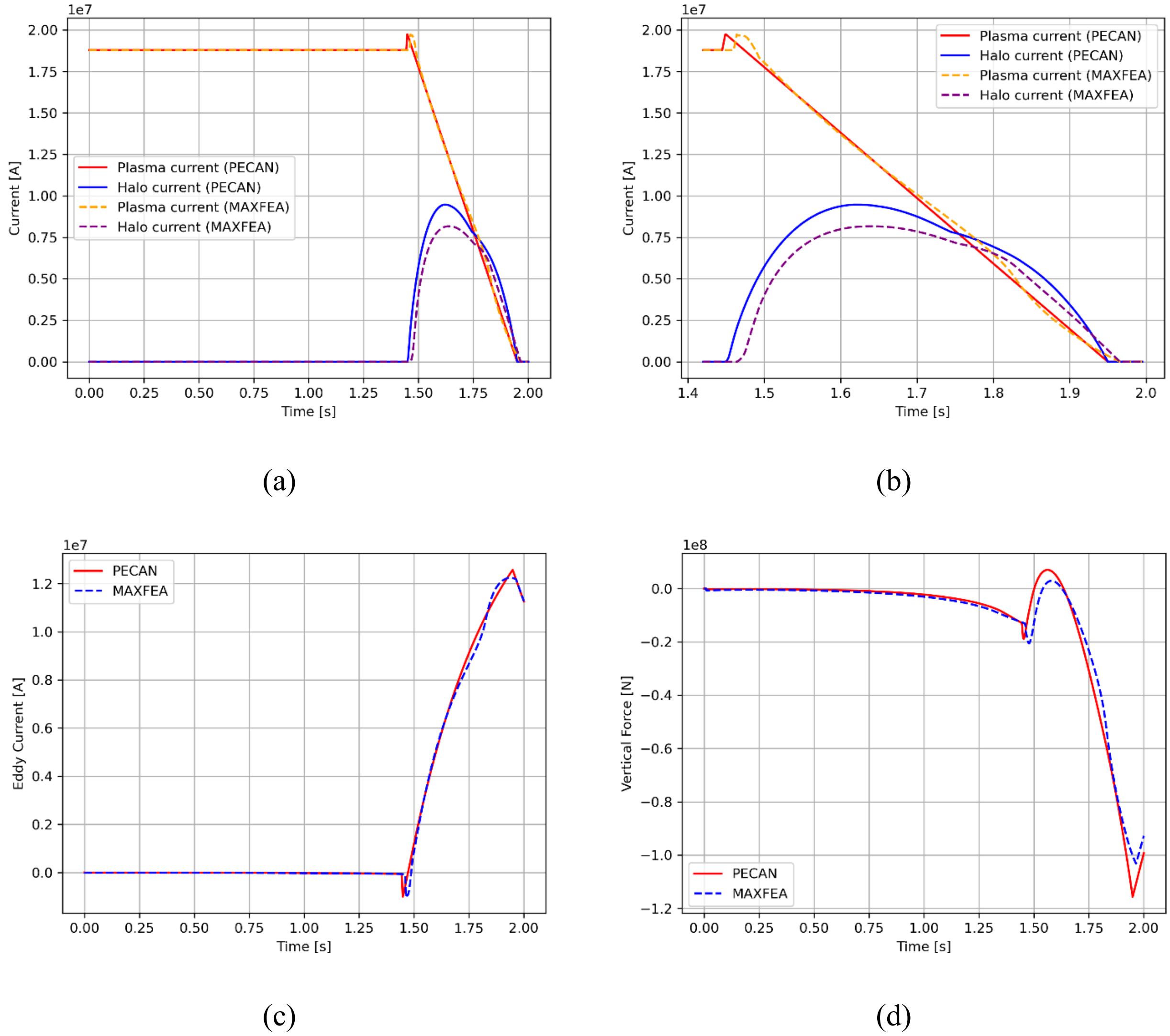

Figure 75: Comparison between PECAN and MAXFEA for a slow DVDE in DEMO baseline 2024. The plots show: (a,b) time evolution of plasma current and halo current, (c) total eddy currents induced in the VV, and (d) overall vertical force on the VV.

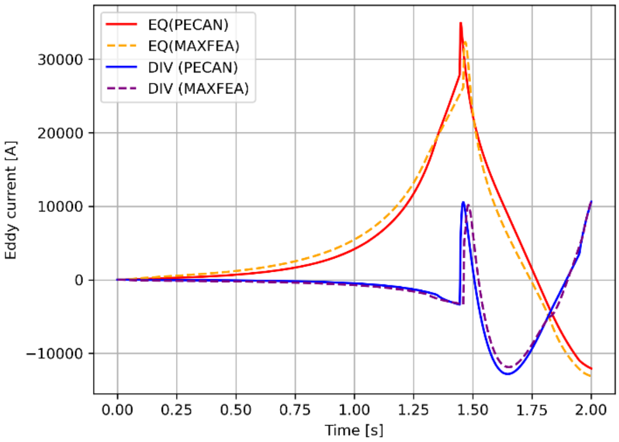

Figure 76: Comparison between PECAN and MAXFEA in-vessel coils currents for a fast DVDE in DEMO baseline 2024.

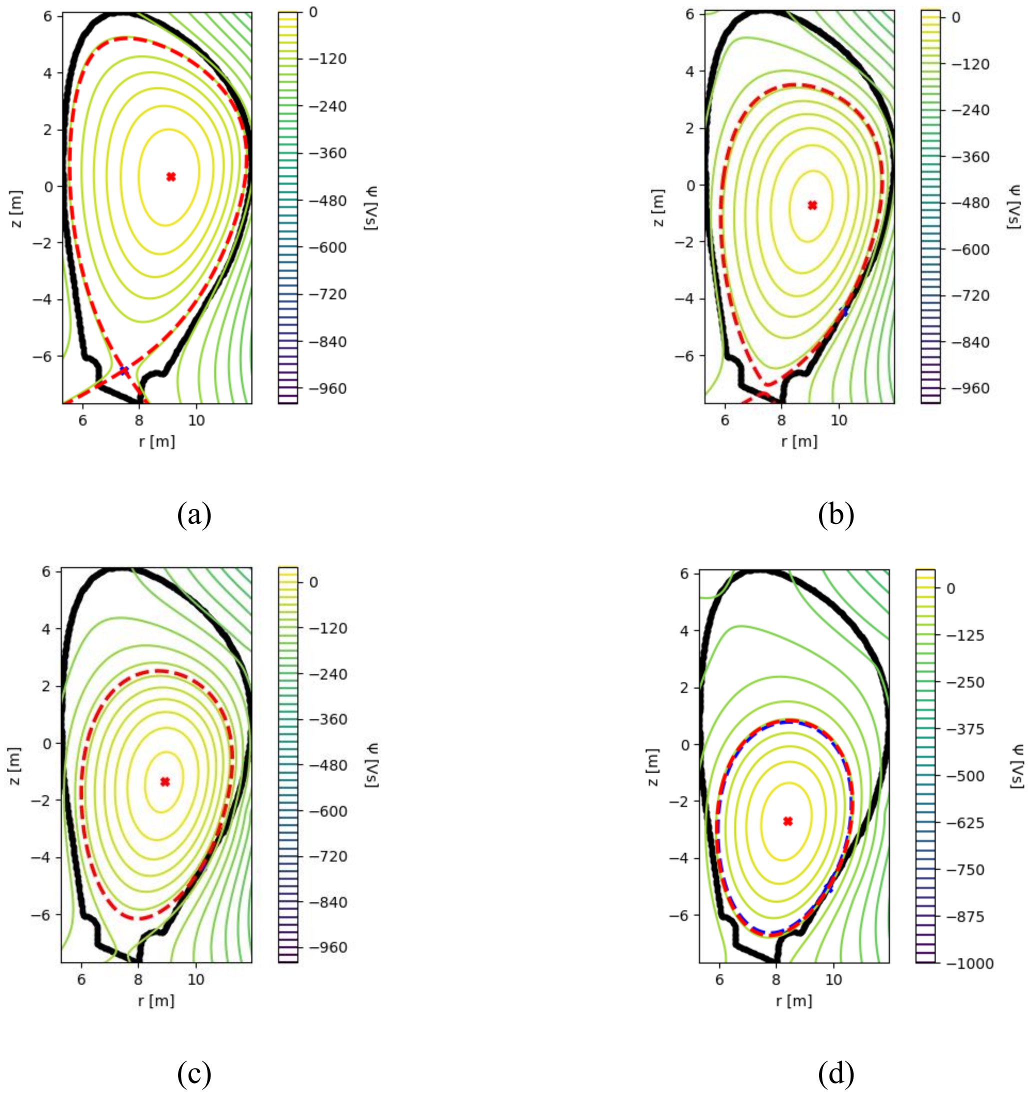

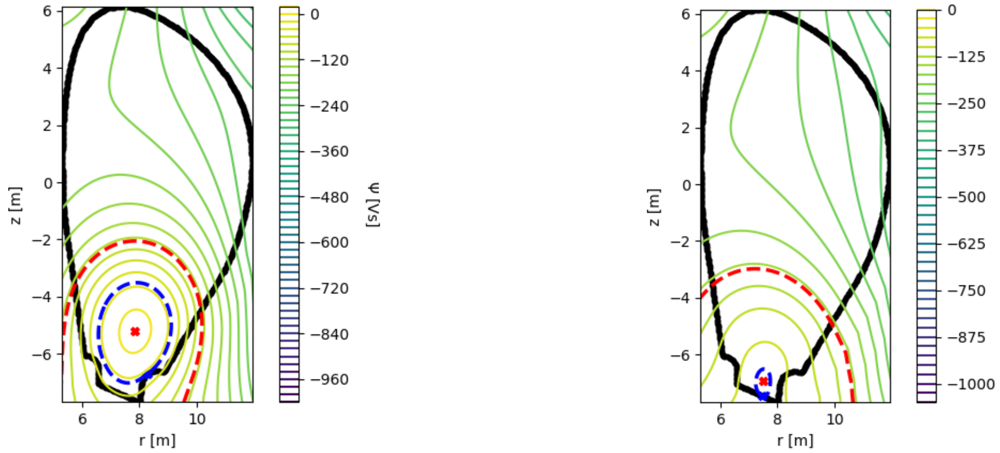

(e) (f)

Figure 77: Snapshots of the plasma boundary evolution during a slow downward VDE in DEMO baseline 2024: (a) equilibrium, (b) diverted to limiter configuration, (c) start of the TQ, (d) start of the CQ, (d) plasma with halo current region carrying (e) ~70% and (f) ~30% of the nominal plasma current during the CQ phase.

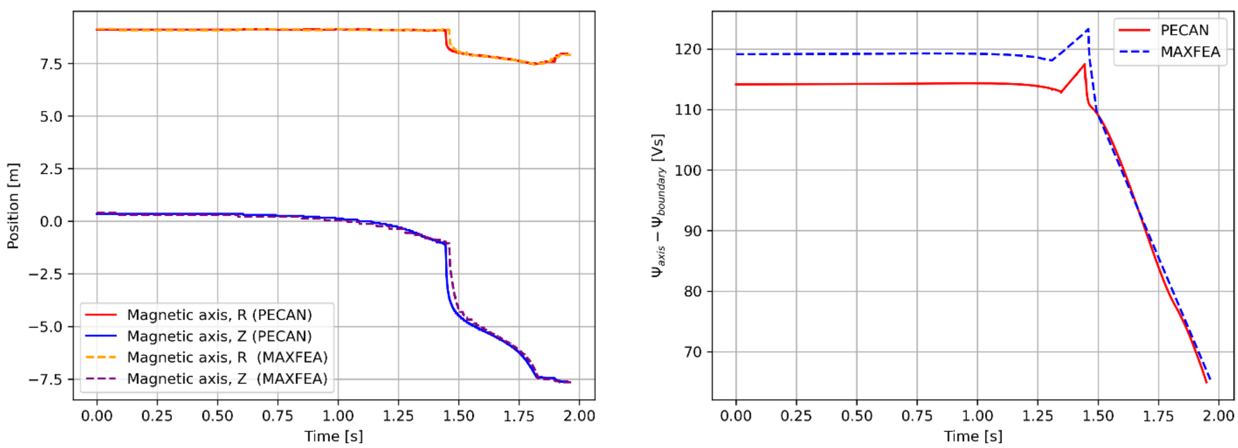

(a) (b)

Figure 78: Comparison between PECAN and MAXFEA for a slow DVDE in DEMO baseline 2024. The plots show: the evolution of (a) the plasma magnetic axis position and (b) the difference between axis and boundary flux during the disruption.

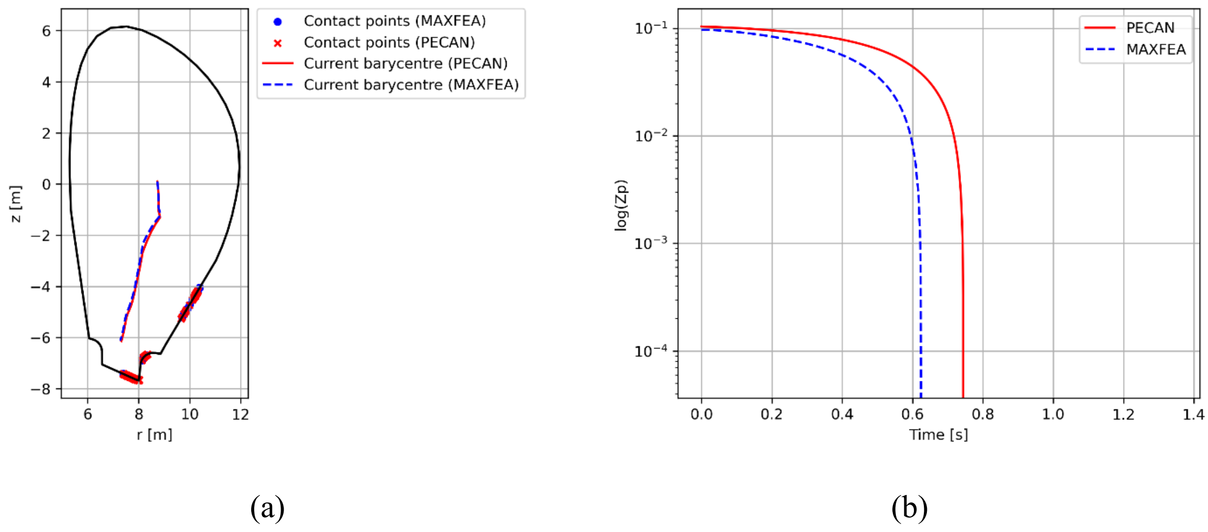

Figure 79: Comparison between PECAN and MAXFEA for a slow DVDE in DEMO baseline 2024. The plots show: (a) the evolution of the plasma current barycentre trajectory during the disruption and (b) the natural logarithm of its vertical coordinate before the contact with the first wall.

As in the fast case, also for the slow case the analysis of the merit figures highlights a time shift in the order of 20 ms between the two codes. The instability growth rate estimated with PECAN amounts to $\gamma \approx 4.05\ s^{-1}$, while the corresponding value obtained with MAXFEA is $\gamma \approx 3.43\ s^{-1}$. Consequently, all the considerations previously discussed remain valid in this case as well.

Table 20: Comparison between PECAN and MAXFEA main engineering parameters for a slow downward VDE in DEMO baseline 2024.

Quantity	PECAN	MAXFEA	Percentage difference [%]
Max. halo current [MA]	9.47	8.17	15.99
Max. eddy current in the VV [MA]	12.57	12.24	2.66
Max. vertical force on the VV [MN]	-11.57	-10.31	12.17

Table 20 reports the comparison between PECAN and MAXFEA for the main engineering parameters of a slow downward VDE in DEMO baseline 2024. The results show that, also for the slow upward VDE, the halo current differs by ~16% and the eddy currents in the VV agree within ~3%, while the vertical force displays a deviation of ~12%. The considerations already discussed for the previous cases remain valid here as well, with PECAN providing more conservative estimates, thus reducing the risk of underestimating the loads on passive components.

TRUST, DSN at EOF – Fast Upward VDE

This section presents the results for the fast upward vertical displacement event (UVDE) in the TRUST downward single-null scenario. The disruption event has been modelled starting from the static equilibrium at EOF instant reported in the previous section. The figures of merit for the comparison between PECAN and MAXFEA are summarized below.

- Figure 80 shows the time evolution of plasma current and halo current, together with the total eddy currents induced in the vacuum vessel and the resulting vertical force.
- Figure 81 contains the snapshots of the plasma boundary evolution during the disruptive event.
- Figure 82 shows the evolution of the plasma magnetic axis position during the disruption and the trend of the difference between axis and boundary flux.
- Figure 83 shows the plasma current barycentre trajectory during the disruption and the contact points between plasma and first wall.
- Table 21 summarizes the comparison between PECAN and MAXFEA main engineering parameters.

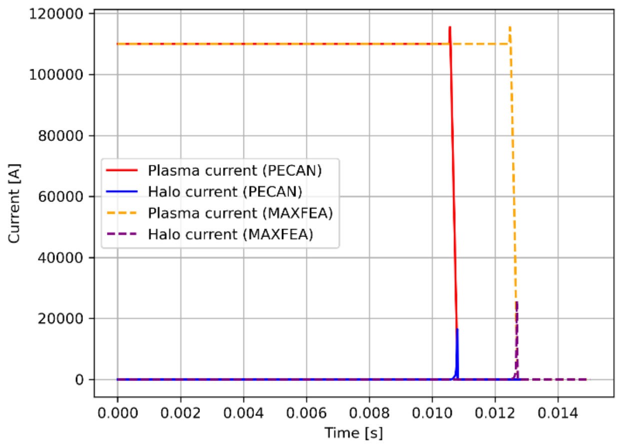

(a)

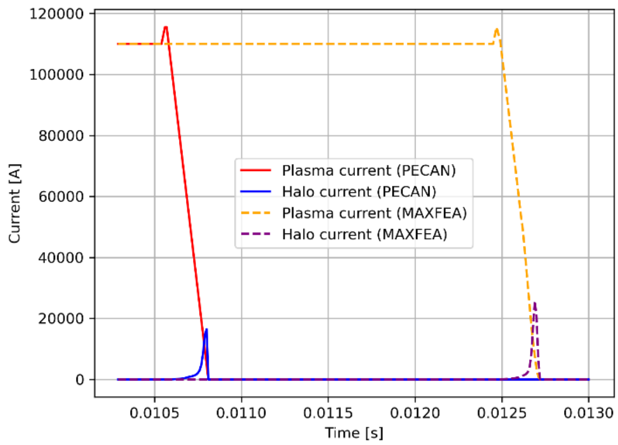

(b)

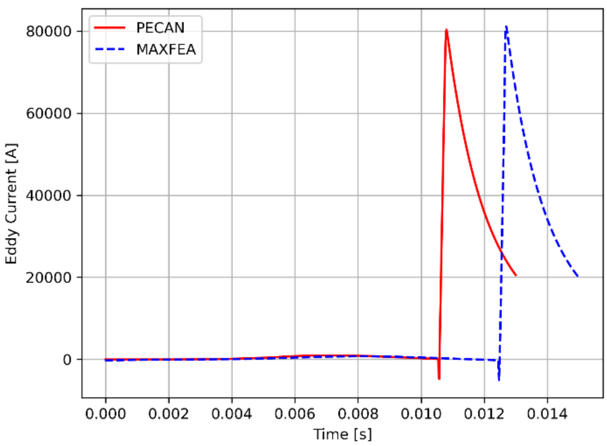

(c)

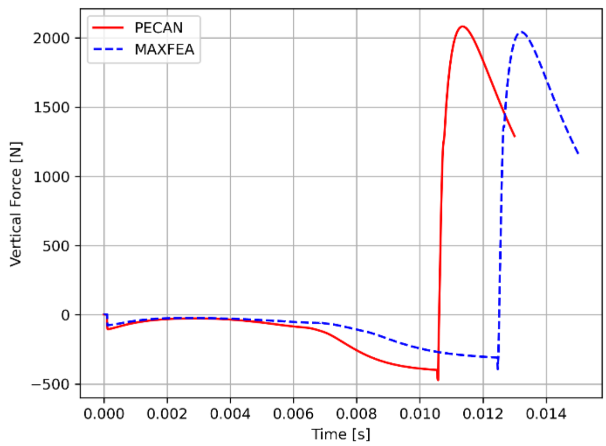

(d)

Figure 80: Comparison between PECAN and MAXFEA for a fast UVDE in TRUST, DSN configuration at EOF. The plots show: (a,b) time evolution of plasma current and halo current, (c) total eddy currents induced in the VV, and (d) overall vertical force on the VV.

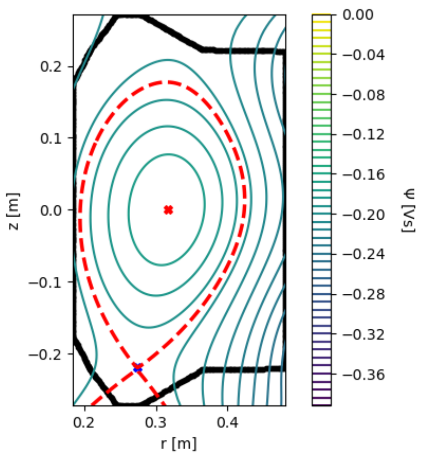

(a)

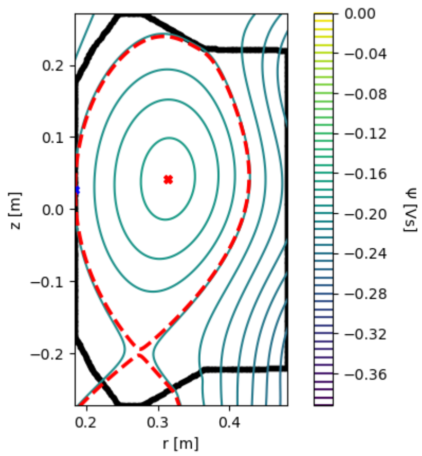

(b)

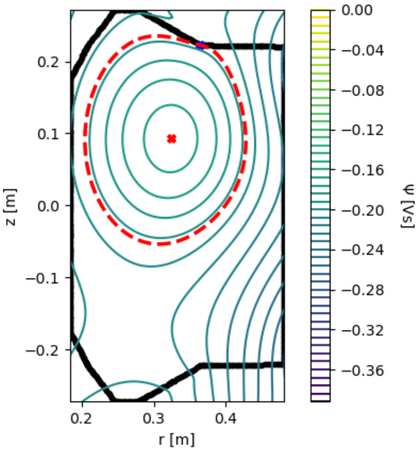

(c)

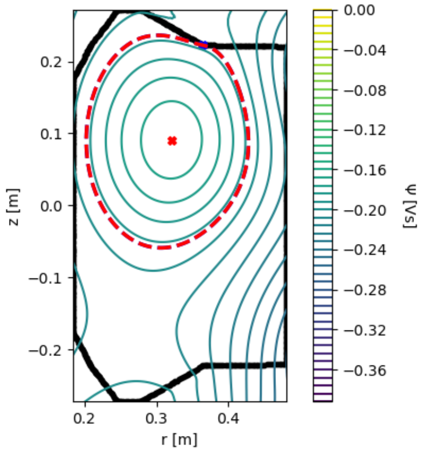

(d)

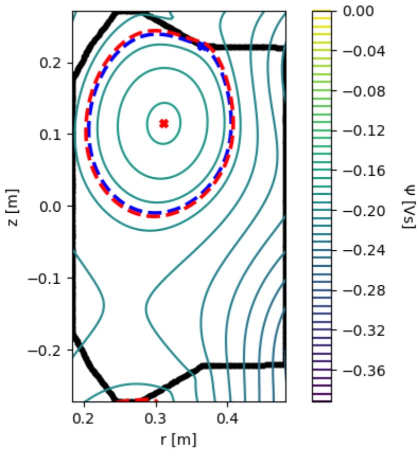

(e)

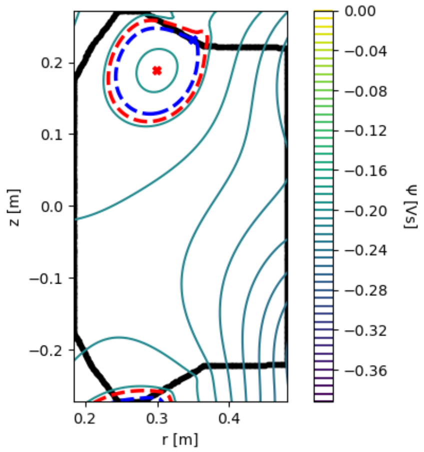

(f)

Figure 81: Snapshots of the plasma boundary evolution during a fast UVDE in TRUST, DSN configuration at EOF: (a) equilibrium, (b) diverted to limiter configuration, (c) start of the TQ, (d) start of the CQ, (d) plasma with halo current region carrying (e) ~70% and (f) ~30% of the nominal plasma current during the CQ phase.

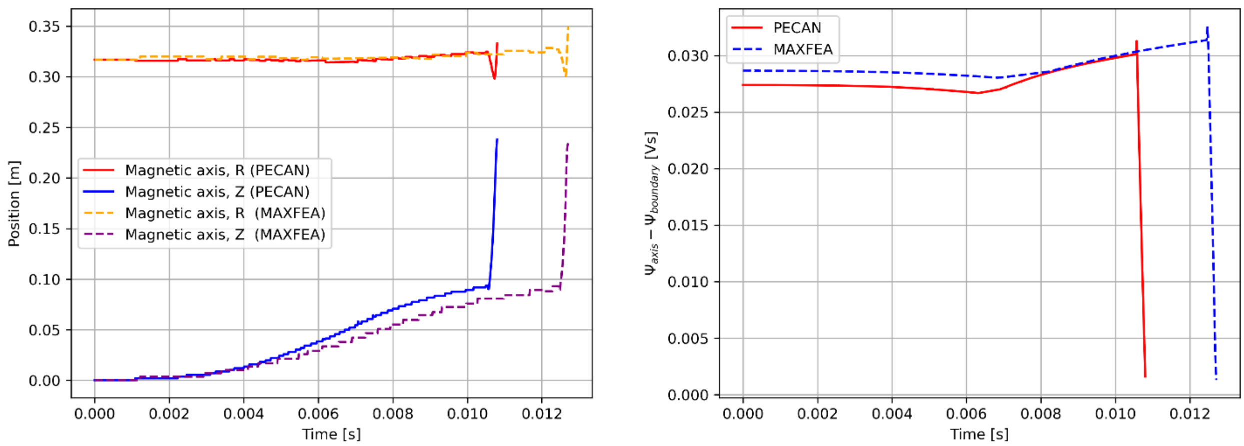

(a) (b)

Figure 82: Comparison between PECAN and MAXFEA for a fast UVDE in TRUST, DSN configuration at EOF. The plots show: the evolution of (a) the plasma magnetic axis position and (b) the difference between axis and boundary flux during the disruption.

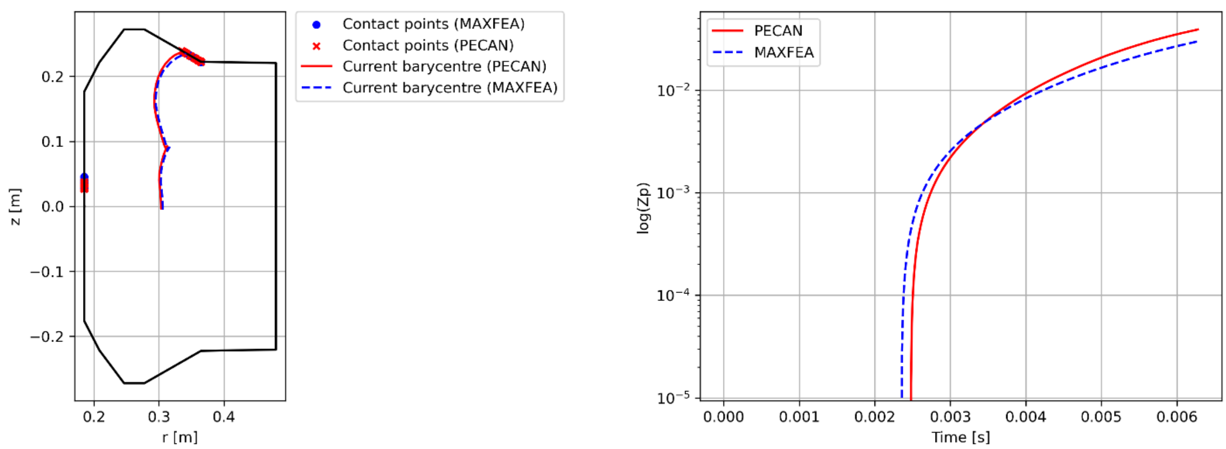

(a) (b)

Figure 83: Comparison between PECAN and MAXFEA for a fast UVDE in TRUST, DSN configuration at EOF. The plots show: (a) the evolution of the plasma current barycentre trajectory during the disruption and (b) the natural logarithm of its vertical coordinate before the contact with the first wall.

The analysis of the merit figures highlights a time shift in the order of 2 ms between the two codes. The instability growth rate estimated with PECAN amounts to $\gamma \approx 604.18\, s^{-1}$, while the corresponding value obtained with MAXFEA is $\gamma \approx 525.38\, s^{-1}$, i.e. a relative difference of approximately 15%. It should be noted that the growth rate computed for TRUST is significantly larger than that obtained for DEMO, as expected from the different scaling factor of the two machines

[59]. Consequently, all the considerations previously discussed remain valid in this case as well, and they provide a consistent explanation for the observed time shift between the two codes.

Table 21: Comparison between PECAN and MAXFEA main engineering parameters for a fast UVDE in TRUST, DSN configuration at EOF.

Quantity	PECAN	MAXFEA	Percentage difference [%]
Max. halo current [kA]	16.48	25.80	-36.12
Max. eddy current in the VV [kA]	80.34	81.11	-0.96
Max. vertical force on the VV [kN]	2.08	2.04	1.96

Table 21 compares PECAN and MAXFEA predictions for the main engineering parameters of a fast upward VDE in TRUST, DSN configuration at EOF. The results show that the maximum eddy currents in the vacuum vessel and the vertical forces are in very good agreement between the two codes, with discrepancies below 2%. A larger difference is observed in the halo current (about –36%), but this is not of particular concern for TRUST. Indeed, halo currents do not represent a critical issue from an engineering standpoint in this device as showed in Section 5.2 and in [33], since the associated forces account only for a minor fraction of the overall load, which is dominated almost entirely by the eddy current contribution. It is also worth noting that in PECAN the forces due to eddy currents are about 2% larger than in MAXFEA, thereby providing a more conservative estimate that enhances safety margins in the design process. Nevertheless, this discrepancy should be further investigated to identify its origin, for instance by carrying out a sensitivity analysis with respect to the mesh discretization and the imposed halo width, evaluating their influence on the predicted halo current.

TRUST, DSN at EOF – Fast Downward VDE

This section presents the results for the fast downward vertical displacement event (DVDE) in the TRUST downward single-null scenario. The disruption event has been modelled starting from the static equilibrium at EOF instant reported in the previous section. The figures of merit for the comparison between PECAN and MAXFEA are summarized below.

- Figure 84 shows the time evolution of plasma current and halo current, together with the total eddy currents induced in the vacuum vessel and the resulting vertical force.
- Figure 85 contains the snapshots of the plasma boundary evolution during the disruptive event.
- Figure 86 shows the evolution of the plasma magnetic axis position during the disruption and the trend of the difference between axis and boundary flux.
- Figure 87 shows the plasma current barycentre trajectory during the disruption and the contact points between plasma and first wall.
- Table 22 summarizes the comparison between PECAN and MAXFEA main engineering parameters.

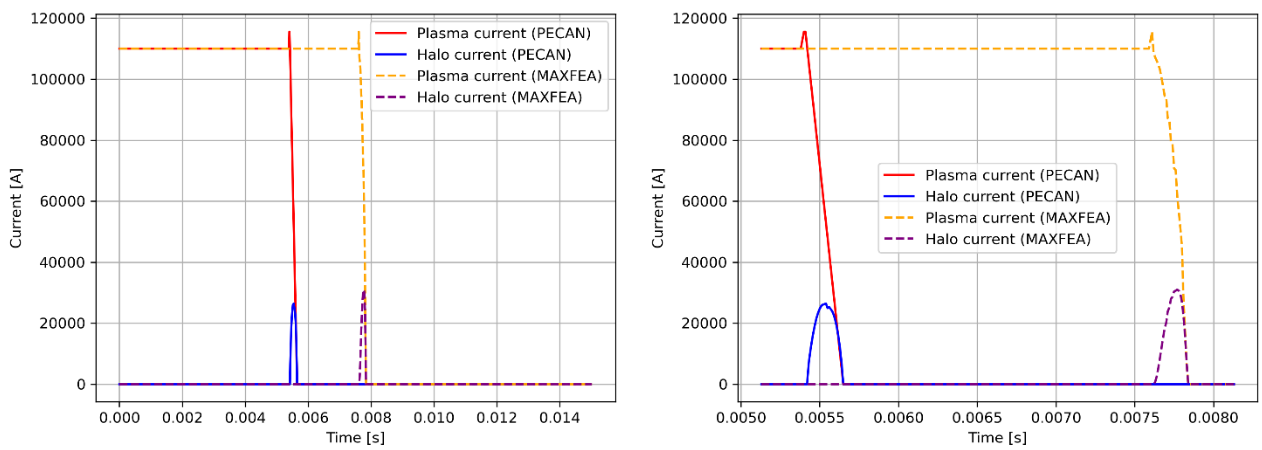

(a) (b)

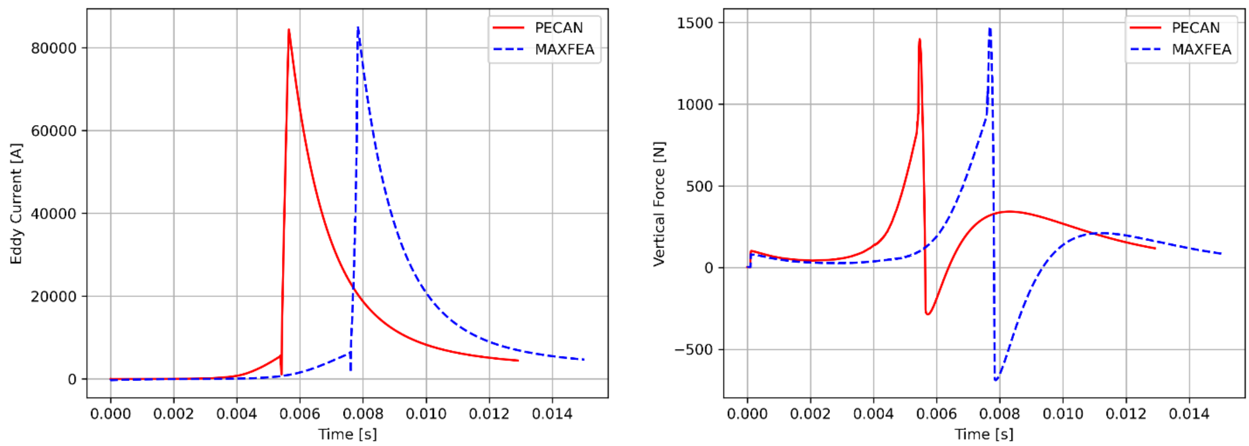

(c) (d)

Figure 84: Comparison between PECAN and MAXFEA for a fast DVDE in TRUST, DSN configuration at EOF. The plots show: (a,b) time evolution of plasma current and halo current, (c) total eddy currents induced in the VV, and (d) overall vertical force on the VV.

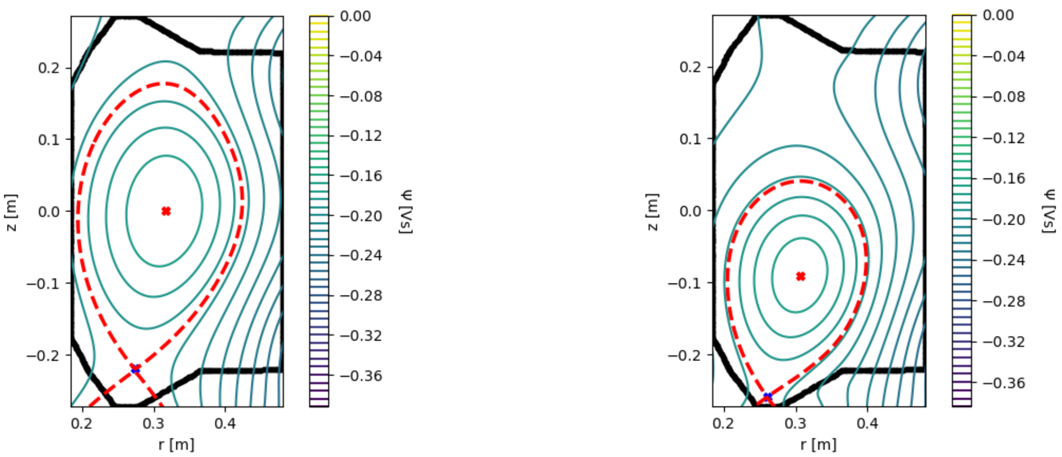

(a) (b)

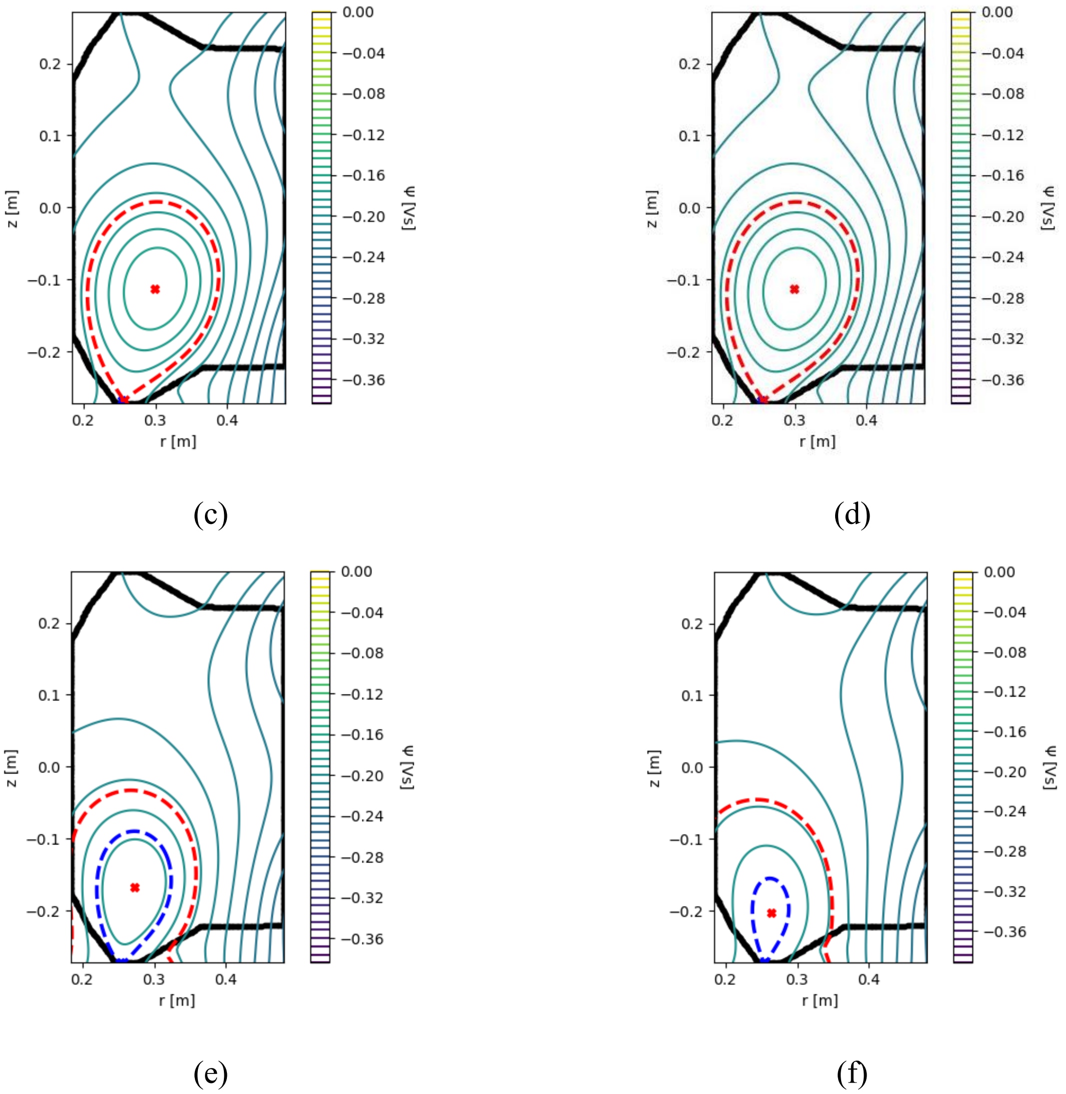

Figure 85: Snapshots of the plasma boundary evolution during a fast DVDE in TRUST, DSN configuration at EOF: (a) equilibrium, (b) q95=2, (c) start of the TQ, (d) start of the CQ, (d) plasma with halo current region carrying (e) ~70% and (f) ~30% of the nominal plasma current during the CQ phase.

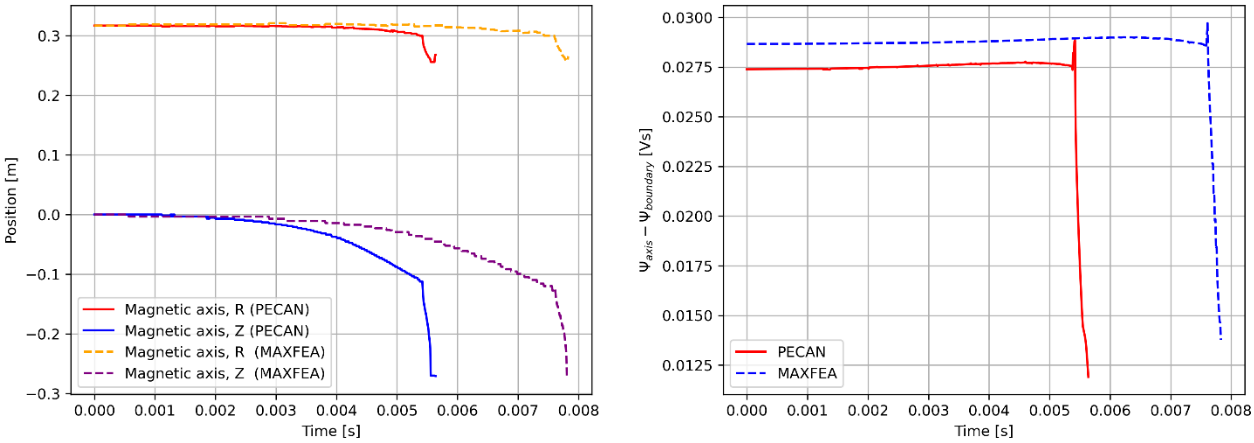

(a) (b)

Figure 86: Comparison between PECAN and MAXFEA for a fast DVDE in TRUST, DSN configuration at EOF. The plots show: the evolution of (a) the plasma magnetic axis position and (b) the difference between axis and boundary flux during the disruption.

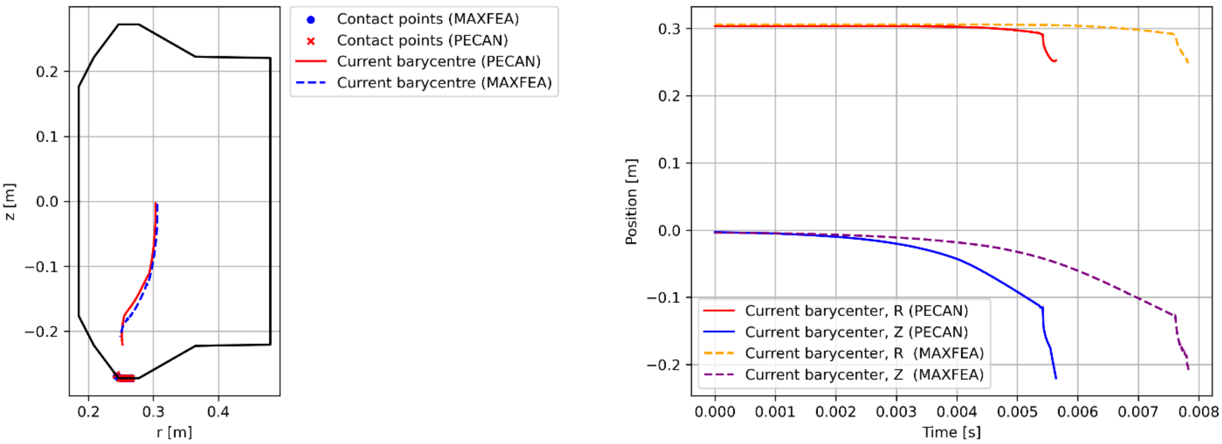

(a) (b)

Figure 87: Comparison between PECAN and MAXFEA for a fast DVDE in TRUST, DSN configuration at EOF. The plots show the evolution of the plasma current barycentre trajectory during the disruption.

The analysis of the merit figures highlights a time shift in the order of 2 ms between the two codes. The instability growth rate estimated with PECAN amounts to $\gamma \approx 796.71\, s^{-1}$, while the corresponding value obtained with MAXFEA is $\gamma \approx 715.13\, s^{-1}$. Consequently, all the considerations previously discussed remain valid in this case as well.

Table 22: Comparison between PECAN and MAXFEA main engineering parameters for a fast DVDE in TRUST, DSN configuration at EOF.

Quantity	PECAN	MAXFEA	Percentage difference [%]
Max. halo current [kA]	26.41	30.99	-14.78
Max. eddy current in the VV [kA]	84.41	85.15	-0.86
Max. vertical force on the VV [kN]	1.40	1.48	-5.28

Table 22 compares PECAN and MAXFEA predictions for the main engineering parameters of a fast downward VDE in TRUST, DSN configuration at EOF. The results confirm the same trend already observed for the upward case: eddy currents in the vacuum vessel and vertical forces are in very close agreement, with discrepancies below 6%, while a larger difference is found in the halo current (about –15%). As previously discussed, this discrepancy is not critical from an engineering perspective, since in TRUST the contribution of halo currents to the total loads is negligible compared to that of the eddy currents. Therefore, the same considerations outlined for the upward case remain valid here as well.

Mesh sensitivity analysis

In order to investigate the role of mesh discretization in determining the accuracy of PECAN analyses, a second simulation was performed for the UVDE fast and slow scenarios of DEMO LAR 24. In this case, particular attention was devoted to the refinement of the vacuum vessel and in-vessel coil regions, which were discretized with a significantly larger number of elements. Actually, the number of (i) nodes and (ii) elements pass respectively from (i) 15030 and (ii) 29963 to (i) 19199 and (ii) 38301.The objective was to verify whether part of the discrepancies observed with respect to MAXFEA could be ascribed to insufficient spatial resolution in those critical components.

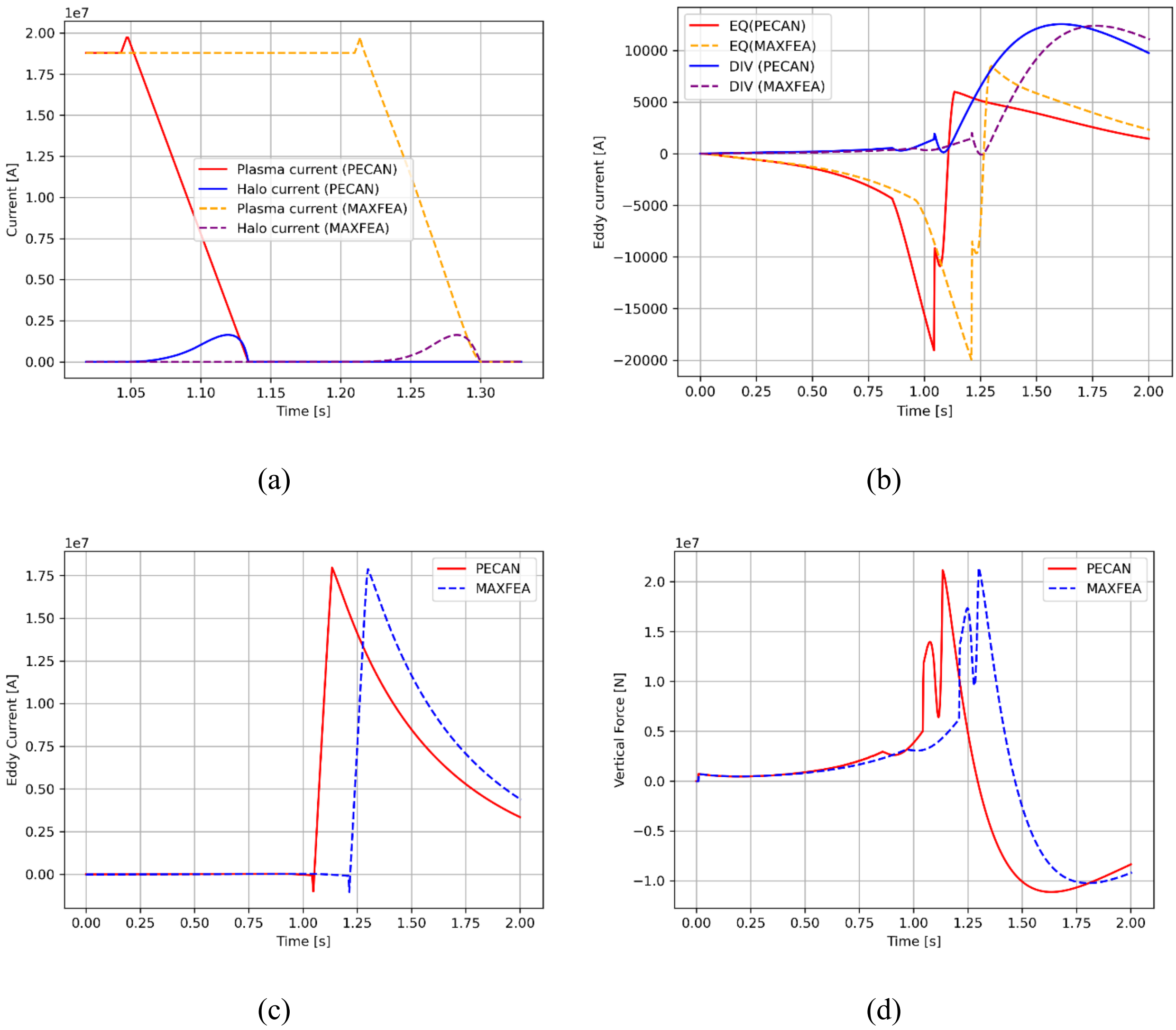

Figure 88: Comparison between PECAN and MAXFEA for a fast UVDE in DEMO baseline 2024 with a refined mesh. The plots show: (a) time evolution of plasma current and halo current, (b) in-vessel coils currents, (c) total eddy currents induced in the VV, and (d) overall vertical force on the VV.

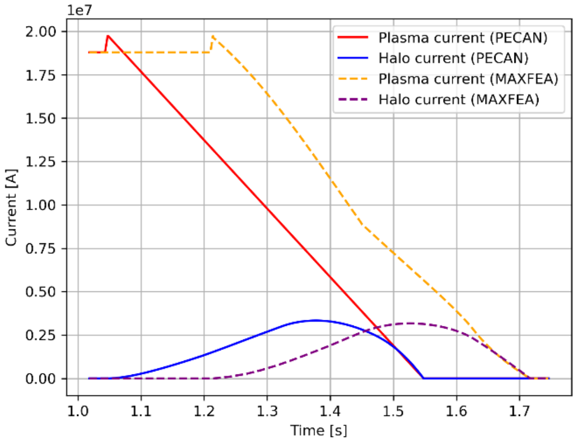

(a)

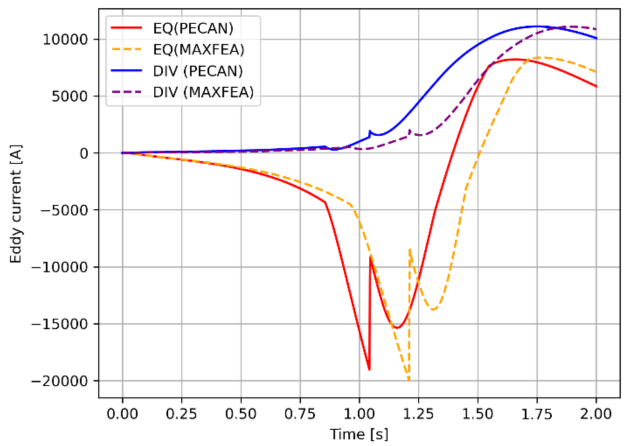

(b)

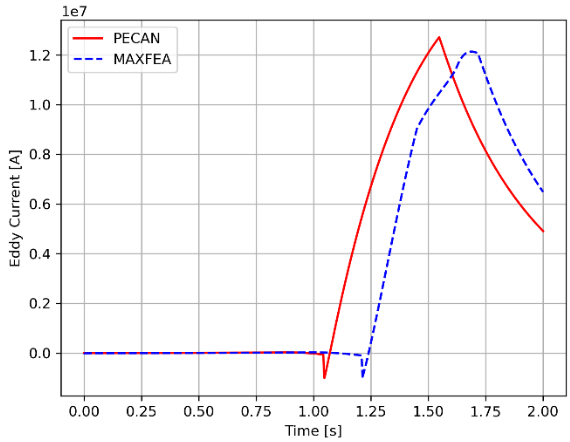

(c)

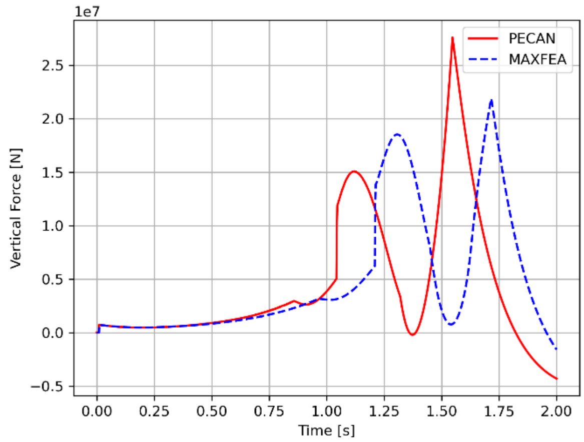

(d)

Figure 89: Comparison between PECAN and MAXFEA for a slow UVDE in DEMO baseline 2024 with a refined mesh. The plots show: (a) time evolution of plasma current and halo current, (b) in-vessel coils currents, (c) total eddy currents induced in the VV, and (d) overall vertical force on the VV.

Table 23: Comparison between PECAN and MAXFEA main engineering parameters for a fast upward VDE in DEMO baseline 2024 with a refined mesh.

Quantity	PECAN	MAXFEA	Percentage difference [%]
Max. halo current [MA]	1.64	1.64	0.52
Max. eddy current in the VV [MA]	17.96	17.87	0.51
Max. vertical force on the VV [MN]	21.15	21.41	-1.22

Table 24: Comparison between PECAN and MAXFEA main engineering parameters for a slow upward VDE in DEMO baseline 2024 with a refined mesh.

Quantity	PECAN	MAXFEA	Percentage difference [%]
Max. halo current [MA]	3.34	3.17	5.15
Max. eddy current in the VV [MA]	12.72	12.14	4.79
Max. vertical force on the VV [MN]	27.59	21.86	26.22

The results confirm that, although a residual time shift between the PECAN and MAXFEA simulations is still present, the discrepancies in terms of halo currents and vertical forces are substantially reduced respect to Table 17 and Table 18. This outcome demonstrates that the refinement of the finite element model is indeed one of the determining factors in achieving consistent results and highlights the importance of carefully balancing numerical accuracy and computational cost in disruption analyses.

As already emphasized in previous analysis, however, further studies are required to assess the influence of additional factors, such as the treatment of the transition between steady-state and transient problems, as well as the effect of differences in the total current distribution due to the fictitious control currents computed at time $t = 0$. For these reasons, the results reported below should be interpreted with caution, as they represent a preliminary step toward clarifying the origin of the discrepancies between the two codes.

6.3 Discussion and Conclusions

The verification and validation activities presented in this chapter confirm the capability of PECAN to accurately reproduce both stationary and transient plasma equilibria in realistic tokamak configurations.

In the stationary regime, the code has been benchmarked against the reference solvers MAXFEA and CREATE-NL, showing an excellent overall agreement in terms of poloidal-flux distribution, current-density profiles, and global equilibrium parameters. Furthermore, the experimental validation performed on the ST40 tokamak demonstrated the consistency of PECAN reconstructions with those obtained using GSFit, confirming the reliability of the implemented numerical formulation. The solver has proven to be robust, modular, and physically consistent, and it is capable of generating fully compliant gEQDSK files through the extended FreeQDSK library. This functionality enables a direct comparison with experimental reconstructions, effectively bridging forward equilibrium simulations and experimental magnetic analysis.

The benchmarking with MAXFEA, CREATE-NL and GSFit validates both the weak formulation and the nonlinear Picard-iteration procedure adopted in PECAN, confirming its reliability for steady-state equilibria under free-boundary conditions. Minor deviations near the plasma boundary were mainly attributed to the different analytical definitions of the input profiles and the boundary-condition implementation of each solver, rather than to intrinsic limitations of the code.

For the transient analyses, the comparison with MAXFEA yielded equally positive results. PECAN successfully reproduced the time evolution of the plasma boundary, the trajectory of the plasma-current centroid, and the eddy currents induced in the surrounding passive structures, confirming the correctness of the coupled FEM–circuit formulation. The largest deviations were observed in the electromagnetic-force time traces, where the peak amplitudes showed greater differences. These discrepancies can be justified by several factors, among which the two most significant ones emerging from the analyses are:

(i) the mesh refinement, as demonstrated by the sensitivity analysis;

(ii) the DG0 approximation of the Ψ-gradient, which would require the use of more refined post-processing procedures, as suggested in [58]

future work will further address this points to fully clarify the problem.

As discussed in Chapter 4, a complete validation of the electromagnetic loads would require dedicated 3D structural analyses, capable of capturing possible asymmetries and localised effects that cannot be represented in 2D axisymmetric simulations. Nevertheless, the forces predicted by PECAN and MAXFEA remain well below the critical thresholds reported for AISI 316L(N) stainless steel. In particular, both codes yield global electromagnetic loads consistent with those reported by [35] and [36] for DEMO, remaining far below the allowable stress limits defined by RCC-MRx at the relevant operating temperature. The same conclusion applies to the TRUST device, where all simulated disruption scenarios produce electromagnetic loads safely below the mechanical design limits.

In view of these results, the next development steps of PECAN will focus on extending its capabilities beyond axisymmetric equilibrium calculations. A dedicated mesher is under development to allow greater flexibility and accuracy in the representation of complex device geometries. In parallel, the circuit coupling architecture will be extended to include more general electrical configurations, enabling the connection of coils and passive loops not only in series and anti-series (currently supported) but also in parallel or hybrid arrangements, thus enhancing the capability to model complex machine topologies and passive networks. Furthermore, a future implementation of the coupling with external multiphysics solvers, such as ANSYS, is planned within the equilibrium computation framework, enabling a direct exchange of field quantities and material responses between PECAN and external finite element environments.

This integration will enable the direct evaluation of three-dimensional electromagnetic loads on passive components, which is essential during plasma transients and disruptive events, when strong spatial asymmetries, halo currents, and localised current paths can significantly affect the mechanical response of the vessel and in-vessel structures. By embedding such coupling directly within the equilibrium solver, PECAN will evolve into a fully coupled electromagnetic–structural environment, capable of predicting the 3D load distribution and stress evolution in real time. These developments will pave the way for predictive design and verification studies of future fusion devices, ensuring that electromagnetic and mechanical aspects are consistently addressed within a unified simulation framework.

Part IV – Magnetic Diagnostics for TRUST

7. Definition of a Minimal Magnetic Diagnostic System for TRUST

Magnetic diagnostics represent one of the fundamental pillars of tokamak research and operation. In all magnetic confinement devices, the ability to accurately measure magnetic fields, magnetic fluxes, and induced currents is essential for understanding plasma behaviour, controlling its position and shape, and ensuring the safe and reliable operation of the device. These diagnostics form the backbone of both plasma equilibrium reconstruction and real-time control systems, enabling plasma stabilization, sustainment of desired magnetic configurations, and mitigation of potentially destructive phenomena such as disruptions or vertical displacement events (VDEs) [5][8][12][42][43].

The importance of magnetic diagnostics is expected to grow even further in future fusion reactors, where plasma control must be achieved with unprecedented accuracy and robustness. In large-scale devices such as ITER, DEMO, and SPARC, a redundant and well-distributed magnetic diagnostic system is indispensable to ensure long-pulse operation and to minimize the risk of damage to in-vessel components [7][14][17][20].

For example, ITER integrates more than 200 flux loops and over 600 magnetic pick-up coils installed on and around the vacuum vessel to monitor the plasma shape and magnetic configuration throughout all operational phases [60]. These sensors must operate in harsh environments characterized by strong electromagnetic transients, neutron fluxes, and high thermal loads, imposing severe design and placement constraints [61][62][63][64].

Smaller or intermediate devices, such as COMPASS in Prague, SMART in Seville and ST40 operated by Tokamak Energy, illustrate how diagnostic systems are scaled and optimized in different machine classes. On COMPASS, for example, more than 400 magnetic diagnostic coils cover the vacuum vessel in both poloidal and toroidal directions, enabling measurement of plasma current density, position, shape, and MHD instabilities with spatial resolution better than ~5 mm [65]. On SMART, the magnetic sensor suite includes Rogowski coils, poloidal/saddle/diamagnetic flux loops and 2D magnetic probes, whose quantity and positions were verified by synthetic equilibrium reconstruction studies [63]. On ST40, the device employs a large number of magnetic sensors (≈85), including Mirnov coils and flux loops, to reconstruct the plasma boundary and plasma current distribution via real-time equilibrium codes. The Mirnov coils, only a few millimetres in size, measure the local magnetic field components at specific positions and orientations, and are protected by ceramic dome-shaped armour to withstand the thermal and electromagnetic loads near the vacuum vessel. The flux loops, in contrast, are much larger—up to 3 m in diameter—and provide integral measurements of the total magnetic flux passing through them, offering a global constraint on the plasma equilibrium. The layout of ST40's magnetic sensors, illustrated in the diagram below, exemplifies the typical configuration adopted in compact high-field spherical tokamaks, and represents a valuable reference for the design of new diagnostic systems in similar devices [41].

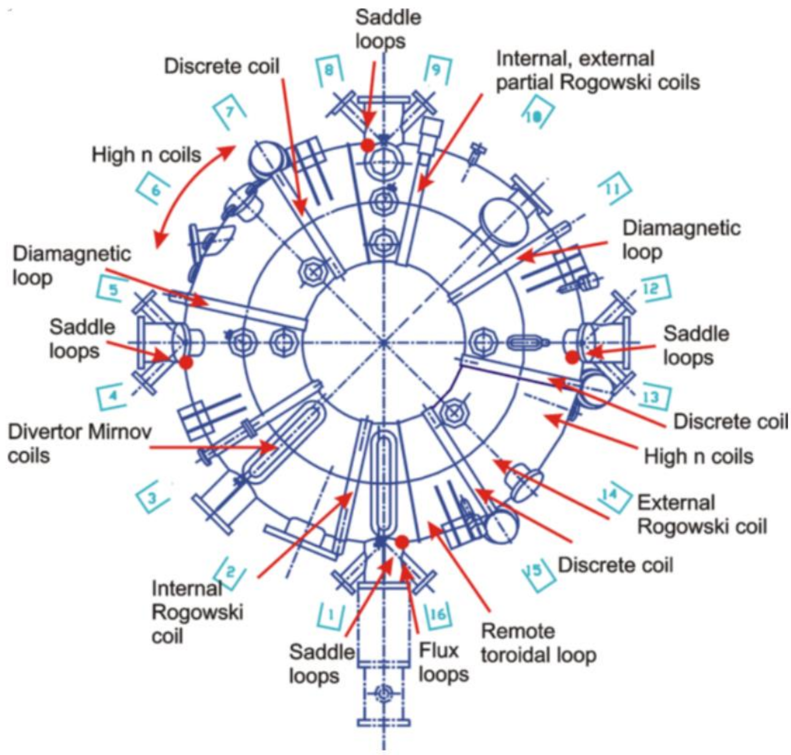

Figure 90: Top view of the magnetic diagnostics on tokamak COMPASS (curtesy of IPP CAS, Institute of Plasma Physics of the Czech Academy of Sciences).

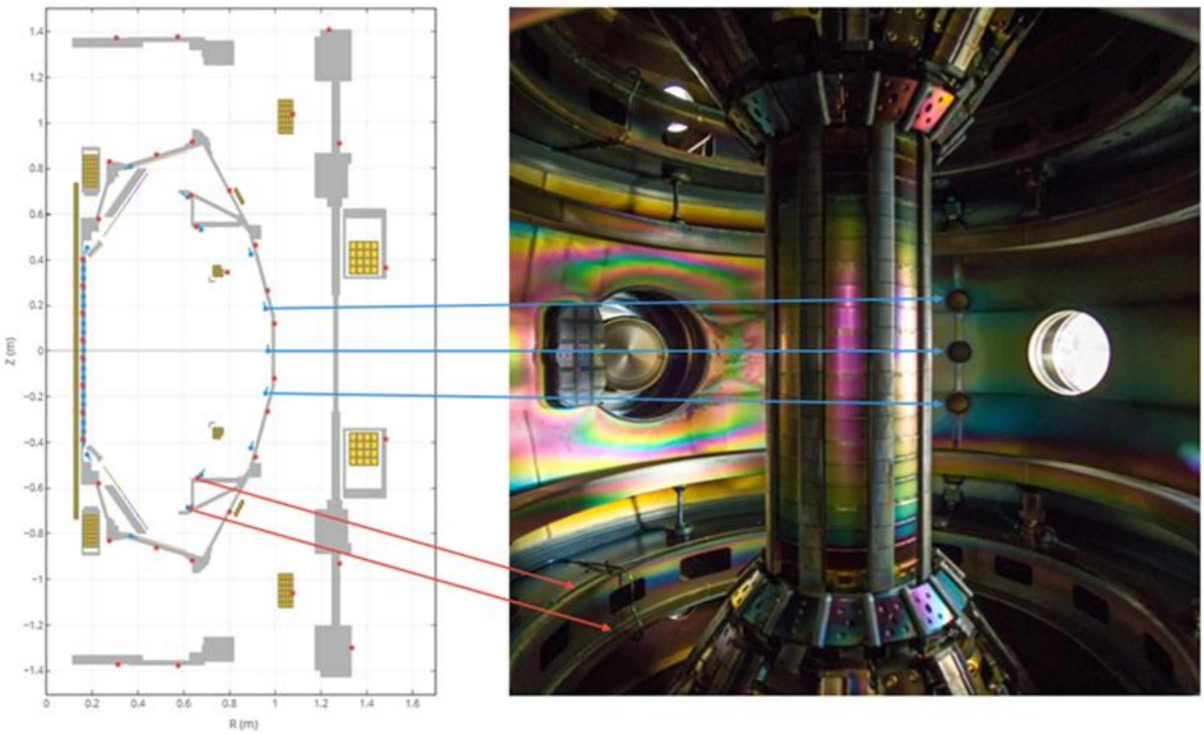

Figure 91: Layout of ST40's magnetic diagnostics.
On the left, poloidal cross-section showing the positions of flux loops (red) and Mirnov coils (blue). On the right, internal view of the ST40 tokamak highlighting the physical placement of the sensors on the vessel wall (curtesy of Tokamak Energy).

From a theoretical standpoint, the reconstruction of plasma equilibrium from external magnetic measurements constitutes a classically ill-posed inverse problem [44][46][49][66][67]. In this context, the measured quantities—magnetic fluxes and field components—represent only indirect observables of the underlying plasma current density distribution. According to Hadamard's definition, an inverse problem is well posed if its solution exists, is unique, and depends continuously on the data. The equilibrium reconstruction problem in tokamaks violates the second and third conditions: multiple internal current distributions can produce indistinguishable external magnetic signatures, and small perturbations or noise in the measured data can lead to large variations in the inferred plasma parameters[41][68][70][71].

This intrinsic non-uniqueness arises because the magnetic field outside the plasma is governed by a Laplacian-like operator in vacuum ($\nabla^2\Psi = 0$), which is inherently non-invertible without internal information. Consequently, the inversion problem must be regularized to ensure physical consistency and numerical stability. Regularization introduces additional information—either through mathematical constraints or physical assumptions—such as prescribed current or pressure profiles, symmetry conditions, or smoothness constraints on the poloidal flux function. Common techniques include Tikhonov regularization, truncated singular value decomposition (TSVD), and Bayesian inference, all aiming to stabilize the solution and prevent overfitting to noisy measurements [66][72][73].

In practical applications, equilibrium reconstruction codes, such as EFIT [66], LIUQUE [72] and GSFit [73], implement these principles by iteratively solving the Grad–Shafranov equation while adjusting the free functions $p'(\Psi)$and $FF'(\Psi)$to minimize the discrepancy between measured and calculated magnetic signals. The problem is typically expressed in a least-squares form,

$$\min_{\theta} \parallel \mathbf{B}_{\text{meas}} - \mathbf{B}_{\text{model}}(\theta) \parallel^2 + \lambda R(\theta) \tag{7.1}$$

where $\mathbf{B}_{\text{meas}}$ and $\mathbf{B}_{\text{model}}$ are the measured and computed magnetic data, $R(\theta)$ is a regularization functional enforcing smoothness or physical constraints, and λ is the regularization parameter controlling the trade-off between accuracy and stability.

The accuracy, resolution, and robustness of the reconstructed equilibrium depend strongly on the diagnostic layout: the number, type, and spatial distribution of the sensors used as input. A dense and geometrically diverse arrangement improves the conditioning of the inverse matrix, reducing parameter correlations and enhancing the sensitivity to the plasma boundary and internal current distribution. Conversely, sparse or poorly distributed sensor sets may lead to rank-deficient or ill-conditioned matrices, resulting in unstable or biased reconstructions[61][62][63][70].

The optimal diagnostic design should therefore aim to maximize the information content of the measurements—quantified, for instance, through the Fisher Information Matrix or singular-value spectrum of the response matrix—while ensuring sufficient redundancy to mitigate measurement noise and hardware failures. This is typically achieved by combining flux loops (which provide integral measurements of the poloidal flux) and magnetic probes (which give local information on the field gradients), positioned both inside and outside the vacuum vessel to capture complementary information [62][61][68].

Additional design considerations include the angular coverage, radial proximity of the probes to the plasma, and the mutual inductance coupling between sensors and conducting structures. For instance, in devices such as COMPASS and SMART, synthetic studies have demonstrated that adding a small number of in-vessel coils can significantly improve boundary reconstruction accuracy even with moderate noise levels (1–3 %) [63][70]. Similarly, in DIII-D and WEST, redundant sensor arrays are exploited not only for equilibrium reconstruction but also for real-time plasma control and disruption prediction [61][62].

In the case of TRUST, a compact university-scale tokamak currently under design at *Università degli Studi della Tuscia* [33], several practical constraints affect the diagnostic design process. The system must rely on locally manufactured sensors and custom data-acquisition hardware, which currently allows the simultaneous acquisition of at most nine magnetic signals. Moreover, due to the lack of ceramic shielding and vacuum-compatible feedthroughs, it is not presently possible to install sensors facing the plasma directly—as would be required for radiation-resistant, high-temperature sensors such as those adopted on ST40 by Tokamak Energy [64].

For these reasons, the diagnostic configuration proposed in this work represents a first minimal setup, primarily designed to provide reliable information on the minimum number of coils required for plasma boundary reconstruction. Naturally, once the machine is realised, the number of probes will be increased as much as possible in order to compare experimental data with theoretical predictions and to identify the optimal probe positions that minimise the number actually required. The system consists of a combination of flux loops and double-axis magnetic probes, which together deliver complementary information: flux loops measure the poloidal magnetic flux, while magnetic probes measure the local radial and vertical components of the magnetic field. This configuration represents the standard diagnostic approach adopted in most existing tokamak experiments, including DIII-D, WEST, SMART, ITER, COMPASS and ST40 [60][61][62][63][64][65].

It must be emphasized that the layout presented here should not be regarded as an optimized design, but rather as an initial guess—a first step toward the development of a consistent and scalable magnetic diagnostic system for TRUST-like devices. Future optimization studies will aim to refine the number and placement of sensors by means of sensitivity analyses and least-squares inversion tests, ultimately determining the minimal configuration that guarantees accurate and robust plasma reconstruction. Such optimization will allow extending the diagnostic capability from simple boundary identification to the reconstruction of internal plasma profiles, in line with the diagnostic strategies adopted in larger facilities such as DIII-D and JET [74].

The preliminary assessment presented in this work has been carried out using the equilibrium reconstruction code EFIT, in combination with the electromagnetic solvers MAXFEA and PECAN. EFIT was employed to evaluate the plasma boundary reconstruction capabilities, while PECAN was used to generate synthetic magnetic signals corresponding to the flux loops and probes, allowing a quantitative validation of the proposed diagnostic configuration.

In the present study, a minimal diagnostic layout was proposed, consisting of three flux loops and six double-axis (2D) magnetic probes, selected according to the hardware and design constraints discussed above. This configuration represents the maximum number of signals that can be simultaneously acquired with the current data acquisition system, while maintaining adequate spatial coverage around the vacuum vessel.

Equilibrium reconstructions were carried out for several characteristic operating scenarios of the TRUST tokamak. The analysis focused primarily on the limiter configuration established immediately after plasma breakdown, at the Start-Of-Flat-top (SOF) instant of the downward single-null (DSN) configuration, and at its End-Of-Flat-top (EOF) condition. For completeness, the study also included the upward single-null (USN) and double-null (DN) equilibria, both evaluated at EOF.

For each configuration, EFIT reconstructions were performed using synthetic magnetic data generated by PECAN, to which normally distributed perturbations were applied in order to simulate measurement uncertainties ranging from 0% to 5%. This approach enabled a systematic evaluation of the diagnostic layout's robustness and sensitivity to experimental noise across the different magnetic configurations.

In addition to the minimal configuration, the same reconstruction procedure was repeated for an alternative, extended diagnostic layout comprising six flux loops and ten double-axis magnetic probes. Although this arrangement currently exceeds the hardware limitations of TRUST, it provides a valuable reference for future optimization studies, when enhanced acquisition systems and radiation-tolerant sensors will allow for a denser and more redundant magnetic network. The comparison between the two layouts highlights the expected improvement in plasma boundary reconstruction accuracy achievable through increased diagnostic coverage, which will guide the next design iteration of the TRUST magnetic system.

7.1 Methodology: Coupling PECAN with EFIT

The methodology adopted in this work leverages the complementary capabilities of PECAN and EFIT, establishing a unified workflow for the quantitative assessment of candidate magnetic diagnostic layouts under realistic operating conditions. The core idea is to employ PECAN as a synthetic diagnostic generator, responsible for computing the magnetic response to prescribed coil currents and plasma profiles, and EFIT as the equilibrium reconstruction tool, evaluating how accurately the plasma boundary can be recovered from the simulated measurements.

This dual approach enables testing the adequacy of different configurations of flux loops and magnetic probes in reproducing the target plasma equilibrium within acceptable uncertainty margins. EFIT was operated within the OMFIT framework [20], which provides a modular environment for managing input data, running equilibrium reconstructions, and post-processing the results.

The integrated workflow proceeds as follows:

1. Reference equilibrium definition

   The process starts from the reference equilibrium for the selected configuration, as introduced in Section 6.2. A consistent gEQDSK file is generated using MAXFEA, containing the plasma boundary and the equilibrium profiles $p'(\Psi)$, $FF'(\Psi)$, $p(\Psi)$, and $F(\Psi)$.

2. Plasma boundary fitting with EFIT (R-mode)

   The gEQDSK file is supplied to EFIT operating in R-mode, where the plasma boundary is prescribed and the currents in the central solenoid (CS) and poloidal-field (PF) coils (treated as F-coils) are adjusted to reproduce the reference equilibrium. This step effectively calibrates EFIT against the target configuration, ensuring its capability to reproduce the equilibrium under idealized, noise-free conditions.

3. Synthetic diagnostics with PECAN

   The coil current distributions obtained from EFIT are imported into PECAN, which solves the axisymmetric magnetostatic problem to compute the magnetic flux and field values at the diagnostic sensor positions. Two diagnostic layouts were analysed:

   a. a minimal layout, consisting of three flux loops and six double-axis (2D) magnetic probes (Figure 92, Layout 1), consistent with the current hardware and acquisition limitations;

b. an extended layout, including six flux loops and ten double-axis probes (Figure 92, Layout 2), exceeding the present acquisition capacity but representative of a feasible future configuration enabled by upgraded electronics and sensor manufacturing.

Since in the present configuration only a limited number of magnetic sensors is available, all positioned on the external surface of the vacuum vessel and therefore relatively far from the plasma, the reconstruction of the poloidal flux map is expected to be affected by measurement noise and by the intrinsic ill-conditioning of the inverse problem. Nevertheless, theoretical analyses have shown that reliable reconstructions can still be achieved even with a small number of measurements, provided that the sensors are located in specific positions.

In particular, [74] demonstrated that the poloidal flux function Ψ can be expressed as a toroidal multipolar expansion in the toroidal coordinates (θ, ω), where ω denotes the poloidal angle:

$$\Psi(\theta, \omega) = -\frac{1}{\sqrt{\cosh\ \theta - \cos\ \omega}} \sum_{m=0}^{\infty} [M_m^{\mathrm{i}}(\theta)\, f_m(\cosh\ \theta) + M_m^{\mathrm{e}}(\theta)\, g_m(\cosh\ \theta)] \cos{(m\omega)} + C \tag{7.2}$$

where M_m^{i} and M_m^{e} represent, respectively, the internal (plasma) and external (coil) multipolar moments, f_m and g_m are the Fock functions of order m and C is a constant representing the effect of an ideal transformer which generates a constant flux function $\Psi = C$. This formulation shows that the magnetic field measured outside the plasma can be represented as a discrete series of harmonics, each associated with a specific multipolar moment.

The multipolar moments themselves are defined as integrals of the toroidal current density $J_\phi(\theta_0, \omega_0)$ that flow inside the torus θ:

$$M_m^{\mathrm{i}}(\theta) = \mu_0 R_0^3 \frac{(2 - \delta_{m0})}{\left(m^2 - \frac{1}{4}\right)} \int_0^{2\pi} d\omega_0 \int_\theta^\infty d\theta_0\, J_\phi(\theta_0, \omega_0) \frac{g_m(\cosh\theta_0)\cos(m\omega_0)}{(\cosh\theta_0 - \cos\omega_0)^{\frac{5}{2}}} \tag{7.3}$$

$$M_m^{\mathrm{e}}(\theta) = \mu_0 R_0^3 \frac{(2 - \delta_{m0})}{\left(m^2 - \frac{1}{4}\right)} \int_0^{2\pi} d\omega_0 \int_\theta^\infty d\theta_0\, J_\phi(\theta_0, \omega_0) \frac{f_m(\cosh\theta_0)\cos(m\omega_0)}{(\cosh\theta_0 - \cos\omega_0)^{\frac{5}{2}}} \tag{7.4}$$

which explicitly show how the current density distribution determines the multipolar decomposition of Ψ.

In practice, the reconstruction can be performed from a discrete set of flux and field measurements taken along a surface at constant θ (for instance, an iso-ω curve in the poloidal plane) identified by the angle θ_{pr}. At the edge of the plasma θ_L, the conditions are those for $\theta_{pr} < \theta < \theta_L$:

$$\begin{cases} M_m^i(\theta) = M_m^i(\theta_{pr}) = constant \\ M_m^e(\theta) = M_m^e(\theta_{pr}) = constant \end{cases} \tag{7.5}$$

Two diagnostic signals are typically defined as:

$$S_\Psi(\omega) = \sqrt{\cosh\theta_{pr} - \cos\omega}\,\Psi_{pr}(\omega)$$

$$S_B(\omega) = \frac{1}{2}\frac{\sinh\theta_{pr}}{\sqrt{\cosh\theta_{pr} - \cos\omega}}\Psi_{pr}(\omega) - \frac{2\pi R_0^2 \sinh\theta_{pr}}{(\cosh\theta_{pr} - \cos\omega)^{\frac{3}{2}}} B_{\mathrm{pr}}(\omega) \tag{7.6}$$

A Fourier analysis of these signals up to a maximum order $m_{\max}$ yields the harmonic coefficients $(S_{\Psi,m}, S_{B,m})$, from which the internal and external moments $(M_m^{\mathrm{i}}, M_m^{\mathrm{e}})$ can be determined through linear inversion:

$$\{S_\Psi(\omega), S_B(\omega)\} \overset{\text{Fourier up to } m_{\max}}{\rightarrow} \{S_{\Psi,m}, S_{B,m}\} \overset{\text{linear inversion}}{\rightarrow} \{M_m^{\mathrm{i}}, M_m^{\mathrm{e}}\} \tag{7.7}$$

This reconstruction is well-conditioned only if the sensors are located along a surface of constant θ — that is, an iso-ω curve — which ensures orthogonality of the harmonic components and prevents spurious coupling among multipoles. These lines should not intersect regions carrying active currents (such as poloidal field or central solenoid coils), since such intersections would mix the plasma-generated field with external contributions and distort the multipolar spectrum.

Analysis in [74] demonstrated that the equilibrium magnetic field can be accurately reconstructed by including moments up to order $m = 3$. Higher-order harmonics contain negligible information for typical aspect ratios and are generally dominated by experimental uncertainty.

Therefore, the number of measurable quantities (and hence the number of required sensors) is directly related to the number of moments retained in the expansion.

Determining both the internal and external moments up to $m_{\max}$ requires solving for $2(m_{\max} + 1)$ unknowns — one pair of coefficients for each harmonic order. For $m_{\max} = 3$, this corresponds to eight coefficients in total. Thus:

- at least eight independent measurements (flux loops and pick-up coils combined) are required to identify all coefficients;
- in practice, an overdetermined system is preferred, with a larger number of sensors used to estimate the coefficients by least squares, improving robustness against noise.

For instance, in the JET application described by [74], a set of 32 sensors (14 flux loops and 18 pick-up coils) allowed accurate determination of all moments up to $m = 3$.

Under these theoretical premises, it can be concluded that even a reduced number of magnetic sensors could, in principle, provide reliable equilibrium reconstructions, provided that their locations are consistent with the multipolar structure of the magnetic field. In the present TRUST configuration, however, the sensors are mounted on the vacuum vessel according to geometrical and mechanical constraints rather than to an optimized multipolar distribution. As a consequence, their positions do not strictly follow iso-ω trajectories, and some degradation of the reconstruction accuracy is therefore expected, especially in the presence of measurement noise and the relatively large distance from the plasma. Future developments will include a dedicated optimization study of sensor placement order to identify the minimum number and optimal arrangement of probes required for accurate equilibrium reconstruction.

4. Plasma boundary reconstruction with EFIT (K-mode)

   The synthetic magnetic signals generated by PECAN are supplied to EFIT operating in K-mode, which reconstructs the plasma equilibrium using only the information provided by the diagnostic set. For each configuration, reconstructions were performed using synthetic data sets with Gaussian noise levels between 0% and 5%, simulating increasing measurement uncertainty. This enables quantifying how reconstruction accuracy degrades as a function of both diagnostic density and noise level.

This workflow highlights the core objective of the present study: to evaluate the capability of minimal and extended magnetic diagnostic layouts to reconstruct the plasma boundary across multiple magnetic topologies.

It is important to emphasize that the study does not pursue a strict cross-code validation between PECAN (and MAXFEA) and EFIT; hence, no constraint was imposed to enforce identical CS and PF current distributions between the solvers. EFIT was deliberately allowed to determine its own current adjustments according to its internal formulation, thereby shifting the focus from code benchmarking to workflow validation and diagnostic layout assessment.

Through this methodology, PECAN acts as a controlled environment for generating diagnostic-like signals, while EFIT provides the reconstruction and analysis framework. The resulting PECAN–EFIT workflow enables:

- a systematic evaluation of diagnostic performance,
- a quantification of reconstruction accuracy under varying noise levels and magnetic configurations, and
- the identification of optimal sensor arrangements for future design iterations.

This coupling strategy represents the first practical implementation of the integrated PECAN–EFIT workflow, establishing a robust and reproducible framework for equilibrium reconstruction studies in tokamak-scale experiments.

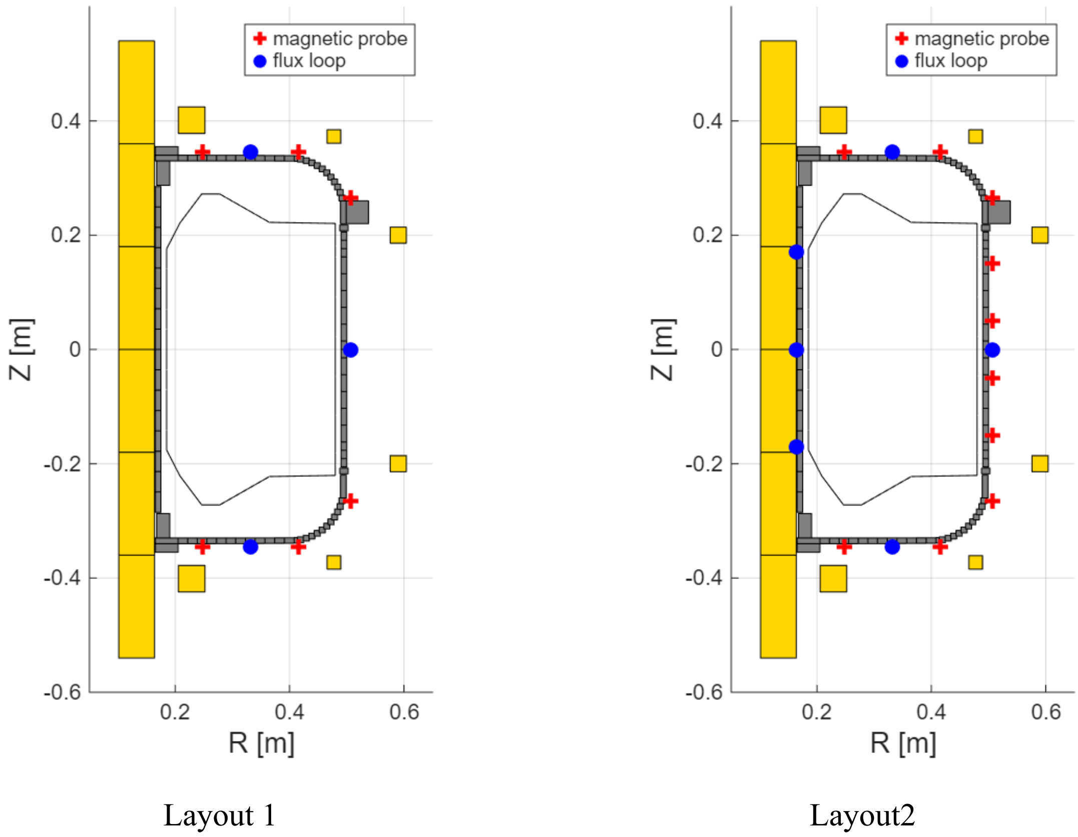

Figure 92: proposals of magnetic diagnostics layout used for TRUST.

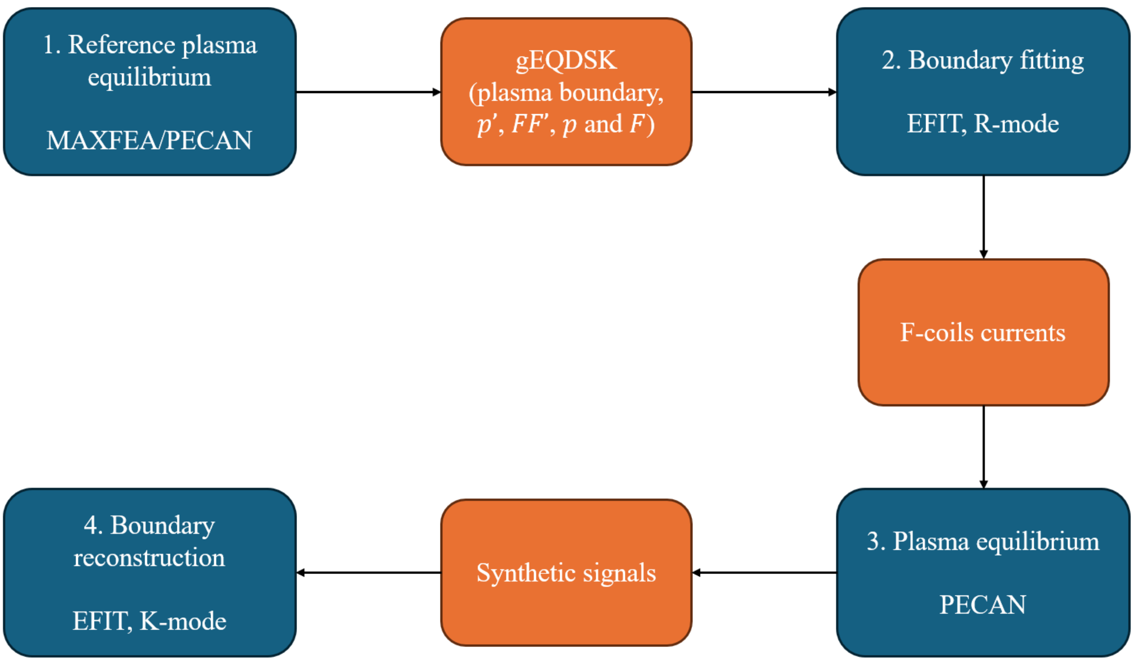

Figure 93: PECAN-EFIT coupling scheme.

7.2 Results

The results obtained from the PECAN–EFIT workflow are presented in this section, with the aim of quantitatively evaluating the performance of the proposed magnetic diagnostic layouts in reconstructing the plasma boundary under different signal configurations and noise conditions. Building on the preliminary feasibility analysis, a systematic set of reconstruction tests was performed to assess how the accuracy and stability of EFIT reconstructions depend on the number and arrangement of active sensors, as well as on the level of synthetic noise applied to their measurements.

7.2.1 Diagnostic Reduction Tests

In the first part of the analysis, progressive reductions of the diagnostic set were investigated for layout 1, in order to determine the minimum number of active sensors required for a successful equilibrium reconstruction. Two reduction strategies were explored:

1. Single flux loop at the midplane.

The uppermost and lowermost flux loops were deactivated by setting their fitting weights to zero, leaving only the midplane loop active. Magnetic probes were then progressively enabled in subsets of 2, 4, and finally all 6 probes.

2. Two flux loops (upper and lower) without the midplane loop.

In this case, the midplane loop was disabled, and the upper and lower loops remained active. Again, subsets of 2, 4, and 6 probes were tested in combination.

Finally, the full diagnostic configuration (three flux loops and six magnetic probes) was analysed as a reference case. The results show that, in all reduced configurations, EFIT was unable to reconstruct the plasma boundary in satisfactory agreement with the reference equilibrium: either the solver failed to converge to a physically meaningful solution, or the reconstructed Last-Closed Flux Surface (LCFS) exhibited large geometric distortions. Conversely, when the full diagnostic set was employed, EFIT successfully reproduced both the plasma boundary and the magnetic-axis position within acceptable accuracy limits. This analysis therefore established that a complete set of three flux loops and six magnetic probes is the minimal requirement for achieving a stable and accurate equilibrium reconstruction for layout 1.

7.2.2 Quantitative Error Metrics

To provide a consistent and reproducible evaluation of the reconstruction performance, two complementary quantitative indicators were introduced.

(a) LCFS Reconstruction Error

The geometric discrepancy between the reconstructed and reference plasma boundaries was quantified using both the maximum radial deviation (E_{LCFS}^{max})and the root-mean-square error (RMSE), defined respectively as

$$\varepsilon_{LCFS,i} = \sqrt{\left[\left(R_{EFIT,i} - R_{ref,i}\right)^2 + \left(Z_{EFIT,i} - Z_{ref,i}\right)^2\right]} \tag{7.8}$$

$$E_{LCFS}^{max} = \max\left(\varepsilon_{LCFS,i}\right) \tag{7.9}$$

$$RMSE_{LCFS} = \sqrt{\left[\left(\frac{1}{N}\right) \Sigma_{\mathrm{i}} \left(\varepsilon_{LCFS,i}\right)^2\right]} \tag{7.10}$$

These quantities directly express the deviation of the reconstructed LCFS from the reference PECAN boundary in physical units (meters).

(b) Ψ-Mapping Error

To assess the overall consistency of the reconstructed poloidal flux, the Ψ-mapping error was computed as the normalized difference between EFIT and PECAN flux maps:

$$\varepsilon_{\Psi,j} = \frac{|\Psi_{EFIT} - \Psi_{PECAN}|}{\Psi_{axis}^{PECAN}} \tag{7.11}$$

and the corresponding max value and RMSE were evaluated inside the vacuum vessel region as

$$E_{\Psi}^{max} = \max\left(\varepsilon_{\Psi,j}\right) \tag{7.12}$$

$$RMSE_{\Psi} = \sqrt{\left[\left(\frac{1}{M}\right) \Sigma_{\mathrm{j}} \left(\varepsilon_{\Psi,j}\right)^2\right]} \tag{7.13}$$

This metric captures the global reconstruction accuracy and complements the geometric error of the LCFS. Among these indicators, the LCFS reconstruction accuracy is considered the primary performance criterion, as it determines the reliability of the diagnostic layout for plasma shape control. The Ψ-mapping error is used as a secondary metric, providing additional insight into the global magnetic-field consistency across the plasma domain.

7.2.3 Noise Sensitivity Scans

After establishing the baseline accuracy under ideal conditions, parametric noise scans were performed to evaluate the sensitivity of the reconstruction to measurement uncertainty. Gaussian perturbations with standard deviations between 0 % and 5 % were added to the synthetic signals generated by PECAN, and EFIT reconstructions were repeated for each noise level and layout configuration.

The resulting trends show a clear correlation between the boundary reconstruction error and the magnetic-axis displacement as functions of the noise amplitude applied to the magnetic probes. As expected, increasing noise levels degrade the reconstruction quality, while configurations with a larger number of active sensors consistently yield more accurate and stable results.

Overall, these results demonstrate that:

- A minimal configuration (three flux loops and six probes) is sufficient for successful boundary reconstruction under low-noise conditions.
- The inclusion of additional sensors in the extended layout improves robustness against measurement noise.
- The PECAN–EFIT workflow provides a consistent framework for quantifying the trade-off between diagnostic density and reconstruction fidelity.

This analysis thus establishes a validated baseline for the TRUST magnetic-diagnostic system, supporting future optimization studies aimed at refining the sensor layout and improving reconstruction performance under experimental operating conditions.

The following paragraphs present the results of the equilibrium reconstructions obtained for the selected operating scenarios of the TRUST tokamak. For each configuration — including the limiter case immediately after plasma breakdown, the downward single-null (DSN) configuration at the Start-Of-Flat-top (SOF) and End-Of-Flat-top (EOF) instants, as well as the upward single-null (USN) and double-null (DN) equilibria at EOF — a series of reconstructions was carried out by progressively varying the level of synthetic noise applied to the magnetic diagnostic signals. This parametric analysis was aimed at quantifying the impact of measurement uncertainty on the accuracy and stability of the EFIT reconstructions.

Limiter configuration after breakdown

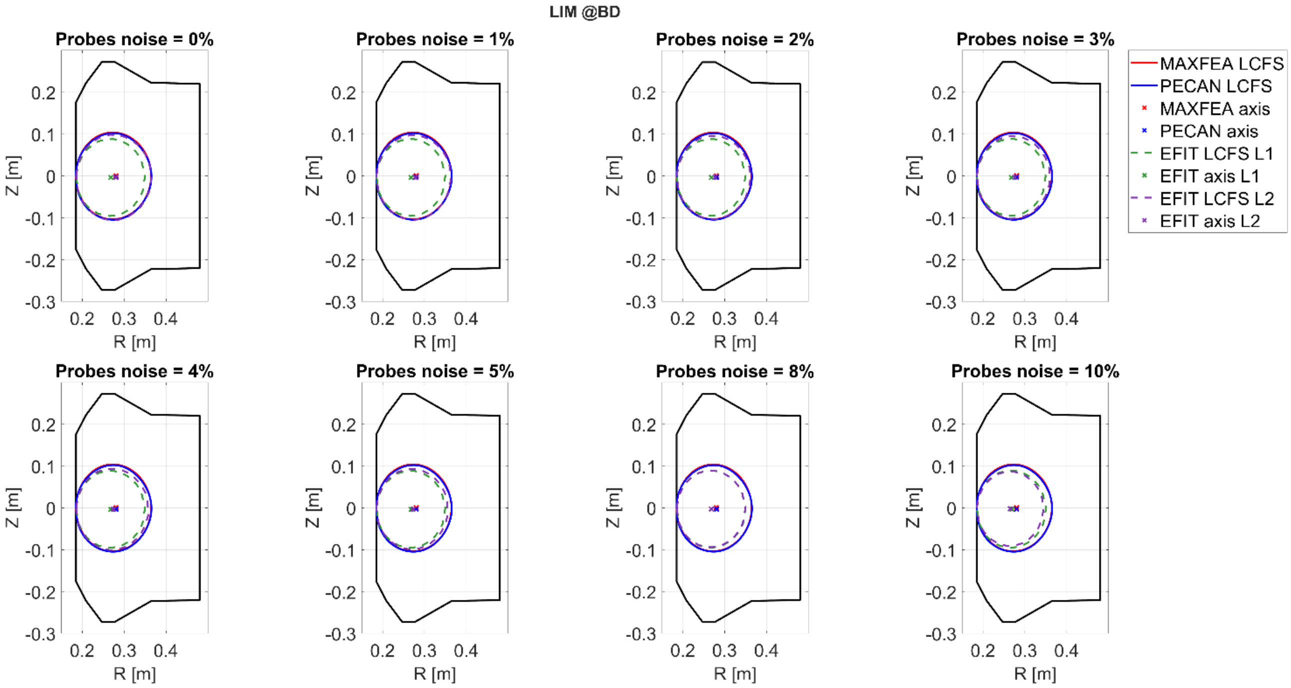

Figure 94: EFIT reconstructions of the plasma boundary compared with the MAXFEA and PECAN last-closed flux surfaces (LCFS) for the limiter configuration after the breakdown phase. Results are shown for increasing levels of synthetic noise applied to the magnetic measurements.

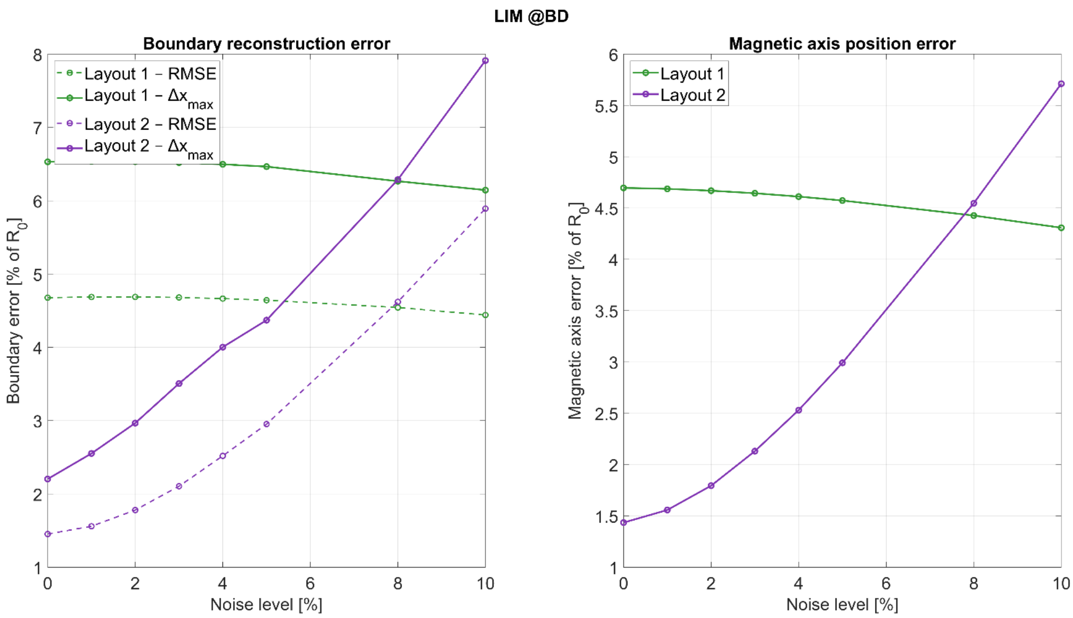

Figure 95: Reconstruction errors on the plasma boundary and magnetic axis obtained from EFIT, evaluated with respect to the reference MAXFEA equilibrium for the limiter configuration after the breakdown phase. The boundary errors are expressed as the root-mean-square (RMSE) and maximum distance between the reconstructed and reference last-closed flux surfaces (LCFS), while the magnetic-axis error corresponds to the displacement of the reconstructed magnetic axis. The errors are normalized respect to the machine radius and reported as a function of the synthetic noise level applied to the magnetic diagnostics.

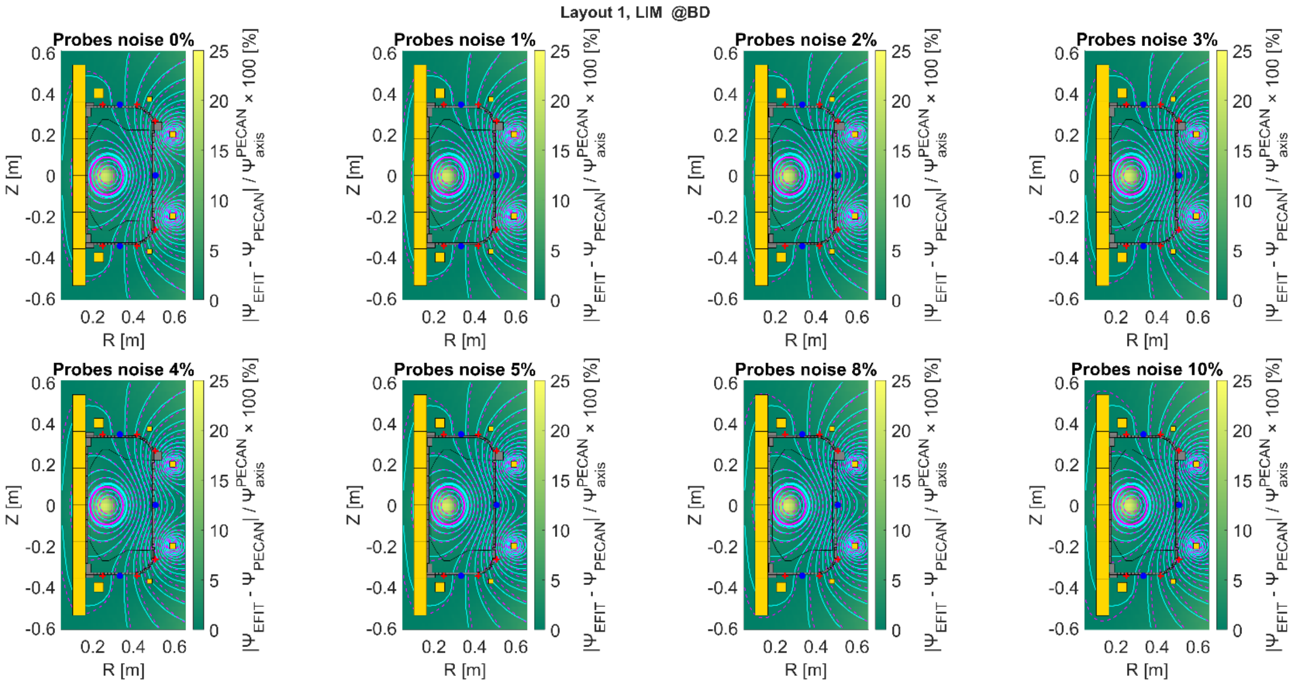

Figure 96: Comparison between EFIT and PECAN poloidal flux maps for increasing levels of synthetic noise applied to the magnetic measurements for the limiter configuration after the breakdown phase (Layout 1). The PECAN reference flux surfaces are shown in cyan, while the EFIT reconstructions are plotted in magenta.

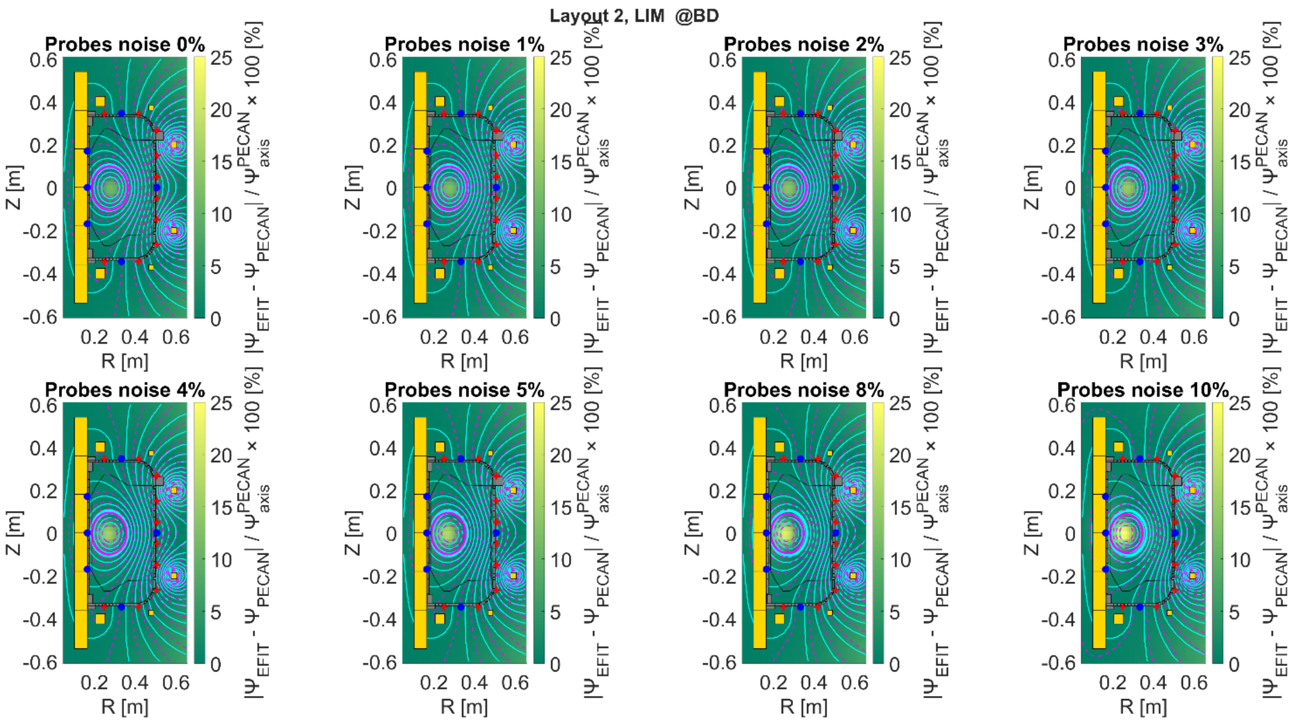

Figure 97: Comparison between EFIT and PECAN poloidal flux maps for increasing levels of synthetic noise applied to the magnetic measurements for the limiter configuration after the breakdown phase (Layout 2). The PECAN reference flux surfaces are shown in cyan, while the EFIT reconstructions are plotted in magenta.

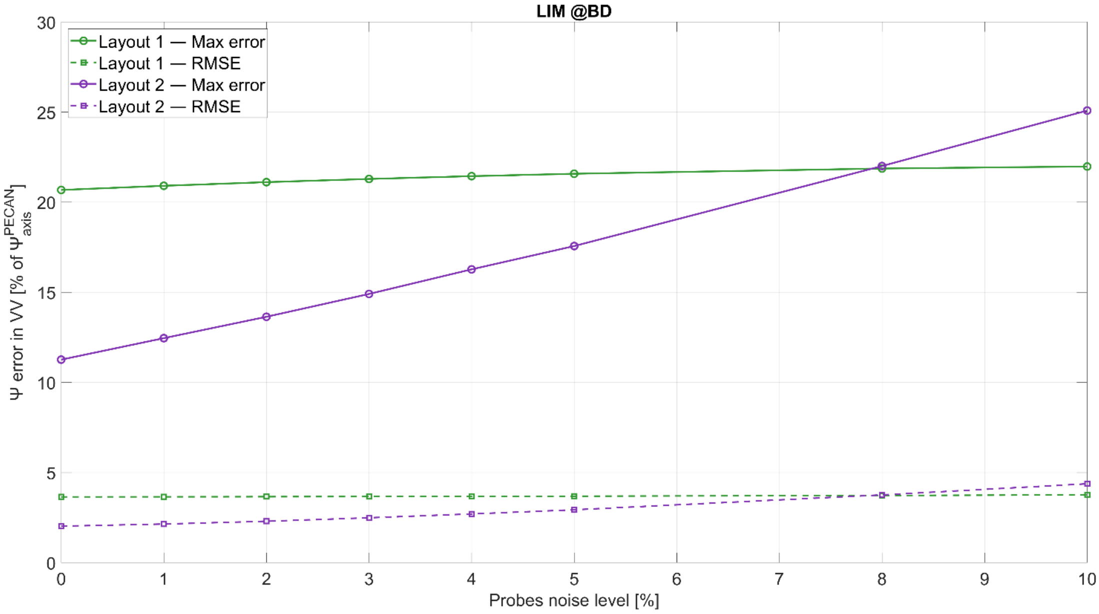

Figure 98: Reconstruction errors on the poloidal flux inside the VV region obtained from EFIT, evaluated with respect to the reference PECAN equilibrium for the limiter configuration after the breakdown phase and normalized respect the PECAN flux on the magnetic axis.

Downward single-null at SOF

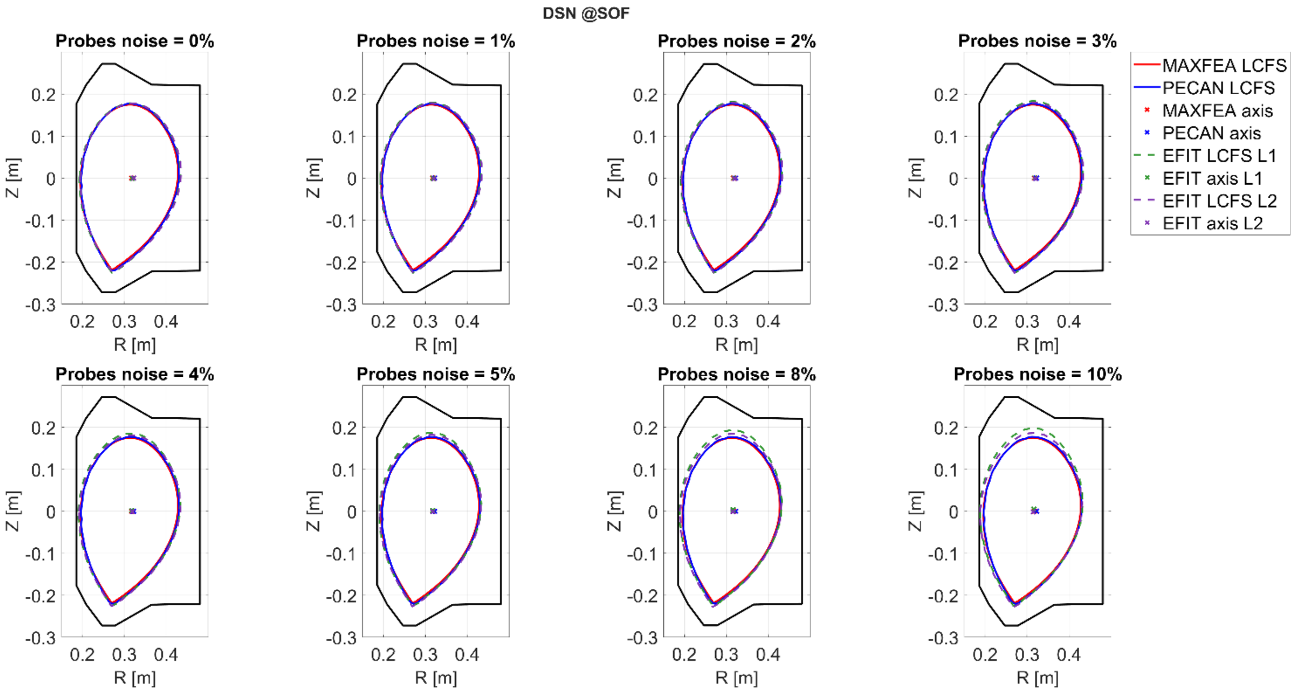

Figure 99: EFIT reconstructions of the plasma boundary compared with the MAXFEA and PECAN last-closed flux surfaces (LCFS) for the downward single-null configuration at SOF. Results are shown for increasing levels of synthetic noise applied to the magnetic measurements.

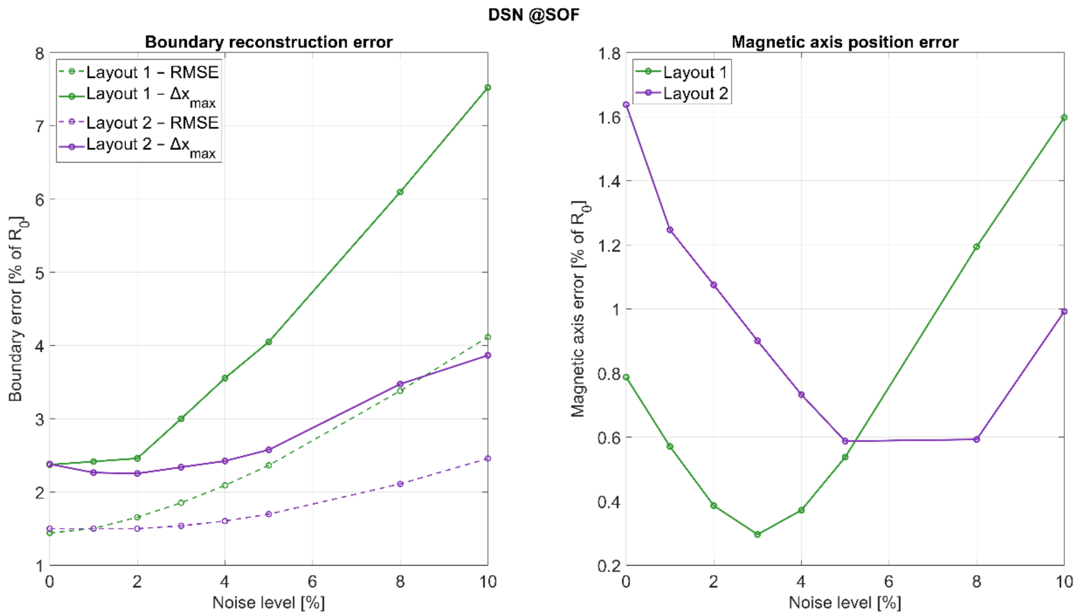

Figure 100: Reconstruction errors on the plasma boundary and magnetic axis obtained from EFIT, evaluated with respect to the reference MAXFEA equilibrium for the downward single-null configuration at SOF. The boundary errors are expressed as the root-mean-square (RMSE) and maximum distance between the reconstructed and reference last-closed flux surfaces (LCFS), while the magnetic-axis error corresponds to the displacement of the reconstructed magnetic axis. The errors are normalized respect to the machine radius and reported as a function of the synthetic noise level applied to the magnetic diagnostics.

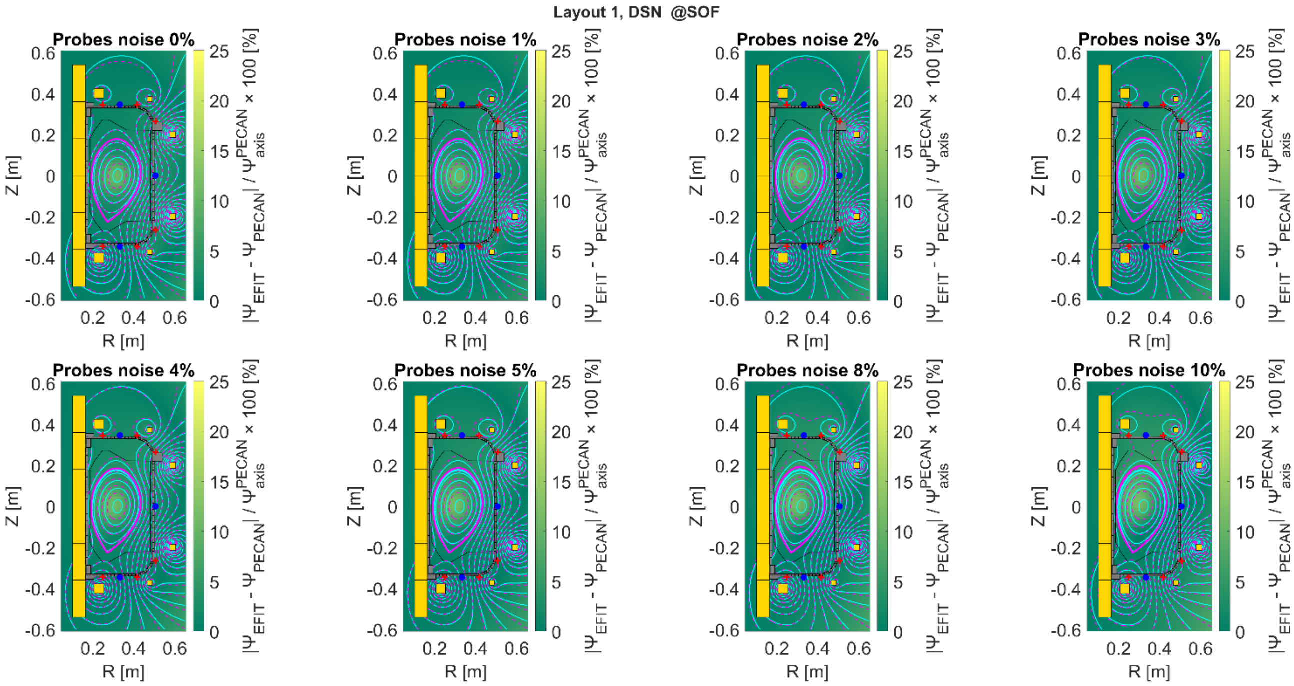

Figure 101: Comparison between EFIT and PECAN poloidal flux maps for increasing levels of synthetic noise applied to the magnetic measurements for the downward single-null configuration at SOF (Layout 1). The PECAN reference flux surfaces are shown in cyan, while the EFIT reconstructions are plotted in magenta.

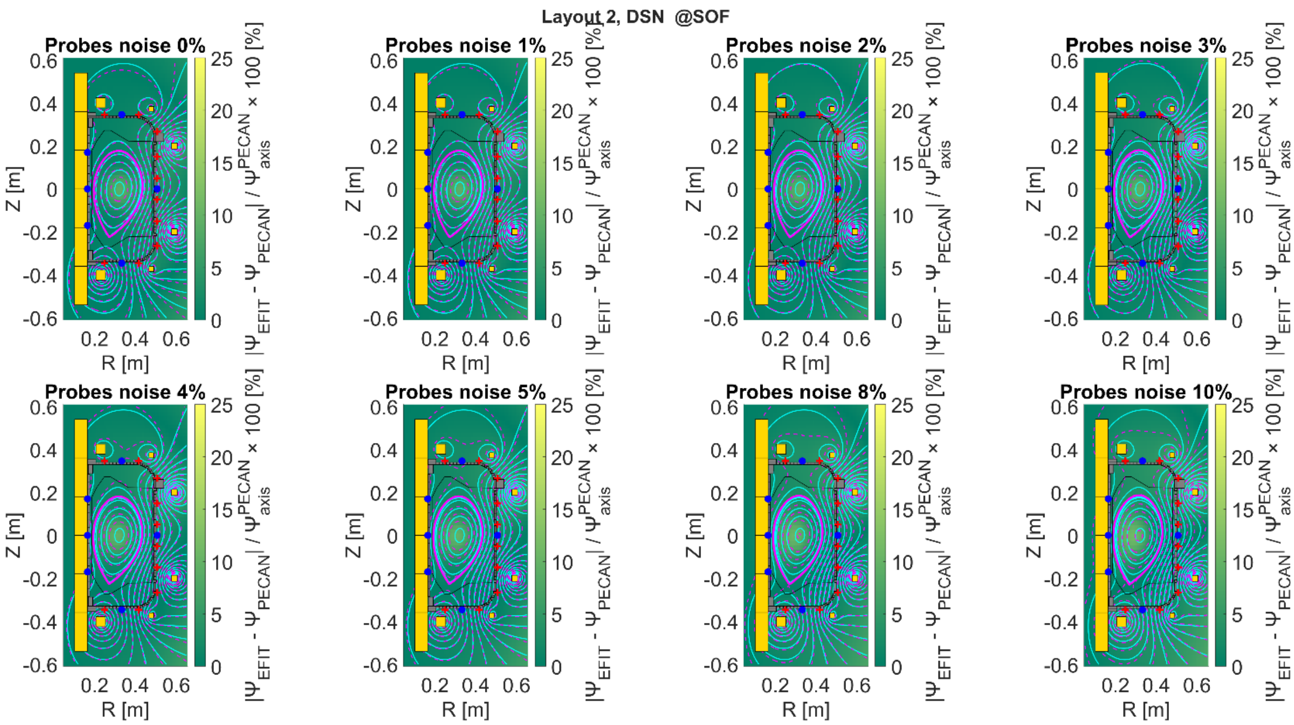

Figure 102: Comparison between EFIT and PECAN poloidal flux maps for increasing levels of synthetic noise applied to the magnetic measurements for the downward single-null configuration at SOF (Layout 2). The PECAN reference flux surfaces are shown in cyan, while the EFIT reconstructions are plotted in magenta.

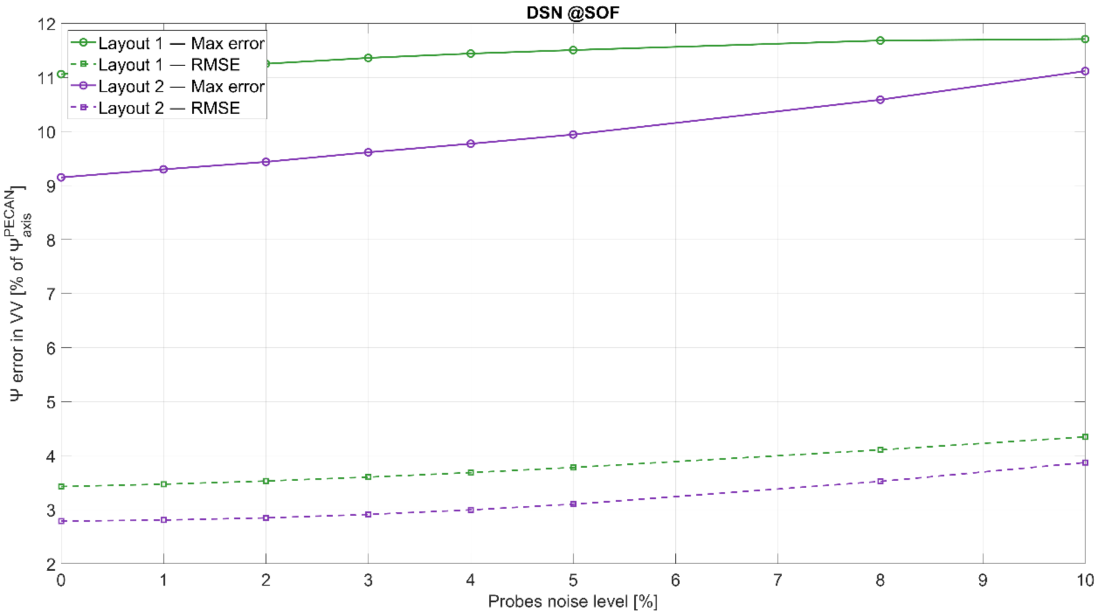

Figure 103: Reconstruction errors on the poloidal flux inside the VV region obtained from EFIT, evaluated with respect to the reference PECAN equilibrium for the downward single-null configuration at SOF and normalized respect the PECAN flux on the magnetic axis.

Downward single-null at EOF

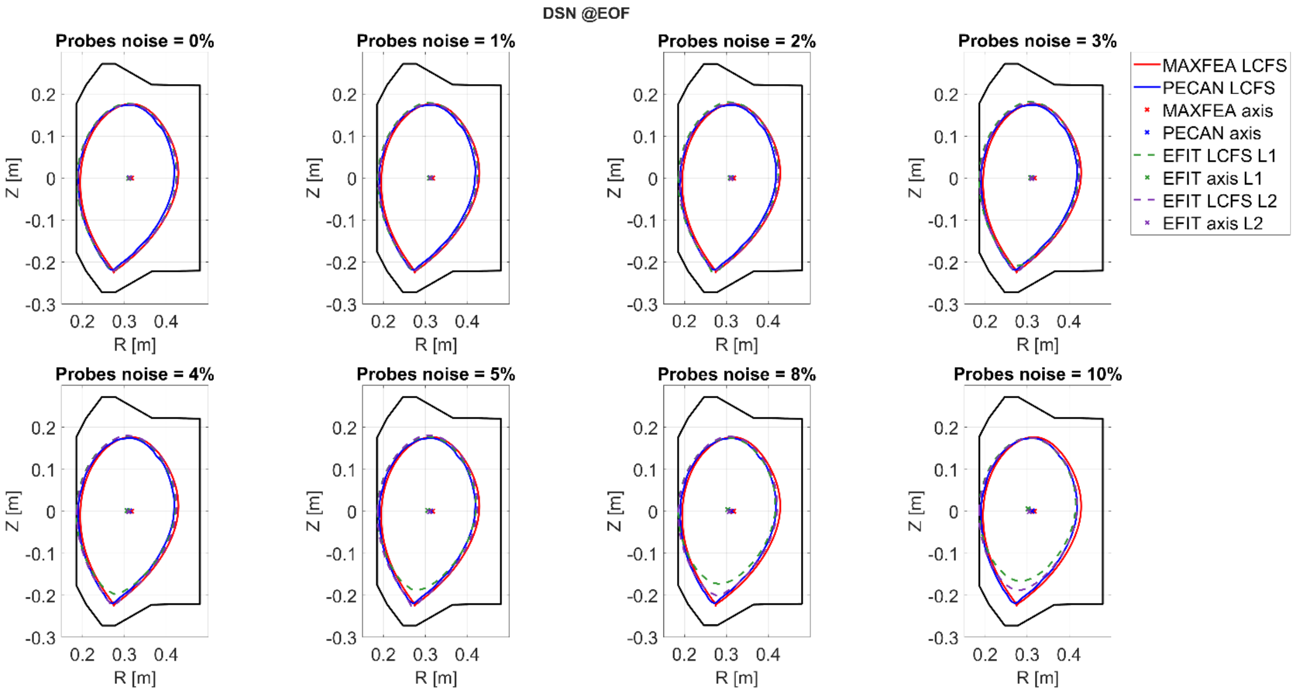

Figure 104: EFIT reconstructions of the plasma boundary compared with the MAXFEA and PECAN last-closed flux surfaces (LCFS) for the downward single-null configuration at EOF. Results are shown for increasing levels of synthetic noise applied to the magnetic measurements.

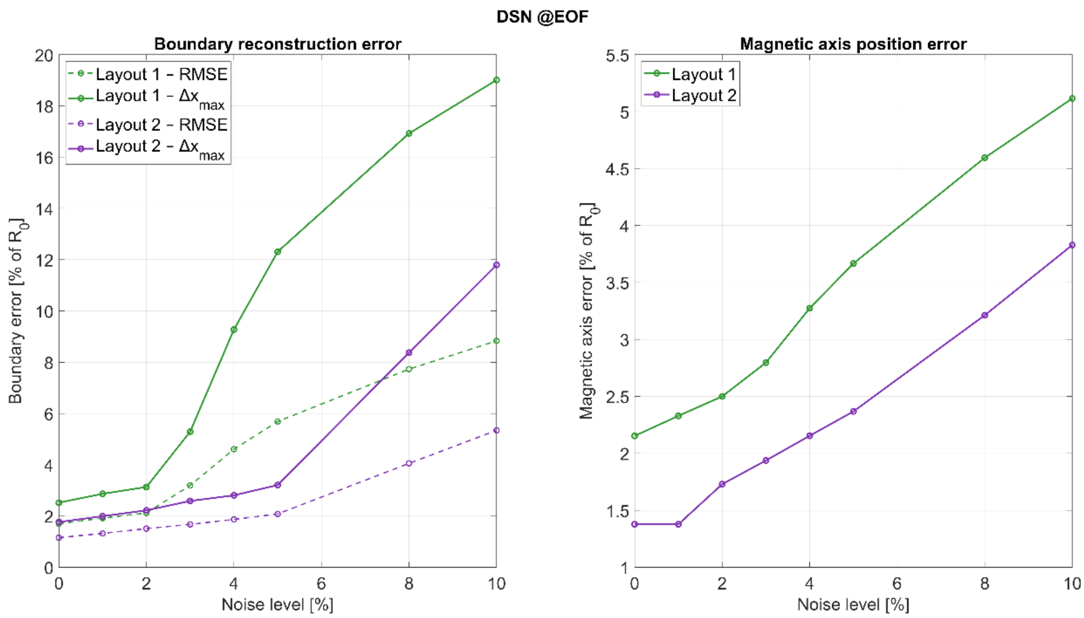

Figure 105: Reconstruction errors on the plasma boundary and magnetic axis obtained from EFIT, evaluated with respect to the reference MAXFEA equilibrium for the downward single-null configuration at EOF. The boundary errors are expressed as the root-mean-square (RMSE) and maximum distance between the reconstructed and reference last-closed flux surfaces (LCFS), while the magnetic-axis error corresponds to the displacement of the reconstructed magnetic axis. The errors are normalized respect to the machine radius and reported as a function of the synthetic noise level applied to the magnetic diagnostics.

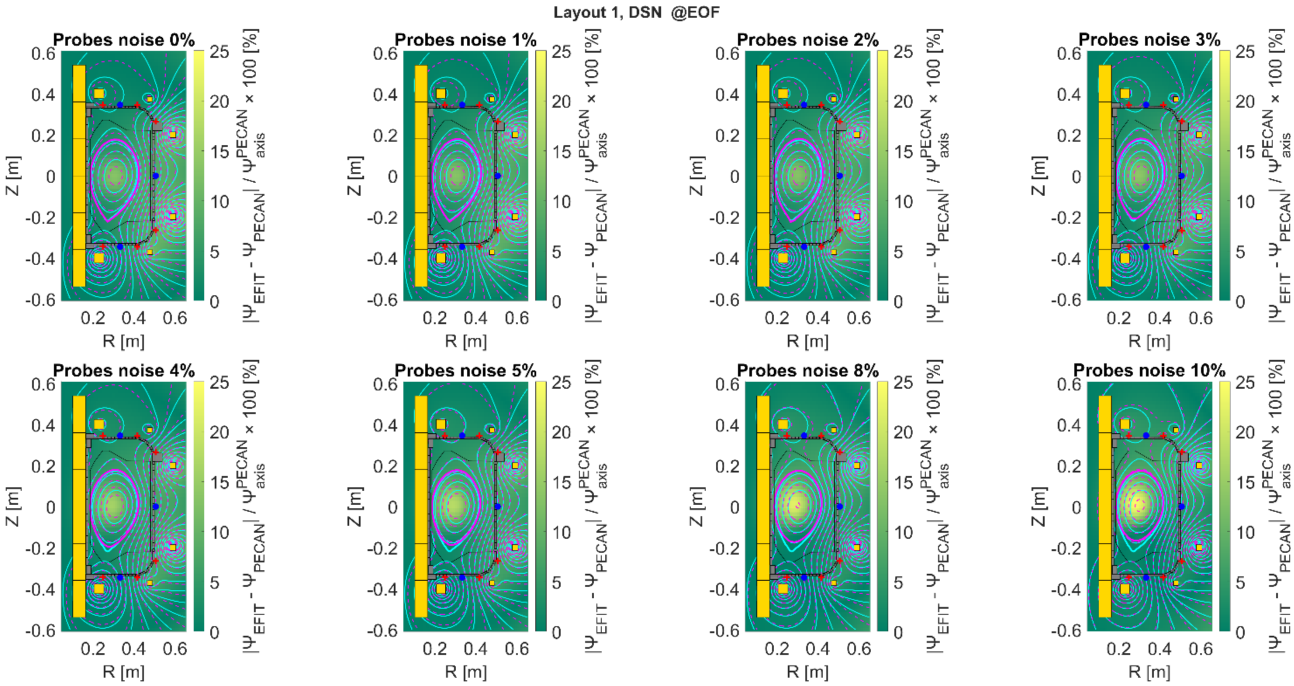

Figure 106: Comparison between EFIT and PECAN poloidal flux maps for increasing levels of synthetic noise applied to the magnetic measurements for the downward single-null configuration at EOF (Layout 1). The PECAN reference flux surfaces are shown in cyan, while the EFIT reconstructions are plotted in magenta.

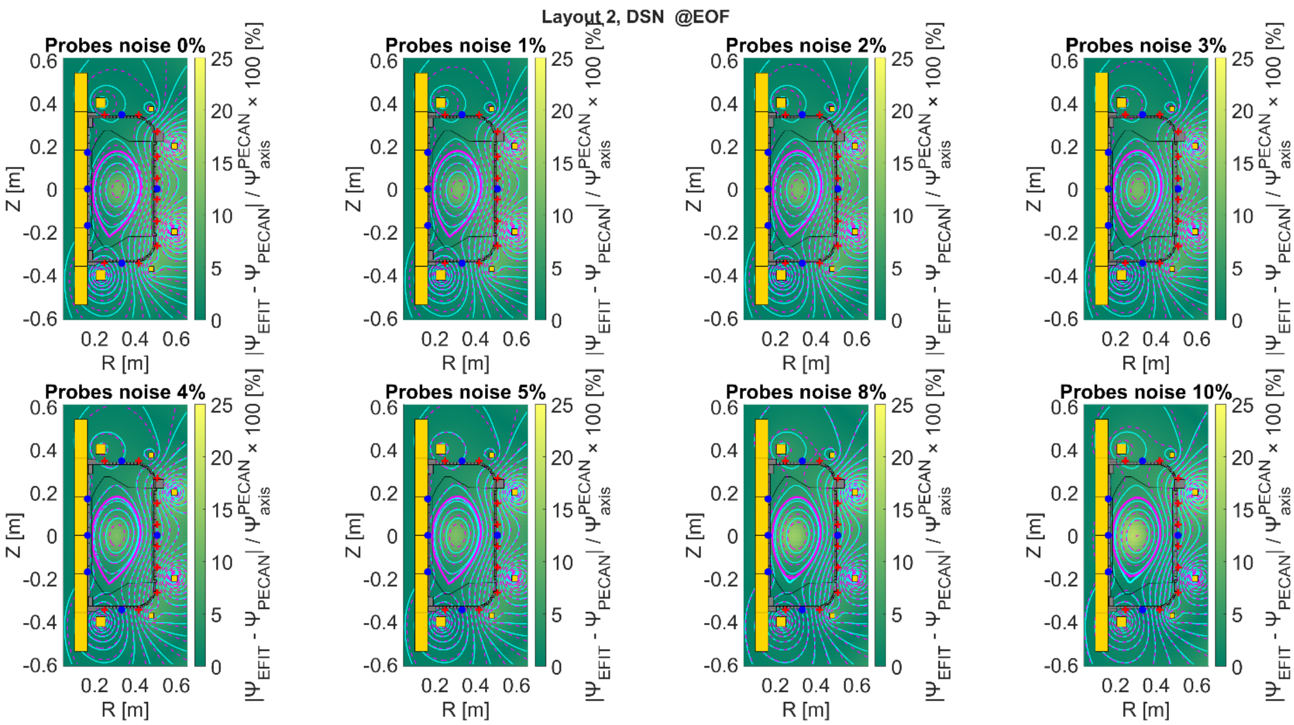

Figure 107: Comparison between EFIT and PECAN poloidal flux maps for increasing levels of synthetic noise applied to the magnetic measurements for the downward single-null configuration at EOF (Layout 2). The PECAN reference flux surfaces are shown in cyan, while the EFIT reconstructions are plotted in magenta.

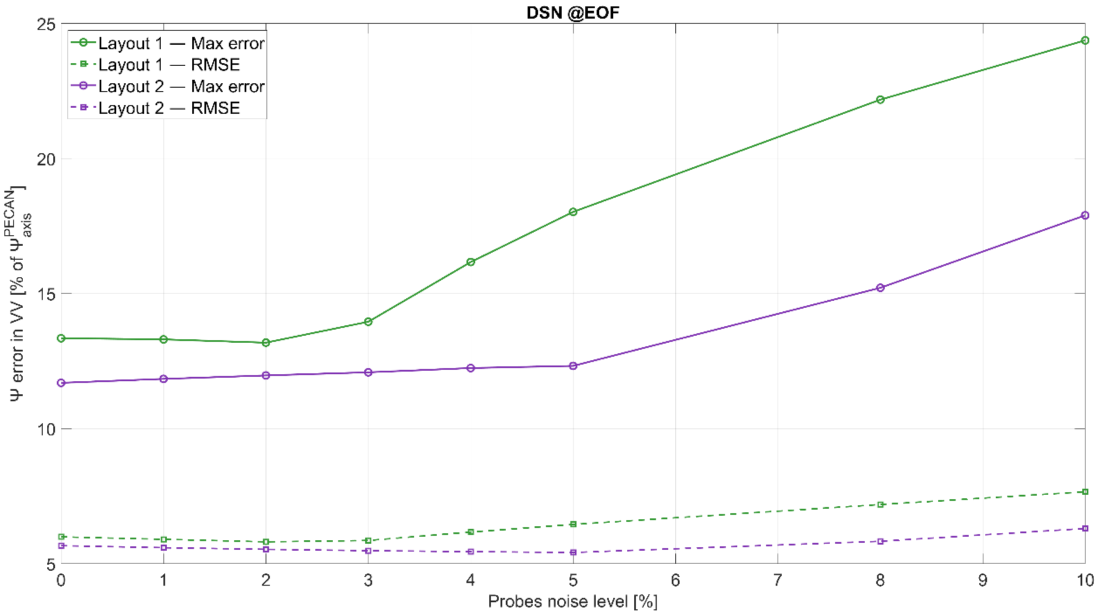

Figure 108: Reconstruction errors on the poloidal flux inside the VV region obtained from EFIT, evaluated with respect to the reference PECAN equilibrium for the downward single-null configuration at EOF and normalized respect the PECAN flux on the magnetic axis.

Upward single-null at EOF

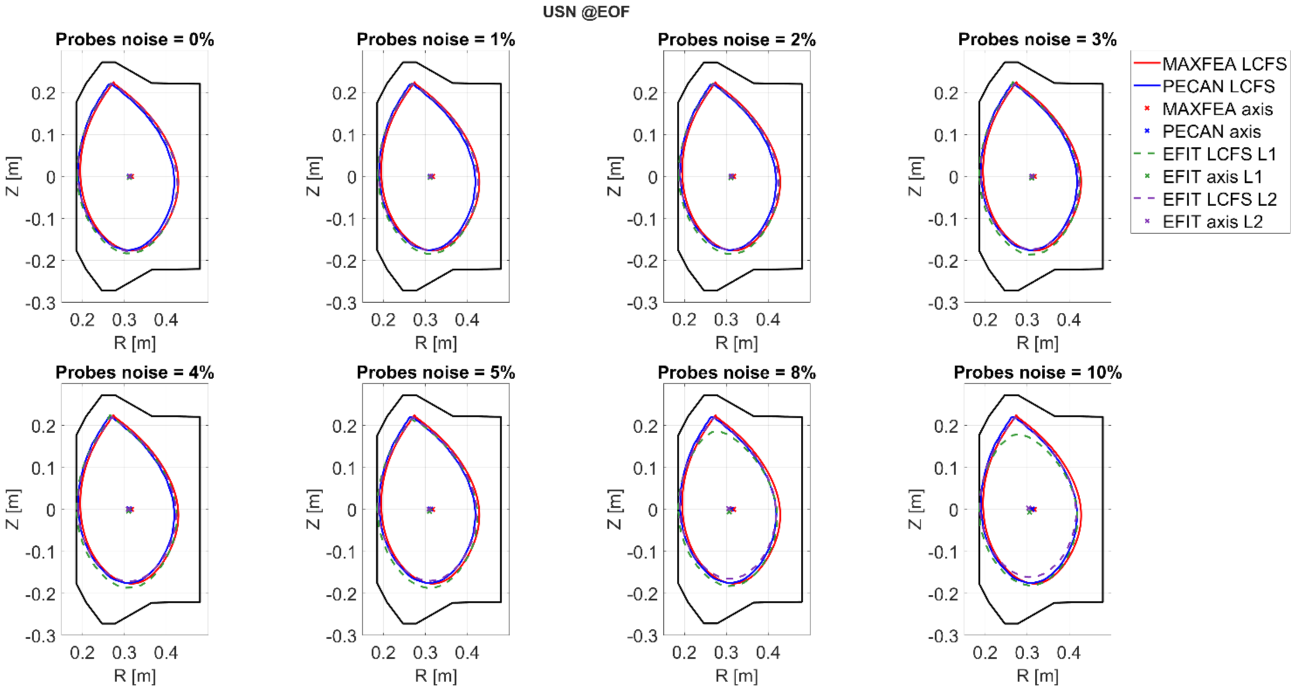

Figure 109: EFIT reconstructions of the plasma boundary compared with the MAXFEA and PECAN last-closed flux surfaces (LCFS) for the upward single-null configuration at EOF. Results are shown for increasing levels of synthetic noise applied to the magnetic measurements.

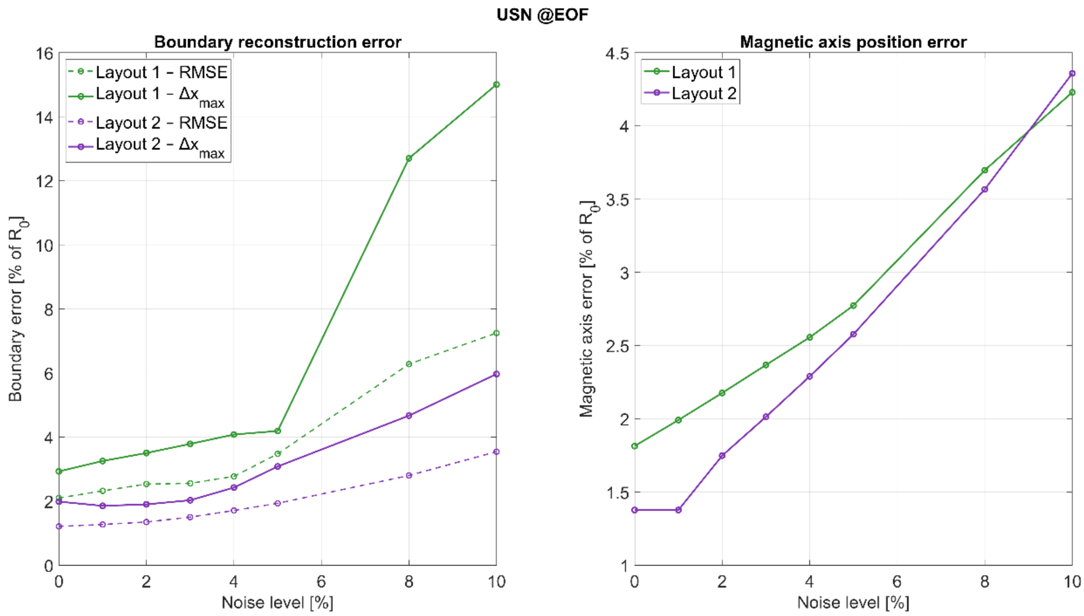

Figure 110: Reconstruction errors on the plasma boundary and magnetic axis obtained from EFIT, evaluated with respect to the reference MAXFEA equilibrium for the upward single-null configuration at EOF. The boundary errors are expressed as the root-mean-square (RMSE) and maximum distance between the reconstructed and reference last-closed flux surfaces (LCFS), while the magnetic-axis error corresponds to the displacement of the reconstructed magnetic axis. The errors are normalized respect to the machine radius and reported as a function of the synthetic noise level applied to the magnetic diagnostics.

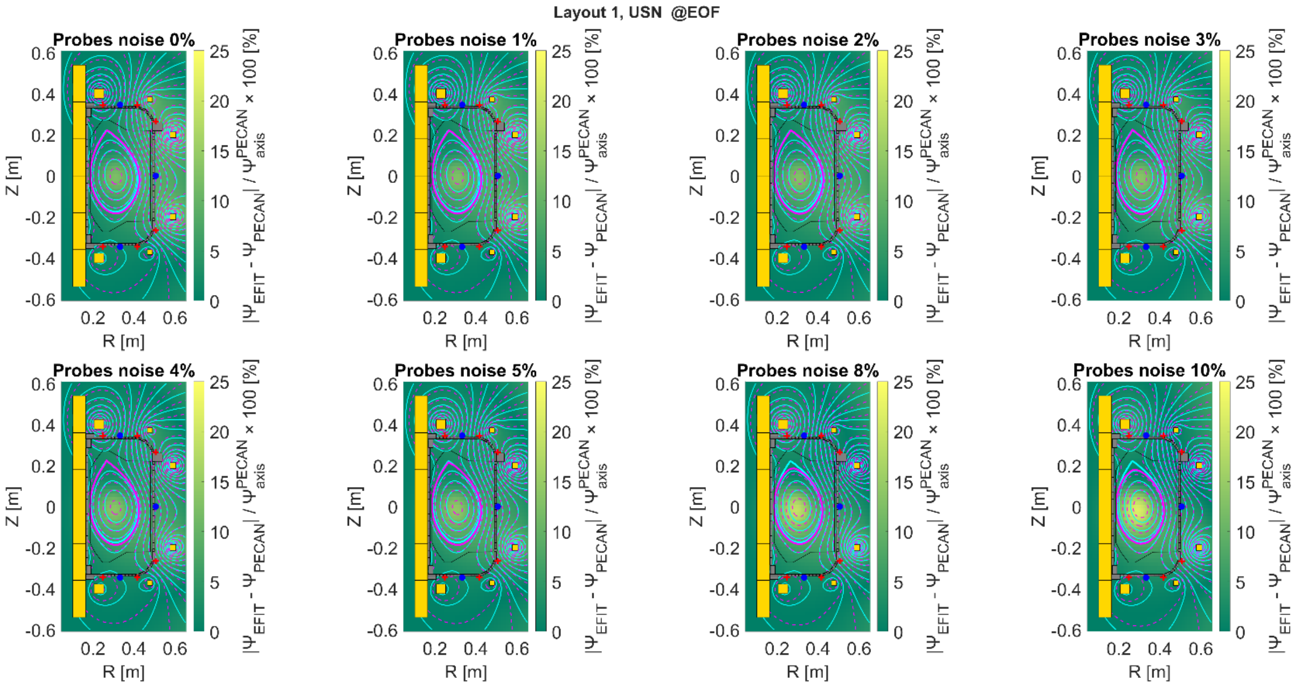

Figure 111: Comparison between EFIT and PECAN poloidal flux maps for increasing levels of synthetic noise applied to the magnetic measurements for the downward single-null configuration at EOF (Layout 1). The PECAN reference flux surfaces are shown in cyan, while the EFIT reconstructions are plotted in magenta.

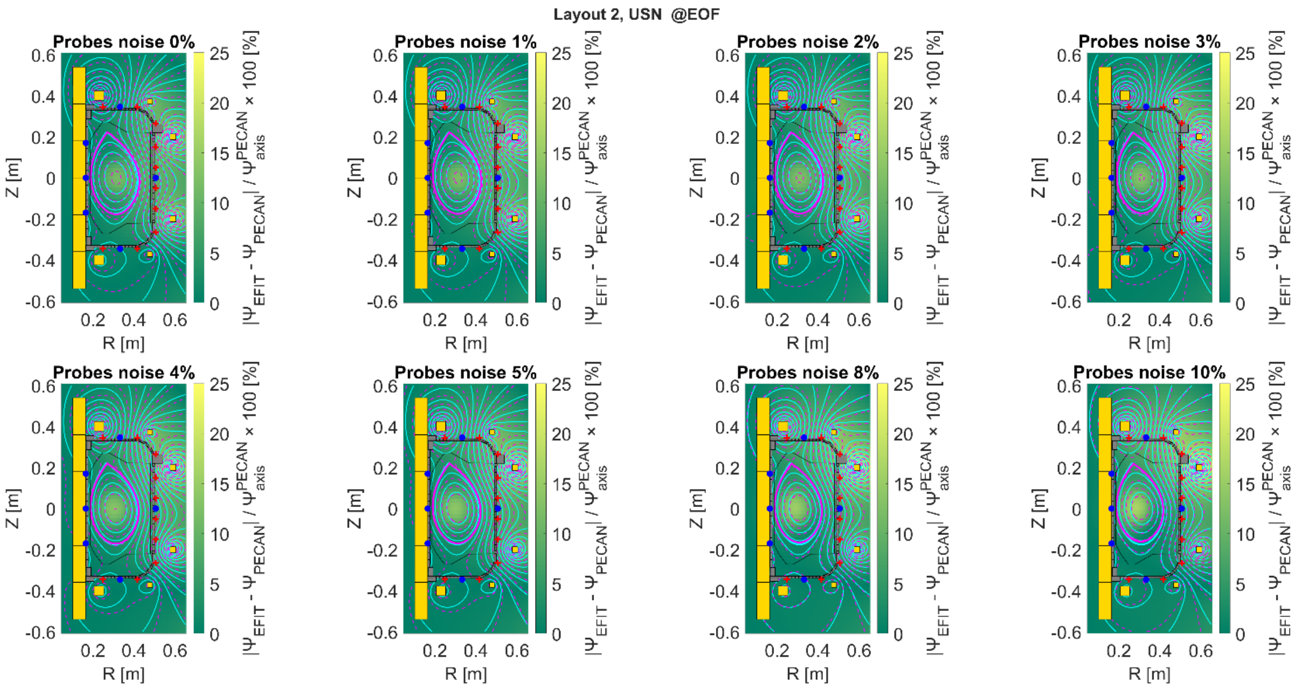

Figure 112: Comparison between EFIT and PECAN poloidal flux maps for increasing levels of synthetic noise applied to the magnetic measurements for the upward single-null configuration at EOF (Layout 2). The PECAN reference flux surfaces are shown in cyan, while the EFIT reconstructions are plotted in magenta.

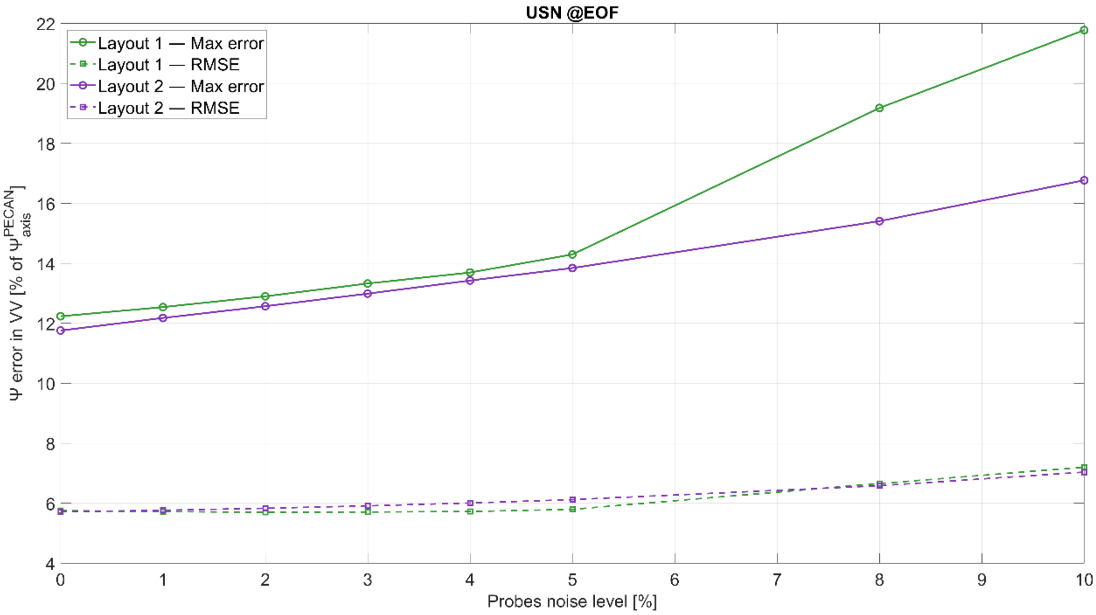

Figure 113: Reconstruction errors on the poloidal flux inside the VV region obtained from EFIT, evaluated with respect to the reference PECAN equilibrium for the upward single-null configuration at EOF and normalized respect the PECAN flux on the magnetic axis.

Double-null at EOF

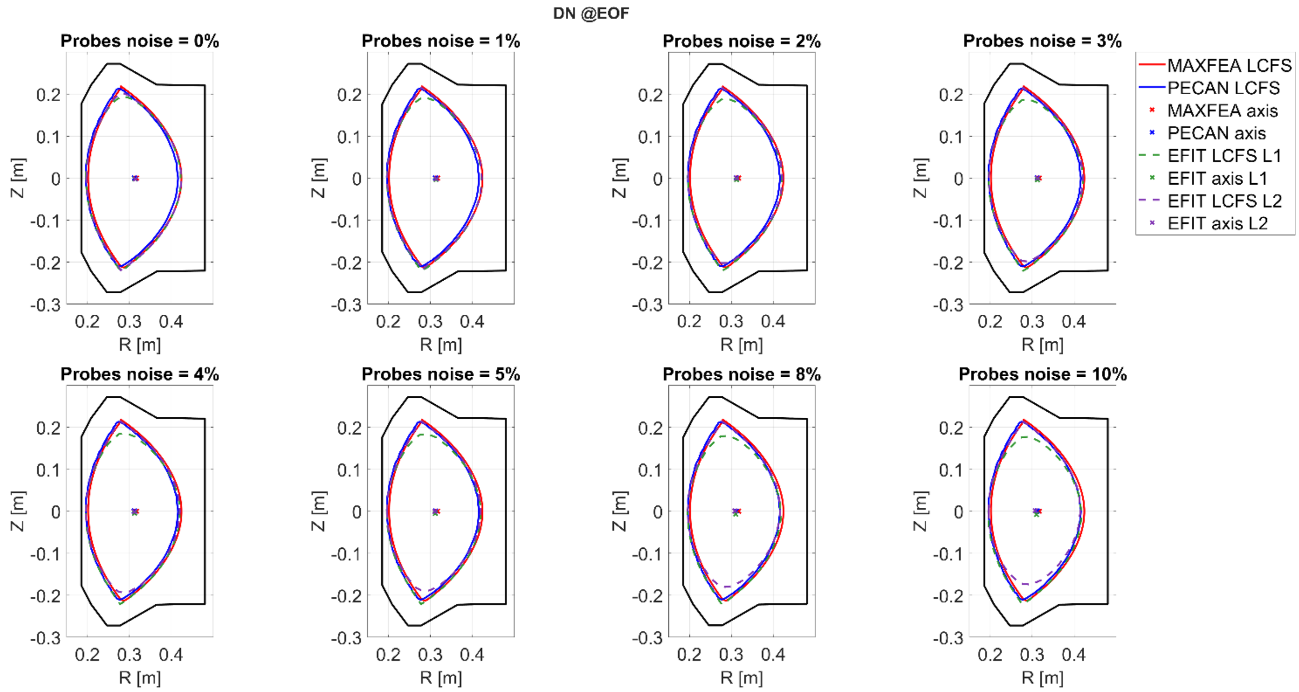

Figure 114: EFIT reconstructions of the plasma boundary compared with the MAXFEA and PECAN last-closed flux surfaces (LCFS) for the double-null configuration at EOF. Results are shown for increasing levels of synthetic noise applied to the magnetic measurements.

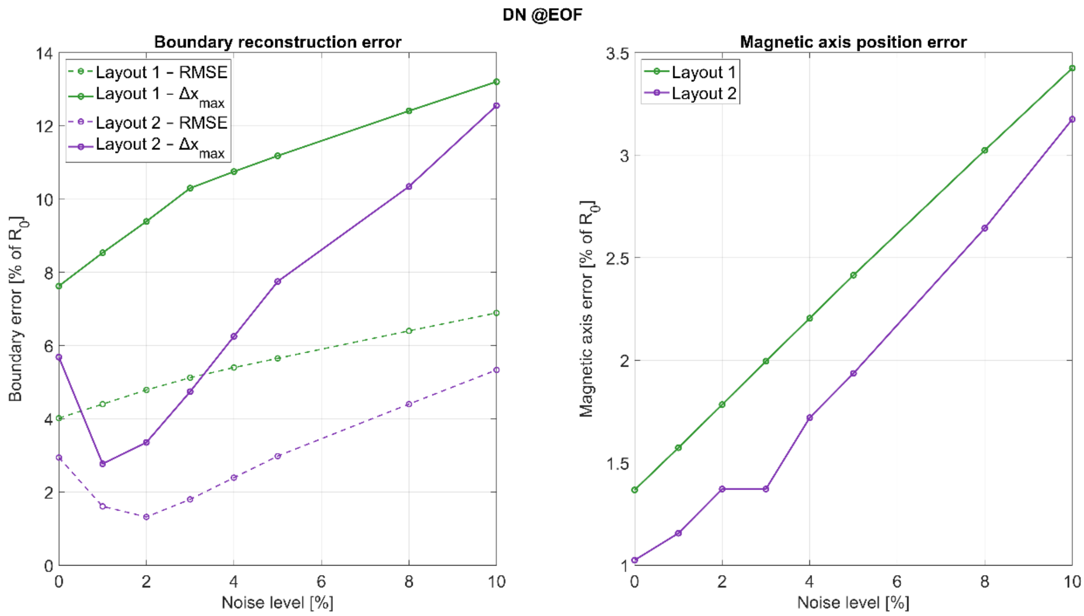

Figure 115: Reconstruction errors on the plasma boundary and magnetic axis obtained from EFIT, evaluated with respect to the reference MAXFEA equilibrium for the double-null configuration at EOF. The boundary errors are expressed as the root-mean-square (RMSE) and maximum distance between the reconstructed and reference last-closed flux surfaces (LCFS), while the magnetic-axis error corresponds to the displacement of the reconstructed magnetic axis. The errors are normalized respect to the machine radius and reported as a function of the synthetic noise level applied to the magnetic diagnostics.

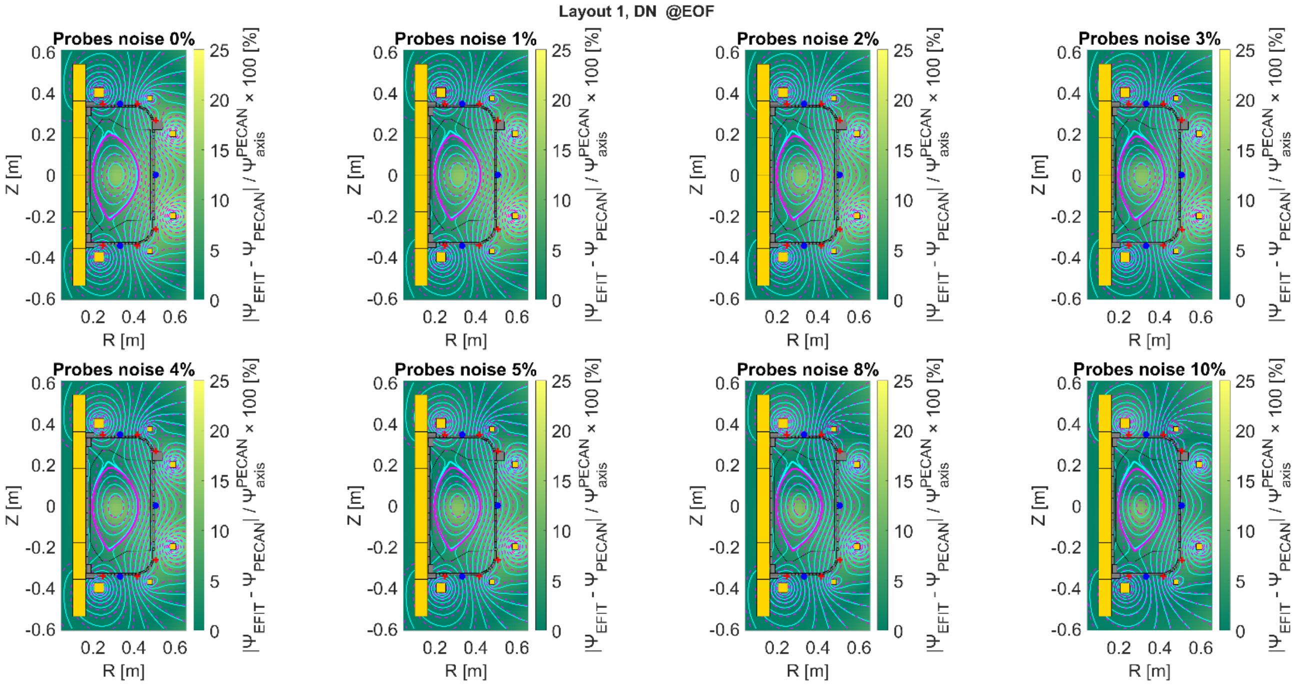

Figure 116: Comparison between EFIT and PECAN poloidal flux maps for increasing levels of synthetic noise applied to the magnetic measurements for the double-null configuration at EOF (Layout 1). The PECAN reference flux surfaces are shown in cyan, while the EFIT reconstructions are plotted in magenta.

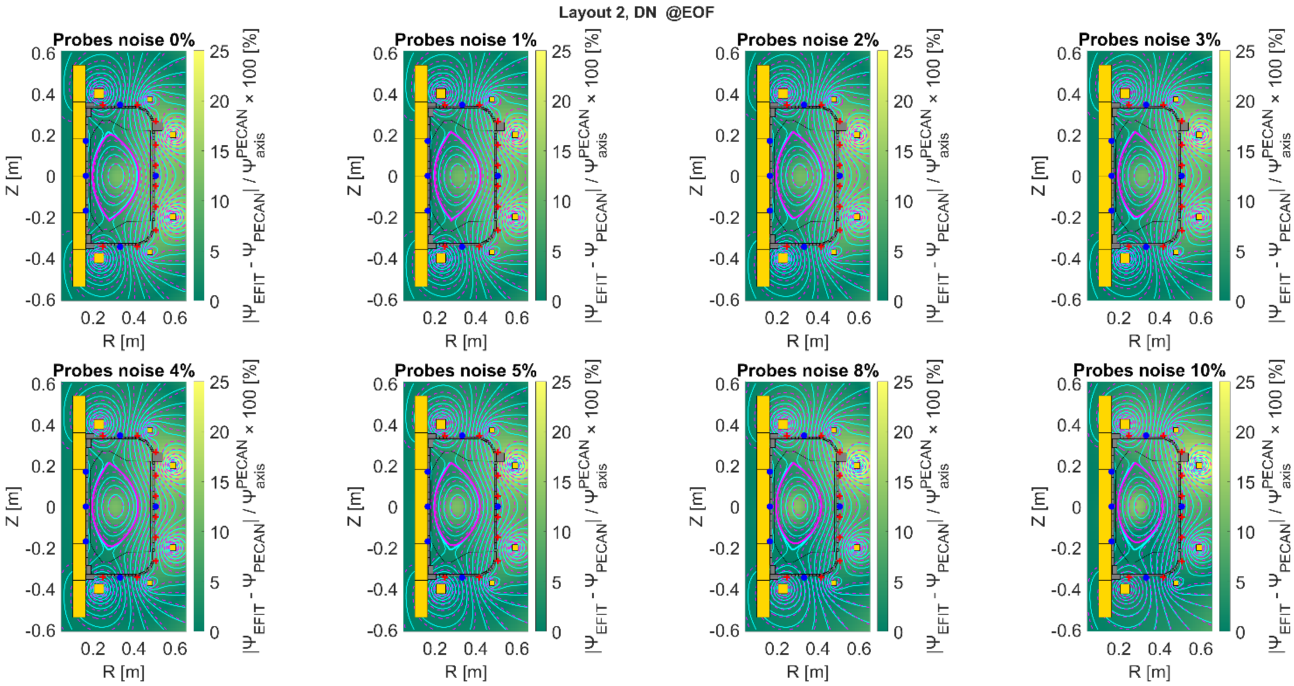

Figure 117: Comparison between EFIT and PECAN poloidal flux maps for increasing levels of synthetic noise applied to the magnetic measurements for the double-null configuration at EOF (Layout 2). The PECAN reference flux surfaces are shown in cyan, while the EFIT reconstructions are plotted in magenta.

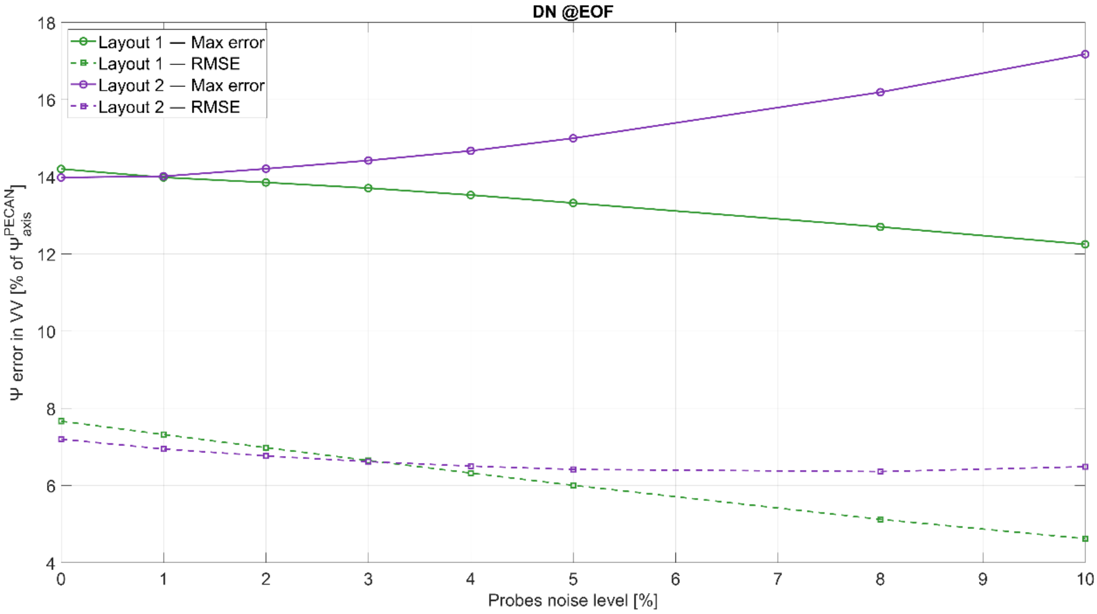

Figure 118: Reconstruction errors on the poloidal flux inside the VV region obtained from EFIT, evaluated with respect to the reference PECAN equilibrium for the double-null configuration at EOF and normalized respect the PECAN flux on the magnetic axis.

7.3 Discussion and Conclusions

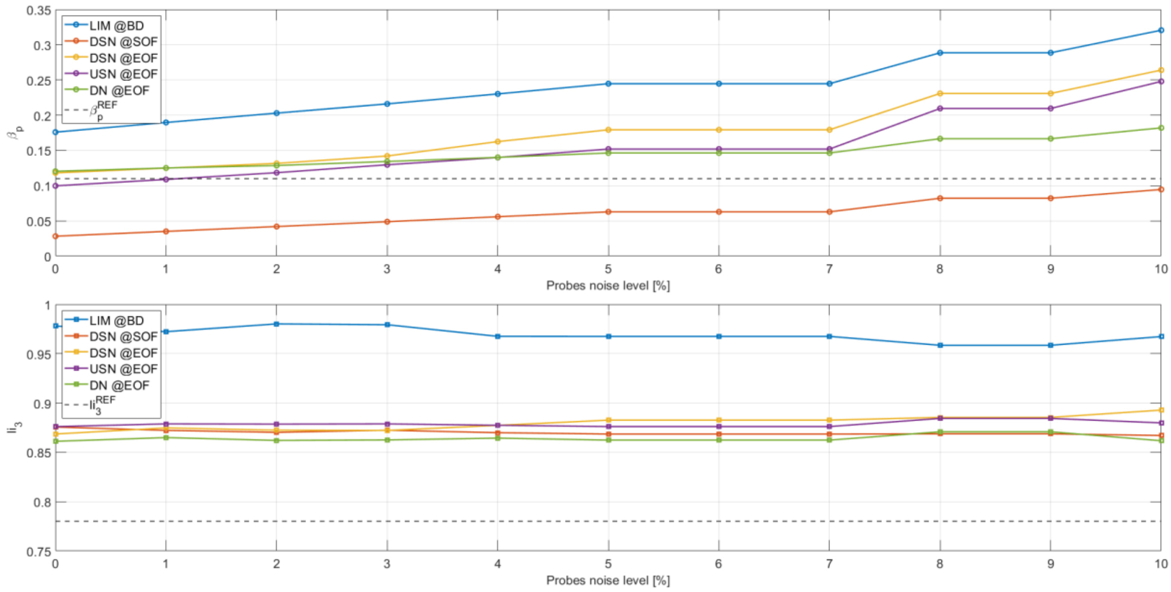

Figure 119: Scan of the poloidal beta and internal inductance values for the different reconstructions performed by EFIT by varying the noise level applied to the magnetic diagnostics. The reference values for β_p and ℓ_{i_3} are about 0.11 and 0.78, respectively.

In general, for all the analysed magnetic configurations of the TRUST tokamak, a nearly linear trend was observed between the imposed noise level and the reconstruction errors on both the

plasma boundary and the magnetic-axis position. This behaviour is fully consistent with expectations: increasing perturbations on the magnetic measurements directly degrade the conditioning of the inverse problem solved by EFIT, leading to a progressive deterioration of the reconstructed equilibrium. Quantitatively, for noise amplitudes up to 1–2 %, the boundary RMSE remains below 1–2 % of the machine radius, and the magnetic-axis displacement within a few millimetres with respect to the reference equilibrium. As the synthetic noise increases to 5 %, the boundary RMSE typically rises to 4–6 %, and the magnetic-axis error to 1–1.5 cm, depending on the configuration and diagnostic layout. The extended layout systematically reduces these errors by roughly 30–40 % compared to the minimal configuration, confirming its higher robustness against diagnostic uncertainty.
A similar correlation was also identified in the Ψ-mapping errors, which quantify the deviation between the reconstructed and reference poloidal flux distributions. For most configurations, the Ψ errors increased monotonically with the diagnostic noise level, confirming that the overall equilibrium reconstruction remains physically consistent and predictably sensitive to the quality of the magnetic measurements.
An exception to this general behaviour was observed for the double-null (DN) configuration. This case represents the most challenging magnetic topology among those analysed, as the presence of two null points substantially reduces the sensitivity of the external magnetic measurements to small perturbations of the plasma boundary. The reconstruction results clearly indicate that, as the measurement noise increases, EFIT tends to converge toward an effectively single-null solution, either upward or downward, instead of preserving the symmetric double-null topology. This effect can be directly observed in the reconstructed flux maps, where one of the nulls progressively disappears as the perturbation amplitude grows.
Such behaviour suggests that the current diagnostic layouts are likely insufficient to guarantee robust reconstruction of a true double-null equilibrium under realistic noise conditions. The anomalous trend of the Ψ-mapping errors, which diverges from the otherwise linear dependence observed in the single-null and limiter cases, should therefore be interpreted with caution. These results call for a dedicated sensitivity study and possibly an optimization of the sensor distribution, aimed at enhancing the ability of EFIT to distinguish between closely spaced magnetic nulls in symmetric configurations.
Concerning the scans of the scalar quantities β_p and l_i [74], the reconstructed trends exhibit deviations from the reference values that remain within reasonable limits but do not always follow a strictly monotonic behaviour with respect to the applied noise. In the present analysis, β_p was

evaluated according to the formulation $\beta_p(1)$, based on the volume-averaged plasma pressure and poloidal magnetic field, while l_i corresponds to the definition $l_i(3)$, normalized with respect to the geometric major radius.

These fluctuations can be attributed to the intrinsic coupling between β_p and l_i in low-elongation equilibria, where uncertainties in the reconstructed poloidal magnetic field tend to affect both quantities in a correlated manner. As discussed in [5], this coupling limits the independent determination of β_p and l_i, since both depend on similar integrals of the magnetic energy density over the plasma volume. Consequently, the modest discrepancies observed here are consistent with the expected sensitivity of these parameters to noise and to minor variations in the reconstructed field topology, rather than indicative of systematic reconstruction errors.

Overall, the results confirm that the proposed diagnostic layouts—particularly the minimal configuration consisting of three flux loops and six double-axis probes—are capable of providing stable EFIT reconstructions under moderate noise levels. Of course, these results also depend on the distance of the probes from the plasma. This distance is expected to increase in larger machines; however, one of the key advantages of a flexible device such as TRUST lies in its ability to assess how the information carried by the multipolar magnetic field produced by the plasma degrades with increasing distance and/or with the presence of noise in the magnetic signals [33]. At the present stage, the primary objective of the diagnostic system is the accurate reconstruction of the plasma boundary, which represents the essential prerequisite for reliable plasma position and shape control in TRUST. Nevertheless, these layouts should be regarded as preliminary design guesses, serving as a first step toward more comprehensive optimization studies aimed at refining sensor placement, improving conditioning, and enhancing robustness against measurement uncertainties in future operation.

8. First Prototypes of Magnetic Sensors

The realization of a reliable set of magnetic diagnostics represents a fundamental step in the development of any tokamak, since the control of plasma position, shape, and stability relies directly on accurate magnetic measurements. In the case of TRUST, the diagnostic system is still under definition, and the initial phase of work has therefore been devoted to the design and construction of prototype magnetic sensors. These prototypes are not intended as final components for the machine, but rather as proof-of-concept devices, developed with the dual objective of:

- Studying the complete design workflow for inductive sensors, from theoretical formulation to construction details.
- Testing calibration procedures in laboratory conditions, in order to validate the expected operating principles and to identify possible limitations of the acquisition chain.

In this context, the effort has been focused on inductive magnetic sensors, chosen for their robustness and widespread application in fusion devices. Their operation is governed by Faraday's law of induction:

$$\mathcal{E} = -\frac{d\Phi_B}{dt} \qquad [V] \tag{8.1}$$

where $\mathcal{E}$ is the induced electromotive force and Φ_B the magnetic flux concatenated with the sensor. In general form, the output voltage can be written as:

$$V_0 = k\frac{dm}{dt} \qquad [V] \tag{8.2}$$

where m represents the physical quantity of interest (magnetic flux, field, or current) and k is the proportionality constant, i.e. the sensitivity of the sensor. After integration and amplification, the physical quantity is recovered as:

$$a = \frac{V_2}{Gk} \tag{8.2}$$

with V_2 the measured voltage after signal processing, G the gain, and k the sensor constant.

The design and construction activities have focused on two sensor types of central relevance for tokamak operation:

- Double-axis magnetic probes (also named Mirnov coils or pick-up coils), intended for the measurement of local components of the poloidal magnetic field. Their sensitivity is expressed as

$$k = NA \qquad \left[\frac{V \cdot s}{T}\right] \tag{8.3}$$

where N is the number of turns and A the coil cross-sectional area. The geometric and electromagnetic properties of the sensor prototype are summarized below.

Table 25: geometric and electromagnetic properties of the magnetic probe prototype

	A [cm^2]	N	L [mH]	R [Ω]	k [Vs/T]
Magnetic probe (x-axis)	547.47	33	0.40	1.35	0.05
Magnetic probe (y-axis)	438.03	31	0.30	1.16	0.04

The sensor was tested in the laboratory to measure the maximum vertical magnetic field B_z produced along the axis of an industrial solenoid powered in current control mode with a sinusoidal excitation of 10 A amplitude at a frequency of 75 Hz. The measured values were then compared with three independent references: (i) the reading obtained from the magnetometer embedded in a smartphone, (ii) the value predicted by a finite element simulation reproducing the experimental setup, and (iii) the measurement provided by the prototype itself, obtained by acquiring the induced voltage across its terminals and converting it into magnetic field using the known sensitivity of the coil.

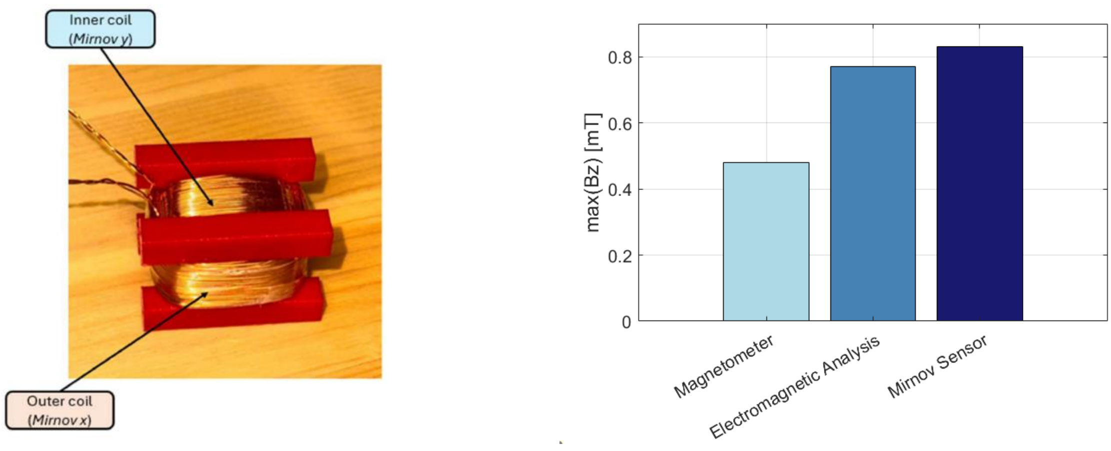

(a) (b)

Figure 120: (a) Prototype of the double–axis magnetic probe constructed for preliminary testing. (b) Summary histogram of the measurement campaign, reporting the maximum vertical magnetic field produced along the axis of an industrial solenoid.

The comparison highlights the consistency of the three approaches while revealing differences in absolute values. The smartphone magnetometer gave the lowest result (~0.5 mT), affected by limited resolution and alignment issues. The electromagnetic simulation predicted ~0.77 mT under idealized conditions, serving as a theoretical reference. The Mirnov sensor measured ~0.83 mT, in close agreement with the simulation, validating the prototype design. The absence of a dedicated calibration introduces some uncertainty, to be addressed in future work.

- Rogowski coils, designed for measuring plasma current and vessel eddy currents. Their sensitivity coincides with their self-inductance:

$$k = \frac{\mu_0 N^2 A}{\ell} \qquad \left[\frac{V \cdot s}{A} \equiv H\right] \tag{8.4}$$

where μ_0 is the magnetic permeability of vacuum, N the number of turns, A the cross-sectional area, and ℓ the coil length. The measured current is obtained from:

$$I = \frac{V_{\text{rog}} \cdot \ell}{\mu_0 N^2 A} \qquad [A] \tag{8.5}$$

A flexible Rogowski prototype, approximately 10 cm in length and consisting of about 160 turns, was constructed and calibrated against a reference clamp meter, using sinusoidal excitation at a fixed frequency of 380 Hz in order to operate within the linear range of the clamp as specified by the manufacturer. During the tests, the amplitude (voltage) of the sinusoidal signal was varied to generate different current values in the conductor, thereby enabling the calibration of the sensor across a range of operating conditions. The calibration confirmed the expected linear dependence of the induced voltage on the current derivative, while systematic offsets and discrepancies in sensitivity were identified, mainly due to acquisition system limitations.

(a)

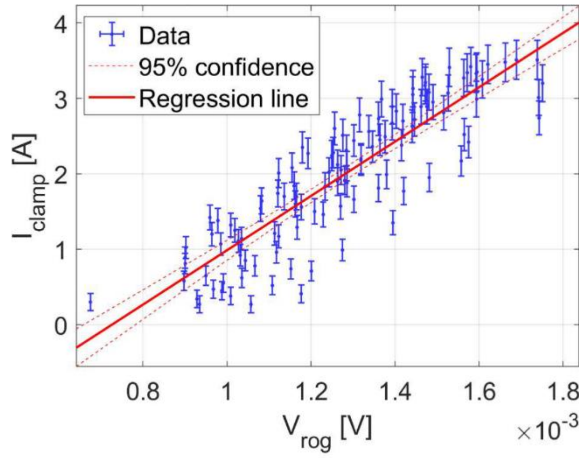

(b)

Figure 121: (a) Prototype of the Rogowski coil realized for preliminary testing. (b) Linear regression obtained during the calibration process, showing the relationship between the reference current and the voltage measured at the sensor terminals.

The intercept of the regression line in Figure 121(b) represents a systematic offset, which is most likely attributable to the acquisition system and to the inclusion of inaccurate or non-representative measurements in the linear fit. The presence of a non-zero intercept implies that the Rogowski coil would generate a finite output voltage even in the absence of current in the primary conductor, an unphysical behaviour that highlights the need for a more refined calibration procedure.

In conclusion, these first prototypes demonstrated the technical feasibility of in-house sensor development for TRUST, while at the same time stressing the preliminary nature of the results. The work carried out provides a solid methodological foundation for the future design of the optimized magnetic diagnostics that will be installed on the tokamak.

Conclusions

This thesis has explored the problem of plasma equilibrium and disruption analysis in tokamaks, combining the development of advanced finite element tools with the design and preliminary realization of magnetic diagnostics for the TRUST device. The work has been articulated along three main directions: the use of MAXFEA to generate a reliable database of disruption scenarios, the development of PECAN as a modern FEM solver for the Grad–Shafranov equation in both steady-state and transient regimes, and the application of these tools to the definition of a minimal magnetic diagnostic layout for TRUST, supported by the construction of sensor prototypes.

The disruption studies carried out with MAXFEA provided a set of reference scenarios for DEMO and TRUST, enabling the quantification of halo currents, eddy currents, and the resulting electromagnetic loads on passive structures. These results confirmed the ability of the code to serve as a predictive tool for the early design phases of fusion devices, especially in assessing the impact of disruptive events on structural integrity.

The development of PECAN represented a significant step forward in engineering plasma scenarios modelling. Implemented in DOLFINx and written in Python, the draft version of the code allows the solution of the Grad–Shafranov equation with a flexible finite element formulation, integrating the plasma with external circuits in a monolithic framework. The solver has been benchmarked against MAXFEA, demonstrating consistency in the reproduction of equilibria, while also offering the capability to address transient dynamics such as eddy currents in passive conductors. This makes PECAN a versatile platform that connects equilibrium reconstruction with disruption analysis in a unified approach. Nevertheless, regarding transient results, possible improvements are still required. In particular, the discrepancies observed with respect to MAXFEA in terms of eddy currents, halo currents, vertical forces, and the time shift of vertical displacement events suggest the need for further investigation. Future work should explore the origin of these differences, starting from refined mesh discretization and more accurate numerical treatments.

The application of these modelling tools to the TRUST device has led to the definition of a preliminary diagnostic layout, tested by generating synthetic magnetic signals with PECAN and reconstructing the plasma boundary using EFIT through the OMFIT framework. In the present study, only a limited number of magnetic probes and flux loops has been considered, consistently with the current hardware constraints of the acquisition system. Despite this limitation, the reconstructions proved capable of reliably reproducing the plasma boundary with an acceptable level of accuracy across different plasma configurations and time instants within the discharge scenario. It should be underlined that the proposed diagnostic arrangement represents a first design guess, which will be further refined and optimised as additional experimental data and improved sensor capabilities become available. In parallel, prototype sensors were constructed and tested, including dual-axis magnetic probes and a flexible Rogowski coil. Laboratory experiments confirmed their ability to detect the imposed magnetic fields and currents with good linearity, although discrepancies in sensitivity and offsets were observed due to limitations in the acquisition chain and the absence of a traceable calibration. These prototypes must therefore be regarded as exploratory devices, providing essential experience for the refined design of the final diagnostic set.

Looking forward, several perspectives emerge naturally from this work. On the modelling side, the PECAN framework will continue to evolve toward a more comprehensive simulation environment. The forthcoming developments include the introduction of a dedicated mesher, the extension of the circuit coupling architecture to handle parallel and hybrid electrical configurations, and the implementation of multiphysics coupling with external solvers such as ANSYS, enabling the evaluation of three-dimensional electromagnetic loads on passive components during plasma transients and disruptive events. These upgrades will progressively lead to a fully coupled electromagnetic–structural solver capable of supporting predictive design studies for next-generation devices.

Concurrently, the integration between PECAN and EFIT will be further consolidated to enable systematic studies on diagnostic placement and reconstruction accuracy, ultimately aimed at the optimisation of the TRUST magnetic layout. The results obtained so far demonstrated that in a machine TRUST like, without any nuclear implication, with the probes relatively close to the plasma and with a low environment noise a limited number of probes and flux loops is sufficient to determine, the plasma boundary with satisfactory accuracy for different plasma configurations and at various time instants within the discharge scenario. Of course in a reactor relevant machine the situation can be completely different, consequently the present diagnostic configuration should be regarded as a first design guess, to be refined and optimised as additional experimental data and sensor capabilities become available.

On the experimental front, the forthcoming commissioning of TRUST will provide essential data for the validation of both the numerical models and the diagnostic system, allowing iterative refinement of the layout, calibration procedures, and reconstruction workflow.

More broadly, the methodologies developed in this work — from the FEM-based synthetic diagnostics and coupled plasma–circuit modelling to the integration with EFIT — represent transferable tools that can be applied to the design and validation of diagnostic systems and disruption analyses in TRUST-like compact tokamaks and other axisymmetric fusion devices.

In conclusion, the work presented in this thesis demonstrates the effectiveness of combining advanced modelling tools with practical diagnostic development. It provides new capabilities for the analysis of plasma equilibria and disruptions, while at the same time delivering concrete input to the design of TRUST. Although further efforts are needed to improve sensor calibration, optimize diagnostic configurations, and validate models against experimental data, the results obtained establish a solid foundation for future progress and offer methodologies of general value for the fusion community.

Acknowledgments

The author would like to express his deepest gratitude to Prof. Giuseppe Calabrò, whose constant guidance and insightful supervision have been fundamental throughout the entire Ph.D. journey.

Special thanks are also extended to Dr. Riccardo Lombroni and Dr. Ivan Maione for their introduction to the PECAN project and for their continuous supervision and valuable support during the development of the related work.

The author wishes to sincerely thank Prof. Flavio Crisanti for the many stimulating discussions and for his scientific supervision of both the theoretical and experimental activities carried out within the TRUST project.

The author would also like to acknowledge the entire Fusion Team of the University of Tuscia, coordinated by Dr. Simone Carusotti, for their technical support and collaborative spirit, and in particular for the assistance provided during the activities related to the TRUST project.

The author is also grateful to Tokamak Energy Ltd. for the fruitful collaboration.

Special thanks are extended to Dr. Francesco Maviglia of the DEMO Central Team for the valuable discussions and exchanges regarding the DEMO activities and for his technical advice related to the analyses performed with the MAXFEA code.

Finally, sincere appreciation is expressed to Dr. Zhengping Luo of ASIPP (*Institute of Plasma Physics, Chinese Academy of Sciences*) for his guidance and support during the implementation and use of the EFIT code for the analysis of the TRUST magnetic diagnostics.

References

[1] International Energy Agency (IEA). (2024). World Energy Outlook 2024. Paris: IEA Publications.

[2] International Atomic Energy Agency (IAEA). (2024). World Fusion Outlook 2024. Vienna: IAEA Publications.

[3] Claessens, M. (2020). ITER: The Giant Fusion Reactor: Bringing a Sun to Earth. Springer.

[4] Stacey, W. M. (2010). Fusion: An Introduction to the Physics and Technology of Magnetic Confinement Fusion. Wiley.

[5] Wesson, J. (2011). Tokamaks (4th ed.). Oxford University Press.

[6] A W Morris et al 2022 Plasma Phys. Control. Fusion **64** 064002

[7] B. Bigot 2019 Nucl. Fusion **59** 112001

[8] Artsimovich L., "Tokamak devices", Nucl. Fusion, vol. 12, no. 2, pp. 215–252, 1972.

[9] Chen F.F., An Introduction to Plasma Physics and Controlled Fusion, 3rd edition, Springer, 2016.

[10] ITER Organization, "The Tokamak Concept", https://www.iter.org/mach/Tokamak

[11] ITER Organization, ITER Technical Basis, IAEA, Vienna, 2002

[12] Kikuchi M., Lackner K., Tran M.Q., Fusion Physics, International Atomic Energy Agency, Vienna, 2012.

[13] Ongena J., Van Oost G., "Energy for future centuries: Will fusion be an inexhaustible, safe and clean energy source?" Fusion Science and Technology, vol. 61, no. 2, pp. 2–21, 2012

[14] Aymar R., Barabaschi P., Shimomura Y., "The ITER design", Plasma Physics and Controlled Fusion, vol. 44, no. 5, pp. 519–565, 2002

[15] C.F. Maggi et al 2024 Nucl. Fusion **64** 112012

[16] Romanelli, F., et al. "Fusion Electricity: A roadmap to the realisation of fusion energy." EFDA, European Fusion Development Agreement, 2012

[17] Federici, G., et al. "Overview of the design approach and prioritization of R&D activities towards an EU DEMO." Fusion Engineering and Design, Vol. 109–111, pp. 1464–1474, 2016

[18] F. Romanelli et al 2024 Nucl. Fusion **64** 112015.

[19] F. Crisanti et al 2024 Nucl. Fusion **64** 106040

[20] Creely AJ, Greenwald MJ, Ballinger SB, et al. Overview of the SPARC tokamak. Journal of Plasma Physics. 2020;86(5):865860502.

[21] M. Scarpari, et al., "Development of SPARC plasma disruption database through electromagnetic predictive MAXFEA modelling", Fusion Eng. Des., Vol. 204, 2024.

[22] E.S. Marmar et al 2015 Nucl. Fusion **55** 104020

[23] K. Hanada, et al., "Overview of recent progress on steady state operation of all-metal plasma facing wall device QUEST", Nuclear Materials and Energy, vol. 27, 2021

[24] O. Grover, et al., "Remote operation of the GOLEM tokamak for Fusion Education", Fusion Eng. Des., vol. 112, 2016.

[25] S.J. Doyle, et al., "Magnetic equilibrium design for the SMART tokamak", Fusion Eng. Des., vol. 171, 2021.

[26] D. Kingham, et al., "The spherical tokamak path to fusion power: Opportunities and challenges for development via public–private partnerships", Phys. Plasmas, Vol. 31, 2024.

[27] J.R. Harrison et al 2024 Nucl. Fusion **64** 112017

[28] J.W. Berkery, et al., "NSTX-U research advancing the physics of spherical tokamaks", Nuclear Fusion, Volume 64,

Number 11, 2024.

[29] S.A.M. McNamara et al 2024 Nucl. Fusion **64** 112020.

[30] R. Lombroni, et al., "Use of MAXFEA code in combination with ANSYS APDL to study the Electro-Magnetic behaviour of the new ST40 Inner Vacuum Chamber (IVC2) proposal during a plasma VDE", Fusion Eng. Des., vol. 192, 2023.

[31] S. Carusotti, et al., "Structural behaviour characterization of ST40 Inner Vacuum Chamber (IVC2) during a plasma VDE using ANSYS Workbench", Fusion Eng. Des., vol. 192, 2023

[32] S. Carusotti, R. Lombroni, M. Scarpari, M. Notazio, A. Pizzuto, F. Crisanti, P. Fanelli, G.Calabrò, "Preliminary study on alternative magnetic layout (AML) for tokamaks reactors in the TRUST project framework" (2025), Engineering and Design, Elsevier

[33] Carusotti S., Scarpari M., Lombroni R., Notazio M., Balbinot L., Crisanti F., Fanelli P., Calabrò G., "Overview of university-class Tokamak TRUST: Preliminary characterization of plasma scenario and disruption studies", Fusion Engineering and Design, 2025

[34] N.W. Eidietis et al., "The ITPA disruption database", Nuclear Fusion, 55 (2015), IOP Publishig

[35] F. Giorgetti, C. Bachmann, V.G. Belardi, G. Calabrò, S. Ciufo, P. Fanelli, M. Fulici, F. Maviglia, S. Minucci, F. Vivio, "Dynamic behaviour of DEMO vacuum vessel during plasma vertical displacement events", Fusion Engineering and Design, Volume 159, October 2020, 111876

[36] R. Mozzillo et al., Preliminary structural assessment of DEMO vacuum vessel against a vertical displacement event, Fusion Engineering and Design, 2016,

[37] C. Bachmann, M. Sugihara, R. Roccella, G. Sannazzaro, Y. Gribov, V. Riccardo, T.C. Hender, S.N. Gerasimov, G. Pautasso, A. Belov, E. Lamzin, M. Roccella, "Specification of asymmetric VDE loads of the ITER tokamak", Fusion Engineering and Design, Vol. 86, 2011, pp. 1915–1919.

[38] Albanese, R., "CREATE-NL+: A robust control-oriented free boundary dynamic plasma equilibrium solver", Fusion Engineering and Design, Vols. 96–97, October 2015, pp. 664–667.

[39] FreeGS, https://github.com/freegs-plasma/freegs

[40] FreeQDSK , https://github.com/freegs-plasma/FreeQDSK

[41] Freidberg JP., "Ideal MHD", Cambridge University Press, 2014.

[42] Ambrosino G., Albanese R., "Magnetic Control of Plasma Current, Position, and Shape in Tokamaks: A survey of modeling and control approaches," IEEE Control Syst., vol. 25, no. 5, pp. 76–92, 2005

[43] G. Sias et al., "Electromagnetic analysis of vertical displacement events in EU-DEMO using the MAXFEA code," Nuclear Fusion, vol. 62, no. 7, 076004, 2022

[44] J. L. Luxon and B. B. Brown, "Magnetic analysis of non-circular cross section tokamaks," Nucl. Fusion, vol. 813, 1982

[45] V. D. Shafranov, "Determination of the parameters β_I and l_i in a tokamak for arbitrary shape of plasma pinch cross-section", Plasma Physics, Vol. 13, pp. 757 to 762

[46] F. Villone, L. Barbato, S. Mastrostefano, and S. Ventre, "Coupling of nonlinear axisymmetric plasma evolution with three-dimensional volumetric conductors," Plasma Phys. Control. Fusion, 2013

[47] S. Miyamoto et al., "Inter-code comparison benchmark between DINA and TSC for ITER disruption modelling," Nucl. Fusion, vol. 54, no. 8, 2014

[48] Barabaschi P., "The MAXFEA code", Plasma Control Technical Meeting, 1993.

[49] Villone F., Ramogida G., Rubinacci G., “Electromagnetic disruption analysis in IGNITOR”, Fusion Engineering and Design, vol. 93, pp. 57-68, 2015.

[50] R. Lombroni, F. Giorgetti, G. Calabrò, P. Fanelli, and F. Villone, “Using MAXFEA code in combination with ANSYS APDL for the simulation of plasma disruption events on EU DEMO,” Fusion Engineering and Design, vol. 170, p. 112697, 2021

[51] F. Giorgetti, et al., “Vertical Displacement Events analysis using MAXFEA code in combination with ANSYS APDL in the final design stage of the DTT Vacuum Vessel”, Fusion Eng. Des., vol. 184, 2022.

[52] I. A. Baratta, J. P. Dean, J. S. Dokken, M. Habera, J. Hale, C. N. Richardson, M. E. Rognes, M. W. Scroggs, N. Sime, and G. N. Wells, “DOLFINx: The next generation FEniCS problem solving environment”, Preprint, ORBilu – University of Luxembourg, 2023. doi: 10.5281/zenodo.10447666. Available: https://orbilu.uni.lu/handle/10993/59327

[53] S. Liu, Q. Tang, and X.-Z. Tang, “A Parallel Cut-Cell Algorithm for the Free-Boundary Grad–Shafranov Problem,” SIAM Journal on Scientific Computing, vol. 43, no. 6, pp. B1263–B1287

[54] https://idm.euro-fusion.org/?uid=2SCEK4 (private communication)

[55] C. Geuzaine and J.-F. Remacle, “Gmsh: A three-dimensional finite element mesh generator with built-in pre- and post-processing facilities”, International Journal for Numerical Methods in Engineering, Vol. 79, Issue 11, pp. 1309–1331, 2009.

[56] Maviglia, F., Bachmann, C., Federici, G., Franke, T., Siccinio, M., et al. (2022). Integrated design strategy for EU-DEMO first wall protection from plasma transients. Fusion Engineering and Design, 177, 113067

[57] Melaragni, L., Scarpari, M., Carusotti, S., Notazio, M., Lombroni, R., Ramogida, G., Migliori, S., Frattolillo, A., Angelucci, M., & Calabrò, G. (2025). Preliminary modeling of disruption plasma scenario in view of a shattered pellet injection in DTT machine. Fusion Science and Technology, 81(5), 515–529

[58] M. Neri, P. Zumbolo, and R. Albanese, “Accurate plasma boundary calculation using linear triangular finite elements,” Comput. Phys. Commun., vol. 311, p. 109574, 2025, doi: 10.1016/j.cpc.2025.109574.

[59] A. Moret, et al., "Vertical instability analysis and control in the TCV tokamak," Nuclear Fusion, vol. 37, no. 6, pp. 825–834, 1997.

[60] G. Vayakis, B. Alper, J. Brzozowski, et al., Development of the ITER magnetic diagnostic set, Rev. Sci. Instrum. 83, 10D712 (2012).

[61] E. J. Strait, Magnetic diagnostic system of the DIII-D tokamak, Rev. Sci. Instrum. 77, 023502 (2006)

[62] P. Moreau, A. Le-Luyer, P. Spuig, P. Malard, F. Saint-Laurent, J. F. Artaud, J. Morales, B. Faugeras, H. Heumann, B. Cantone, M. Moreau, C. Brun, R. Nouailletas, E. Nardon, B. Santraine, A. Berne, P. Kumari, S. Belsare, and the WEST Team, The new magnetic diagnostics in the WEST tokamak, Rev. Sci. Instrum. 89, 10I117 (2018)

[63] F. Puentes-del Pozo, P. Vicente-Torres, D. J. Cruz-Zabala, S. Munaretto, M. Garcia-Munoz, E. Viezzer, A. Mancini, A. Rodriguez-Gonzalez, J. Sanchez-Gamino, and J. Segado-Fernandez, Design and development of the magnetic diagnostic systems for the first operational phase of the SMART tokamak, Rev. Sci. Instrum. 95, 083503 (2024)

[64] Tokamak Energy Ltd. “ST40 Magnetic Diagnostics Overview.” Technical Note, 2024.

[65] IPP Prague. “Magnetic diagnostics of the COMPASS tokamak.” ipp.cas.cz, 2024.

[66] L.L. Lao et al., Reconstruction of Current Profile Parameters and Plasma Shapes in Tokamaks, Nucl. Fusion 25, 1611 (1985).

[67] O. Meneghini and L.L. Lao, Integrated Modeling of Tokamak Experiments with OMFIT, Plasma and Fusion

Research 8, 2403009 (2013).
[68] Moret, J.-M., Buhlmann, F., Fasel, D., Hofmann, F., & Tonetti, G. (1992). Magnetic measurements on the TCV Tokamak (CRPP Report No. LRP 28107). École Polytechnique Fédérale de Lausanne, Centre de Recherches en Physique des Plasmas (CRPP).
[69] Schmitt, J. C., Bialek, J., Lazerson, S., & Majeski, R. (2014). Magnetic diagnostics for equilibrium reconstructions with eddy currents on the lithium tokamak experiment. Review of Scientific Instruments, 85(11), 11E814.
[70] Jiráková, K., Kovanda, O., Adamek, J., Komm, M., & Seidl, J. (2019). Systematic errors in tokamak magnetic equilibrium reconstruction: A study of EFIT++ at tokamak COMPASS. Journal of Instrumentation, 14(11), C11020.
[71] Romero, J. A., & Svensson, J. (2013). Optimisation of out-vessel magnetic diagnostics for plasma boundary reconstruction in tokamaks. arXiv preprint arXiv:1301.7617.
[72] J.-M. Moret, et. al., "Tokamak equilibrium reconstruction code LIUQE and its real time implementation", Fusion Eng. Design, 91, 2015.
[73] P. F. Buxton, GSFit, https://github.com/tokamak-energy/gsfit, 2025
[74] F. Alladio, F. Crisanti, “Analysis of MHD equilibria by toroidal multipolar expansions”, 1986 Nucl. Fusion 26 1143

Appendix

Verification and Validation Example: Magnetostatics - Single Coil

This appendix presents a simple verification and validation (V&V) test performed on the electromagnetic solver to assess its accuracy in reproducing the magnetic field generated by a single axisymmetric current loop. The configuration represents a fundamental benchmark problem, allowing direct comparison between the numerical solution obtained through the finite element formulation and the analytical Biot–Savart law.

The test considers a single circular coil of radius $R_c = 5\ mm$ placed at $(0.5, 0.0)\ m$ of the D-shaped computational domain ($R_{domain} = 10\ m$), ideally carrying a steady toroidal current of $I_c = 1$ MA. The magnetic permeability is assumed to be that of vacuum:

$$\mu_0 = 4\pi \times 10^{-7}\ \text{H/m}$$

The numerical simulation is performed with a second-order finite element discretization (CG2) on a structured triangular mesh, refined near the coil cross-section. The total current is uniformly distributed in the coil region so that: $J_\phi = I_c/A_c$, where A_c is the coil's cross-sectional area. The poloidal flux distribution calculated by PECAN is reported in Figure 122.

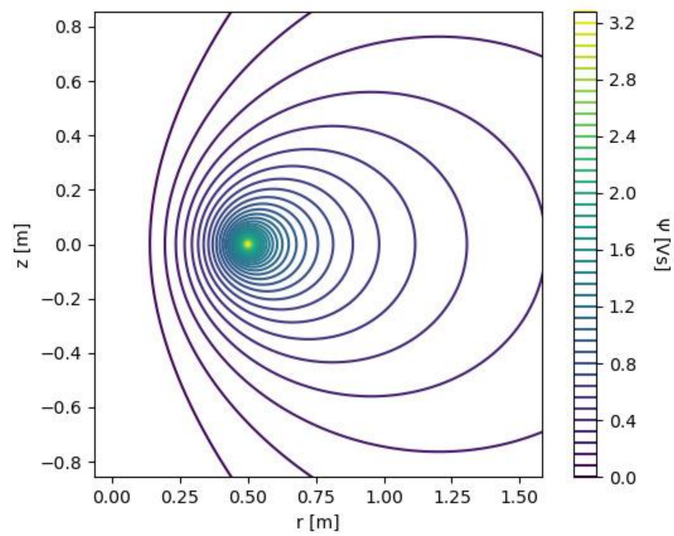

Figure 122: poloidal magnetic flux generated by a single coil

For a thin circular filament of radius R_c centered at $(0, Z)$ carrying a steady current I_c, the vertical component of the magnetic field along the coil axis is given by the Biot–Savart law:

$$B_z(0, Z) = \frac{1}{2}\frac{\mu_0 I_c R_c^2}{(\mathrm{R}^2 + (Z - Z_c)^2)^{3/2}}$$

With R ideally equals to 0 along the coil axis.

This expression is valid under the assumption that the coil cross-section is negligible compared to its radius. In the present case, the coil thickness is sufficiently small to justify this filament approximation, which allows analytical comparison with the numerical results.

The comparison between the numerical and analytical values of B_Z along the coil axis ($R = 0$) is shown in Figure 123, demonstrating a good agreement between the two solutions.

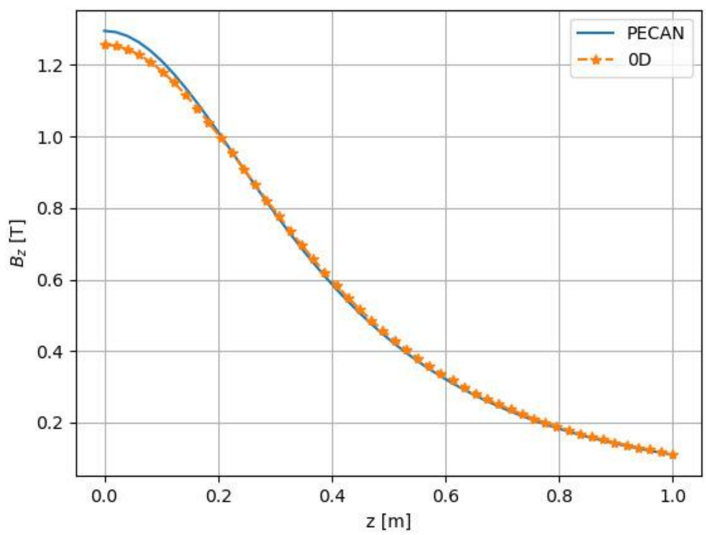

Figure 123: comparison between the numerical and analytical values of B_Z along the coil axis ($R = 0$).

Verification and Validation Example: Transient – Single Passive Circuit

This appendix presents a verification and validation (V&V) test performed on the transient electromagnetic solver to assess its accuracy in reproducing the inductive coupling between active and passive coils. The configuration reproduces the physical conditions of the DEMO-LAR 2024 model, which is the same configuration adopted for the analyses presented in Chapters 4.1 and 6.

In this test, the vacuum vessel is considered as a non-conductive region, so that only the coupling between the active coil and the passive divertor circuit is evaluated. A linear current ramp-down is imposed on one of the central solenoid modules (the CS3U module), while the induced current in the divertor circuit (DIV) is computed and compared with the theoretical value expected from Faraday's law.

The DIV circuit is represented by two coils connected in anti-series, each consisting of 9 turns, placed symmetrically near the divertor region. The corresponding electrical parameters, derived from the MAXFEA code, are: $L = 4.4 \times 10^{-3}$ H, $R = 2.09 \times 10^{-2}\ \Omega$ and mutual inductance with the driving coil $M = 4.36 \times 10^{-7}$ H.

The governing differential equation describing the induced current I_{DIV} in the passive circuit is:

$$L \frac{dI_{DIV}}{dt} + RI_{DIV} = -M \frac{dI_{CS}}{dt}$$

which expresses the Faraday law for a single-turn equivalent loop. Its discrete analytical solution, used as reference for the numerical validation, reads:

$$I_{DIV}^{n+1} = \alpha I_{DIV}^{n} - \frac{M}{L}\left(I_{CS}^{n+1} - I_{CS}^{n}\right), \text{with } \alpha = e^{-\frac{\Delta t}{\tau}},\ \tau = \frac{L}{R}$$

The numerical simulation is carried out using a second-order finite element discretization (CG2) on the DEMO-LAR 2024 axisymmetric mesh. The solver computes, at each time step, the evolution of both the poloidal magnetic flux and the induced currents in the passive conductors. The imposed time step is $\Delta t = 10^{-4}$ s, and the total simulated duration is $t_{end} = 3 \times 10^{-3}$ s.

The current in the CS3U module is linearly decreased from its initial value of -8.63 MA to zero through a series of discrete events. The corresponding evolution of the induced current in the DIV circuit is automatically obtained from the electromagnetic coupling between the two regions.

Figure 123 reports the comparison between the induced current calculated by PECAN and the theoretical 0D solution derived from the previous expression together with the imposed current ramp-down in the CS3U coil. The two curves are almost perfectly superimposed throughout the transient, confirming that the solver correctly reproduces the physical mechanism of inductive coupling governed by Faraday's law.

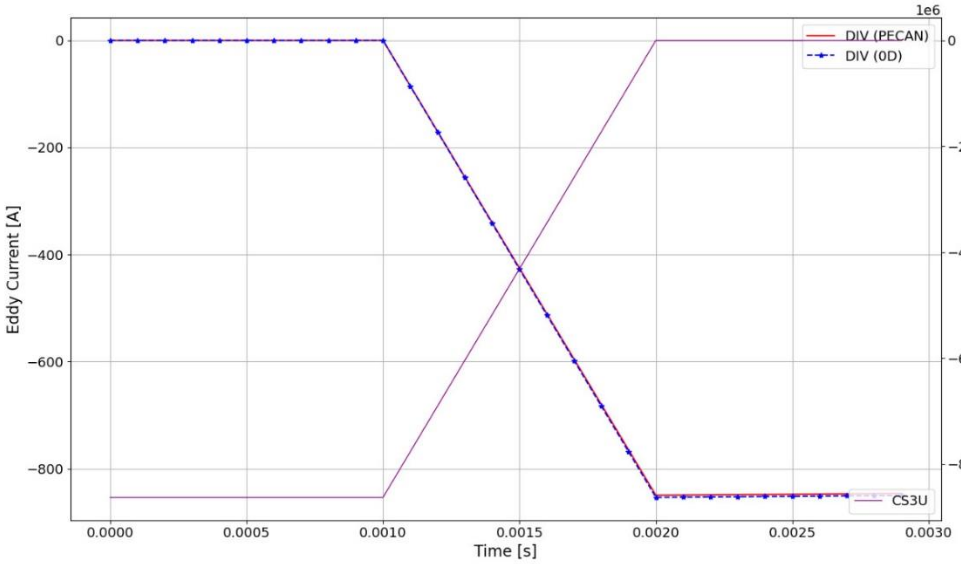

Figure 124: comparison between the induced current calculated by PECAN and the theoretical 0D solution derived from the previous expression together with the imposed current ramp-down in the CS3U coil.

Verification and Validation Example: Transient – Coupled Passive Circuits

This appendix presents a verification and validation (V&V) test performed on the transient electromagnetic solver to assess its accuracy in reproducing the mutual inductive coupling between multiple passive circuits. The configuration reproduces the physical conditions of the DEMO-LAR 2024 model, which is the same configuration adopted for the analyses presented in Chapters 4.1 and 6.

As in the previous benchmark, the vacuum vessel is considered as a non-conductive region, so that the induced currents arise solely from the electromagnetic coupling between the active central solenoid (CS) and the passive divertor and equatorial circuits. A linear current ramp-down is imposed on the CS3U module, while the induced currents in both the divertor circuit (DIV) and the equatorial circuit (EQ) are computed and compared with the theoretical values predicted by the coupled circuit equations derived from Faraday's law.

The DIV and EQ circuits are each composed of two coils connected in anti-series, with 9 turns per coil, positioned respectively near the divertor region and around the equatorial plane. Their self-inductances, resistances, and mutual inductances (from MAXFEA data) are:

$$L_{DIV} = 4.4 \times 10^{-3}\ \mathrm{H}, R_{DIV} = 2.09 \times 10^{-2}\ \Omega$$
$$L_{EQ} = 8.7 \times 10^{-3}\ \mathrm{H}, R_{EQ} = 3.47 \times 10^{-2}\ \Omega$$
$$M_{DIV,EQ} = M_{EQ,DIV} = -2.07 \times 10^{-4}\ \mathrm{H}.$$

The mutual inductances with the driving CS3U coil are $M_{CS,DIV} = 4.36 \times 10^{-7}$ H and $M_{CS,EQ} = 2.84 \times 10^{-6}$ H.

The transient evolution of the induced currents I_{DIV} and I_{EQ} can be described by the following coupled differential system:

$$\begin{cases} L_{11}\dfrac{dI_{DIV}}{dt} + R_{11}I_{DIV} + L_{12}\dfrac{dI_{EQ}}{dt} = -M_{CS,DIV}\dfrac{dI_{CS}}{dt} \\ L_{21}\dfrac{dI_{DIV}}{dt} + R_{22}I_{EQ} + L_{22}\dfrac{dI_{EQ}}{dt} = -M_{CS,EQ}\dfrac{dI_{CS}}{dt} \end{cases}$$

The corresponding 0D analytical reference model is implemented using a Backward Euler time-integration scheme, which provides the theoretical prediction of the induced currents for direct comparison with the finite element (FEM) solution obtained by PECAN.

The numerical simulation is performed using a second-order finite element discretization (CG2) on the DEMO-LAR 2024 axisymmetric mesh, with a time step of $\Delta t = 10^{-4}$ s and a total simulation time of $t_{end} = 3 \times 10^{-3}$ s. At each time step, the solver computes the evolution of the poloidal magnetic flux and the corresponding eddy currents in the two passive loops. The imposed CS3U current decreases linearly from its initial value of -8.63 MA to zero.

Figure 125 shows the comparison between the induced currents in the DIV and EQ circuits calculated by PECAN and those obtained from the analytical 0D coupled model, together with the imposed CS3U current ramp-down. The agreement between the numerical and theoretical curves is excellent, with the FEM solution reproducing both the amplitude and phase of the induced transients.

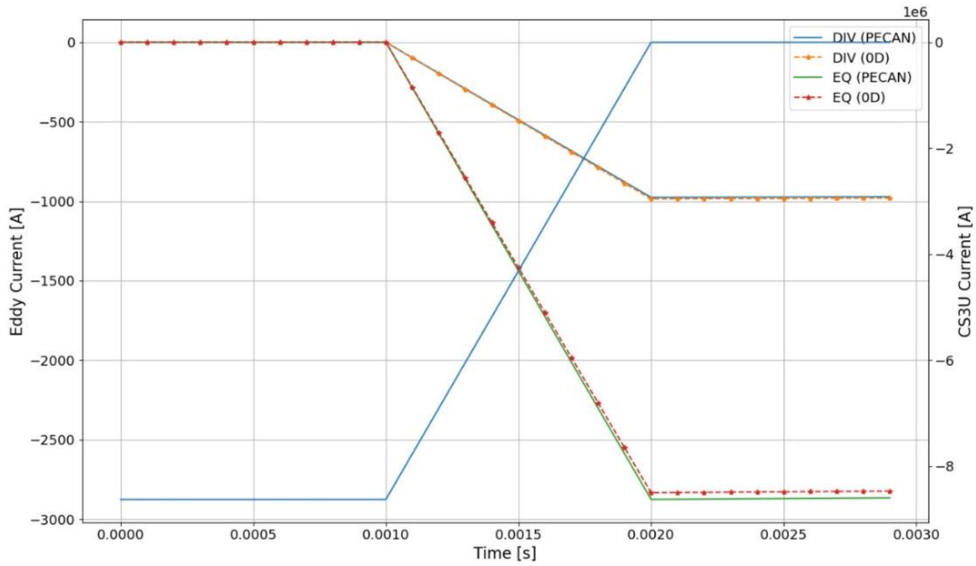

Figure 125: comparison between the induced currents in the DIV and EQ circuits calculated by PECAN and those obtained from the analytical 0D coupled model, together with the imposed CS3U current ramp-down.